A New Era for Direct Detection Experiments: Probing New Neutrino Physics at Dark Matter Detectors with Solar Neutrinos

DORIAN WARREN PRAIA-DO-AMARAL

PRAIA-DO-AMARAL, DORIAN WARREN (2023) A New Era for Direct Detection Experiments: Probing New Neutrino Physics at Dark Matter Detectors with Solar Neutrinos. Doctoral thesis, Durham University.

A New Era for Direct Detection Experiments:

Probing New Neutrino Physics at Dark Matter Detectors with Solar Neutrinos

Dorian W. P. Amaral

A Thesis presented for the degree of
Doctor of Philosophy

Department of Physics
Durham University
United Kingdom

February 2023

A New Era for Direct Detection Experiments:

Probing New Neutrino Physics at Dark Matter Detectors with Solar Neutrinos

Dorian W. P. Amaral

Submitted for the degree of Doctor of Philosophy

February 2023

Abstract: Dark matter direct detection experiments are about to hit a complex obstacle—the irreducible background of solar neutrinos. While this will complicate the search for dark matter, it will usher in the beginning of a new search for beyond Standard Model neutrino physics. However, the use of solar neutrinos as a signal of novel physics in these detectors is still in its infancy. To further explore the potential of next-generation and far-future direct detection experiments in this vein, we consider how deviations in the solar neutrino rate can be used as an indirect probe of new physics in the neutrino sector. We consider beyond Standard Model extensions that can serve as solutions to the present tension in the muon's anomalous magnetic moment, as well as the more general framework of neutrino non-standard interactions. In all cases, we find that future direct detection experiments will be able to either probe as-yet unconstrained new neutrino physics or provide us with information complementary to dedicated neutrino experiments. We conclude that direct detection experiments are poised to become key players in the field of neutrino physics, contributing to a compelling research mission beyond their search for dark matter.

Contents

List of Figures

List of Abbreviations

BNL Brookhaven National Laboratory.

BP Benchmark Point.

BSM Beyond Standard Model.

CC Charged Current.

CCM Coherent Captain Mills.

CEνNS Coherent Elastic Neutrino-Nucleus Scattering.

CL Confidence Level.

DARWIN DARk matter WImp xenoN observatory.

DD Direct Detection.

DM Dark Matter.

EνES Elastic Neutrino-Electron Scattering.

EM Electromagnetic.

ER Electron Recoil.

ESS European Spallation Source.

EW Electroweak.

FCNC Flavour-Changing Neutral Currents.

G2 Generation-2.

G3 Generation-3.

GWS Glashow-Weinberg-Salam.

GXe Gaseous Xenon.

HVP Hadronic Vacuum Polarisation.

HZ High-Metallicity.

LAr Liquid Argon.

LH Left-Handed.

LXe Liquid Xenon.

LZ Low-Metallicity.

LZ LUX-ZEPLIN.

MOT Muons On Target.

NC Neutral Current.

NR Nuclear Recoil.

NSI Non-Standard Interaction.

PMNS Pontecorvo-Maki-Nakagawa-Sakata.

RH Right-Handed.

RRPA Relativistic Random-Phase Approximation.

S1 Primary Scintillation signal.

S2 Secondary Scintillation signal.

SM Standard Model.

SNO Sudbury Neutrino Observatory.

SS Spallation Source.

SSB Spontaneous Symmetry Breaking.

SSM Standard Solar Model.

TPC Time Projection Chamber.

VEV Vacuum Expectation Value.

WIMP Weakly Interacting Massive Particle.

WZ Wess-Zumino.

Declaration

The work in this thesis is based on research carried out at the Institute for Particle Physics Phenomenology at Durham University. No part of this thesis has been submitted elsewhere for any degree or qualification. This thesis is partly based on joint research, as detailed below.

- Chapter 5 is based on Ref. [1], "Solar Neutrino Probes of the Muon Anomalous Magnetic Moment in the Gauged $U(1)_{L_\mu - L_\tau}$", published in the Journal of High Energy Physics.
- Chapter 6 is based on Ref. [2], "Confirming $U(1)_{L_\mu - L_\tau}$ as a Solution for $(g-2)_\mu$ with Neutrinos", published in the European Physical Journal C.
- Chapter 7 is based on Ref. [3], "A Direct Detection View of the Neutrino NSI Landscape", a preprint at the time of submission.

Acknowledgements

To my supervisor, David G. Cerdeño, thank you for your support and guidance throughout the past four years. You have guided me as a physicist and shown me what doing research is all about.

To my collaborators, Andrew Cheek, Patrick Foldenauer, and Elliott Reid, you have made the work not only possible but so much more enjoyable. Thank you all for that. Patrick, I would like to thank you especially for helping me on my future path as a scientist, as well as for proofreading part of this thesis.

To Andrew Blance, Parisa Gregg, and Joseph Walker, PhD life would certainly have been a lot bleaker without the antics of OC321 (*let's have some fun*). Thank you all for making life brighter just by being you. Joe, I would like to extend my gratitude to you in particular. We have talked about every topic under the Sun, and I would like to think that we have walked this path, however difficult, together.

To Louise, thank you for everything. All of it. 26 years of it and what is to come. You have always been there, no matter what and no matter when, and I have always known that. Without you, this would have only been a dream. Thank you for giving me the power to make it a reality.

To Michelle and Kevin, I completed so much of my work while being supported by you. I am immensely thankful for your generosity, understanding, and love. To the Children of the Earth, you are all wonderful.

Finally, to Alice, words cannot express how grateful I am for you. You have been my everything, and I cannot imagine having done any of this without you. Thank you for your patience, your warmth, and your support. Thank you for believing in me, being beside me, and caring for me. Most of all, thank you for your love. You have mine. Forever and always.

CHAPTER 1

Introduction

Dart matter (DM) direct detection (DD) experiments have achieved an incredible feat. Following only a few decades of operation, they have significantly constrained the potential properties of the paradigmatic dark matter candidate—the weakly interacting massive particle. However, these experiments are about to hit a complicated obstacle. The next generation of DD experiments will become so sensitive that they will begin to expose themselves to an irreducible background of solar neutrinos. While this will pose a serious complication for the dark matter search, it will herald the beginning of a new search for new physics in the neutrino sector. The potential of DD experiments in this vein remains a topic of intense research, providing them with a compelling research mission beyond the hunt for dark matter. If these experiments are to remain relevant in the decades to come, the case for such an alternative mission is a critical one to make.

In this thesis, we will further develop the case for the use of DD experiments as neutrino observatories. Using the flux of neutrinos generated by solar fusion reactions, we will explore how potential deviations from the expected neutrino scattering rate can be used as an indirect probe of new physics in the neutrino sector. We will argue that, through their unique ability to detect both nuclear and electron recoils, future DD experiments will be able to provide competitive, if not leading, results beyond those of dedicated neutrino experiments. Through this thesis, we provide the DD community with a guiding light into a bold new era of physics exploration.

We begin by introducing the neutrino as a particle within the Standard Model (SM) and slightly beyond it in Chapter 2. This chapter follows the history of the neutrino: from the first hints of its existence in radioactivity experiments in the late 19th-century to the eventual discovery of neutrino oscillations in the early 21st-century. We discuss the fundamentals of electroweak theory and neutrino oscillations, focusing in particular on the propagation of solar neutrinos. We conclude with a brief account of how to give the neutrino a mass.

We introduce DD experiments in Chapter 3, where we focus on their utility as neutrino observatories as opposed to DM particle explorers. We begin with a brief historical account of these experiments. We then motivate their use in the field of neutrino physics by charting their course to neutrino-level sensitivities. Driven by this, we lay out the SM theory behind solar neutrino scattering with nuclei and electrons. We finish this chapter by introducing the DD experiments we have considered in this thesis, briefly discussing some of the experimental details we have implemented to make our analyses as sophisticated as possible.

In Chapter 4, with the SM theory laid out, we move on to exploring the beyond Standard Model (BSM) extensions we have considered in this work. We first motivate the need for new physics in the leptonic sector by discussing two modern-day physics puzzles: the tension in the muon's anomalous magnetic moment [4,5], which forms the principal motivator for the majority of our work, and the tension in the present-day value of the Hubble constant [6, 7]. We then introduce the gauged $U(1)_{L_\mu - L_\tau}$ model—a particularly elegant BSM extension that can simultaneously explain both of these mysteries at once. Moreover, we introduce an effective $U(1)_{L_\mu}$ model that, although theoretically less well-motivated than the $U(1)_{L_\mu - L_\tau}$, forms an excellent model with which to compare to the $U(1)_{L_\mu - L_\tau}$, exhibiting remarkably similar phenomenology to it. Finally, we present the framework of neutrino non-standard interactions (NSIs), providing a general, effective description of potential new neutrino physics.

We begin arguing the contention of this thesis in Chapter 5, where we explore neutrino probes of the gauged $U(1)_{L_\mu - L_\tau}$. We first compute the limits set by the neutrino-dedicated experiments CENNS-10 LAr [8] and Borexino [9,10]. This allows us to compare their results to those attained by DD experiments, where we begin with an analysis of the (recently neutralised [11]) electron-recoil excess reported by the XENON1T collaboration [12]. We then move on to projecting the limits that next-generation (SuperCDMS [13], LZ [14], and XENONnT [15]) and far-future (DARWIN [16] and DarkSide-20k [17]) DD experiments can place in the $U(1)_{L_\mu - L_\tau}$ parameter space.

Motivated by our results and the increased tension in the muon's anomalous magnetic moment reported by Fermilab in 2021 [5], we move on to develop a strategy to confirm the $U(1)_{L_\mu - L_\tau}$ as the underlying solution to this modern hint of new leptonic physics in Chapter 6. We construct this strategy using the near-future muon beam experiment NA64μ [18,19], a selection of proposed liquid argon spallation source experiments [20–22], and, critically, the liquid-xenon based DD experiments LZ, XENONnT, and DARWIN. For each of these experiments, we assess their sensitivities to several benchmark points in the $U(1)_{L_\mu - L_\tau}$ solution region by performing a series of parameter reconstructions. Throughout this study, we compare the phenomenology of the $U(1)_{L_\mu - L_\tau}$ to that of generic potential realisations of a $U(1)_{L_\mu}$, attempting to disentangle their signatures from one another by using these experiments both independently and in combination.

Finally, in Chapter 7, we move beyond the $U(1)_{L_\mu - L_\tau}$ model and more generally consider the power of DD experiments in probing NSIs—a formalism describing the effective behaviour of potential BSM neutrino physics [23]. We begin by developing a novel framework in which to embed these effective interactions, extending the previous parametrisation by allowing for NSIs with the electron [24]. We highlight the need for this framework by illustrating how bounds set on NSIs by the CENNS-10 LAr experiment are highly dependent on the assumption one makes for the strength of the electron contribution. We then use our framework to place bounds on the NSI landscape using LZ, XENONnT, and DARWIN. We situate our results in the broader context of NSI global studies in the case of nuclear recoils [24,25] and a recent spectral analysis of the Borexino Phase-II data in the case of electron recoils [26]. In this final study, we most clearly showcase the potential of DD experiments in the search for new physics in the neutrino sector.

CHAPTER 2

Fundamentals of Neutrino Physics

It is no contention that the neutrino is one of the most fascinating particles in the SM. It has taken a leading role in the development of the SM as we know it, and, yet, it has defied to be confined to its bounds. Doubtless, to learn how upcoming and far-future DD experiments can teach us about the nature of neutrino physics beyond the SM, we will have to introduce the neutrino itself. The ideas we will develop here for solar neutrinos in particular will be instrumental in our phenomenological study of BSM physics in the neutrino sector.

In this chapter, we will introduce the neutrino as a particle in the SM and beyond. We will commence with a historical introduction to the neutrino—from the discovery of radioactive decay to the eventual development of SM electroweak theory. We will then, in broad brush strokes, cover the main ideas behind the electroweak sector, including the important prediction that neutrinos are massless. Following this, we will come to learn how solar and atmospheric neutrino experiments accumulated evidence for the case of massive neutrinos through neutrino flavour conversions, introducing the basics of solar neutrino physics in the process. Finally, we will develop the fundamental theory behind neutrino oscillations in both vacuum and matter, concluding with a brief account of how to give the neutrino a mass.

2.1 The Road to the Neutrino

The history of the neutrino begins in 1896, with a Nobel Prize-winning discovery. Having learned of Röntgen's discovery of what we now dub 'X-rays', Henri Becquerel sought to learn more about this mysterious phenomenon. He hypothesized that phosphorescent materials, such as uranium salts, were responsible, producing X-rays when illuminated by sunlight. During one overcast day in Paris, believing his experiment to have led to nothing, he stored away his photographic plates alongside the uranium salts, hoping to be more successful the next time. Becquerel, possibly for the sake of completeness, decided to develop these plates anyway, expecting to see next to nothing on them. He was struck, however, to find that they displayed strong images, having been irradiated by the uranium salts themselves. In what is surely one of the most serendipitous moments in all of science, Henri Becquerel had discovered radioactivity [27–31].

A period of intense research followed. The interests of Marie and Pierre Curie in particular had piqued, and they began their research into uranium in earnest. M. Curie discovered that uranium caused the air around it to become electrically conductive, with its activity dependent only on the amount of uranium present. She hypothesized that this radiation was emanating from processes concerning the uranium atoms themselves, as opposed to any molecular processes [32]. Her research led her to discover several other radioactive elements, including thorium, radium, and polonium [33, 34]. In 1903, Becquerel, M. Curie, and P. Curie were jointly awarded the Nobel Prize in physics in recognition of their services to research into radioactivity.

Ernest Rutherford had also become interested in radioactivity. In 1899, he found that the radiation produced by uranium was composed of at least two different types, which he called α- and β-rays [35] (γ-rays would not be discovered until a year later by Paul Villard [36]). By studying how the current produced by the ionised air around the uranium could be altered by obscuring it with metal foils, he found that only some of the ionising radiation could be removed. This experiment would inspire the famous Geiger-Marsden experiment [37], which would reveal the inner structure of the atom [38]. In 1900, Becquerel, using Joseph Thomson's measurement of the electron mass made a few years earlier [39], found that the mass-to-charge ratio of the emitted β-particles was the same as that of the electron [40]—β-particles were simply electrons.

Indeed, the study of β-decay would eventually lead us to the neutrino. James Chadwick, in 1914, measured the energy spectrum of the emitted β-electrons. Unlike the spectra of $\alpha-$ and $\gamma-$radiation, which were effectively monochromatic with energies equal to the energy difference between the initial and final atomic states, the spectrum of β-radiation was broad and continuous [41]. This posed a dire problem for physicists at the time: it appeared that the law of conservation of energy was being violated. Even Niels Bohr was led to postulate that energy conservation was true merely in a statistical sense (c.f. for example Ref. [42]). What is more, measurements of the total angular momentum before and after the β-decay also pointed towards a violation of angular momentum conservation.

To remedy these problems, Wolfgang Pauli, in a famous 1930 letter entitled 'Dear Radioactive Ladies and Gentlemen', proposed the existence of a third particle emitted during β-decay [43]. This particle had to be a neutral fermion and be much lighter than the proton, taking away whatever energy and angular momentum the electron did not undetected. Such a particle would save the fundamental laws of both energy and angular momentum conservation [44].

While Pauli was the first to postulate the existence of this new hypothetical particle, it was Enrico Fermi who, in 1933, formalised the idea [45]. He developed his landmark theory of β-decay, perhaps the first milestone in the theory of weak interactions, calling the new particle the neutrino to resemble its neutral and very light

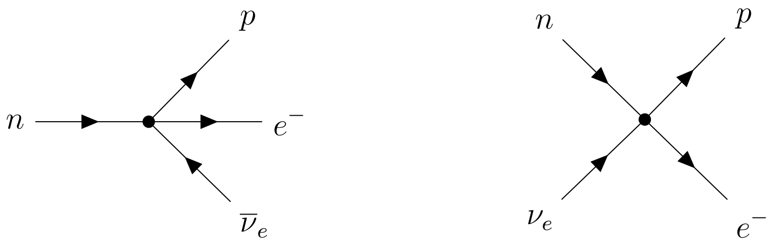

Figure 2.1: β-decay (left) and inverse β-decay (right). As per Fermi theory, both processes are shown as a four-point contact interaction.

nature. In Fermi's theory, β-decay was characterised by a neutron transforming into a proton, producing an electron and the newly theorised neutrino[1]. The diagram for this interaction, which is a four-point contact interaction in Fermi theory, is shown in Fig. 2.1.

Throughout the next two decades, Fermi theory would be regarded as an incredible theoretical success. However, finding experimental evidence for the neutrino seemed all but impossible. A 1934 calculation by Hans Bethe and Rudolf Peierls predicted that the cross section for inverse β-decay, shown in Fig. 2.1, could be as small as $\sigma \lesssim 10^{-44}\,\mathrm{cm}^2$. This vanishingly small interaction strength led them to claim that a physical observation of it would be all but unachievable [46]. The experimental case for the neutrino looked bleak.

It would be another two decades before technology caught up with the neutrino. After dropping the idea of using a nuclear bomb as a source of sufficient anti-neutrinos, Los Alamos National Laboratory physicists Frederick Reines and Clyde Cowan decided to use the fluxes from recently developed nuclear reactors to attempt to observe inverse β-decay directly. The experiment, which was part of a larger initiative dubbed *Project Poltergeist*, consisted of a ton-scale detector composed of water doped with cadmium and a liquid scintillator target placed within a few meters of the Savannah River nuclear reactor [47].

The idea was simple. The anti-neutrinos produced from the nuclear reactor would

---

[1] Of course, today we know that the emitted particle is in fact an anti-neutrino to conserve lepton number.

react with the hydrogen in the water, initiating the inverse β-decay process. The emitted positron would then annihilate with a surrounding electron, producing a pair of photons. Meanwhile, the neutron, freely travelling through the detector, would eventually slow down and be captured by the cadmium in the water. Following this, the cadmium would de-excite, emitting a single photon with a characteristic energy. The signal, which consisted of a pair of prompt photons produced by the annihilation of the positron and a single delayed photon due to the capture of the neutron, would be detected by the liquid scintillator surrounding the detector [47, 48]. By June 1956, Reines and Cowan had grown confident in their results, and they sent Pauli a telegram notifying him that they had, indeed, 'definitely detected neutrinos' [47]. They published their discovery shortly thereafter [49].

With the neutrino experimentally confirmed, the next decade was dedicated to better understanding its mysterious properties and developing a theory of weak interactions consistent with observations. The famous $\theta - \tau$ puzzle, in which apparently the same particle (what we now call the K^+ meson) could decay via two different channels, eventually led us to recognise that the weak interaction violates charge-parity (CP) symmetry [50–52]. In the first-ever spallation source experiment, conducted at Brookhaven National Laboratory (BNL), the muon neutrino was discovered, establishing not only that neutrinos came in different flavours but also that flavour was a conserved property [53–55]. Finally, after years of intense work on the theoretical underpinnings of the weak interaction [51, 56–61], Glashow-Weinberg-Salam (GWS) theory was born, unifying the weak and electromagnetic forces under one common framework [62–64]. This framework is the cornerstone of our modern-day understanding of electroweak interactions within the Standard Model.

2.2 Neutrinos in the Standard Model: Electroweak Theory

Within the SM, neutrino interactions are governed by electroweak (EW) theory: a unification of the electromagnetic and weak interactions. At its core, it is a gauge theory centred around the $SU(2)_L \times U(1)_Y$ symmetry group of the broader SM group, which includes a description of the strong force. Together with spontaneous symmetry breaking (SSB) and the Higgs mechanism, EW theory dictates how all SM particles interact with the EW force, as well as how they acquire mass. We will briefly develop these ideas in this section; however, for a more complete treatment of EW theory, please refer to, for example, Ref. [65–67].

EW theory is based on two important groups, $SU(2)_L$ and $U(1)_Y$. The subscript L on the first group tells us that it only acts on left-handed (LH) chiral fermion fields. Indeed, right-handed (RH) fields are left unchanged by transformations under this group, and they are therefore singlets under it. The $SU(2)_L$ group consists of three generators, T^a, which can be represented in terms of the Pauli matrices: $T^a = \sigma^a/2$. In a gauge theory, each of these generators corresponds to a gauge boson field, W^a_μ, that couples to particles that are charged under $SU(2)_L$—that is, it couples to their weak isospin.

The second of these groups, $U(1)_Y$, has only one generator—the hypercharge generator, Y. It unifies the weak and electromagnetic interactions through the Gell-Mann-Nishijima relation [68, 69],

$$Q_{\text{EM}} = T_3 + \frac{Y}{2}\,, \tag{2.2.1}$$

where T_3 is the third component of a particle's $SU(2)_L$ isospin, Q_{EM} is its electromagnetic (EM) charge, and Y is its hypercharge. The gauge boson associated with this group is the hypercharge boson, B_μ.

In the SM, we have three generations of quarks and leptons. Their LH chiral parts pair up to form $SU(2)$ doublets, which transform under its fundamental representation:

$$L^i \equiv \left\{ \begin{pmatrix} \nu_{eL} \\ e_L \end{pmatrix}, \begin{pmatrix} \nu_{\mu L} \\ \mu_L \end{pmatrix}, \begin{pmatrix} \nu_{\tau L} \\ \tau_L \end{pmatrix} \right\}, \quad \text{and} \quad Q^i \equiv \left\{ \begin{pmatrix} u_L \\ d_L \end{pmatrix}, \begin{pmatrix} c_L \\ s_L \end{pmatrix}, \begin{pmatrix} t_L \\ b_L \end{pmatrix} \right\}, \quad (2.2.2)$$

where $i \in \{1, 2, 3\}$ indexes a particular generation. The RH chiral parts, on the other hand, are $SU(2)$ singlets, and they are therefore uncharged under the weak interaction. These are

$$e^i_R \equiv \{e_R, \mu_R, \tau_R\}, \quad u^i_R \equiv \{u_R, c_R, t_R\}, \quad \text{and} \quad d^i_R \equiv \{d_R, s_R, b_R\}, \quad (2.2.3)$$

where we have labelled them according to the first generation fermions. Note that, as no RH chiral neutrino has been observed, it is omitted in the SM. As we will see, this has an important consequence: the neutrino, within the confines of the SM, is massless.

The SM behaviour of these fields, as well as the behaviour of the EW bosons, is entirely encapsulated by the EW Lagrangian. We can decompose it into four separate Lagrangians:

$$\mathcal{L}_{\text{EW}} = \mathcal{L}_{\text{gauge}} + \mathcal{L}_{\text{fermion}} + \mathcal{L}_{\text{Higgs}} + \mathcal{L}_{\text{Yukawa}} . \quad (2.2.4)$$

Each of these terms describes a particular aspect of the theory.

The first term contains the pure gauge boson kinetic terms and describes the behaviour of the gauge bosons. In the EW sector, it is given by

$$\mathcal{L}_{\text{gauge}} = -\frac{1}{4} W_{\mu\nu} W^{\mu\nu} - \frac{1}{4} B_{\mu\nu} B^{\mu\nu} , \quad (2.2.5)$$

where $W_{\mu\nu}$ and $B_{\mu\nu}$ are, respectively, the field strength tensors of the $SU(2)_L$ and $U(1)_Y$ gauge bosons. From this term, we can derive the self-coupling interactions of each of these bosons.

The second term contains the kinetic terms of both the gauge bosons and the fermions. For any one particular generation, it reads

$$\mathcal{L}_{\text{fermion}} = i\overline{L}^i \not{D} L^i + i\overline{Q}^i \not{D} Q^i + \sum_{f\in\{e,u,d\}} i\overline{f}_R \not{D} f_R \,. \tag{2.2.6}$$

where $\overline{\psi} \equiv \psi^\dagger \gamma^0$ and $\not{a} \equiv \gamma^\mu a_\mu$. The covariant derivative, D_μ, ensures the gauge invariance of the theory,

$$D_\mu \equiv \partial_\mu - igW_\mu^a \tau^a - \frac{1}{2} i g' Y B_\mu \,, \tag{2.2.7}$$

where g and g' are the gauge couplings of the weak isospin and hypercharge groups, respectively.

Expanding Eq. (2.2.6), we retrieve the interaction terms between the fermions and the gauge bosons. We can divide these interactions into those associated with a charged current (CC) and those associated with a neutral current (NC), both of which can then be further subdivided into quark and lepton interactions. Their respective Lagrangians are

$$\mathcal{L}_{\text{CC}} = -\frac{g}{2\sqrt{2}} \left(j_+^\mu W_\mu^+ + j_-^\mu W_\mu^- \right) \,, \tag{2.2.8}$$

$$\mathcal{L}_{\text{NC}} = -e j_\gamma^\mu A_\mu - \frac{g}{2\cos\theta_W} j_Z^\mu Z_\mu \,, \tag{2.2.9}$$

with the vector currents

$$\begin{gathered} j_+^\mu = \overline{\psi}_u \gamma^\mu (1-\gamma^5) \psi_d \,, \quad j_-^\mu = (j_+^\mu)^\dagger \,, \\ j_\gamma^\mu = -Q_{\text{EM}} \overline{\psi} \gamma^\mu \psi \,, \quad j_Z^\mu = \overline{\psi} \gamma^\mu \left[(T_3 - 2Q_{\text{EM}} \sin^2\theta_W) - T_3 \gamma^5 \right] \psi \,. \end{gathered} \tag{2.2.10}$$

Here, we have defined the general field ψ to be the sum of the LH and RH parts of the fields in Eqs. (2.2.2) and (2.2.3) (except for the neutrino field, which only comes in LH form), and $\psi_{u(d)}$ as a field with $T_3 = {}^{+}_{(-)}1/2$. Moreover, we have respectively identified the physical gauge bosons $W_\mu^\pm$, Z_μ, and A_μ as the usual weak charged, weak neutral, and electromagnetic gauge bosons. The angle θ_W is the Cabibbo weak-mixing angle, and Q_{EM} is the electromagnetic charge accompanying any particular field ψ. We note that the structure of the CC interaction follows that of a $V - A$

theory [61], allowing the weak force to violate parity.

The Higgs doublet, H, is described by the third term of Eq. (2.2.4). It is given by

$$\mathcal{L}_{\text{Higgs}} = (D_\mu H)^\dagger (D^\mu H) - V(H)\,, \tag{2.2.11}$$

where $V(H)$ is the Higgs potential, $V(H) = \mu^2 H^\dagger H + \lambda (H^\dagger H)^2$. For $\lambda > 0$, which ensures that the potential is bounded from below, and $\mu^2 < 0$, we find a non-zero vacuum expectation value (VEV) for the Higgs, $v \approx 246\,\text{GeV}$ [70]. This leads to the so-called Higgs mechanism and the SSB of the EW symmetry group,

$$SU(2)_L \times U(1)_Y \to U(1)_{\text{EM}}\,. \tag{2.2.12}$$

After SSB, the physical weak gauge bosons and every charged fermion acquire a mass. The nature of their masses is described by the fourth and final term of Eq. (2.2.4)

Known as the Yukawa term, the fourth term contains the couplings between the fermions and the Higgs. It is given by

$$\mathcal{L}_{\text{Yukawa}} = -Y^e_{ij}\left(\overline{L}^i H e^j_R\right) - Y^u_{ij}\left(\overline{Q}^i \tilde{H} u^j_R\right) - Y^d_{ij}\left(\overline{Q}^i \tilde{H} d^j_R\right) + \text{h.c.}\,, \tag{2.2.13}$$

where Y is the Yukawa matrix describing the Higgs-fermion couplings and the CP conjugated Higgs field is $\tilde{H} = i\sigma^2 H^\star$. After the Higgs acquires a VEV, these terms lead to the quarks and charged leptons acquiring a mass. For any given field expressable as the sum of its left- and right-handed parts, $\psi \equiv \psi_L + \psi_R$, SSB leads to Dirac mass terms of the form

$$m_\psi \overline{\psi}\psi = m_\psi (\overline{\psi}_L \psi_R + \overline{\psi}_R \psi_L)\,, \tag{2.2.14}$$

where $m_\psi = y_\psi v/\sqrt{2}$, with the coefficients y_ψ arising from the diagonalisation of the Yukawa matrix. An interesting consequence of this diagonalisation in the quark sector stems from the fact that the diagonalised matrices for the up and down quark pairs do not quite match. This leads to up- and down-type mixing across the generations during CC interactions, which is characterised by the famous CKM matrix.

EW theory, as it was devised throughout the 20th-century, has been widely successful in describing a broad range of phenomena. One important prediction it makes is that neutrinos, with no accompanying RH field, cannot acquire a Dirac mass term as per Eq. (2.2.14). Thus, within the SM, neutrinos are massless particles. As we will see in the next section, solar neutrino (and atmospheric neutrino) observations challenge this prediction. Indeed, we will see that these observations force us to conclude that neutrinos are massive particles, opening the door to physics beyond the SM.

2.3 Solar Neutrinos

The Sun is powered by a series of thermonuclear fusion reactions. During some of these reactions, intermediate, proton-rich nuclei are produced whose binding forces are unable to balance the increased electric repulsion caused by the excess protons. These unstable nuclei eventually decay through either β^+-decay or electron-capture, transforming redundant protons into neutrons and creating electron neutrinos in the process. This effectively makes solar neutrinos byproducts of sunshine.

Two groups of reactions are responsible for energy generation in the Sun: the pp chain and the CNO cycle. Both of these groups ultimately produce ^{4}He nuclei, electron neutrinos, and 26.7 MeV-worth of energy. The majority of this energy is released as photons, with the remaining fraction taken by the kinetic energy of the produced neutrinos.

The pp chain, which we show diagrammatically in Fig. 2.2, dominates solar energy production [71]. It also consists of the most neutrino-producing processes, responsible for five of the eight neutrino populations created in the Sun via fusion[2]. These

---

[2] The Sun also contains a population of thermal neutrinos produced via thermal processes that occur within the solar plasma [73]. However, these neutrinos have typical energies of $\sim$ keV, and they therefore do not appreciably contribute to the signatures we consider in this work.

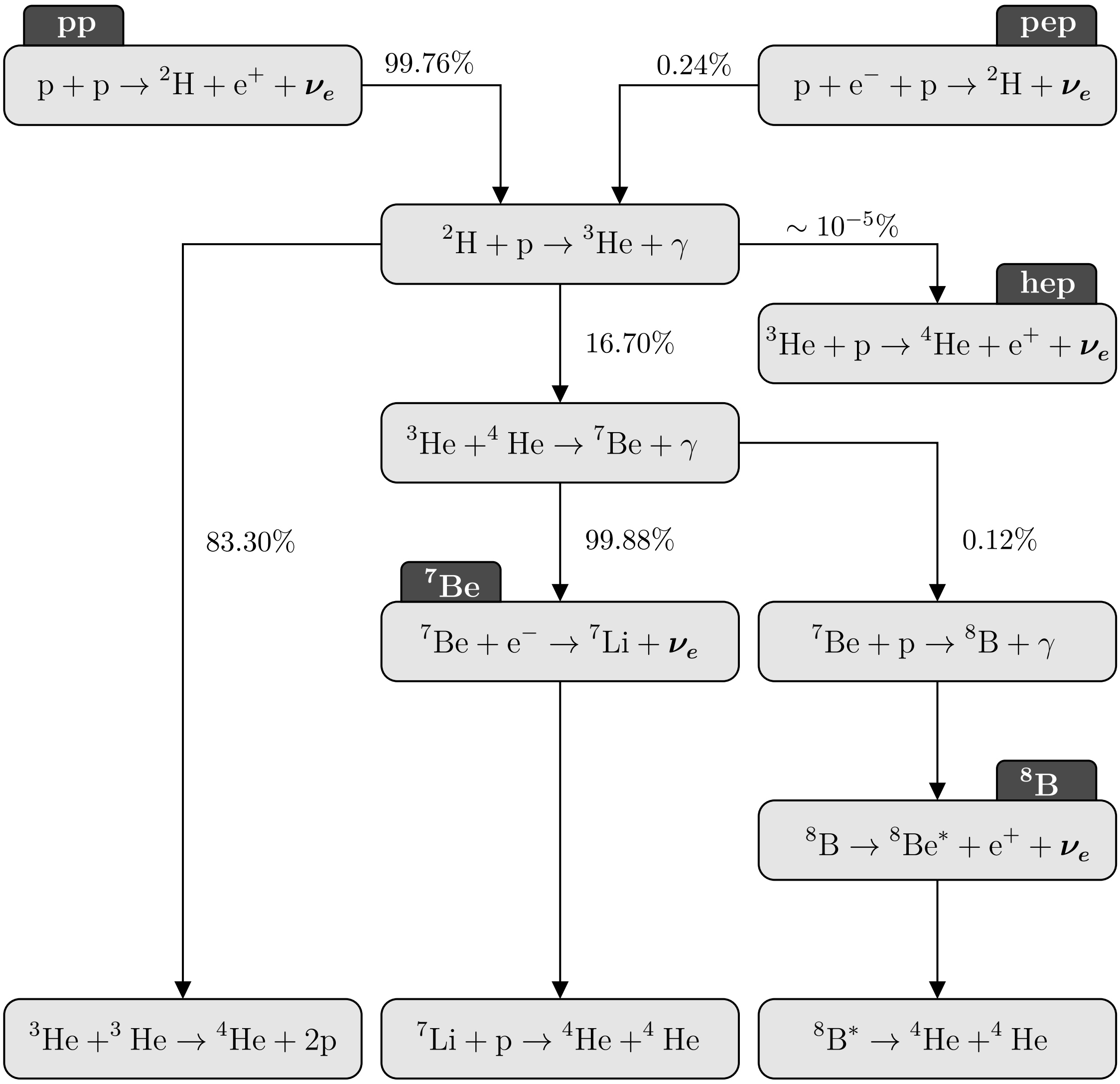

Figure 2.2: The reactions that make up the pp chain [71]. The five reactions that contribute to the solar neutrino flux are flagged with the name given to their flux.

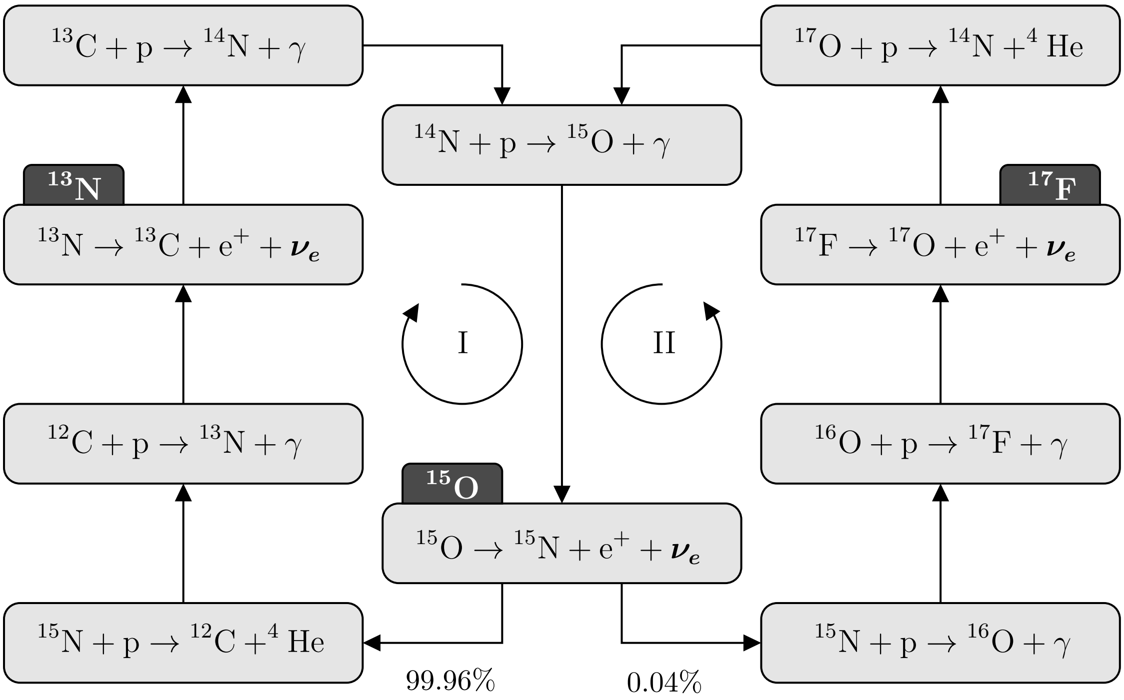

Figure 2.3: The reactions that make up the CNO cycle, which itself is composed of two sub-cycles, labelled I and II [72]. The three reactions that contribute to the solar neutrino flux are flagged with the name given to their flux.

processes are highlighted in Fig. 2.2, and the neutrinos produced via any particular process are named according to it: pp, pep, hep, ^{7}Be, and ^{8}B. The ^{7}Be neutrinos can be further split into $^7\mathrm{Be}_{384\,\mathrm{keV}}$ and $^7\mathrm{Be}_{861\,\mathrm{keV}}$ neutrinos, depending on which orbital electron is captured.

The CNO cycle occurs alongside the pp chain, likewise fusing hydrogen into helium. Unlike the pp chain, however, it proceeds via a series of heavy element catalysts: carbon, nitrogen and oxygen. We show this particular group of reactions in Fig. 2.3, where we see that it is driven by two smaller sub-cycles: the CNO-I and CNO-II cycles. Altogether, they produce three neutrino populations: ^{13}N, ^{15}O, and ^{17}F. The CNO cycle is sub-dominant to the pp chain in terms of energy production in the Sun; this is because its rate of energy production has a much greater dependence on the core temperature, with $\epsilon_{\mathrm{CNO}} \propto T_c^{18}$ compared with $\epsilon_{\mathrm{pp}} \propto T_c^4$. However, for much heavier main sequence stars, which have considerably higher core temperatures, the CNO cycle dominates [71].

The energy spectrum for each solar neutrino flux, as well as important thermodynamical solar profiles, are provided by standard solar models (SSMs). SSMs are mathematical descriptions of the Sun based on stellar evolution equations, giving us a snapshot of the solar state at any particular time [74]. Given a certain set of inputs, these equations are solved from when the Sun enters the main sequence to the present day. As such, they must predict present-day solar observations, such as the solar luminosity, radius, and surface (photospheric) composition [75,76]. Today, SSMs typically use two spectroscopic studies, GS98 [77] and AGSS09 [78], to calibrate to the present-day photospheric composition. We will discuss SSMs in greater detail in Chapter 5, only noting now that these studies differ in what they predict for the present-day photospheric metalicity[3] and that we use the B16-GS98 SSM, developed by Ref. [74], for the majority of this work.

We show the predicted electron neutrino fluxes under the B16-GS98 SSM in Fig. 2.4.

---

[3] In this context, a metal is any element that is heavier than helium. The solar metallicity quantifies the fraction of hydrogen to metals in the Sun.

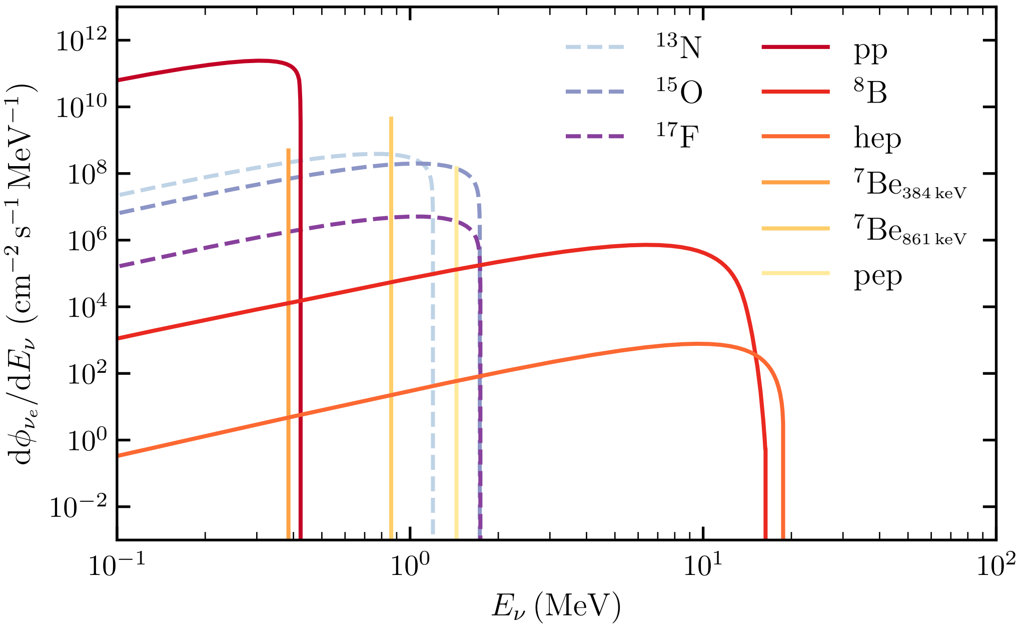

Figure 2.4: The neutrino flux spectra under the B16-GS98 high metallicity SSM. The shapes of the spectra have been taken from Ref. [79], and their overall normalisations have been read from Ref. [74]. The solid lines correspond to the fluxes produced by processes in the pp chain, while dashed lines correspond to those produced by processes in the CNO cycle. The units for the mono-energetic neutrinos are $\mathrm{cm}^{-2}\,\mathrm{s}^{-1}$.

We note in particular that low-energy pp neutrinos contribute the most to the total neutrino flux, accounting almost entirely for it—$\phi(\mathrm{pp}) \sim 10^{11}\,\mathrm{cm}^{-2}\,\mathrm{s}^{-1}$. The largest high-energy neutrino contribution is from ^{8}B neutrinos, with $\phi(^{8}\mathrm{B}) \sim 10^{7}\,\mathrm{cm}^{-2}\,\mathrm{s}^{-1}$. As we will see in Chapter 3, pp and ^{8}B neutrinos are responsible for the majority of the expected events in neutrino-electron and neutrino-nucleus scattering, respectively.

Of all the neutrino fluxes, those associated with the CNO cycle are the least well understood. The rates of the CNO cycle reactions critically depend on the abundances of the heavy elements that catalyse them, and they are hence linked to the total solar metallicity. This quantity has not yet been pinned down, with some studies preferring a high-metallicity Sun and others pointing towards a low-metallicity solution. Depending on which metallicity the SSM takes as its input, the CNO cycle fluxes can vary by as much as $\sim 30\%$ [72]. This forms part of a much broader issue known as the solar metallicity problem [80–84], which we discuss further in Chapter 5.

In 1964, John Bahcall and Raymond Davis Jr. proposed an experiment to measure the solar neutrino fluxes. Located almost 1.5 km underground in the Homestake Gold Mine, South Dakota, the experiment was to test the idea that the Sun was powered by hydrogen to helium fusion. The experimental details were laid out by Davis Jr., with a companion paper by Bahcall building the theoretical foundation for it [85, 86].

The Homestake experiment was based on the same idea that was initially proposed by Pontecorvo in 1946 to detect the existence of neutrinos [87]. They would expose 100,000 gallons of C_2Cl_4 to solar neutrinos, allowing the chlorine to capture a neutrino and become an unstable isotope of argon via the reaction

$$^{37}\mathrm{Cl} + \nu_e \to {}^{37}\mathrm{Ar} + e^- \,. \tag{2.3.1}$$

The argon would then be extracted and its eventual decay through electron capture measured, providing indirect evidence of the inverse β-decay process. Indeed, this choice of elements made the experiment feasible at the outset; Bahcall noticed that a 'superallowed' transition from the ground state of ^{37}Cl to the 5.1 MeV excited state of ^{37}Ar enhanced the expected capture rate for ^{8}B neutrinos by ~ 20-fold [85].

The first results of the Homestake experiment were announced in 1968, reporting a neutrino capture rate no greater than $3 \times 10^{-36}\,\mathrm{s}^{-1}$ per ^{37}Cl atom [88]. However, updated calculations by Bahcall predicted a value almost triple that amount [89]. Known as the solar neutrino problem, this discrepancy marked the beginning of a three-decade-long struggle to reconcile theory with experiment.

Independent corroboration with several experiments quickly followed. The water Cherenkov Kamiokande experiment in Japan, re-purposed to look for solar neutrinos, likewise measured a deficit using neutrino-electron scattering with ^{8}B neutrinos [90–95]. Soon after, they also found a smaller fraction of muon to electron neutrinos than expected from atmospheric neutrinos [96]. The experiments SAGE [97–102], based in Russia, and GALLEX [103–106], based in Italy, used the same inverse β-decay idea as Homestake, but they used gallium instead of chlorine. This afforded them a lower threshold, giving them access to pp and ^{7}Be neutrinos. Their result showed a $\sim 50\%$ deficit compared to the theoretical expectation—a smaller deficit than that measured by Homestake, but a deficit nonetheless[4].

Meanwhile, helioseismological studies appeared to agree with the SSM predictions of Bahcall [107]. Different SSM constructions also did not seem to be able to account for the observed rates, and even SSMs that were forced to yield the counts measured by the Kamiokande experiment were then in tension with the results of the Homestake experiment [108]. Indeed, it seemed that the only way to reconcile theory with experiment was to invoke physics beyond the Standard Model. Ideas included neutrino flavour oscillations with both SM interactions [23, 109–112] (discussed in Section 2.4) and non-standard interactions [23, 113–115] (discussed in Section 4.2.5), neutrino decays [116], and spin-flavour precessions due to a non-zero neutrino magnetic moment [117–119].

Finally, through 2001 to 2003, this stalemate between theory and experiment was broken by the Sudbury Neutrino Observatory (SNO) [120–123]. Also a water Cherenkov detector, SNO was sensitive to CC, NC, and elastic neutrino-electron scattering. This gave them the key to the solar neutrino problem, as they were able to separate electron neutrino events, exclusively measured by the CC channel, from the rest of the data, which included interactions from all flavours. By comparing the CC and NC fluxes, they found that only $\sim 1/3$ of ^{8}B neutrinos were arriving as electron neutrinos; the majority of them had oscillated to ν_μ and ν_τ. Combined with the unprecedentedly precise neutrino-electron scattering data from the Super-Kamiokande experiment [124, 125], they were also able to show that the total number of neutrinos was in agreement with the prediction of Bahcall.

---

[4] We will see in Section 2.4.4 that this less significant deficit is due to the way that pp neutrinos interact with matter in the Sun compared to ^{8}B neutrinos.

The conclusion was inescapable: the electron neutrinos born in the Sun arrived on Earth as a mixture of all three different flavours. The solar neutrino problem was solved. Together with the first evidence of neutrino oscillations from atmospheric neutrinos supplied by Super-Kamiokande in 1998 [126], the SNO result provided irrefutable evidence of neutrino physics beyond the Standard Model.

2.4 Neutrino Oscillations

In 1967, before the results of the Homestake experiment had even been released, Pontecorvo predicted that solar electron neutrinos could transition to a different flavour and decrease the expected electron neutrino capture rate [109]. After precisely this type of deficit was observed at Homestake, Pontecorvo and Gribov developed the theory underlying neutrino oscillations, considering the case of two-neutrino mixing in vacuum [110].

2.4.1 Vacuum Oscillations

As we saw in Section 2.2, neutrinos are fundamentally born during weak interactions; they are therefore inherently created in flavour eigenstates. However, if neutrinos are massive, these flavour eigenstates do not necessarily coincide with the mass eigenstates of the neutrino—these latter states are the ones that propagate in spacetime[5]. Given a flavour eigenstate, $|\nu_\alpha\rangle$, we can write it as a linear combination of the mass basis states, $|\nu_i\rangle$, as

$$|\nu_\alpha\rangle = \sum_i U^*_{\alpha i} \, |\nu_i\rangle \ , \tag{2.4.1}$$

where $U^*_{\alpha i}$ is the overlap between the two states.

---

[5] One may then be curious as to why the quarks, which also exhibit mixing between flavour and mass eigenstates, are then not observed to oscillate. In principle, this is entirely possible; however, the interaction scale of quarks is set by the QCD scale, $\Lambda^{-1}_{\text{QCD}}$, such that a quark does not propagate very far before it interacts with matter and its free state is disturbed.

Suppose that we begin with a neutrino in a particular flavour state α, such that $|\nu(t=0)\rangle = |\nu_\alpha\rangle$. To track its evolution, we evolve its mass eigenstates according to the Schrödinger equation,

$$i\frac{\mathrm{d}}{\mathrm{d}t}\left|\nu_i(t)\right\rangle = \mathcal{H}\left|\nu_i(t)\right\rangle \,, \tag{2.4.2}$$

where $\mathcal{H}$ is the Hamiltonian in the mass basis. As these states are eigenstates of the Hamiltonian, we have that

$$\mathcal{H}\left|\nu_i\right\rangle = E_i\left|\nu_i\right\rangle \,, \tag{2.4.3}$$

with the energy eigenvalues

$$E_i = \sqrt{|\boldsymbol{p_i}|^2 + m_i^2}\,. \tag{2.4.4}$$

Solving Eq. (2.4.2) tells us that any particular mass eigenstate evolves according to the unitary time operator, $U(t) \equiv \exp(-i\mathcal{H}t)$. If a state begins in the state $|\nu_i(0)\rangle$, then, after some time t, it will evolve into the state

$$\left|\nu_i(t)\right\rangle = U(t)\left|\nu_i(0)\right\rangle = e^{-iE_i t}\left|\nu_i(0)\right\rangle \,. \tag{2.4.5}$$

Thus, our flavour eigenstate at time t will be

$$\left|\nu(t)\right\rangle = \sum_i U^*_{\alpha i} e^{-iE_i t}\left|\nu_i(0)\right\rangle \,. \tag{2.4.6}$$

We see that, in general, this state will be in a different linear combination of the mass eigenstates to the one in which it began, and it will therefore no longer necessarily be in the flavour α.

The probability amplitude of this state finding itself in the flavour eigenstate $|\nu_\beta\rangle$, where β is in general different to α, is then

$$\begin{aligned} \mathcal{A}_{\alpha\beta}(t) \equiv \langle\nu_\beta|\nu(t)\rangle &= \sum_i\sum_j U^*_{\alpha i} U_{\beta j} e^{-iE_i t}\left\langle\nu_j(0)|\nu_i(0)\right\rangle \\ &= \sum_i U^*_{\alpha i} U_{\beta i} e^{-iE_i t}\,, \end{aligned} \tag{2.4.7}$$

where we have used the fact that the mass eigenstates form an orthonormal basis, $\langle\nu_j|\nu_i\rangle = \delta_{ij}$. Therefore, the probability of a neutrino transitioning from flavour α

to flavour β at time t is given by

$$P_{\alpha\beta}(t) = |\mathcal{A}_{\alpha\beta}(t)|^2 = \sum_i \sum_j U^*_{\alpha i} U_{\beta i} U^*_{\alpha j} U_{\beta j} e^{-i(E_i - E_j)t} \,. \tag{2.4.8}$$

Note that this result is general and applies to any number of realisable neutrino flavours.

As neutrinos are ultra-relativistic particles, $m_i^2/|\boldsymbol{p}_i|^2 \ll 1$, we can re-write Eq. (2.4.4) as

$$E_i \simeq |\boldsymbol{p}_i| + \frac{m_i^2}{2|\boldsymbol{p}_i|} \simeq E_\nu + \frac{m_i^2}{2E_\nu} \,, \tag{2.4.9}$$

where in the last step we have assumed that the total neutrino energy is dominated by its momentum, $E_\nu \simeq |\boldsymbol{p}_i|$, and neglected its mass in comparison. We have also assumed that all of the mass eigenstates are created with the same energy E_ν, which is equivalent to modelling these eigenstates as plane waves instead of as more general wavepackets[6]. We can use this result—along with the fact that $t \simeq L$ (the full distance travelled) for ultrarelativistic neutrinos—to re-express Eq. (2.4.8) in the slightly simpler and more usual form

$$P_{\alpha\beta}(L) = |\mathcal{A}_{\alpha\beta}(L)|^2 = \sum_i \sum_j U^*_{\alpha i} U_{\beta i} U^*_{\alpha j} U_{\beta j} \exp\left(-i\frac{\Delta m^2_{ij}}{2E_\nu} L\right) \,, \tag{2.4.10}$$

where we have defined the difference in square masses as $\Delta m_{ij} \equiv m_i^2 - m_j^2$ and replaced the dependence on time with a dependence on the distance between the source and the detector. Note that the common phase factor $\exp(-iE_\nu L)$ has cancelled; this is the consequence of a more general result that any common phase factor in the Hamiltonian has no impact on the final measured probability.

The interference between mass eigenstates is characterised by the oscillatory term appearing in Eq. (2.4.10). In practice, a detector can be insensitive to these oscillations if its finite resolution cannot resolve them. Defining the characteristic oscillation length of any particular neutrino species as

$$l_{\text{osc}} \equiv \frac{2E_\nu}{\Delta m^2_{ij}} \,, \tag{2.4.11}$$

---

[6] The full wavepacket treatment ultimately leads to the same results. See, for example, Ref. [67].

we can identify the resolution-limited regime as that in which $L \gg l_{\text{osc}}$. In this case, the observed oscillatory behaviour is greatly suppressed, and a detector instead measures the time-averaged probability, which is equivalent to the incoherent sum

$$\langle P_{\alpha\beta} \rangle = \sum_i |U_{\alpha i}|^2 |U_{\beta i}|^2 \,. \tag{2.4.12}$$

As we will see, for the oscillations exhibited by neutrinos produced in the Sun, this is always the case.

2.4.2 Two-Neutrino Mixing

The simplest case of neutrino oscillations occurs when we only have two neutrino flavours, which we will label according to the first two generations: e and μ. As we will see in Section 2.4.4, this is also the most relevant case for solar neutrinos, as we can express the more realistic three-neutrino problem as an effective two-neutrino one.

In the two-neutrino case, the flavour and mass eigenstates are related by the unitary matrix

$$U = \begin{pmatrix} \cos\theta_{12} & \sin\theta_{12} \\ -\sin\theta_{12} & \cos\theta_{12} \end{pmatrix} , \tag{2.4.13}$$

where θ_{12} is the mixing angle between the two mass eigenstates. If $\theta_{12} = 0$ or $\theta_{12} = \pi/2$, there is no mixing, and the flavour eigenstates are equivalent to one of the two mass eigenstates. Conversely, if $\theta_{12} = \pi/4$, there is maximal mixing between the two mass eigenstates. Using Eq. (2.4.10), we find that, for a neutrino state initially in the flavour $\alpha = e$, the two-neutrino transition probability is given by

$$P^{2\nu}_{e\mu}(L) = \sin^2 2\theta_{12} \sin^2 \left(\frac{\Delta m^2_{21}}{4E_\nu} L \right) . \tag{2.4.14}$$

If the distance the neutrinos travel to the point of detection is much larger than their characteristic oscillation length, the probabilities are averaged over. In this case, we measure the incoherent probabilities

$$\langle P_{e\alpha}^{2\nu} \rangle = \begin{cases} 1 - \frac{1}{2}\sin^2 2\theta_{12} & \text{if } \alpha = e \\ \frac{1}{2}\sin^2 2\theta_{12} & \text{if } \alpha = \mu \end{cases} . \tag{2.4.15}$$

We show the two-neutrino mixing probabilities in Fig. 2.5 for the case $2\theta_{12} = \pi/4$. The full calculation exhibits the coherent oscillatory behaviour, and we see that the oscillation frequencies quickly increase as $L/E_\nu \to \infty$. The solid lines show what an experiment might actually measure—a smearing of these oscillations with respect to some experimental resolution. To produce them, we have convolved the results of the full calculation with a Gaussian response function, taking the resolution of the experiment to be a fraction of the expected measurement of L/E_ν: $\sigma = 0.1\langle L/E_\nu \rangle$. We note in particular the behaviour at large distances, where the probabilities converge to their average values given in Eq. (2.4.15).

2.4.3 Three-Neutrino Mixing

The case of three-neutrino mixing is more complicated. The flavour and mass eigenstates are now related through a 3 × 3 unitary matrix, such that

$$\begin{pmatrix} \nu_e \\ \nu_\mu \\ \nu_\tau \end{pmatrix} = \begin{pmatrix} U_{e1} & U_{e2} & U_{e3} \\ U_{\mu 1} & U_{\mu 2} & U_{\mu 3} \\ U_{\tau 1} & U_{\tau 2} & U_{\tau 3} \end{pmatrix} \begin{pmatrix} \nu_1 \\ \nu_2 \\ \nu_3 \end{pmatrix} , \tag{2.4.16}$$

where we have simplified our notation to $|\nu\rangle \to \nu$. This mixing matrix is known as the Pontecorvo-Maki-Nakagawa-Sakata (PMNS) matrix [127]. It can be parametrised by three mixing angles (θ_{12}, θ_{23}, and θ_{13}) and a phase angle (δ_{CP}) that quantifies the degree of CP violation (with $\delta_{\mathrm{CP}} = 0$ or $\delta_{\mathrm{CP}} = \pi$ indicating no violation).

The PMNS matrix can, in the case of a Dirac neutrino (see Section 2.4.6), be written as the product of three independent transformations,

$$U = R_{23} W_{13} R_{12} \,, \tag{2.4.17}$$

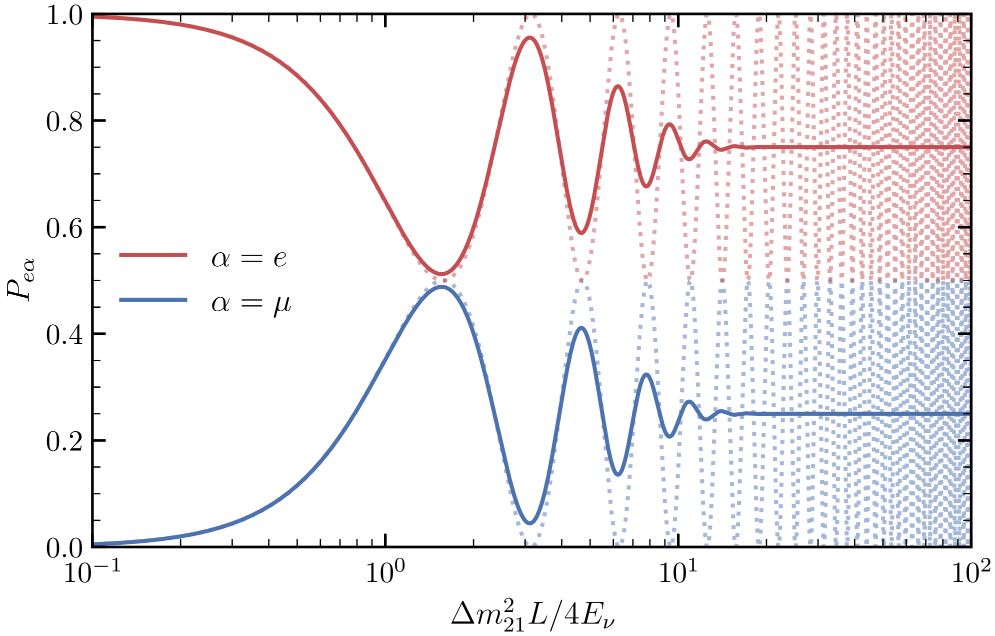

Figure 2.5: Two-neutrino mixing in vacuum. The red (blue) line shows the survival (transition) probability. The dashed lines show the result of the full calculation, with no experimental averaging. The solid lines contain detector-averaging effects, where the full calculation has been convolved with a Gaussian response function with resolution $\sigma = 0.1\langle L/E_\nu\rangle$.

with

$$R_{12} \equiv \begin{pmatrix} c_{12} & s_{12} & 0 \\ -s_{12} & c_{12} & 0 \\ 0 & 0 & 1 \end{pmatrix}, \quad R_{23} \equiv \begin{pmatrix} 1 & 0 & 0 \\ 0 & c_{23} & s_{23} \\ 0 & -s_{23} & c_{23} \end{pmatrix}, \tag{2.4.18}$$

$$\text{and} \quad W_{13} \equiv \begin{pmatrix} c_{13} & 0 & s_{13}e^{-i\delta_{\text{CP}}} \\ 0 & 1 & 0 \\ -s_{13}e^{i\delta_{\text{CP}}} & 0 & c_{13} \end{pmatrix},$$

where $c_{ij} \equiv \cos\theta_{ij}$ and $s_{ij} \equiv \sin\theta_{ij}$[7]. Performing these transformations, we retrieve

---

[7] Note that in the case of a Majorana neutrino (see Section 2.4.6), Eq. (2.4.17) would also incur the additional transformation $D \equiv \text{diag}[\exp(-i\phi_1), 1, \exp(-i\phi_2)]$, where ϕ_1 and ϕ_2 are Majorana phases. However, these phases have no effect on neutrino oscillations as they induce a common phase contribution to the propagation Hamiltonian. We have therefore neglected it.

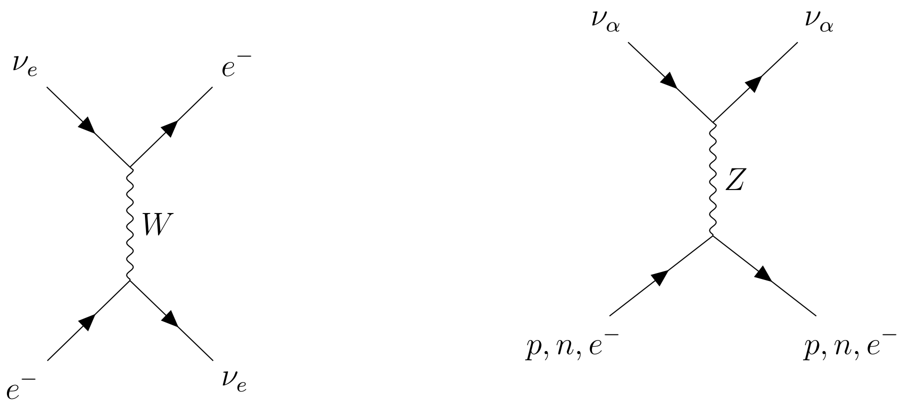

Figure 2.6: The processes responsible for matter effects in the Sun. The CC interaction (left) only occurs between electron neutrinos and electrons. The NC interaction (right) occurs between all neutrino types ($\alpha \in \{e, \mu, \tau\}$) and all the matter content of the Sun.

the usual form of the PMNS matrix,

$$U = \begin{pmatrix} c_{12}c_{13} & s_{12}c_{13} & s_{13}e^{-i\delta_{\mathrm{CP}}} \\ -s_{12}c_{23} - c_{12}s_{23}s_{13}e^{i\delta_{\mathrm{CP}}} & c_{12}c_{23} - s_{12}s_{23}s_{13}e^{i\delta_{\mathrm{CP}}} & s_{23}c_{13} \\ s_{12}s_{23} - c_{12}c_{23}s_{13}e^{i\delta_{\mathrm{CP}}} & -c_{12}s_{23} - s_{12}c_{23}s_{13}e^{i\delta_{\mathrm{CP}}} & c_{23}c_{13} \end{pmatrix}. \tag{2.4.19}$$

To calculate the various probabilities, we would simply insert this matrix into our master equation Eq. (2.4.10). While there are various regimes in which the complicated result of the general formula simplifies [67], we will forego these calculations here. We will instead move on to the more interesting and pertinent case of neutrino oscillations in matter.

2.4.4 Matter Effects

As we saw in Section 2.3, the solar neutrino problem was witnessed by a number of experiments, all of which agreed that the observed solar neutrino flux was much lower than expected. However, not all of them agreed on the exact size of this reduction. The Homestake experiment, which was primarily sensitive to high-energy ^{8}B neutrinos, measured a rate that was lower than Bahcall's prediction by almost a factor of three. On the other hand, the gallium experiments SAGE and GALLEX, which observed the lower energy pp neutrinos, reported a deficit of only around 50%. This tension, which had to be resolved to completely solve the solar neutrino problem, is completely accounted for when we include how matter can affect neutrinos on their way out of the Sun.

The CC interactions that produce neutrinos require matter to be present to begin with. Once created, neutrinos must propagate through the medium, scattering as they do so. This can have a dramatic effect on neutrino propagation compared to the vacuum case. In 1985, Stanislav Mikhev and Alexei Smirnov showed that, when matter is present and varies along a neutrino's trajectory, it is possible to have resonant flavour transitions, occurring when it passes through a region in which the mixing is maximal [111, 112]. This is the so-called MSW effect.

Lincoln Wolfenstein showed that neutrinos propagating in matter experience a potential due to their elastic forward scattering with the surrounding particles in the medium [23]. This potential arises from the CC and NC interactions we introduced in Section 2.2; we show the relevant diagrams in Fig. 2.6. Of particular note is the fact that only electron neutrinos undergo CC scattering; the muon and tau neutrinos are only able to interact via the NC interaction. Ultimately, this means that the potential associated with NC scattering is irrelevant for neutrino oscillations, as they contribute a common phase factor to the matter Hamiltonian. These potentials can be derived from the CC and NC Lagrangians of Eq. (2.2.8). We find that they are given by

$$V_{\mathrm{CC}}(x) = \sqrt{2} G_F N_e(x) \quad \text{and} \quad V_{\mathrm{NC}}(x) = -\frac{1}{\sqrt{2}} G_F N_n(x)\,, \tag{2.4.20}$$

where G_F is the Fermi constant, and N_e and N_n are, respectively, the electron and neutron number densities of the medium, which can generally vary with distance. Note that only neutrons ultimately contribute to the NC potential: this is due to the fact that, for electrically neutral media, the electron and proton contributions cancel out. Using these potentials, we can then define the interaction Hamiltonian,

$\mathcal{H}_I$, such that

$$\mathcal{H}_I(x)\,|\nu_\alpha\rangle = V_\alpha\,|\nu_\alpha\rangle\ , \tag{2.4.21}$$

where the potential associated with flavour α is given by

$$V_\alpha \equiv \delta_{e\alpha} V_{\mathrm{CC}} + V_{\mathrm{NC}}\,. \tag{2.4.22}$$

A state initially born in flavour α will evolve according to the full Hamiltonian, $\mathcal{H}$. This is the sum of the Hamiltonian governing the neutrino-matter interactions, $\mathcal{H}_I$, and the free Hamiltonian governing the free propagation of neutrinos in vacuum. This latter Hamiltonian was the subject of the last section—for n neutrino species, it can be represented by the diagonal matrix $\mathrm{Diag}(m_1^2, m_2^2, \ldots, m_n^2)$ in the mass basis. To combine these two Hamiltonians together, we must bring them to the same basis. It is most convenient to do this in the flavour basis.

We can write the Schrödinger equation for this system as usual in ket-notation. However, to afford us the use of matrix notation in what follows, we will write it in terms of the amplitudes $\psi_{\alpha\beta}(x) \equiv \langle\nu_\beta|\nu_\alpha(x)\rangle$. We find that the evolution of the system is then governed by

$$i\frac{\mathrm{d}}{\mathrm{d}x}\boldsymbol{\psi}_\alpha(x) = \mathcal{H}(x)\boldsymbol{\psi}_\alpha(x) = \left(U\mathcal{H}_0 U^\dagger + \mathcal{H}_I(x)\right)\boldsymbol{\psi}_\alpha(x)\,, \tag{2.4.23}$$

where we have defined the amplitude vector $\boldsymbol{\psi}_\alpha \equiv (\psi_{\alpha\alpha}, \psi_{\alpha\beta}, \ldots)^\intercal$.

Two-Neutrino Mixing

As in the vacuum case, the simplest mixing scenario is the one in which we only have two neutrino species. As we will see in Section 2.4.5, the three-neutrino case relevant for solar neutrino oscillations simplifies to an effective two-neutrino problem. We will therefore briefly cover the basics of this simplified mixing problem.

The evolution of the flavour eigenstates is determined by Eq. (2.4.23). We will assume that we begin with a neutrino in the flavour $\alpha = e$, which has the potential to oscillate to the flavour $\alpha = \mu$. After removing diagonal terms that lead to an irrelevant common phase factor, the evolution of this system is governed by the effective Hamiltonian

$$i\frac{\mathrm{d}}{\mathrm{d}x}\begin{pmatrix}\psi_{ee}\\ \psi_{e\mu}\end{pmatrix} = \frac{1}{2E_\nu}\left[U\begin{pmatrix}0 & 0\\ 0 & \Delta m^2_{21}\end{pmatrix}U^\dagger + \begin{pmatrix}A_{\mathrm{CC}}(x) & 0\\ 0 & 0\end{pmatrix}\right]\begin{pmatrix}\psi_{ee}\\ \psi_{e\mu}\end{pmatrix} \tag{2.4.24}$$

where we have defined $A_{\mathrm{CC}}(x) \equiv 2E_\nu V_{\mathrm{CC}}$. Note that Eq. (2.4.24) has no dependence on the neutral current potential: this is because it appears in equal measures along every diagonal entry within the SM, and it therefore contributes a redundant common phase to the problem. However, as we will see in Chapter 4, new physics effects outside of the SM are not necessarily flavour blind, and in these cases the NC current can impact neutrino oscillations.

The effective Hamiltonian in Eq. (2.4.24) can be written as

$$\mathcal{H}^{\mathrm{eff}}(x) = \frac{1}{4E_\nu}\begin{pmatrix}-\Delta m^2_{21}\cos 2\theta_{12} + A_{\mathrm{CC}}(x) & \Delta m^2_{21}\sin 2\theta_{12}\\ \Delta m^2_{21}\sin 2\theta_{12} & \Delta m^2_{21}\cos 2\theta_{12} - A_{\mathrm{CC}}(x)\end{pmatrix}, \tag{2.4.25}$$

which is position-dependent due to a generally varying electron number density in the medium. To evolve the flavour states, we diagonalise this matrix, hoping to arrive at an evolution equation that is governed by a diagonal Hamiltonian and reducing the task to exponentiating a diagonal matrix. We can complete this diagonalisation via the unitary matrix

$$U^m(x) \equiv \begin{pmatrix}\cos\theta^m_{12}(x) & \sin\theta^m_{12}(x)\\ -\sin\theta^m_{12}(x) & \cos\theta^m_{12}(x)\,,\end{pmatrix} \tag{2.4.26}$$

where $\theta^m_{12}(x)$ is now the mixing angle between the two mass eigenstates in matter, taken at position x. This leads to the now diagonalised effective matter Hamiltonian $\mathcal{H}^m = \mathrm{Diag}(E^m_1, E^m_2)$, with

$$E^m_1(x) = A_{\mathrm{CC}}(x) - \frac{\Delta m^2_{21}}{4E_\nu}\sqrt{p^2 + q^2(x)}\,, \tag{2.4.27}$$

$$E^m_2(x) = A_{\mathrm{CC}}(x) + \frac{\Delta m^2_{21}}{4E_\nu}\sqrt{p^2 + q^2(x)}\,, \tag{2.4.28}$$

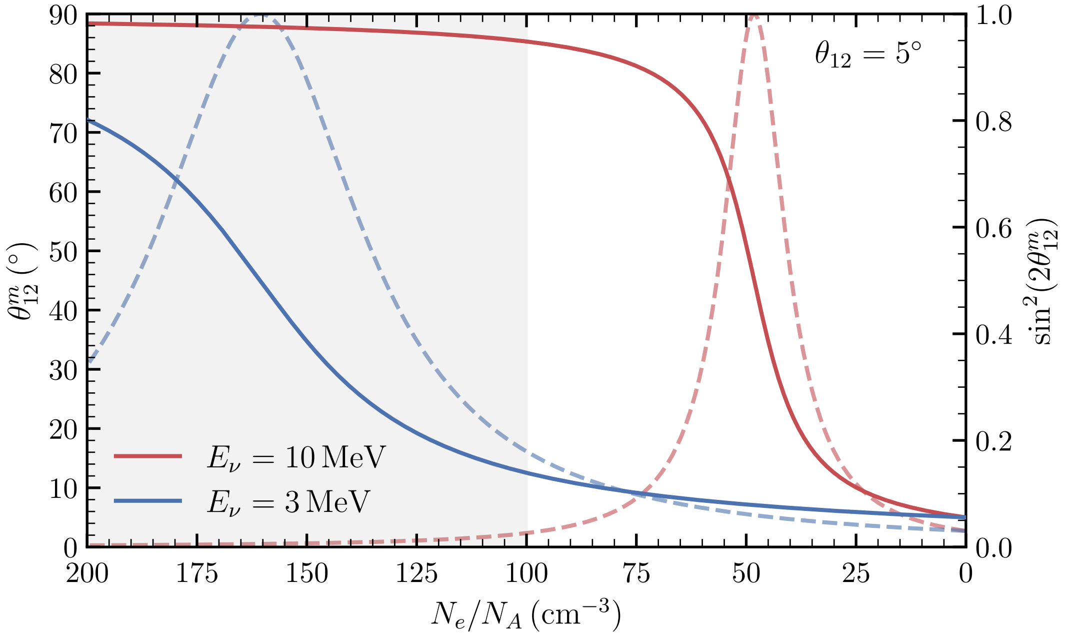

Figure 2.7: The variation in θ_{12}^m (left axis, solid) and $\sin^2 2\theta_{12}^m$ (right axis, dashed) with decreasing matter potential for neutrinos of energies 3 MeV (blue) and 10 MeV (red). The potential is parametrised in terms of the electron number density, which is expressed in units of Avogadro's number. Neutrinos produced in the Sun will travel from the dense solar core to vacuum—i.e. from left to right in the figure. The grey region depicts potentials inaccessible to the Sun, whose electron number density peaks at the core with a value of $N_e \approx 100 N_A\,\mathrm{cm}^{-3}$.

where we have made the simplifying definitions

$$p \equiv \sin 2\theta_{12} \qquad \text{and} \qquad q(x) \equiv \cos 2\theta_{12} - \frac{A_{\mathrm{CC}}(x)}{\Delta m_{21}^2}\,. \tag{2.4.29}$$

The difference between the two energy eigenstates is modified in matter to

$$\Delta E_{21}^m(x) = \frac{\Delta m_{21}^2}{2E_\nu}\sqrt{p^2 + q^2(x)}\,. \tag{2.4.30}$$

Finally, the matter mixing angle, θ_{12}^m, can be shown to satisfy the relations

$$\sin 2\theta_{12}^m(x) = \frac{p}{\sqrt{p^2+q^2(x)}}\,, \quad \cos 2\theta_{12}^m(x) = \frac{q}{\sqrt{p^2+q^2(x)}}\,, \quad \text{and} \quad \tan 2\theta_{12}^m(x) = \frac{p}{q(x)}\,. \tag{2.4.31}$$

From Eq. (2.4.31), we see that a new effect comes into play that was absent in the case of vacuum oscillations. If the potential reaches a point at which $q \to 0$, then we find that $\theta_{12}^m \to \pi/4$. At this point in the medium, the mixing between the flavour eigenstates is maximal; this can be interpreted as a *resonance* effect. This occurs when the potential satisfies the condition

$$N_{e,\,\mathrm{res}} = \frac{\Delta m_{21}^2 \cos 2\theta_{12}}{2\sqrt{2} G_F E_\nu}\,. \tag{2.4.32}$$

We can understand this effect from Fig. 2.7, where we vary θ_{12}^m and $\sin^2 2\theta_{12}^m$ with electron number density. Suppose that a solar neutrino, always born in the state $|\nu_e\rangle$, is created deep within the solar core at the position x_0. If $N_e(x_0) \gg N_{e,\,\mathrm{res}}$, where the resonance occurs at the positions of the peaks in $\sin^2 2\theta_{12}^m$, then $\theta_{12}^m \approx \pi/2$ at x_0, and $|\nu_\alpha(x_0)\rangle \approx |\nu_2\rangle$. The neutrino state is then almost entirely composed of the second mass eigenstate. As the neutrino propagates outwards towards regions of decreasing potential, it crosses the resonance point and continues towards the solar surface, where the potential vanishes. If the neutrino crosses this resonance adiabatically (more on this to follow), then it remains in the state $|\nu_2\rangle$ throughout, where $|\nu_2\rangle = \sin\theta_{12}\,|\nu_e\rangle + \cos\theta_{12}\,|\nu_\mu\rangle$. If the vacuum mixing angle is small, then, as $\theta_{12}^m = \theta_{12}$ at the surface of the Sun, $|\nu_2\rangle \approx |\nu_\mu\rangle$, and the neutrino, which was initially in the electron flavour eigenstate, transitions almost entirely to the muon flavour eigenstate. This is the MSW effect, which can serve to reduce the expected population of electron neutrinos compared to the vacuum case dramatically.

If a neutrino is low enough in energy, then $N_{e,\,\mathrm{res}}$ occurs at high enough values that the resonance is never crossed. This corresponds to the blue line of Fig. 2.7, where the resonance happens at a number density that is higher than the maximum solar value, $N_e \approx 100 N_A\,\mathrm{cm}^{-3}$. In this case, the neutrino population is well-described by vacuum oscillations, and the MSW effect can be largely ignored. This is precisely why measurements with low-energy pp neutrinos showed a much smaller deficit compared to the high-energy ^{8}B neutrinos, which are greatly influenced by the MSW effect. We note that the values in Fig. 2.7 were computed with the much lower value for the vacuum mixing angle of $\theta_{12} = 5^\circ$ compared to the solar value of $\theta_{12} \approx 35^\circ$ [128]. This was to highlight more clearly where the resonances occur, as the peaks produced with lower angles are sharper. For the solar value, resonances disappear for $E_\nu \lesssim 1\,\mathrm{MeV}$.

With $\mathcal{H}^{\mathrm{eff}}$ diagonalised, we can transform to the mass basis using $\boldsymbol{\psi}_e = U_m(x)\boldsymbol{\phi}_e(x)$. This allows us to re-express Eq. (2.4.24) in terms of the mass eigenstates in matter:

$$i\frac{\mathrm{d}}{\mathrm{d}x}\begin{pmatrix}\phi_{e1}\\ \phi_{e2}\end{pmatrix} = \begin{pmatrix}-\Delta E^m_{21} & -i\dot{\theta}^m_{12}\\ i\dot{\theta}^m_{12} & \Delta E^m_{21}\end{pmatrix}\begin{pmatrix}\phi_{e1}\\ \phi_{e2}\end{pmatrix}. \tag{2.4.33}$$

We see that the Hamiltonian contains off-diagonal terms that depend on the rate of change of the matter mixing angle, making Eq. (2.4.33) difficult to solve.

Nevertheless, if we evolve through small enough distances δx, then $\dot{\theta}^m_{12}(x) \approx 0$. The above Hamiltonian then reduces to an effective diagonal matrix, given by $\mathcal{D}(x) \sim \mathrm{Diag}[-\Delta E^m_{21}(x), \Delta E^m_{21}(x)]$. We can then evolve the mass eigenstates along this infinitesimal path, transform back to the flavour basis, re-diagonalise at the new point in space, and repeat this procedure to arrive at the flavour state along a finite path length. In practice, this is akin to evolving the state through a series of slabs of constant density with thicknesses δx. We find that the amplitude vector after N slabs is given by

$$\begin{aligned}\boldsymbol{\psi}_\alpha(x_N) &= U_m(x_{N-1})\exp\left[-i\mathcal{D}(x_{N-1})\delta x\right]U_m^\dagger(x_{N-1})\\ &\times U_m(x_{N-2})\exp\left[-i\mathcal{D}(x_{N-2})\delta x\right]U_m^\dagger(x_{N-2})\\ &\times \ldots\\ &\times U_m(x_0)\exp\left[-i\mathcal{D}(x_0)\delta x\right]U_m^\dagger(x_0)\boldsymbol{\psi}_\alpha(x_0)\,,\end{aligned} \tag{2.4.34}$$

where $x_i \equiv x_{i-1} + \delta x$.

In general, the problem of neutrino propagation through matter, characterised by Eq. (2.4.33), must be solved numerically. However, for slow enough variations in the mixing angle, $\theta^m_{12}(x)$ will not change significantly between the distances δx. Within this approximation, $U_m^\dagger(x_i)U_m(x_{i-1}) \approx 1$, and, as $\delta x \to 0$, Eq. (2.4.34) simplifies to

$$\boldsymbol{\psi}_\alpha(x_N) = U_m(x_N)\exp\left[-i\int_{x_0}^{x_N}\mathcal{D}(x)\,\mathrm{d}x\right]U_m^\dagger(x_0)\boldsymbol{\psi}_\alpha(x_0)\,. \tag{2.4.35}$$

This is known as the *adiabatic approximation.* It is identical to having no mixing between the mass eigenstates in matter, with each state evolving separately at each point in space. Defining the adiabaticity parameter

$$\gamma \equiv \frac{|\Delta E_{21}|}{2|\dot{\theta}_{12}^m|}\,, \tag{2.4.36}$$

we see that when $\gamma \gg 1$, the diagonal terms in the Hamiltonian of Eq. (2.4.33) dominate, and we can neglect the off-diagonal elements. If $\gamma \gg 1$ at the point of maximum violation of adiabaticity, where γ takes its lowest value, then the evolution can be treated as adiabatic, and we can resort to the simplified relation in Eq. (2.4.35). As we will see in the next section, this is pertinent to the case of solar neutrino oscillations, as the density of the solar medium varies slowly enough for us to make this approximation.

We can combine the adiabatic approximation with the fact that, for large propagation lengths, the mass eigenstate arrives at a detector in an incoherent superposition of states. We can then discard any cross terms giving us interferences of the form $U_{\alpha i}U_{\alpha j}^{m\star}$ and keep only those terms where flavour states overlap with the same mass eigenstates (equivalent to taking a trace). This gives us the probabilities

$$P_{e\alpha}^{2\nu}(E_\nu) = |\psi_{e\alpha}|^2 = \sum_i |U_{\alpha i}|^2 |U_{ei}^m(x_0)|^2\,, \tag{2.4.37}$$

where we have used the initial conditions $\boldsymbol{\psi}_e(x_0) = (1,0)^\intercal$ and the fact that, at the point of detection, $U_m(x_N) = U$—the vacuum mixing matrix. We see that the probabilities at detection depend only on the initial and final states of the system, with no dependence on the details of the intermediate propagation states. Thus, the position-dependence is removed from the probabilities, which become functions of the single variable E_ν coming from A_{CC}. Finally, using Eq. (2.4.37), we get that the transition probability is given by

$$P_{e\alpha}^{2\nu}(E_\nu) = \frac{1}{2}\left[1 - \cos 2\theta_{12} \cos 2\theta_{12}^{m}(x_0)\right] , \tag{2.4.38}$$

from which the survival probability can be retried by unitarity.

2.4.5 Three-Neutrino Mixing

As in the case of vacuum mixing, the three-neutrino problem is generally more difficult to solve. However, there are simplifying approximations we can make that not only make the problem analytically tractable but are also appropriate in the case of solar neutrinos. In particular, we will see that we can reduce the evolution of three neutrino states into that of an effective two neutrino system, allowing us to use our above results.

Given an initial state in the flavour $\alpha = e$, its evolution is governed by the Schrödinger equation

$$i\frac{\mathrm{d}}{\mathrm{d}x}\boldsymbol{\psi}_e = \frac{1}{2E_\nu}\left[U\begin{pmatrix} 0 & 0 & 0 \\ 0 & \Delta m_{21}^2 & 0 \\ 0 & 0 & \Delta m_{31}^2 \end{pmatrix}U^\dagger + \begin{pmatrix} V_{\mathrm{CC}} & 0 & 0 \\ 0 & 0 & 0 \\ 0 & 0 & 0 \end{pmatrix}\right]\boldsymbol{\psi}_e\,, \tag{2.4.39}$$

where U is now the PMNS matrix, $U = R_{12}W_{13}R_{12}$, and the amplitude vector is $\boldsymbol{\psi}_e = (\psi_{ee}, \psi_{e\mu}, \psi_{e\tau})^\intercal$. Defining the matrix $O \equiv R_{12}W_{23}$, such that $U = OR_{12}$, it is illuminating for us to switch to what we will call the solar neutrino basis, $\tilde{\boldsymbol{\psi}}_e = O^\dagger\boldsymbol{\psi}_e$. In this basis, the evolution of $\boldsymbol{\psi}_e$ is determined by the Hamiltonian

$$\tilde{\mathcal{H}} = \frac{1}{2E_\nu}\begin{pmatrix} s_{12}^2\Delta m_{21}^2 + c_{13}^2 A_{\mathrm{CC}} & c_{12}s_{12}\Delta m_{21}^2 & -c_{13}s_{13}e^{-i\delta_{\mathrm{CP}}}A_{\mathrm{CC}} \\ c_{12}s_{12}\Delta m_{21}^2 & c_{12}^2\Delta m_{21}^2 & 0 \\ -c_{13}s_{13}e^{i\delta_{\mathrm{CP}}}A_{\mathrm{CC}} & 0 & \Delta m_{31}^2 + s_{13}^2 A_{\mathrm{CC}} \end{pmatrix} . \tag{2.4.40}$$

If the mass-squared hierarchies are such that $\Delta m_{31}^2 \gg \Delta m_{21}^2 \sim A_{\mathrm{CC}}$, then we find that the bottom-right entry of the Hamiltonian dominates. For solar neutrinos, the current best-fit values for these parameters (normal-ordering) are $\Delta m_{31}^2 =$

$(2.510^{+0.027}_{-0.027}) \times 10^{-3}\,\mathrm{eV}^2$ and $\Delta m^2_{21} = (7.42^{+0.21}_{-0.20}) \times 10^{-5}\,\mathrm{eV}^2$ [128], and the maximal value for A_{CC}, using the solar electron number density of Ref. [129], is $\sim 10^{-4}\,\mathrm{eV}^2$ for neutrinos of energy $E_\nu \sim 10\,\mathrm{MeV}$. Thus, for solar neutrinos, the above inequalities are satisfied, and the third eigenvalue of the Hamiltonian is well-approximated by $\Delta m^2_{31}/2E_\nu$. This implies that the third mass eigenstate propagates freely without interacting with the others. The evolution of this system is then dictated by

$$\tilde{\mathcal{H}} = \begin{pmatrix} \tilde{\mathcal{H}}^{\mathrm{eff}} & \mathbf{0}_{2\times 1} \\ \mathbf{0}_{1\times 2} & \Delta m^2_{31}/2E_\nu \end{pmatrix} , \tag{2.4.41}$$

where $\tilde{\mathcal{H}}^{\mathrm{eff}}$ is the 2×2 Hamiltonian of Eq. (2.4.25) with A_{CC} replaced with the effective potential $\tilde{A}_{\mathrm{CC}} = c^2_{13} A_{\mathrm{CC}}$. Thus, we see that the three-neutrino problem reduces to an effective two-neutrino one, combined with a third freely propagating neutrino state. We can therefore use the two-neutrino mixing results, making suitable replacements of $A_{\mathrm{CC}} \to \tilde{A}_{\mathrm{CC}}$. We note that the adiabaticity parameter, defined in Eq. (2.4.36), for solar neutrinos is such that $\gamma_{\mathrm{min}} \sim 10^3$, and the adiabatic approximation is valid in this case. Indeed, in analogy with Eq. (2.4.35), we find that the state vector evolves as

$$\boldsymbol{\psi}_e(x_N) = U \begin{pmatrix} \exp\left[-i \int_{x_0}^{x_N} \mathcal{D}(x)\,\mathrm{d}x\right] & \mathbf{0}_{2\times 1} \\ \mathbf{0}_{1\times 2} & \exp\left[-i\Delta m^2_{31}/2E_\nu\right] \end{pmatrix} U^\dagger(x_0)\boldsymbol{\psi}_e(x_0) \,. \tag{2.4.42}$$

In the incoherent regime, the probabilities are given by the three-neutrino analogue of Eq. (2.4.37),

$$P_{e\alpha}(E_\nu) = \sum_i |U_{\alpha i}|^2 |U^m_{ei}(x_0)|^2 \,, \tag{2.4.43}$$

yielding the probabilities

$$\begin{aligned} P_{ee}(E_\nu) &= c^4_{13} P^{2\nu}_{ee} + s^4_{13} \,, \qquad (2.4.44) \\ P_{e\mu}(E_\nu) &= c^2_{13} \left[c^2_{23} \left(1 - P^{2\nu}_{ee}\right) + s^2_{13} s^2_{23} \left(1 + P^{2\nu}_{ee}\right) + \Delta_{\mathrm{CP}} \right] , \\ P_{e\tau}(E_\nu) &= c^2_{13} \left[s^2_{23} \left(1 - P^{2\nu}_{ee}\right) + s^2_{13} c^2_{23} \left(1 + P^{2\nu}_{ee}\right) - \Delta_{\mathrm{CP}} \right] , \end{aligned}$$

where we have defined the CP-dependent parameter

$$\Delta_{\rm CP}(\theta_{12}^m) \equiv \frac{1}{2} s_{13} \sin(2\theta_{23}) \sin(2\theta_{12}) \cos(2\theta_{12}^m) \cos(\delta_{\rm CP}) \,. \tag{2.4.45}$$

Since solar neutrino experiments such as SNO are only sensitive to ν_μ and ν_τ through NC interactions, only P_{ee} is relevant. This is because, within the SM, the NC potential is the same for all neutrino flavours, and one cannot differentiate between these neutrinos through NC interactions. For the second- and third-generation neutrinos, it is therefore enough to know the sum of $P_{e\mu}$ and $P_{e\tau}$, which is merely given by $1 - P_{ee}$. However, as we shall see in Chapter 4, new physics effects can introduce flavour-specific effects, making an explicit expression for the flavour fractions invaluable. As far as we are aware, analytical expressions for the solar electron neutrino transition probabilities in this regime have not been given before.

To use Eq. (2.4.44), we must know the value of the mixing parameters. Each of these parameters has been measured via a neutrino oscillation experiment that is sensitive to it. Accelerator experiments—such as Minos [130], T2K [131], and NOvA [132]—and experiments that are able to measure atmospheric neutrinos—such as Super-Kamiokande [133] and IceCube [134]—observe the survival and transition probabilities of muon neutrinos and are hence sensitive to θ_{23}. These experiments are also sensitive to anti-neutrinos, and can therefore also get a handle on $\delta_{\rm CP}$. Reactor experiments—such as KamLAND [135], Chooz [136], and Daya Bay [137]—measure the survival probability of anti-electron neutrinos, pinning down θ_{13} and Δm^2_{12}. Finally, as can be seen from Eq. (2.4.44), once θ_{13} is known, solar neutrino experiments are sensitive to the parameters in $P^{2\nu}_{ee}$: θ_{12} and Δm^2_{12}. When combined with data from reactor experiments, solar neutrino data can place greater constraints on Δm^2_{12} [128, 138]. All of these experiments can be incorporated into a global analysis of oscillation parameters to give us their best-fit values and confidence regions. For our analyses, we use the most up-to-date NuFIT 5.1 global fit results, which are summarised in Ref. [128].

Finally, we must choose a value to take for $\cos 2\theta^m_{12}(x_0)$ in Eq. (2.4.38). We can

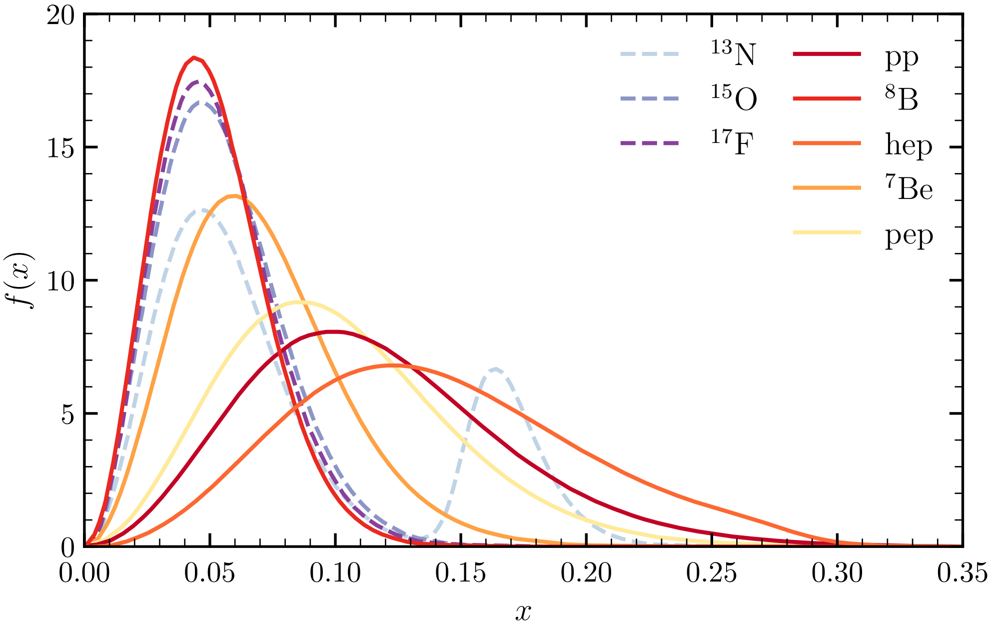

Figure 2.8: The normalised electron neutrino production regions, $f(x)$, with fractional solar radius, $x \equiv r/R_\odot$, as calculated from the BP16-GS98 SSM Ref. [74]. The fluxes associated with the primary pp fusion chain are shown as solid lines, while those associated with the CNO cycle are shown as dashed lines.

define a spatially averaged result for it using the normalised spatial distribution, $f(r)$, governing where each neutrino flux is produced,

$$\langle \cos 2\theta_{12}^m(x_0) \rangle = \int_0^1 f(x) \cos 2\theta_{12}^m(x) \, \mathrm{d}x \,, \tag{2.4.46}$$

where we have introduced the fractional solar radius, $x \equiv r/R_\odot$. The spatial distributions for each population are SSM-dependent; we have used the BP16-GS98 predictions calculated by Ref. [74]. These are shown in Fig. 2.8.

Our results for the SM probabilities are shown in Fig. 2.9. We have broken down each probability into source-specific curves to illustrate the effect of the average in Eq. (2.4.46). For solar neutrino experiments, the most important curves to read are the electron survival probabilities, which are shown as solid lines. In particular, we see that the high-energy ^{8}B neutrinos are greatly affected by the MSW effect, with their survival probability falling to $\sim 1/3$. The low-energy pp neutrinos, on

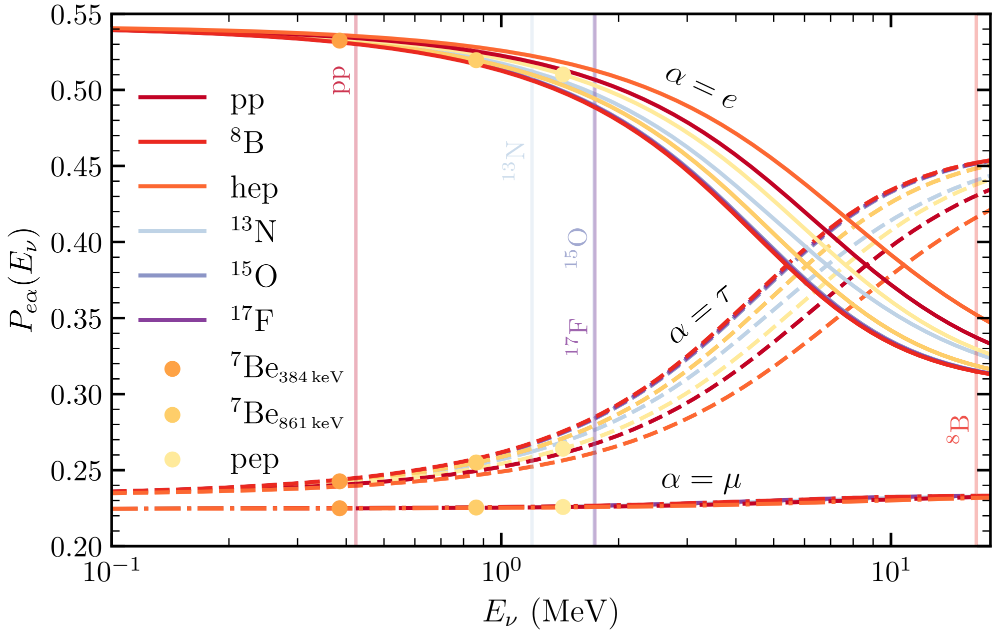

Figure 2.9: The electron neutrino survival (solid) and transition probabilities (dash-dotted for $e\mu$ and dashed for $e\tau$) in the three-neutrino paradigm. The differently coloured lines show the probabilities for the various neutrino fluxes produced in the Sun. The vertical lines denote the highest energy neutrino for any given flux. The maximum value of the energy range coincides with the highest energy hep neutrinos, $E_\nu \approx 18\,\mathrm{MeV}$.

the other hand, are well-described by the vacuum mixing angle, $\theta_{12}^{m} \approx \theta_{12}$. This is precisely what we see in experiments that probe different neutrino energy ranges, with ^{8}B-sensitive experiments like Homestake measuring a greater deficit in electron neutrino events compared with experiments sensitive to pp neutrinos, such as SAGE and GALLEX. Indeed, through this observation, the MSW effect was confirmed, and the solar neutrino problem was finally put to rest.

2.4.6 Neutrino Masses

The evidence for neutrino oscillations is now overwhelming. They imply that there is a mismatch between the flavour states that neutrinos are inherently created in and the states in which they propagate—the mass eigenstates. This, of course, requires that neutrinos have mass; however, the SM predicts that no such mass-giving term exists. Thus, BSM physics must be invoked to give these neutral leptons a mass, and we will now briefly comment on how such terms can be introduced.

Generally, the nature of the added mass term depends on the nature of the neutrino. Neutrinos are considered to be either Dirac, Majorana, or some combination of the two. Both of these neutrino types can be defined by how the neutrino relates to its anti-particle. In the case of Dirac neutrinos, these two particles are fundamentally different from one another. For Majorana neutrinos, on the other hand, the anti-particle of the neutrino is itself, $\overline{\nu} = \nu$. The phenomenology of these possibilities is very different, and it is then no surprise that the way in which they can acquire a mass is also different.

Dirac Neutrinos

The case of Dirac neutrinos is perhaps the most straightforward. Dirac masses stem from the Yukawa Lagrangian in EW theory, Eq. (2.2.13). After SSB, the Yukawa term endows fermions with Dirac masses via the product of their LH and RH chiral fields. Thus, to give neutrinos a Dirac mass, we must introduce a RH neutrino field, ν_R, for each flavour, adding the additional Yukawa term:

$$\mathcal{L}^{\text{Dirac}}_{\text{Mass}} = -Y^{\nu}_{ij} \left(\overline{L}^i \tilde{H} \nu^j_R \right) + \text{h.c.}\,. \tag{2.4.47}$$

After the Higgs acquires a VEV, neutrinos then acquire masses $m^{\nu}_i = y^{\nu}_i v/\sqrt{2}$, for $i \in \{1, 2, 3\}$, in complete analogy with Eq. (2.2.14).

It is worth noting two important points about the nature of Dirac neutrinos. Firstly, the newly introduced RH fields must be singlets under all symmetry groups of the SM, since they cannot interact with the SM (otherwise, we would have seen them). These RH neutrinos are typically called sterile neutrinos, interacting only gravitationally[8]. Secondly, cosmological bounds place a strict upper limit on the sum

---

[8] One can introduce additional BSM physics to act as a non-gravitational 'portal' to these

of neutrino masses, $\sum_i m_i^\nu < 0.12\,\mathrm{eV}$ [6]. As a Dirac neutrino would have a mass proportional to the Higgs VEV, this would require its Yukawa coupling to be of order $y^\nu \lesssim 10^{-12} \sim 10^{-6} y^e$, where y^e is the electron Yukawa coupling. However, the SM already suffers for a hierarchy problem in the fermion Yukawa couplings, with no explanation for why these couplings span six orders of magnitude across the three generations. Introducing this additional neutrino Yukawa coupling would exacerbate this issue.

Majorana Neutrinos

As neutrinos are neutral particles, their fields satisfy the Majorana condition,

$$\psi^C \equiv C\overline{\psi}^{\intercal} = \psi\,, \tag{2.4.48}$$

where ψ^C is known as the charge-conjugate field and C is the charge conjugation matrix. As anti-particles are described by their charge-conjugate fields, this means that the neutrino could be its own anti-particle—a Majorana particle. In this case, we can construct a Dirac mass term using purely the LH field, with its RH counterpart given by $\nu_R = \nu_L^C$,

$$\mathcal{L}_{\text{Mass}}^{\text{Majorana}} = -\frac{1}{2} m^\nu \overline{\nu_L^C} \nu_L + \text{h.c.}\,. \tag{2.4.49}$$

Worryingly, Majorana neutrinos violate lepton number conservation, as the Majorana mass term is not invariant under global $U(1)$ gauge transformations:

$$\nu_L \to e^{i\alpha} \nu_L \implies \overline{\nu_L^c} \nu_L \to e^{2i\alpha} \overline{\nu_L^C} \nu_L\,. \tag{2.4.50}$$

No lepton number violating processes have been observed so far; however, their observation would act as a signature of Majorana neutrinos. Searches for neutrinoless double beta-decay, a prime candidate of such a process, are being intensely pursued for precisely this purpose [141–143].

---

new fields. One example is the neutrino dipole portal, in which active neutrinos have a non-zero transition-magnetic moment that allows them to up-scatter to the heavier, sterile neutrino state [139, 140].

It is a curious fact that, should the SM be an effective low-energy realisation of a richer and higher energy theory, the lowest dimension operator that could be added to the SM realises Majorana neutrinos. This is the so-called dimension-5 Weinberg operator,

$$\mathcal{L}_{d=5} = \frac{C_5}{\Lambda} \left(\overline{L}^c \tilde{H}\right) \left(\tilde{H}^\intercal L\right) , \tag{2.4.51}$$

where C_5 is some weighting coefficient in the theory, and Λ is the scale of new physics. After SSB, this BSM Lagrangian gives us a mass term precisely of the form of Eq. (2.4.49).

Ultimately, a combination of both Dirac and Majorana neutrinos is used to give neutrinos mass. These combined mass mechanisms are known as the seesaw mechanisms, and they come in different types depending on how one chooses to UV complete the effective Weinberg operator. For reviews on these models, see, for example, Ref. [144, 145]. Note that these mass models generate neutrino masses at tree-level; however one can also have ‘radiative’ neutrino masses induced at loop-level through models such as the scotogenic model [146, 147].

CHAPTER 3

Neutrino Physics at Direct Detection Experiments

Dark matter direct detection experiments, as their name suggests, are typically employed in the search for dark matter. However, a new search is on the horizon. The next generation of DD experiments will become so sensitive that they will begin to expose themselves to an irreducible background of neutrino events, marked by the so-called neutrino floor. This will complicate the hunt for dark matter, but it will usher in the beginning of a new search for BSM neutrino physics. DD experiments, with their large exposures and low energy thresholds, present a wealth of untapped potential in this vein that could provide leading results beyond those of neutrino-dedicated experiments. It is this potential that is the subject of this thesis.

In this chapter, we will introduce the concepts behind DD experiments, focusing on how they can be used to detect solar neutrinos. We will begin with a brief historical account of DD experiments, focusing on their typical application to the search for DM. We will then turn to neutrinos, making the case for why future DD experiments are set to play key roles in the search for new neutrino physics. Following this, we will lay the theoretical foundations for neutrino scattering with nuclei and electrons at DD experiments, commenting on the experimental details we have considered to make our analyses as sophisticated as possible. Finally, we will introduce the DD experiments that have inspired this work, describing each of their operations and projected experimental specifications.

3.1 Dark Matter Direct Detection Experiments

In 1984, riding the wave of excitement set up by the solar neutrino problem and recent advancements in the up-and-coming field of neutrino astronomy, Andrzej Drukier and Leo Stodolsky proposed a new type of neutrino detector [148]. Based on the NC process of coherent elastic neutrino-nucleus scattering (CEνNS), the detector would be able to measure nuclear recoils (NRs) of energies 10^{-3}–$10\,\mathrm{keV}$. This made them sensitive to neutrinos with $E_\nu \sim 1$–$10\,\mathrm{MeV}$, giving them access to a broad range of fascinating neutrino physics. For instance, as a spallation source experiment, it could be used to test the SM prediction of the CEνNS rate. On the other hand, as a solar neutrino experiment, it would be able to join the ranks of neutrino experiments already pointing to the Sun, measuring the solar neutrino flux through a new interaction channel and yielding additional insights into the nature of the solar neutrino problem[1].

The following year, however, it was pointed out by Mark Goodman and Edward Witten that such a detector could also be used to detect certain DM candidates [149]. Indeed, two of the three candidates they had in mind are what we today call weakly interacting massive particles (WIMPs)—massive DM particles with interaction strengths of a similar order to that of the weak interaction. They found that a detector based on the coherent elastic scattering of nuclei with DM particles in the galactic halo would be sensitive to WIMP masses of 1–10^6 GeV (for spin-independent couplings).

---

[1] In an alternate history, such an experiment would have observed *no* deficit in the solar neutrino flux, as CEνNS is flavour blind. Together with measurements from CC interactions, it would have provided us with the key to the solar neutrino problem that SNO supplied in 2001-2003.

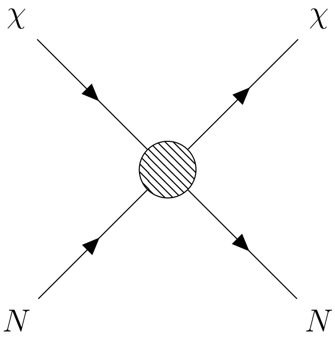

Figure 3.1: The effective coherent elastic scattering between a DM particle, χ, and a nucleus, N, looked for at DD experiments.

While the detector proposed by Drukier and Stodolsky was never built, the theoretical foundation they, Goodman, and Witten laid forms the basis of modern DD experiments. Motivated by the so-called WIMP miracle (the fact that such DM particles can realise the DM relic abundance we observe today [150]), DD experiments primarily look for the coherent elastic scattering between WIMPs and a variety of target nuclei. The scattering with a DM particle, χ, is usually considered as an effective interaction, as illustrated in Fig. 3.1. By looking for this process, or its lack thereof, DD experiments teach us about the nature of DM.

The last three decades have been an exciting and productive period for DD experiments, and excellent reviews on the topic can be found in Refs. [151, 152]. Today, a great expanse of the WIMP parameter space—described by the WIMP mass, m_χ, and the WIMP-nucleon cross section, $\sigma_{\chi n}$[2]—has been ruled out, lessening the motivation for this popular DM candidate. The last wave of DD experiments concluded with the construction of the XENON1T [153] experiment; however, a new generation of experiments is on its way.

Indeed, a plethora of next-generation and far-future DD experiments have now been proposed [151]. Should a signal fail to be detected, these experiments are set to provide us with the leading constraints in the WIMP parameter space. In fact, as we are about to see, they are projected to reach such astonishing sensitivities that

---

[2] For the sake of argument, we only consider spin-independent cross sections here. WIMPs may also interact via spin-dependent interactions.

they will begin to observe scattering events induced by solar neutrinos. This will provide them with a complementary research mission beyond the search for DM, realising the initial ideas of Drukier and Stodolsky.

3.2 The Case for Neutrino Physics

Neutrinos form a pesky background for DD experiments. With their extremely small cross sections, neutrinos cannot be shielded against, and the NR signature they leave in a detector can be difficult to disentangle from that of a WIMP. The ever-present flux of neutrinos—which can come from the Sun (c.f. Section 2.3), the atmosphere [154], diffuse supernovae [155], and even the Earth itself [156]—therefore forms a chronic, irreducible background for the DM hunt at DD experiments.

This has led to the concept of the so-called 'neutrino floor': a discovery limit in the WIMP parameter space representing those cross sections below which a DM signal would be statistically lost in the sea of neutrino events. We show the neutrino floor, as calculated by Ref. [160] using the ideas first established in [161], in Fig. 3.2. The idea behind this calculation is that, for a given WIMP mass, that cross section is found at which 90% of hypothetical DD experiments would still be able to reject the neutrino-only hypothesis at a confidence level of 3σ. The floor itself is defined by the boundary of the red region, and we see that it is broadly characterised by two regions in the WIMP mass: a low-mass region ($m_\chi \lesssim 6\,\mathrm{GeV}$) where it extends to cross sections of order $\sigma_{\chi n} \sim 10^{-45}\,\mathrm{cm}^2$, and a high-mass region where it is contained to much smaller cross sections. The first of these is due to solar neutrinos, with ^{7}Be neutrinos producing NR signatures similar to those of very low-mass WIMPS and ^{8}B neutrinos causing a similar issue for $m_\chi \sim 6\,\mathrm{GeV}$. Above this mass, the WIMP signal is too energetic to be produced by solar neutrinos, but they can instead be mimicked by the higher energy atmospheric and diffuse supernovae neutrinos, which defines the second, higher mass regime of the neutrino floor [161][3]. We see, therefore, that

---

[3] We note that, should a WIMP reside below the neutrino floor, its signal could, in theory, be

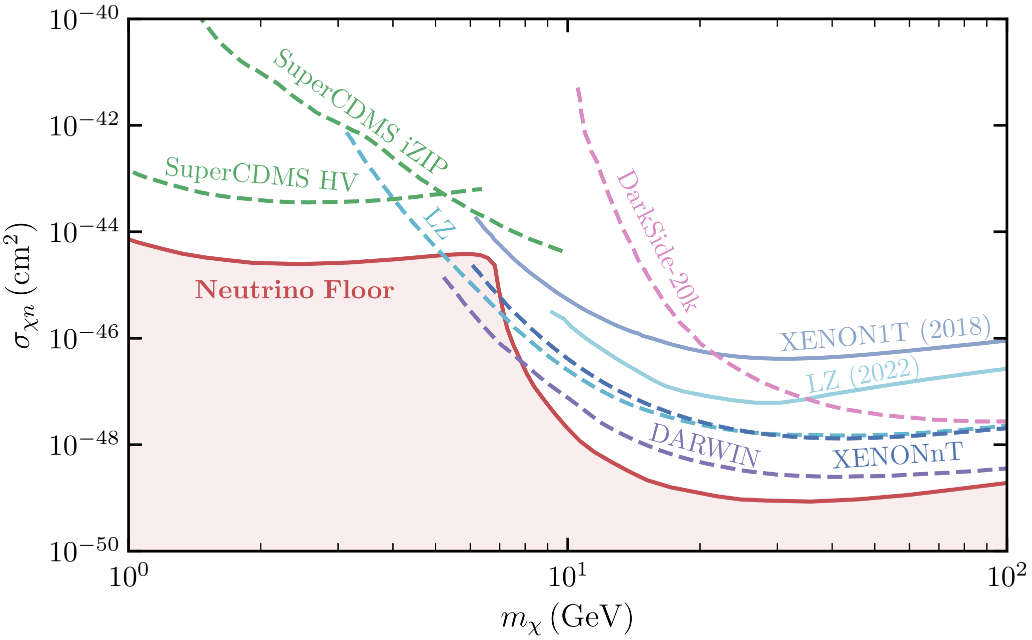

Figure 3.2: The projected 90% CL limits of the considered upcoming and far-future DD experiments relative to the neutrino floor. We show the projections from SuperCDMS at SNOLAB [13], LZ [157], XENONnT [15], DARWIN [16], and DarkSide-20k [17]. We also show the previous limit set by the XENON1T collaboration [158] and the limit recently set by LZ [159]. The 'neutrino floor', as calculated for a xenon target [160], is shown in red.

as far as the DM hunt is concerned, this irreducible neutrino background presents DM DD experiments with a serious obstacle in their mission to detect ever-weaker WIMP candidates.

However, we can re-interpret this 'obstacle' under a significantly more positive light. Through ever-decreasing energy thresholds and ever-increasing detector exposures, DD experiments are set to reach such incredible sensitivities that they will begin to observe neutrinos with high statistical significance. This will present them with a

---

disentangled from the neutrino background. This could be done either by using measurements that bypass the floor to some degree—such as by using complementary targets [162], diurnal/annual modulation [163, 164], or directional information [165, 166]—or by simply having enough statistics and a better handle on the neutrino flux uncertainties. This latter strategy has led to the more contemporary term 'neutrino fog' appearing in the literature, reflecting the fact that this fog can be lifted given high enough exposures or better knowledge of the neutrino flux normalisations [163, 167–170].

new and compelling opportunity beyond the search for DM.

In fact, next-generation and far-future DD experiments are on a direct collision course with the neutrino floor. In Fig. 3.2, we show the projected 90% confidence level (CL) limits of the future DD experiments we focus on in this work: LUX-ZEPLIN (LZ) [171], XENONnT [15], SuperCDMS at SNOLAB [13], DarkSide-20k [17], and the DArk matter WImp xenoN observatory (DARWIN) [16]. We see that the xenon-based experiments LZ, XENONnT, and DARWIN will begin to probe the ^{8}B shoulder and will therefore measure a significant number of solar neutrino scattering events. The germanium-based SuperCDMS experiment, the projections for which we have split into those from the HV and iZIP detectors (more details in Section 3.4.2), will not be far behind them. Moreover, the DarkSide-20k detector, based on argon, will likely not be able to see a significant number of solar neutrinos; however, they are encroaching on the even weaker atmospheric neutrino signal, and, as we will see in Chapter 5, a low-threshold version of DarkSide-20k would be sensitive to solar neutrinos. In Fig. 3.2, we also show the limits set by the XENON1T experiment [158] and, more recently, by the commissioning run of the LZ experiment [159]. These experiments have begun to approach the solar neutrino part of the neutrino floor, and the sensitivity reached by the XENON1T experiment has already been motivation enough for the collaboration to perform a ^{8}B-dedicated search [172].

The landscape we present in Fig. 3.2 sets the scene for our work. The next era of DD experiments *will* become sensitive to solar neutrinos, and, as such, they will become excellent probes of potential BSM physics in the neutrino sector. As we will see in Chapter 4, such BSM physics can impact both the NR and ER (electron recoil) scattering cross sections, and, by comparing the predicted phenomenology of these models to measurements of the solar neutrino scattering rate, DD experiments will be able to place limits on, or potentially even make a discovery of, new neutrino physics. Indeed, while we have focused on the coherent scattering of nuclei with neutrinos, as this poses an existential threat to the WIMP hunt, elastic neutrino-electron scattering (EνES) will also become an important ER background, or in our case signal, for these next-era detectors.

This more optimistic approach of breaking through the neutrino floor has already been the subject of intense research. These studies broadly focus on how this solar neutrino signal can be used to teach us more about the nature of solar physics, neutrino oscillations, and BSM neutrino physics [173–183]. In this work, we will follow suit, showing how DD experiments can use solar neutrinos as powerful probes of both light new physics in the neutrino sector (Chapters 5 and 6) and, more generally, neutrino non-standard interactions (Chapter 7). However, before we introduce these new physics models, we will lay the theoretical foundations for CEνNS and EνES, both of which we will make reference to throughout the remainder of this work.

3.3 Neutrino Scattering at Direct Detection Experiments

The theoretical scattering rate between a DD target and a colliding particle is usually described by the differential rate spectrum. This tells us how many recoils to expect per unit time and per unit mass of a detector at a particular recoil energy, E_R. For neutrino scattering at a DD experiment, the total differential rate for nuclear- and electron-recoil events is given by[4]

$$\frac{\mathrm{d}R}{\mathrm{d}E_R}(E_R) = n_T \sum_r \sum_\alpha \int_{E_\nu^{\mathrm{min}}} \frac{\mathrm{d}\phi^r_{\nu_e}}{\mathrm{d}E_\nu}(E_\nu) P_{e\alpha}(E_\nu) \frac{\mathrm{d}\sigma^\alpha_{\nu T}}{\mathrm{d}E_R}(E_R, E_\nu)\, \mathrm{d}E_\nu\,, \tag{3.3.1}$$

where n_T is the number of targets available to interact per unit mass of a detector, $\mathrm{d}\phi^r_{\nu_e}/\mathrm{d}E_\nu$ is the electron neutrino flux produced by the solar nuclear fusion reaction r (pp, ^{8}B, etc.), $P_{e\alpha}(E_\nu)$ is the probability of an electron neutrino transitioning to a

---

[4] We will see in Chapter 4 that this relation is only true for the case of flavour-conserving interactions. When we add BSM flavour-violating effects, we must consider how the mixed-state flavour system arriving at the Earth interacts with the detector more carefully. We will study such interactions in the context of DD experiments in Chapter 7.

neutrino of flavour α, and $\mathrm{d}\sigma^{\alpha}_{\nu T}/\mathrm{d}E_R$ is the differential cross section for the scattering process between a neutrino of flavour α and the target T (which can be either a nucleus or an electron). In the case of a nuclear target, $n_T = 1/m_N$, where m_N is the mass of the nucleus, and in the case of an electron target, $n_T = Z/m_N$, where Z is the number of protons (or equivalently electrons) per nucleus. The neutrino flux produced by each nuclear fusion reaction in the Sun is shown in Fig. 2.4, and the relevant SM transition probabilities are shown in Fig. 2.9. The integral above runs from the minimum neutrino energy required to produce a recoil of energy E_R with a target of mass m_T,

$$E_\nu^{\mathrm{min}} = \frac{E_R + \sqrt{E_R^2 + 2m_T E_R}}{2}\,. \tag{3.3.2}$$

The number of expected neutrino events between any two recoil energies, E_1 and E_2, quickly follows from Eq. (3.3.1):

$$N(E_1, E_2) = \varepsilon \int_{E1}^{E_2} \frac{\mathrm{d}R}{\mathrm{d}E_R}\,\mathrm{d}E_R\,, \tag{3.3.3}$$

where $\varepsilon \equiv MT$ is the exposure of an experiment, given by the product of the total detector mass and the detector livetime.

When considering the differential rates of NRs and ERs, we will make a distinction between the two energy scales associated with them. For the former, we will attribute to it the unit of nuclear-recoil-equivalent energy ($\mathrm{keV_{nr}}$), while, for the latter, we will use the unit of electron-equivalent energy ($\mathrm{keV_{ee}}$). This is because the recoil energies associated with NRs and ERs translate to different *observed* energies in a detector. We will expand on this in greater detail in Section 3.3.3, where we will introduce the concept of signal ‘quenching’.

For the new physics models we consider in this work, only two quantities in Eq. (3.3.1) will be impacted: the transition probabilities, $P_{e\alpha}$, and the (flavour-specific) differential scattering cross section, $\mathrm{d}\sigma^{\alpha}_{\nu T}/\mathrm{d}E_R$. For the former, BSM physics can enter at the level of the matter effects that affect neutrino oscillations in the Sun (this is the MSW effect we saw in Section 2.4.4). For the latter, new physics will contribute

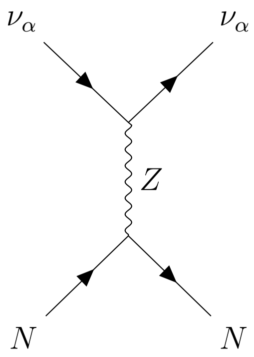

Figure 3.3: The NC interaction responsible for CEνNS.

terms to the EW interaction Lagrangian in Eq. (2.2.4), introducing new neutrino scattering interactions. We will discuss these effects in Chapter 4, where we present the BSM physics we have considered. Presently, however, we will treat the neutrino phenomenology at DD experiments predicted by the SM in combination with neutrino oscillations.

3.3.1 Coherent Elastic Neutrino-Nucleus Scattering

Coherent elastic neutrino-nucleus scattering was first predicted by Daniel Freedman in 1973 as a test of the recently developed SM EW theory [184]. He argued that, just as a weak NC interaction exists between neutrinos and electrons, so too must an NC process occur between neutrinos and nuclei. This process, depicted in Fig. 3.3, features a neutrino scattering coherently with an entire nucleus (as opposed to incoherently with only a single nucleon). The result is that the cross section of the process benefits from an enhancement that goes as the square of the atomic mass, $A^2 = (Z + N)^2$, where Z and N are the number of protons and neutrons in the nucleus, respectively. Indeed, Freedman predicted that, for energies of order $E_\nu \sim 100\,\mathrm{MeV}$, the cross section for a nucleus with as few nucleons as even carbon ($A = 12$) would be as large as $\sigma \sim 10^{-38}\,\mathrm{cm}^2$. This cross section is orders of magnitude larger than that of the inverse β-decay process we encountered in Section 2.1, which, as we saw in Section 2.3, the Homestake experiment successfully used to detect solar neutrinos.

Despite its enhanced cross section, CEνNS eluded researchers for over four decades after Freedman's prediction. The issue came not from the theoretical strength of the process, but rather from the experimental hurdle of detecting the low-energy nuclear recoils involved. Even for high-energy neutrinos with $E_\nu \sim 100\,\mathrm{MeV}$, a heavy nucleus will recoil with energies of order $E_R \sim 1\,\mathrm{keV}$. It took until 2017 to discover this elusive phenomenon, detected by the COHERENT collaboration at the Oak Ridge National Laboratory Spallation Neutron Source, where they witnessed CEνNS with neutrinos scattering off a CsI target [185]. They have since observed this process using a liquid argon target [8], as well as performed measurements of the CEνNS cross section itself [186]. All of their results have thus far been consistent with SM predictions, marking another great success for the SM.

Within the SM, the (flavour-blind) differential scattering cross section for CEνNS is given by [184, 187]

$$\frac{\mathrm{d}\sigma^{\alpha}_{\nu N}}{\mathrm{d}E_R} = \frac{G_F^2 m_N}{\pi}\left(1 - \frac{m_N E_R}{2E_\nu^2}\right)\frac{Q_{\nu N}^2}{4} F^2(E_R)\,, \tag{3.3.4}$$

where m_N is the mass of the recoiling nucleus, and the coherence is encapsulated in the factor

$$Q_{\nu N} \equiv N - (1 - 4\sin^2\theta_W)Z\,. \tag{3.3.5}$$

The nuclear form factor, $F(E_R)$, accounts for the fact that the nucleus is not a point-like particle but is rather composed of nucleons distributed according to some spatial distribution functions. This factor quantifies the decoherence that occurs when the de Broglie wavelength associated with the momentum transfer, $q = (2m_N E_R)^{1/2}$, is no longer large compared to the scale of the nucleus. This leads the effective cross section in Eq. (3.3.4) falling with increasing q [188]. For low values of q, it is effectively unity, $F(q^2 \to 0) \sim 1$.

A commonly used form factor is the Helm form factor, which treats the nucleus as a solid sphere with a Gaussian smearing around its edges [189]. It has the benefit that its form is given analytically:

$$F(q^2) = \frac{3j_1(qR_0)}{qR_0} \exp\left(-q^2 s^2/2\right) , \tag{3.3.6}$$

where j_1 is the first-order spherical Bessel function of the first kind, R_0 is the effective nuclear radius, and s is a measure of the nuclear skin thickness. R_0 can be parametrised such that Eq. (3.3.6) approximates the more realistic, though non-analytic, Fermi (or Woods-Saxon) form factor. This parametrisation is given by [188]

$$R_0 = \sqrt{c^2 + \frac{7}{3}\pi^2 a^2 - 5s^2} , \tag{3.3.7}$$

where c and s are variables that must be fitted to data, and a is a parameter related to s. All of these quantities are connected to the root-mean-square radius of the nucleon distributions, $r_{\rm RMS}$, which are experimentally measurable quantities. One can therefore fit the parameters in Eq. (3.3.7) to data, and from the muon scattering measurements of Ref. [190], they are fitted to [188]

$$c \approx (1.23A^{1/3} - 0.60)\,\text{fm} , \quad s \approx 0.9\,\text{fm} , \quad \text{and} \quad a \approx 0.52\,\text{fm} . \tag{3.3.8}$$

We note that the form factor is, in general, nucleon dependent, with two separate form factors, $F_p(E_R)$ and $F_n(E_R)$, for the proton and the neutron; this is due to their generally different spatial distribution functions. Equating these two functions to one another, $F_p(E_R) \simeq F_n(E_R) \equiv F(E_R)$, allows us to write the CEνNS cross section in the form shown in Eq. (3.3.4), where the form factor appears as a global scaling. However, we must be careful with this approximation, as the experimental best-fit values and uncertainties in the rms radii of the proton and neutron distributions are significantly different. While the $r_{\rm RMS}$ of the proton is well-known, that of the neutron is poorly constrained, as it depends on measurements completed at hadronic experiments, which are subject to large uncertainties themselves [191]. For momentum transfers of $q \lesssim 20\,\text{MeV}$, these uncertainties only have an $\sim 1\%$ effect on the form factor; however, for larger q, their impact can be as large as $\sim 5\%$ [191]. Therefore, while not important for CEνNS with solar neutrinos, for the energies

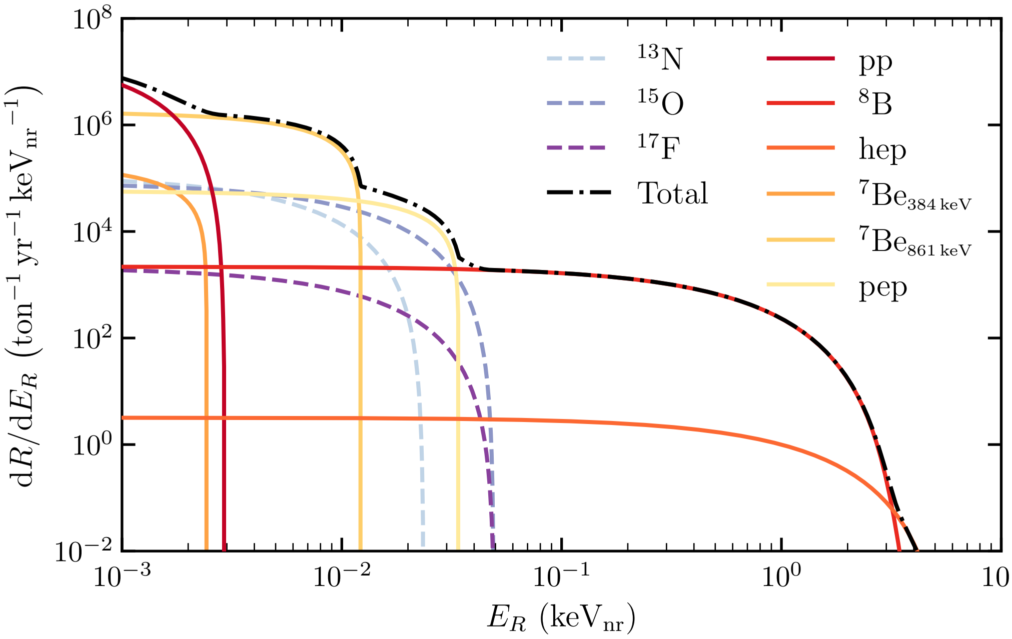

Figure 3.4: The differential rate spectrum for solar neutrino CEνNS with a ^{131}Xe target. The total spectrum (dash-dotted) is broken down into flux-specific contributions (solid).

involved in experiments such as COHERENT, these differences must be taken into account once other systematic uncertainties have been sufficiently reduced. This is crucial when interpreting the CEνNS rate in terms of new physics effects, as they can cause deviations of a similar order to the form factor uncertainties [191, 192].

We show the expected CEνNS rate due to solar neutrinos for the case of a ^{131}Xe target in Fig. 3.4. The total rate is broken down into contributions from each solar neutrino flux, the energy spectra for which are shown in Fig. 2.4. As we will see in Section 3.4, DD experiments typically have NR thresholds in the range $E_{\mathrm{thresh}} \sim 0.1$–$10\,\mathrm{keV}_{\mathrm{nr}}$, making ^{8}B neutrinos the main contributors to the CEνNS signal. We note that the rates for other targets are broadly similar, with lighter nuclei generally shifting to higher energies and lower overall rates. This is because lighter nuclei benefit from the fact that they can scatter more energetically, but their smaller size means that the coherence effect is substantially reduced, with the cross section in Eq. (3.3.4) scaling as $\sim A^2$.

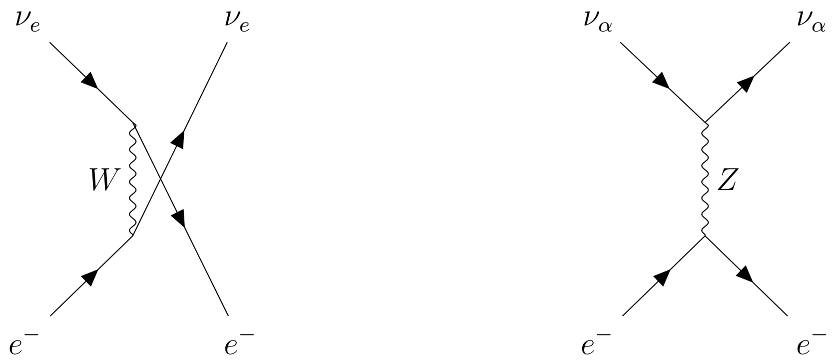

Figure 3.5: The processes responsible for EνES. The CC interaction (left) is only accessible to electron neutrinos. The NC interaction (right) is available to neutrinos of all flavours.

3.3.2 Elastic Neutrino-Electron Scattering

Elastic neutrino-electron scattering played a key role in our discussion of solar neutrinos in Section 2.3. In particular, we saw that the water Cherenkov detectors Super-Kamiokande and SNO used this process to provide us with the critical puzzle piece that helped us solve the solar neutrino problem—namely, a difference in the number of neutrinos interacting via charged and neutral currents. This was no easy feat, as the cross sections involved in EνES are of order $\sigma \sim 10^{-42}\,\mathrm{cm}^2$ [193], and they are not improved by any coherence effects like in the CEνNS case. However, as electrons are very light, even low-energy pp neutrinos can produce ERs of sufficiently high energies to be measurable by these detectors. This, combined with the high flux of these neutrinos, makes EνES with solar neutrinos a realistically observable phenomenon.

The three processes responsible for EνES within the SM are shown in Fig. 3.5. These include the CC interaction, which only occurs with electron neutrinos, and the NC interaction, which occurs with all neutrinos. The cross section is therefore flavour-specific and is given by

$$\frac{\mathrm{d}\sigma^{\alpha}_{\nu e}}{\mathrm{d}E_R} = \frac{2G_F^2\, m_e}{\pi} \left[(g_1^\alpha)^2 - g_1^\alpha\, g_2^\alpha\, \frac{m_e E_R}{E_\nu^2} + (g_2^\alpha)^2 \left(1 - \frac{E_R}{E_\nu}\right)^2 \right] , \tag{3.3.9}$$

where m_e is the electron mass, and g_1^α and g_2^α are the flavour-specific weak couplings.

They are given by

$$g_1^\alpha = g_L^e + \delta_{\alpha e} \qquad \text{and} \qquad g_2^\alpha = g_R^e \,, \tag{3.3.10}$$

where g_L^e and g_R^e are the LH and RH couplings between the electron and the Z-boson,

$$g_L^e = \sin^2\theta_W - \frac{1}{2} \qquad \text{and} \qquad g_R^e = \sin^2\theta_W \,. \tag{3.3.11}$$

The cross section in Eq. (3.3.9) is relevant for a free electron that is unencumbered by any potential well. However, the electrons we deal with in a DD experiment are always, through one means or another, bound to the detector medium. In the case of liquid noble gas detectors, electrons are bound to the target atoms themselves. For solid semiconductor targets, they are better described as residing in valence and conduction bands, whereby electrons in the former band must be promoted to the latter band via the injection of a band-gap energy before they can move freely within the lattice. These binding effects can have a sizeable impact on the expected event rate compared to the free electron case when the deposited energy, E_R, is comparable to electron binding energies, reducing the number of expected counts by as much as ∼20–30% [194]. It therefore behoves us to capture these effects to make for a realistic analysis.

The first correction we can make is to weigh the free-electron cross section by the number of orbital electrons that can be freed with a particular energy deposit. This is equivalent to inserting a (normalised) step-function into Eq. (3.3.9), such that the cross section is scaled as

$$\frac{\mathrm{d}\sigma_{\nu e}^\alpha}{\mathrm{d}E_R} \to \frac{1}{Z}\sum_{i=1}^{Z}\Theta\left(E_R - B_i\right)\frac{\mathrm{d}\sigma_{\nu e}^\alpha}{\mathrm{d}E_R} \,, \tag{3.3.12}$$

where Θ is the Heaviside step-function and B_i is the binding energy of the i^{th} electron. This approximation was first introduced by Ref. [195] to more realistically model EνES in reactor experiments, and it has been shown to be consistent with the predictions provided by quantum mechanical sum rules [196–198]. However, when E_ν and E_R become comparable to low-energy atomic binding effects, this

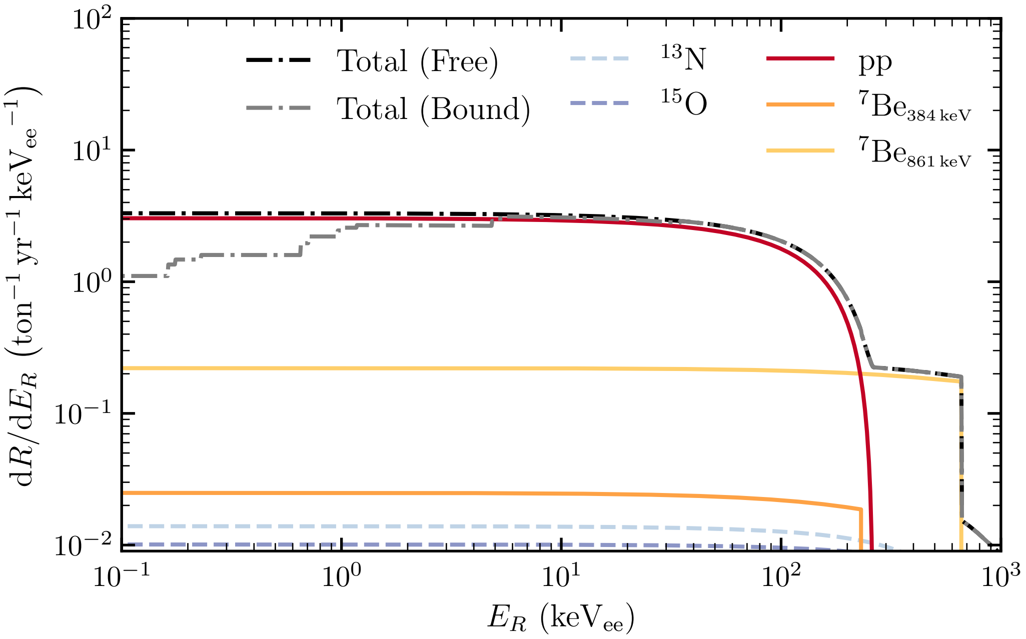

Figure 3.6: The differential rate spectrum for EνES with solar neutrinos with a ^{131}Xe target. The total spectrum (dash-dotted) is broken down into flux-specific contributions (solid). The result under the assumption of a free electron is shown in black, whereas that with the stepping approximation, which considers the electron binding energies, is shown in grey.

approximation begins to falter [199]. *ab initio* calculations based on the relativistic random-phase approximation (RRPA) [200–203], which properly takes into account the many-body dynamics involved in the collisions of interest to us, have shown a consistent suppression of the rate at low recoil energies for both germanium [199,204] and xenon [194, 205]. We will return to the RRPA in Chapter 6, where we will use it to implement a more sophisticated analysis for xenon-based DD experiments.

We show the differential rate spectrum for EνES for the case of a ^{131}Xe target in Fig. 3.6. Like that of the CEνNS case, the rate is broken down into flux-specific contributions. The first contrast we can make with the CEνNS rate is that, with no enhancements to the cross section, the EνES rate for an ER of any given energy is orders of magnitude lower than an NR of the same energy. The EνES spectrum, however, stretches to significantly higher energies, extending to recoils beyond $10^3\,\mathrm{keV_{ee}}$. This is because the electron is $\sim 10^{-5}$ times as heavy as a nuclear target, allowing for low-energy neutrinos to produce high-energy recoils. We see this explicitly in the contribution from the high-flux pp neutrinos, which produce recoils of up to $E_R \approx 250\,\mathrm{keV_{ee}}$. In fact, the scattering events caused by pp neutrinos form the dominant contribution to the EνES rate, making them the main component of the neutrino ER signal. Indeed, combined with the fact that the energy threshold for ERs is much lower than that for NRs (due to the signal quenching effect we discuss in Section 3.3.3), pp neutrinos, and to a lesser extent ^{7}Be neutrinos, typically form the main constituents of the total (NR + ER) neutrino event rate at DD experiments.

Also shown in Fig. 3.6 is the result of the stepping-approximation, which we show by means of a grey, dash-dotted line. To produce this stepped weighting, we have used the binding energy data from Ref. [194]. We see that the effect of this correction is to gradually suppress the rate at lower energies, reflecting the fact that fewer electrons can be released from their orbitals with lower energy depositions. However, at high deposited energies ($E_R \approx 30\,\mathrm{keV_{ee}}$ for xenon), this effect disappears, as the incoming neutrino energy is sufficient to free all electrons from their potential wells. This is true even when more sophisticated corrections are used to model atomic binding effects, such as the RRPA [194]. We note that, for a different target element, the rate spectrum will differ in where the binding energy effects take place, and it will also incur an overall scaling of Z/A due to a change in the number of total available electrons per unit detector mass.

3.3.3 Experimental Considerations

Before introducing the DD experiments that have inspired our work, we will briefly comment on important experimental details that we have included in our analyses. These serve to make our studies more sophisticated, such as the inclusion of resolution effects, and, in the case of quenching factors, possible at all when we ultimately combine the expected rates from both NR and ER events.

Quenching Factors

In practice, DD experiments do not directly measure the recoil energy of a target, E_R. Instead, they rely on interpreting the signal from a set of detection channels. These channels typically include signals from phonons, ionised electrons, and scintillation photons, and the channel (or channels) that a DD experiment has available to it depends on the detector technology employed. Given a signal of a particular characteristic, it can be mapped to a particular recoil energy.

However, we must be careful when performing this mapping. Following a collision with an incoming particle, a target will recoil with energy E_R, and the resulting signal will, in general, be different depending on whether the collision occurred with a nucleus or with an electron. This is because these two targets propagate very differently within the detector medium post-collision and are thus subject to different energy-loss signals [151, 152, 206]. Electrons, by virtue of their smaller size and charge, drift through the detector practically undisturbed. Nuclei, on the other hand, undergo a cascade of collisions with neighbouring atoms, quickly losing energy to their surroundings as heat. Consequently, the signal produced by a recoiling nucleus tends to be much weaker than that created by an electron for the same energy deposition. It is therefore crucial that we are able to reconstruct the initial recoil energy from the detected signal accurately, as the details of the physics we are interested in are encoded in this quantity.

Thankfully, a great deal of theoretical and experimental efforts have been made to help us perform this reconstruction. The amount by which an NR signal is suppressed, or ‘quenched’, relative to an ER signal is described by a so-called quenching factor. Once one energy scale has been calibrated—typically the ER scale as ERs undergo little-to-no quenching—this factor can then be used to move between ER and NR energies. It is defined as

$$Q(E_R) \equiv \frac{E_{ee}\,(\mathrm{keV_{ee}})}{E_R\,(\mathrm{keV_{nr}})}\,, \tag{3.3.13}$$

and it tells us how much of the initial recoil energy of a nucleus, E_R (measured in units of $\mathrm{keV_{nr}}$), is transformed into observable energy in a detector, E_{ee} (measured in units of $\mathrm{keV_{ee}}$). It can be interpreted as the ratio of the detectable energy produced by an electron recoil relative to that produced by a nuclear recoil for the same energy deposition, E_{ee}. This quenching, which is in general energy-dependent, is intrinsic to the detector material and is therefore independent of any experimental details [151]. Different mathematical descriptions for Q exist for different target materials, which must be verified by experimental measurements of it.

Experimentally, the quenching factor is determined by observing the detector response to collisions with particles of known energy. The E_{ee} scale is first calibrated using a source of monochromatic γ-rays, which cause ERs of a known energy distribution. The E_R scale is then set by the detector response to collisions caused by a source of monochromatic neutrons, which can then be compared to the relative response of ERs. The quenching factor follows directly from these calibrations[5]. Monte Carlo methods based on detector simulations can also be used to get a handle on Q [151, 152].

Theoretically, mathematical descriptions of Q aim to predict the amount of nuclear motion energy that is ultimately transformed into observable energy. Different models must be used for different detector technologies, as the nature of the detectable signal will generally be different. However, all of these models ultimately rely on the Lindhard quenching factor, which describes how the energy deposited onto a nucleus partitions into energy associated with nuclear motion and that associated

---

[5] We note that DD experiments usually measure *relative* quenching factors. These factors quantify how many quanta (ionisation or photoelectrons) are produced after an NR recoil with the same energy deposition as an ER recoil with known energy.

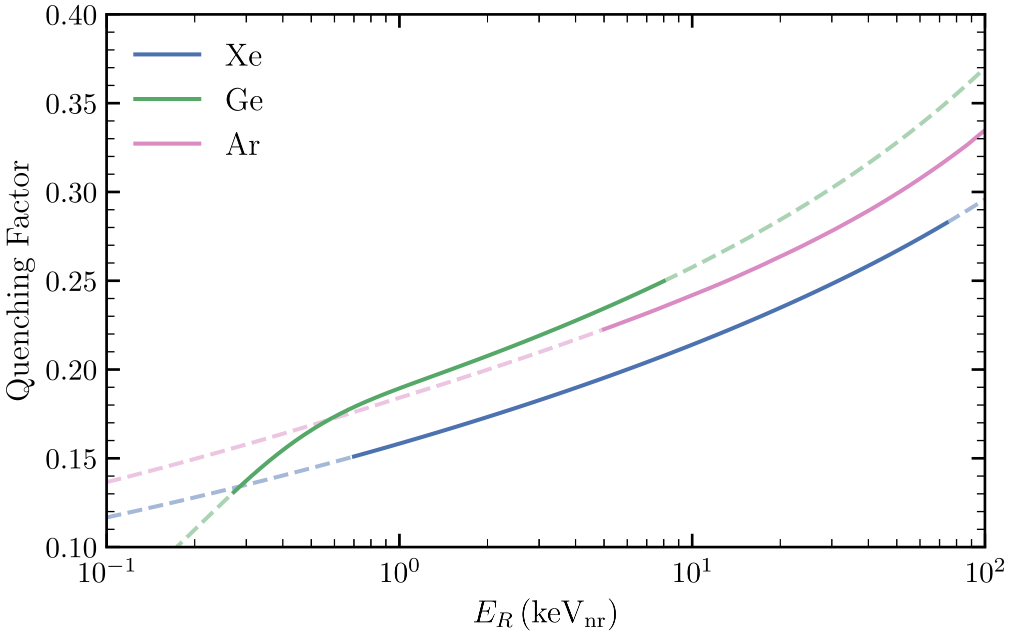

Figure 3.7: The quenching factors we have used in this work, based on fitted models to data from xenon (blue) [207], germanium (green) [208], and argon (pink) [209] targets. Note that, for germanium, the shown quenching factor models the ionisation yield, which we ultimately use in the phonon quenching of Ref. [210]. The solid lines show the results of each quenching factor model within the energy regions for which they have been verified by existing data. The dashed lines show where, for the purposes of visualisation, we have extrapolated them beyond these regions.

with electronic effects [206]. It is given by

$$Q_{\rm Lindhard} = \frac{kg(\varepsilon)}{1+kg(\varepsilon)}\,, \tag{3.3.14}$$

where $k \equiv 0.133Z^{2/3}A^{-1/2}$ in Lindhard's original description, and

$$g(\varepsilon) \equiv 3\varepsilon^{0.15} + 0.7\varepsilon^{0.6} + \varepsilon\,, \tag{3.3.15}$$

with $\varepsilon \equiv 11.5Z^{-7/3}(E_R/\mathrm{keV_{nr}})$. Physically, k is the proportionality factor in the electronic stopping power, telling us how quickly a nucleus loses its kinetic energy to electronic energy. It is usually left as a free parameter that is fitted to data, as it can hold the greatest uncertainty in the model [206].

We show the target-specific quenching factors we have used in Fig. 3.7. Each of them is based on a model fitted to experimental data spanning some energy range in E_R, and where we have evaluated a model within the same energy domain is shown as a solid line. For the purposes of visualisation, we have extrapolated these models beyond the regions where they have been experimentally tested, which we show by means of a dashed line. At low energies, complex atomic binding effects can arise that are not captured by models fitted at higher energies, so they may not accurately describe the quenching effect [211–213]. Throughout our work, we have been careful to use the fitted quenching factor models only within the domains where they have been verified by data. We will describe each of these models in greater detail in Section 3.4, where we connect each of them to a particular DD experiment.

We note that it is this quenching, which captures the different behaviours of NRs and ERs, that can be used to discriminate between the two types of scattering event. By calibrating an energy scale with one signal and then using another signal to compare the reconstructed energies, ERs can often be confidently separated from NRs in what is usually described as an experimental 'cut'. Of course, some ERs will always leak into the NR signal, and some NRs will always be inadvertently cut. Energy thresholds are often chosen such that ERs can almost be totally eliminated while retaining a relatively high NR acceptance rate [151,152]. These thresholds are set by the efficiencies of particular experiments.

Efficiency and Resolution Effects

Experiments are neither infinitely sensitive nor infinitely precise; experimental efficiency and resolution functions capture these unavoidable detector imperfections. Improving these facets of an experiment is always an ongoing mission for DD experiments, as it allows them to not only improve their signal in their regions of interest, but also lower their energy thresholds to give them sensitivity to lower energy phenomena. We have incorporated efficiency effects throughout our work, including the effects of finite resolutions in Chapters 6 and 7 to improve our analysis further.

The efficiency of an experiment can be accounted for by folding an efficiency function, $\epsilon(E_R)$, into the expected rate spectrum,

$$\frac{\mathrm{d}R}{\mathrm{d}E_R} \to \frac{\mathrm{d}R}{\mathrm{d}E_R}\epsilon(E_R)\,. \tag{3.3.16}$$

This function, which is generally energy dependent, is close to unity at high E_R, where the produced signal can be captured with high certainty, but it rapidly eliminates the signal at low E_R, where a detector will have a low chance of triggering. Typically, the threshold energy of an experiment is quoted as that E_R at which its efficiency reaches 50%.

Additionally, the finite precision, or resolution, of an experiment can cause the expected recoil spectrum at any given energy to become smeared over a range of energies. This results in the reconstructed recoil energy, E_R, differing from the true recoil energy, E'_R. As measurements are always made with respect to the electron-equivalent energy scale, this smearing occurs at the level of E_{ee}. For a given resolution function $f(E_{ee}, E'_{ee})$, which depends on both the measured and true energies, the observed spectrum is given by convolving the true spectrum with f. Assuming a Gaussian resolution function with energy-dependent width $\sigma(E'_{ee})$, the observed spectrum is then

$$\frac{\mathrm{d}R}{\mathrm{d}E_{ee}} = \int_0^\infty \frac{\mathrm{d}R}{\mathrm{d}E'_{ee}}\epsilon(E'_{ee})\frac{1}{\sigma(E'_{ee})\sqrt{2\pi}}\exp\left[-\frac{(E_{ee}-E'_{ee})^2}{2\sigma^2(E'_{ee})}\right]\mathrm{d}E'_{ee}\,, \tag{3.3.17}$$

where we have included efficiency effects and where $\mathrm{d}R/\mathrm{d}E'_{ee}$ is given by Eq. (3.3.1) (with $E'_{ee} = E'_R$ for electron recoils). In the case of NRs, the CEνNS spectrum must first be converted to the electron-equivalent energy scale, which can be done via the quenching factor transformation

$$\frac{\mathrm{d}R}{\mathrm{d}E_{ee}} = \left(Q(E_R) + \frac{\mathrm{d}Q}{\mathrm{d}E_R}(E_R)E_R\right)^{-1}\frac{\mathrm{d}R}{\mathrm{d}E_R}\,. \tag{3.3.18}$$

Experiments will usually give a measure of their resolution through the quantity $\sigma(E'_{ee})/E_{ee'}$, where they measure by how much a signal spreads for a known energy deposit. This quantity is high for low energies and low for high energies, reflecting the fact a detector performs better at higher energies.

We note that, when calculating the total rate between the (electron-equivalent) energies E_1 and E_2, we can swap the order of integration to remove the integral over the measured energy. We get that

$$R(E_1, E_2) = \int_0^\infty \frac{\mathrm{d}R}{\mathrm{d}E'_{ee}} \epsilon(E'_{ee}) \Phi(E'_{ee}, E_1, E_2)\, \mathrm{d}E'_{ee}\,, \tag{3.3.19}$$

where we have defined the response function, Φ, as

$$\Phi(E'_{ee}, E_1, E_2) \equiv \frac{1}{2}\left[\mathrm{erf}\left(\frac{E_2 - E'_{ee}}{\sigma(E'_{ee})\sqrt{2}}\right) - \mathrm{erf}\left(\frac{E_1 - E'_{ee}}{\sigma(E'_{ee})\sqrt{2}}\right)\right]\,, \tag{3.3.20}$$

and where $\mathrm{erf}(z)$ is the error function.

3.4 Next-Generation and Far-Future DD Experiments

We will conclude this chapter by introducing the upcoming and far-future DD experiments that have inspired our analyses. We will respectively refer to these experiments as generation-two (G2) and generation-three (G3) experiments. As we discussed in Section 3.1, all of these experiments have the potential to observe solar neutrinos through both CEνNS and EνES—especially those breaking through the neutrino floor. They are therefore poised to act as key players in the future of not only DM physics, but also neutrino physics. In Table 3.1, we summarise their projected configurations as well as the signals they are able to measure, which we break down into ionisation (I), phonon (P), and scintillation (S) signals. We note that, while we show the nominal specifications for the experimental exposures and NR thresholds from the respective experiment design reports, we take the freedom of varying these parameters in our analyses to explore the full potential of each of these detectors.

Exp.	Gen.	Target	ε (ton yr)	$E_{\rm th}$ (keV$_{\rm nr}$)	Signal
LZ [14]	G2	^{131}Xe	15.34	6	I + S
XENONnT [15]	G2		20	4	
DARWIN [16]	G3		200	6.6	
SuperCDMS iZIP [13]	G2	^{73}Ge	0.056	0.272	I + P
SuperCDMS HV [13]			0.044	0.040	
DarkSide-20k [17]	G3	^{40}Ar	100	30	I + S

Table 3.1: The base experimental configurations we consider in this work. We list the generation of the experiment as being either next-generation (G2) or far-future (G3). The written target is the main isotope present in an experiment. We take the experimental exposures and NR thresholds from the respective design reports. The signals observed can include ionisation (I), phonon (P), and scintillation (S) signals.

3.4.1 LZ, XENONnT, and DARWIN

The LZ [214] and XENONnT [15] detectors are both G2 DD experiments. LZ is based at the Sanford Underground Research Facility (South Dakota, USA) and is projected to have a total exposure of 15.34 ton yr, corresponding to running the 5.6 ton experiment for 1000 livedays. XENONnT, based at the Laboratori Nazionali del Gran Sasso (Italy), will be the next iteration of the XENON1T [215] experiment and is planned to have an exposure of 20 ton yr. The DARWIN [16] experiment, on the other hand, is a G3 DM observatory, expected to begin its first science run in 2023 and have the much higher exposure of 200 ton yr. Their nominal thresholds, optimised for the DM search to avoid neutrino events, are all similarly placed at $E_{\rm thresh} \approx 4$–$7\,{\rm keV_{nr}}$. Despite these high thresholds, however, they are all projected to break through the neutrino floor, piercing through the ^{8}B shoulder, as can be seen from Fig. 3.2. With their large target sizes and high volumes, these experiments offer us our best hope of seeing a large number of high-energy solar neutrinos at a DD experiment.

All of these experiments are based on the same detector technology: they all employ double-phase time-projection chambers (TPCs). TPCs are large cylindrical vats that are filled with a liquid noble element in the centre and its corresponding gaseous phase at the ends, with an electric field applied across the chamber. In this case, these vats are filled with liquid xenon (LXe) and gaseous xenon (GXe). The LXe acts as the main target for an incoming particle, which collides with a xenon atom and either excites it or ionises it. If excited, the xenon eventually relaxes, releasing a prompt scintillation photon in the UV range that can be detected by photomultiplier tubes; these photons are typically referred to as the primary scintillation signal (S1). If ionised, the released electrons either drift towards the GXe, where they produce proportional scintillation photons and create a delayed secondary scintillation signal (S2), or recombine in the liquid phase to produce further scintillation photons that enhance the S1 signal. Recoiling atoms also disturb the surrounding medium, causing further atoms to undergo these same processes.

The S1 and S2 signals can be used to get a handle on potential sources of background. The delay between the S1 and S2 signals allows these experiments to determine the depth at which a collision occurred[6], allowing them to reject surface events that are more likely to have been caused by background sources. Moreover, the relative size of these signals gives them the ability to discriminate between NR and ER events. As we saw in Section 3.3.3, NR events produce a much smaller ionisation signal for the same deposited energy compared to an ER event, so the S2 signals caused by NRs are considerably smaller than those produced by ERs. Consequently, the S1 signal, which is weaker than the S2 signal, largely dictates the energy threshold, as it can only be lowered so far until the S1 signal disappears and the ability to perform NR/ER discrimination is lost. We note, however, that several S2-only analyses have been completed, foregoing this discriminatory power for a lower energy threshold [216–218]. Indeed, we will take advantage of this fact when justifying the

---

[6] In fact, the S2 signal also allows for (x, y)-position reconstruction. Combined with the time-delay information, this gives TPCs access to the full set of interaction observables: $(\mathrm{S1}, \mathrm{S2}, x, y, z, t)$.

lower thresholds we use throughout this work.

For these xenon-based experiments, we use the Lindhard model of Eq. (3.3.14) as our quenching factor, shown in Fig. 3.7. This has been shown to be a good description of the energy partition for LXe experiments as long as one uses the total S1 + S2 signal, which is composed of both ionisation electrons and scintillation photons [219]. For the k-factor, we use the best-fit value determined by the LUX collaboration, $k = 0.1735$, who validated the Lindhard model down to energies as low as $0.7\,\mathrm{keV}_{\mathrm{nr}}$ [207]. This model also agrees well with the results from the calibrations of other xenon-based DD experiments [220–227], which are collated in the review by Ref. [228].

3.4.2 SuperCDMS at SNOLAB

The next-generation SuperCDMS experiment has now been successfully relocated to SNOLAB—an underground facility in the Vale Inco Mine in Sudbury, Canada [13]. Located at a depth of 2 km, it boasts increased shielding from cosmic ray muon backgrounds compared to its predecessor, which was housed in the Soudan Mine in Minnesota [229]. With its low energy thresholds ($E_{\mathrm{th}} \sim 100\,\mathrm{eV}$), it is projected to give us the best low-mass WIMP limits yet [13], which we show in Fig. 3.2.

The SuperCDMS experiment uses the semiconductor targets germanium and silicon, which are cryogenically cooled to sub-Kelvin temperatures. A collision with one of these crystal targets produces phonon excitations that are measurable through minuscule temperature rises in the detector material. As a nucleus propagates through the detector, electron-hole pairs are also produced, which can be collected if an electric field is applied across it. In a phenomenon known as the Luke-Neganov effect [230, 231], these electron-hole pairs cause further phonon excitations as they move through the detector medium, enhancing the phonon signal. The total signal is therefore a combination of a primary phonon and a secondary ionisation signal, with the latter allowing for the discrimination between NRs and ERs, as the ionisation signal produced by NRs is much smaller than that caused by ERs (see Section 3.3.3). We note that, due to the greater planned volume of germanium used at the SuperCDMS experiment, we will focus on this target material throughout our work.

SuperCDMS employs two types of detectors to take advantage of these different signals: a high-voltage (HV) detector and an interleaved Z-sensitive ionisation phonon (iZIP) detector. The latter, with an expected full exposure of 56 kg yr and threshold of 0.272 $\mathrm{keV_{nr}}$, interleaves phonon and ionisation sensors, allowing for the discrimination of surface events—which are composed of background recoils—and bulk events—which are more likely to be a signal. Moreover, the electric field applied across the iZIP detectors enables them to distinguish between NR and ER events. The HV detector, with a predicted full exposure of 44 kg yr and much lower threshold of 0.040 $\mathrm{keV_{nr}}$, differs from the iZIP detector by the application of a much stronger electric field [13]. This greatly increases the phonon signal arising from the Luke-Neganov effect, resulting in a lower energy threshold compared to the iZIPs. However, this comes at a cost: they are unable to discriminate between NRs and ERs. This is because Luke-Neganov phonons become the dominant contribution to the overall phonon signal, leading to the phonon readout effectively becoming proportional to the ionisation signal.

When converting between the NR and ER scales, we consider the total signal as only being composed of phonons for both the HV and iZIP detectors. This is due to the fact that, despite the iZIP detectors having the power to detect both ionisation and phonon signals, the signal produced by recoiling nuclei is primarily phonon based [13]. The quenching factor we use must then be able to describe the quenching of the deposited energy in terms of phonon energy, which is the sum of the recoil energy E_R and the phonon energy generated by Luke-Neganov phonons. To perform this quenching, we follow the prescription of Ref. [210], which uses the ionisation yield, $Y(E_R)$, to describe how much of the initial atomic phonon energy is converted into an ionisation signal. This yield, as it pertains to germanium, has been the subject of many studies [208, 232–243], and we parametrise it according to the form introduced by Ref. [208], which is built from the Lindhard model and a series of functions that correct for experimental and material effects[7]. We show this total yield function in Fig. 3.7, which has been fitted to data as low as $0.272\,\mathrm{keV_{nr}}$.

3.4.3 DarkSide-20k

The DarkSide-20k [17] experiment is a G3 detector, employing essentially the same TPC technology as the xenon-based experiments of Section 3.4.1 but with argon. It is aimed to have an initial exposure of 100 ton yr and will take advantage of argon's abundant natural occurrence, making it easier to scale up. Indeed, with its large exposure, it is expected to give us the best limits in the high-mass region of the WIMP parameter space, falling close to the background of atmospheric neutrinos seen in Fig. 3.2.

The key difference between argon and xenon TPC experiments lies in how they perform NR/ER discrimination. This is of crucial importance in argon detectors, as the natural abundance of the radioactive isotope ^{39}Ar in the detector makes for a large ER background [151]. Generally, the ratio of the S1 and S2 signals is not enough to sufficiently reduce this increased background [244], so another, powerful method is used in combination with it. Known as 'Pulse Shape Discrimination', this technique uses the different decay times of the excited states in liquid argon following a collision with an incoming particle. The relative size of the populations of these excited states is different depending on whether a collision occurred with a nucleus or an electron, and the difference in decay times (measured as the prompt S1 scintillation signal) can be used to perform NR/ER discrimination [245]. However, a large number of scintillation photons must be measured to use this technique, leading to the higher energy threshold of $30\,\mathrm{keV_{nr}}$ in the case of DarkSide-20k [17].

---

[7] We note that, very recently, the SuperCDMS collaboration completed its own measurement of this yield in Ref. [232], performing a fit to its own Lindhard-based yield function. We encourage the use of this more recent, and more relevant, yield for future studies involving SuperCDMS in the same energy domain.

The total quenching factor we use for argon, which accounts for both the S1 and S2 signal, is based on the model built by Ref. [209]. This description uses the ideas of Ref. [246], combining the Lindhard factor, describing the atomic energy loss into electrical energy, with Birk's saturation law [247], describing the loss of the scintillation signal. We show this total quenching factor in Fig. 3.7, which has been verified down to $5\,\mathrm{keV_{nr}}$ and agrees with data from ARIS [209] and DarkSide-50 [248]. It is also in broad agreement with the measurements of Refs. [249–251].

CHAPTER 4

New Physics in the Neutrino Sector

The SM of particle physics is surely one of humankind's greatest achievements. Describing to astonishing detail many of the small-scale physics we are sensitive to today, it is our best theory of the world of the very small. However, many readily observable phenomena that refuse to be explained by the SM. From the fact that our galaxy manages to stick itself together with DM to the mystery of neutrino oscillations that we saw in Chapter 2, we now have overwhelming evidence that the SM is incomplete. Finding increasingly more cracks in the SM is one of the primary goals of modern physics, giving us a greater wealth of information with which to base models of BSM physics. Neutrinos, having already displayed non-standard behaviour, are one of the most popular candidates with which to look for this, and how DD experiments might help us to reveal more of their mysteries is the subject of intense research.

In this chapter, we will introduce the new leptonic physics models that we will focus on in this work. We will first motivate the need for this kind of BSM physics in the form of the growing tension in the muon's anomalous magnetic moment, which forms the basis of our work in Chapters 5 and 6, and the tension in the value of the Hubble constant, which we use as a secondary motivator. We will then introduce the gauged $U(1)_{L_\mu - L_\tau}$ model—a particularly elegant explanation to both of these modern mysteries. We will also introduce generic realisation of a $U(1)_{L_\mu}$ model, which, though theoretically less well-motivated, functions as an excellent model with which to compare to the $U(1)_{L_\mu - L_\tau}$ due to its similar phenomenology. Finally, we will present the framework of NC neutrino non-standard interactions, which is the subject of Chapter 7 and acts as a general effective description of BSM neutrino physics.

4.1 Motivation

We begin by introducing two modern-day physics mysteries that have motivated much of our work. The first of these is the tension anomalous magnetic moment of the muon, which has largely guided the work of Chapters 5 and 6. We will see that an elegant way to explain this tension is to introduce a new force mediator that couples to the second- and third-generation leptons, therefore introducing new physics in the neutrino sector. The second of these mysteries is the tension in the present-day value of the Hubble parameter. A secondary motivator of our work, it can be simultaneously explained through the same BSM extension.

4.1.1 The Muon's Anomalous Magnetic Moment

Any electrically charged particle with non-zero intrinsic spin possesses a magnetic dipole moment, $\boldsymbol{\mu}$. All leptons, therefore, admit a magnetic dipole moment, and the muon—with a charge of $-e$, a spin of $1/2$, and a mass of m_μ—has a dipole moment of

$$\boldsymbol{\mu}_\mu = -g_\mu \left(\frac{e}{2m_\mu} \right) \boldsymbol{S} \,, \tag{4.1.1}$$

where $\boldsymbol{S}$ is the muon's spin vector and g_μ is the muon's gyromagnetic ratio, or g-factor. This latter quantity is an intrinsic property of the muon, quantifying by how much $\boldsymbol{\mu}_\mu$ differs from the classically derived result of $g_\mu = 1$.

A hallmark achievement of Paul Dirac's was to derive a value for the gyromagnetic ratio of the electron, $g_e = 2$ [252]. However, following from the Dirac equation, this result is not specific to the electron: it is a general result for all charged fermions if they are considered to be structureless, point-like particles. This prototypical value for the g-factor can be interpreted as the tree-level result of a coupling between a charged lepton and an electromagnetic field. Today, we understand that this tree-level process is not the end of the story: higher-order, radiative corrections are needed to describe this coupling completely. We can quantify the effect of these higher-order corrections through the anomalous magnetic dipole moment of the charged lepton, a_l, defined as

$$a_l \equiv \frac{g_l - 2}{2}\,. \tag{4.1.2}$$

This is simply the fractional difference in the particle's g-factor compared to the tree-level result of Dirac.

Inspired by the anomalies arising in the hyperfine structure of the hydrogen atom [253, 254], Julian Schwinger calculated the very first radiative correction to the electron's magnetic dipole moment [255]. His result corresponded to the lowest order, loop level QED correction, equivalent to the contribution of a single photon propagator. He predicted the first anomalous value of $a_e \approx \alpha/2\pi$, where $\alpha \approx 1/137$ is the fine-structure constant. This result is famously engraved on Schwinger's gravestone.

This result, however, is the first of many higher-order corrections. The complete picture must take into account all possible radiative processes that can take place at the QED vertex, which we visualise as an effective interaction in Fig. 4.1. To calculate a_l in full is to capture the full breadth of the quantum theory describing this simple interaction between leptons and photons. The more precisely we calculate this quantity, therefore, the more we can push the SM to its limits when

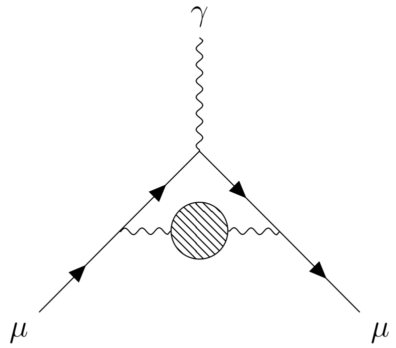

Figure 4.1: Radiative corrections to the muon's anomalous magnetic moment. This effective loop process can represent corrections of infinitely high order both within and outside the SM.

experimentally measuring it.

For the anomalous magnetic moment of the muon, a_μ, the complete SM contribution can be expressed as the sum of all possible QED, EW, and hadronic vacuum polarisation (HVP) contributions,

$$a_\mu^{\text{SM}} = a_\mu^{\text{QED}} + a_\mu^{\text{EW}} + a_\mu^{\text{HVP}} \,. \tag{4.1.3}$$

The QED contribution arises from loops containing photons and leptons. Loops containing the EW gauge bosons and the Higgs give us the EW input. The hadronic contribution, which is the most difficult to calculate of all and the subject of intensive research [256–265], stems from loops containing hadrons within vacuum polarisation loops. We illustrate some of the processes contributing to each of these terms in Fig. 4.2. The total uncertainty in the final value of a_μ in Eq. (4.1.3) is dominated by uncertainties in HVP processes, and we must therefore be careful to incorporate the various tensions in a_μ^{HVP} in the calculation. Ref. [266], building on the results of an extensive body of work on the subject [256–265, 267–275], carefully calculated what is now the accepted value of a_μ:

$$a_\mu^{\text{SM}} = 116591810(43) \times 10^{-11} \,. \tag{4.1.4}$$

The quest to experimentally verify whether a_μ agrees with the theoretical SM result has been a long and exciting one. We will briefly review its almost 70-year history

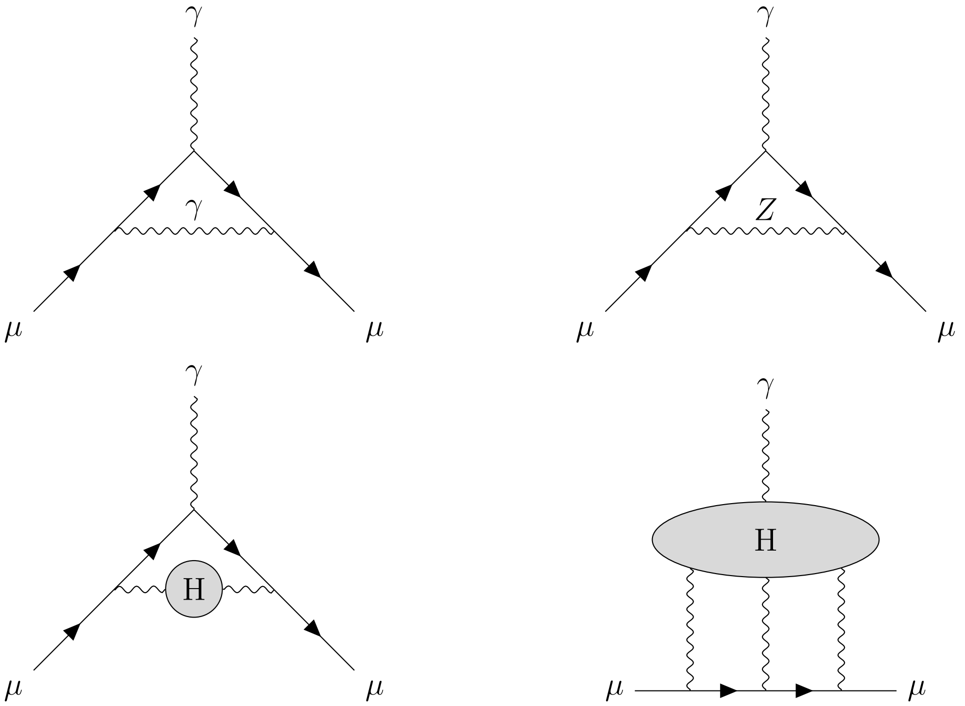

Figure 4.2: Higher-order corrections to the muon's anomalous magnetic moment within the SM. From most to least contributing, these are first-order QED (top left) and weak (top right) processes, leading-order hadronic (H) vacuum polarization (bottom left), and hadronic light-by-light contributions.

below, outlining the journey we have taken to measure one of the most precisely known quantities in all of physics. We provide a summary of the evolution of its measurement in Table 4.1.

Experimental interest in the muon's anomalous magnetic moment began at CERN in 1957, with the first results published in 1965 [277]. A total of three experiments were run over the course of over 20 years [276–278]—each one improving on the precision of the last. Their aim was twofold: to provide ever more stringent tests of QED and to look for effects beyond QED [279]. The particular interest in a_μ followed the lead of the recent measurement of the electron's anomalous magnetic moment, which agreed with the theoretical value at the time to great accuracy [280]. Due to the muon's much higher mass compared to that of the electron ($m_\mu/m_e \approx 200$), the virtual photon contributions to a_μ were expected to be much larger than those to a_e. Indeed, second-order vacuum polarisation effects, un-probable by the electron due

Year	Exp.	a_μ $\left(\times 10^{-11}\right)$	Prec. (ppm)	SM Tension	Ref.
1979	CERN	116592400(850)	7	0.7σ	[276]
2004	BNL	116592080(63)	0.54	3.5σ	[4]
2021	FNAL	116592040(54)	0.46	3.3σ	[5]
2021	FNAL + BNL	116592061(41)	0.35	4.2σ	[5]

Table 4.1: The history of the measurements of the muon's anomalous magnetic moment. We show the averaged results of the experiments that have measured a_μ, together with their precisions and tensions with the theoretical SM result.

to its low mass, were unlocked to these experiments. Moreover, possible new physics effects that serve to increase the value of a_μ, such as the first-order exchange of a new vector boson, would go as m_μ^2, giving these experiments an advantage in searching for BSM physics. The final CERN result, averaged over muons and anti-muons, was published in 1979 and had an averaged precision of 7 ppm [276, 279],

$$a_\mu^{\text{CERN}} = 116592400(850) \times 10^{-11} \,, \tag{4.1.5}$$

which agreed well with the theoretical value at the time of

$$a_\mu^{\text{SM, CERN}} = 116592100(830) \times 10^{-11} \,. \tag{4.1.6}$$

Thus, following the results of all three CERN experiments, measurements of a_μ suggested no hints of new physics in the leptonic sector.

It was 20 years before experiments once again probed the a_μ, and it was Brookhaven National Laboratory (BNL) that took up the gauntlet. Using methods first pioneered by CERN, but with improved technology, the BNL E821 experiment set out to perform five further measurements of a_μ [4, 281–284]. By this point, the theoretical determination of a_μ had matured to include higher order corrections of the processes outlined in Eq. (4.1.3), and its experimental determination therefore stood to test the SM more stringently than before. The final, averaged result of the BNL runs, released in 2004 with a precision of 0.54 ppm, was [4, 285]

$$a_\mu^{\text{BNL}} = 116592080(63) \times 10^{-11} \,. \tag{4.1.7}$$

At the time, this brought a 2.2—2.7σ tension to the SM prediction, depending on how the HVP radiative corrections were taken into account. Indeed, after further such corrections were incorporated into the theoretical value of a_μ, giving us the present value shown in Eq. (4.1.4), this tension was increased to 3.5σ. Thus, the BNL result indicated a possible discrepancy with the SM value, hinting at potential new physics at play and the upheaval of the SM. It would be almost another two decades before a_μ was explored again.

In April 2021, Fermilab's Muon $g-2$ collaboration released the results of the most precise measurement of the muon's anomalous magnetic moment to date [5]. The E989 experiment at Fermilab used many of the techniques used by BNL, but it benefited from several experimental improvements [5, 286]. Their result, which reached a precision of 0.46 ppm, was

$$a_\mu^{\text{FNAL}} = 116592040(54) \times 10^{-11} \,, \tag{4.1.8}$$

differing from the SM result by 3.3σ. Taking the average of the Fermilab and BNL results, we find that

$$a_\mu^{\text{FNAL+BNL}} = 116592061(41) \times 10^{-11} \,, \tag{4.1.9}$$

raising the tension with the SM significantly to 4.2σ[1]. This final result provides us with the greatest tension in the anomalous magnetic moment of the muon since its first measurement in 1979, differing from the SM result of Eq. (4.1.4) by

$$\Delta a_\mu = 251(59) \times 10^{-11} \,. \tag{4.1.10}$$

---

[1] We note that a recent lattice QCD calculation of the leading-order HVP processes can significantly alleviate this tension [287]. However, this comes at the expense of creating a tension with e^+e^- data and worsening fits to EW variables, such as the masses of the EW gauge bosons [288].

This tension, often quoted as the $(g-2)_\mu$ tension, could signal another nail in the SM coffin should it reach a discovery-level significance of 5σ,

Due to the gauge invariance of the $SU(2)_L$ SM symmetry group, any new physics that we introduce for the heavy, charged leptons should also impact their corresponding neutrinos. By virtue of this, hints of new physics with the muon more broadly suggest BSM physics with the second-generation leptons. Thus, the a_μ tension provides us with a tantalising hint of BSM physics for the muon neutrino, and, for this reason, it forms the key motivator in Chapters 5 and 6, where we use it as our inspiration for the study of light new physics in the neutrino sector.

4.1.2 The Hubble Tension

We have empirically known that our Universe is expanding since the early 20th-century. In 1929, the American astronomer Edwin Hubble, following his measurements of the redshifts of Cepheid variables within distant galaxies, discovered that all galaxies appear to be receding from us at a rate proportional to their distance away from us [289]. This relationship, which has famously come to be known as Hubble's law, can be expressed as

$$v = H(t)d\,, \tag{4.1.11}$$

where v is the recessional velocity of a galaxy that is following the Hubble flow, d is the distance to the galaxy from an observer, and $H(t)$ is the constant of proportionality between these quantities, known as the Hubble parameter. This quantity is a cornerstone of modern cosmology, enabling us to make predictions about the expansion history of our Universe.

The present-day value of the Hubble parameter, known as Hubble's constant H_0, is a difficult quantity to determine. There are ultimately two ways of measuring it: either through direct measurements of the recession velocities and distances of distant galaxies, or through cosmological fits to CMB data. Due to where the focus is placed in these techniques, the values determined using them are commonly referred to as late- and early-time measurements of H_0, respectively. We will briefly outline how these methods work and how they lead to a worrying problem in cosmology: the Hubble tension.

The power spectrum of the CMB contains a wealth of information about the early history of our Universe. Assuming a particular cosmology, we can use this spectrum to fit the parameters describing our cosmological model. The 6-parameter ΛCDM model treats our Universe as being composed of three energy densities: dark energy, cold dark matter, and ordinary baryonic matter. It is widely regarded to be the standard of cosmological models, as it can explain many of the phenomena we observe in our cosmos. A fit to the CMB power spectrum using the ΛCDM model was last performed in 2018 by the Planck collaboration, who inferred a value for the present-day Hubble parameter of $H_0 = (67.4 \pm 0.5)\,\mathrm{km\,s^{-1}\,Mpc^{-1}}$ [6].

Alternatively, direct, late-time measurements of H_0 rely on careful measurements of the recession velocities of distant galaxies and their distances away from us. This allows us to use Eq. (4.1.11) to fit to the value of H_0. However, while recession velocities are typically easy to determine, distances turn out to be difficult to measure. To find the distances to different bodies in the Universe, we use what is called the 'distance ladder': a set of distance-measuring techniques tailored to how far away the object is, wherein each 'rung' of the ladder is calibrated using the technique of the last. For instance, to measure the distance to the closest stars to us in the Milky Way, we can use trigonometric parallax to relate the angular shift in the apparent position of a star to its distance away from the Sun. On the other hand, to measure the distances to distant galaxies, we must rely on 'standard candles'—objects with known luminosities or luminosity relations—the distances to which we first calibrate using this parallax technique. As Hubble's law only pertains to the velocities of objects that follow the Hubble flow, such as galaxies or galaxy clusters, we are primarily interested in ladder rungs that rely on these so-called standard candles.

There have been many late-time measurements of H_0, which have relied on a variety of standard candles (c.f. Fig. 2 of Ref. [290]). The most recent of these measurements was performed earlier this year by the SH0ES collaboration, who used Cepheid variables and type Ia supernovae, observed with the Hubble Space Telescope, to arrive at the significantly higher value of $H_0 = (73.04 \pm 1.04)\,\mathrm{km\,s^{-1}\,Mpc^{-1}}$ [7]. This result is in $\sim 5\sigma$ tension with the early-time, high-precision measurement of the Planck collaboration, and it is known as the H_0, or Hubble, tension.

This discrepancy presents a significant problem to modern cosmology. It calls into question either the calibration of the distance ladder or our understanding of the early- or late-time cosmology of the standard ΛCDM model [291][2]. In the latter case, the ΛCDM would need to be extended with physics beyond the Standard Model, introducing new physics that modifies the early- or late-time history of the universe. This alleviates the H_0 tension by introducing new parameters that can be fitted to the CMB power spectrum, allowing the fitted value of H_0 to find a new minimum that potentially both agrees with CMB data and the late-time measurements of H_0. Many one-parameter extensions have been proposed for this purpose, including those with a non-zero curvature for the Universe, a dynamical dark energy component, and a higher number of effective neutrino species in the early Universe [293–299]. Indeed, we will see in the next section how introducing a new light mediator that couples to both the second- and third-generation leptons can significantly alleviate the H_0 tension by altering precisely this final quantity.

---

[2] We note that measurements of H_0 using stars on the Tip of the Red Giant Branch—red giants undergoing a helium flash—instead of Cepheids arrive at the slighter lower value of $H_0 = (69.8 \pm 1.8)\,\mathrm{km\,s^{-1}\,Mpc^{-1}}$ [292]. This value is in agreement with the CMB data presented by Planck to 1.3σ and with the Cepheid-calibrated SH0ES result to 1.6σ. However, while this measurement presents us with a halfway-house between these values, it neither explains their discrepancy nor precludes an explanation of it with a cosmological model beyond the ΛCDM model.

4.2 New Physics Interactions

4.2.1 The Minimally Gauged $U(1)_{L_\mu - L_\tau}$

The SM Lagrangian is invariant under the accidental global symmetries $U(1)_{B,L_e,L_\mu,L_\tau}$, corresponding to gauging the total baryon number, B, and the individual lepton numbers, L_α (with $\alpha \in \{e,\, \mu\,\tau\}$). We can combine the last three of these symmetries into groups conserving either the difference between the total baryon number, creating $U(1)_{B-L}$, or the difference between different individual lepton numbers, creating groups of the form $U(1)_{L_\alpha - L_\beta}$ (for $\alpha \neq \beta$). These latter groups, and their linear combinations, can be promoted to gauge groups that extend the SM without the need to introduce anomaly-correcting fermionic field content[3].

Of these three anomaly-free gauge groups, the $U(1)_{L_\mu - L_\tau}$ group can be used to elegantly explain the $(g-2)_\mu$ tension we introduced in Section 4.1.1. Extending the SM by a minimally gauged $U(1)_{L_\mu - L_\tau}$ introduces a new gauge boson, a so-called 'hidden photon', that couples to the second- and third-generation leptons. Due to its coupling to the muon, this hidden photon contributes an additional diagram to the radiative corrections that take place at the muon-photon vertex and, for particular values of its gauge coupling and mass, it can exactly account for the observed deviation in $(g-2)_\mu$. Owing to its theoretical elegance and continued potential to explain this possibly profound tension with the SM, it has been the subject of many studies [300–304]. Before discussing precisely how it can alleviate this tension, we will briefly outline how we can add this new particle to the SM.

To introduce this hidden photon into the SM, we simply add the relevant terms to the EW Lagrangian of Eq. (2.2.4). In the gauge basis, we can write the $U(1)_{L_\mu - L_\tau}$-extended Lagrangian as

$$\mathcal{L} = \mathcal{L}_{\text{EW}} - \frac{1}{4} X_{\alpha\beta} X^{\alpha\beta} - \frac{\epsilon_Y}{2} B_{\alpha\beta} X^{\alpha\beta} - \frac{m_X^2}{2} X_\alpha X^\alpha - g_{\mu\tau} j_\alpha^{\mu-\tau} X^\alpha \,, \tag{4.2.1}$$

---

[3] The group $U(1)_{B-L}$ can also be promoted to form an anomaly-free gauge theory as long as we also add an extra three right-handed neutrinos to cancel the anomalies that are introduced.

where X_α is the gauge field of the new hidden photon of mass m_X, $X_{\alpha\beta}$ is its associated field strength tensor, ϵ_Y parametrises the strength of the kinetic mixing between the SM photon and new hidden photon, and $g_{\mu\tau}$ is the gauge coupling. All other quantities have the same definitions we provided in Section 2.2. The gauge current of the new symmetry, which describes its tree-level interactions, is given by

$$j_\alpha^{\mu-\tau} = \overline{L}^2 \gamma_\alpha L^2 + \overline{\mu}_R \gamma_\alpha \mu_R - \overline{L}^3 \gamma_\alpha L^3 - \overline{\tau}_R \gamma_\alpha \tau_R \,. \tag{4.2.2}$$

Ultimately, we observe such interactions in the mass basis, so we must rotate to it to study the phenomenology of this new particle. We find that the interaction Lagrangian of the mass eigenstate of X_α, A'_α, is given by

$$\mathcal{L}_{\text{int}} = -\left(e j_\alpha^{\text{EM}}, g_Z j_\alpha^Z, g_{\mu\tau} j_\alpha^{\mu-\tau}\right) K \begin{pmatrix} A^\alpha \\ Z^\alpha \\ A'^\alpha \end{pmatrix} , \tag{4.2.3}$$

where, to leading order in the kinetic mixing parameter and hidden photon mass, the coupling matrix, K, is such that

$$K = \begin{pmatrix} 1 & 0 & -\epsilon_{\mu\tau} \\ 0 & 1 & 0 \\ 0 & \epsilon_{\mu\tau} \tan\theta_W & 1 \end{pmatrix} \tag{4.2.4}$$

Here, the rotated kinetic mixing term, $\epsilon_{\mu\tau}$, is given by

$$\epsilon_{\mu\tau} = \epsilon_Y \cos\theta_W \,. \tag{4.2.5}$$

Note that, in this regime, the mass of this eigenstate is equal to that of the original gauge field, $m_{A'} = m_X$.

From Eq. (4.2.3) and Eq. (4.2.4), we see that the physical hidden photon, A', couples to both the $j_\alpha^{\mu-\tau}$ via its own gauge interactions and to the electromagnetic current, j_α^{EM}, via the kinetic mixing parameter. We can capture these interactions through

$\boldsymbol{f}$	e	ν_e	$(\nu_\mu,\, \mu)$	$(\nu_\tau\,, \tau)$	q_d	q_u
$\boldsymbol{c_f}$	$\epsilon_{\mu\tau} e$	0	$g_{\mu\tau}$	$-g_{\mu\tau}$	$\frac{1}{3}\epsilon_{\mu\tau} e$	$-\frac{2}{3}\epsilon_{\mu\tau} e$

Table 4.2: The coupling coefficients for each SM fermion in the interaction between the massive hidden photon A'_α and the fermionic vector current $\overline{f}\gamma^\alpha f$. Coefficients are given to leading order in the kinetic mixing parameter, $\epsilon_{\mu\tau}$. We show only the couplings to the first-generation quarks, but this is trivially extended to the second and third generations.

the effective interaction Lagrangian

$$\mathcal{L}_{\text{int}} = -c_f \overline{f}\gamma^\alpha f A'_\alpha\,, \tag{4.2.6}$$

where the coupling coefficients for each fermion, c_f, are summarised in Table 4.2. Of particular note is the fact that the couplings between the second- and third-generation leptons have opposite signs. This is because, under the $U(1)_{L_\mu - L_\tau}$ model, these leptons are oppositely charged. For each flavour α, we can write this new 'dark' charge, Q'_α, as

$$Q'_\alpha \equiv \begin{cases} 0 & \text{if } \alpha = e \\ 1 & \text{if } \alpha = \mu \\ -1 & \text{if } \alpha = \tau \end{cases}, \tag{4.2.7}$$

and it implies that the effects we expect from interactions between leptons and A' will be highly flavour specific.

The kinetic mixing parameter, $\epsilon_{\mu\tau}$, is generally a function of the momentum transfer flowing through the loop, q^2. While it can occur with both the SM photon and the Z boson, for $q^2 \ll m_Z^2$ (where m_Z is the mass of the Z-boson), it can be well-approximated to occur only with the SM photon. In this case, we can depict the mixing as per Fig. 4.3, where muon and tau leptons run through the loop. This loop can be matched to an effective mixing parameter, given by

$$\epsilon_{\mu\tau}\left(q^2\right) = \frac{e g_{\mu\tau}}{2\pi^2}\int_0^1 x(1-x)\left[\ln\left(\frac{m_\mu^2 - x(1-x)q^2}{m_\tau^2 - x(1-x)q^2}\right)\right]\mathrm{d}x\ . \tag{4.2.8}$$

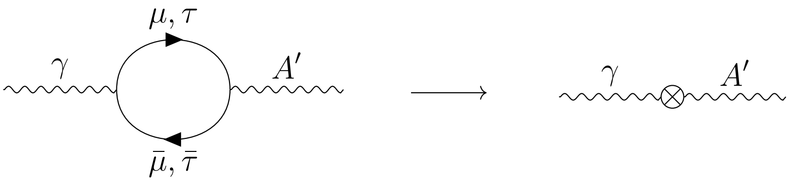

Figure 4.3: The kinetic mixing between the SM photon and the new $U(1)_{L_\mu - L_\tau}$ hidden photon. We show the full loop diagram (left) and the effective interaction matched to it (right). This matching is what leads to the introduction of the kinetic mixing parameter, $\epsilon_{\mu\tau}$.

If we further have that $q^2 \ll m_\mu^2$, which is an appropriate approximation for the processes we consider here, we can write this more succinctly as

$$\epsilon_{\mu\tau}\left(q^2 \ll m_\mu^2\right) \simeq \frac{e g_{\mu\tau}}{6\pi^2} \ln\left(\frac{m_\mu}{m_\tau}\right) \approx -\frac{g_{\mu\tau}}{70} \, . \tag{4.2.9}$$

Thus, with this mixing set by scale of the muon and the tau, the $U(1)_{L_\mu - L_\tau}$ hidden photon is completely defined by only two parameters: its gauge coupling and its mass.

4.2.2 Resolving Modern Physics Tensions

The tensions we introduced in Section 4.1 can both, in theory, be resolved by incorporating a $U(1)_{L_\mu - L_\tau}$ hidden photon into the SM. Within certain regions of its two-dimensional parameter space, this new force carrier has the desired properties to either significantly ameliorate the H_0 tension or completely account for the measurements of a_μ. In fact, within a small region of this parameter space, both of these tensions can be dealt with simultaneously, giving us a highly motivated target region to probe.

Perhaps most motivating of all is the fact that we can entirely explain the $(g-2)_\mu$ tension using this new particle. To leading-order, the $U(1)_{L_\mu - L_\tau}$ hidden photon contributes to the magnetic moment of the muon through the one-loop process

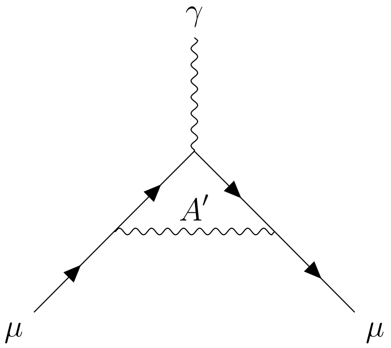

Figure 4.4: The leading order contribution of the new $U(1)_{L_\mu - L_\tau}$ gauge boson, A', to the anomalous magnetic moment of the muon.

shown in Section 4.2.2. This contribution is given by [305,306]

$$\begin{aligned}\Delta a_\mu &= Q_\mu'^2 \frac{g_{\mu\tau}^2}{4\pi^2} \int_0^1 \frac{u^2(1-u)}{u^2 + (m_{A'}/m_\mu)^2(1-u)} \mathrm{d}u \\ &\simeq Q_\mu'^2 \frac{g_{\mu\tau}^2}{4\pi^2} \times \begin{cases} 1/2 & \text{if } m_{A'} \ll m_\mu \\ m_\mu^2/m_{A'}^2 & \text{if } m_{A'} \gg m_\mu \end{cases}\end{aligned} \tag{4.2.10}$$

where Q'_μ is the charge of the muon under the new gauge symmetry, given in Eq. (4.2.7). Equating Δa_μ to the observed tension given in Eq. (4.1.10), we can use this relation to draw a region in the $U(1)_{L_\mu - L_\tau}$ parameter space than can exactly account for this tension within its error margin. Indeed, from Eq. (4.2.10), we see that we expect it to be flat (mass-independent) for low masses of the hidden photon and linear in $m_{A'}$ for high masses. We show the region in the $U(1)_{L_\mu - L_\tau}$ parameter space where a hidden photon can explain the measured value of Δa_μ to 2σ in Fig. 4.5, which we discuss further below.

The second tension—that in H_0—can be alleviated by altering the early-time expansion history of the Universe, which we can achieve by increasing the number of effective neutrino species, N_{eff}. This quantity, which describes the number of neutrino species present at the time that neutrinos decoupled from the early-Universe radiation bath, has a value of $N_{\text{eff}}^{\text{SM}} = 3.045$ within the SM[4] [313–315]. However,

---

[4] We note that this value is slightly higher than the expected three neutrino species that we see in the SM. This is due to entropy transfers from e^+e^- annihilations to neutrinos, neutrino

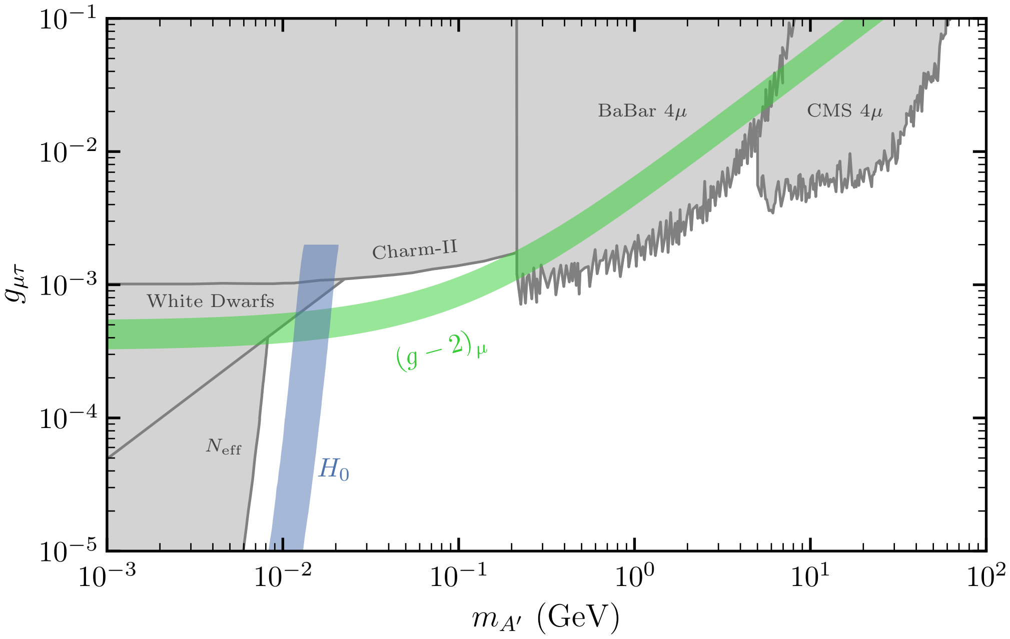

Figure 4.5: The current $U(1)_{L_\mu - L_\tau}$ landscape. The most stringent 90% CL limits (grey) are shown, corresponding to constraints on $\Delta N_{\rm eff}$ [299], white dwarf cooling [302], neutrino-trident production at Charm-II [307,308], and four-muon searches at BaBar [309] and CMS [310]. Also shown are the $(g-2)_\mu$ 2σ (green) and H_0 (blue) preferred regions.

an increase in this quantity of $\Delta N_{\rm eff} \approx 0.2$–$0.5$ can significantly relax the H_0 tension, and this can be done by introducing a new light $U(1)_{L_\mu - L_\tau}$ gauge boson to the early Universe. Such a boson can be made to be in thermal equilibrium with the SM particle bath, leaving this equilibrium through the cooling of the Universe, at which point the production processes begin to become disfavoured. The remaining hidden photons then decay into muon and tau neutrinos, increasing the value of $N_{\rm eff}$ if these decays occur after neutrinos decouple from the remainder of the radiation bath. Additionally, the non-zero kinetic mixing between A' and the SM photon can delay when this decoupling occurs, which can also increase the value of $N_{\rm eff}$. For a hidden photon mass of mass $m_{A'} \approx 10\,$MeV, these effects give us the desired change of $\Delta N_{\rm eff} = 0.2$–0.5.

---

oscillations, finite temperature corrections, and the fact that neutrinos do not decouple from the thermal bath instantaneously [311–314].

We show the regions in the $U(1)_{L_\mu - L_\tau}$ parameter space where the tensions in $(g-2)_\mu$ and H_0 can be ameliorated in Fig. 4.5. The green band represents the area within this space where $(g-2)_\mu$ can be completely explained to 2σ, whereas the blue band shows that region in which the H_0 tension can be significantly reduced. We see that there exists a small region at $m_{A'} \approx 15\,\mathrm{MeV}$ and $g_{\mu\tau} \approx 4 \times 10^{-4}$ where both of these tensions can be accounted for simultaneously. In grey, we show the most stringent presently existing bounds in this space. These limits are from constraints on ΔN_{eff} [299], white dwarf cooling [302], neutrino trident production at Charm-II [307, 308], and four-muon searches at BaBar [309] and CMS [310]. Interestingly, there still remains a large, unprobed area of this parameter space that can explain the $(g-2)_\mu$ tension, including the region that can simultaneously explain both this and the H_0 tension at once. Cutting into this novel part of the $U(1)_{L_\mu - L_\tau}$ parameter space is our main motivator for the studies we conduct in Chapters 5 and 6.

4.2.3 CEνNS and EνES with the $U(1)_{L_\mu - L_\tau}$

The kinetic mixing between the SM photon and the $U(1)_{L_\mu - L_\tau}$ hidden photon gives us an additional interaction between neutrinos and electrically charged particles. In addition to the usual SM scattering processes responsible for CEνNS and EνES we saw in Section 3.3, the new A' induces a further possible interaction, shown in Fig. 4.6. This new process adds additional contributions to the CEνNS and EνES scattering cross sections, which can impact the expected phenomenology at experiments sensitive to these processes. Indeed, it is because of this mixing that DD experiments, as well as other experiments sensitive to these scattering processes, have access to new physics models such as the $U(1)_{L_\mu - L_\tau}$ despite their lack of direct gauge couplings to the first-generation particles.

The new scattering process made available by the A' augments the CEνNS cross

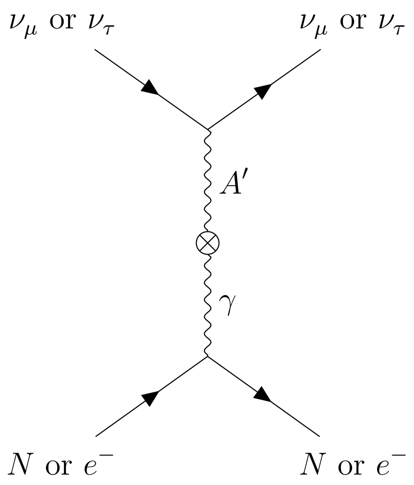

Figure 4.6: The contributing diagram of the $U(1)_{L_\mu - L_\tau}$ hidden photon to both CEνNS and EνES. The kinetic mixing with the SM photon is shown explicitly.

section we first met in Section 3.3.1, which now reads

$$\frac{\mathrm{d}\sigma^{\alpha}_{\nu N}}{\mathrm{d}E_R} = \frac{G_F^2 m_N}{\pi}\left(1 - \frac{m_N E_R}{2E_\nu^2}\right) \times \left\{ \frac{Q_{\nu N}^2}{4} + \frac{g_{\mu\tau} e \epsilon_{\mu\tau} Q_{\nu N} Q'_{\nu_\alpha N}}{\sqrt{2} G_F \left(2 m_N E_R + m_{A'}^2\right)} + \frac{g_{\mu\tau}^2 e^2 \epsilon_{\mu\tau}^2 Q'^2_{\nu_\alpha N}}{2 G_F^2 \left(2 m_N E_R + m_{A'}^2\right)^2} \right\} F^2\left(E_R\right) . \tag{4.2.11}$$

Here, we have introduced the coherence factor $Q'_{\nu_\alpha N}$, which represents the effective interaction between neutrinos of flavour $\alpha \in \{e, \mu, \tau\}$ and nuclei via the exchange of a hidden photon. It is defined by $Q'_{\nu_\alpha N} \equiv Z Q'_\alpha$, with Q'_α given by Eq. (4.2.7). Note that the dependence on the total number of protons reflects the fact that the $U(1)_{L_\mu - L_\tau}$ gauge boson couples to the nucleus via its kinetic mixing with the SM photon, and so the total effect is proportional to the total electric charge of the nucleus.

The fact that second-generation leptons are positively charged under $U(1)_{L_\mu - L_\tau}$ has interesting phenomenological properties. The cross section in Eq. (4.2.11) can be thought of as consisting of three different terms: an SM-only term, an interference term between the SM and the new BSM effect, and a BSM-only term. The first and last terms, regardless of the neutrino flavour, are always positive; however, as the kinetic mixing parameter is itself negative, the interference term for $\alpha = \mu$ is strictly

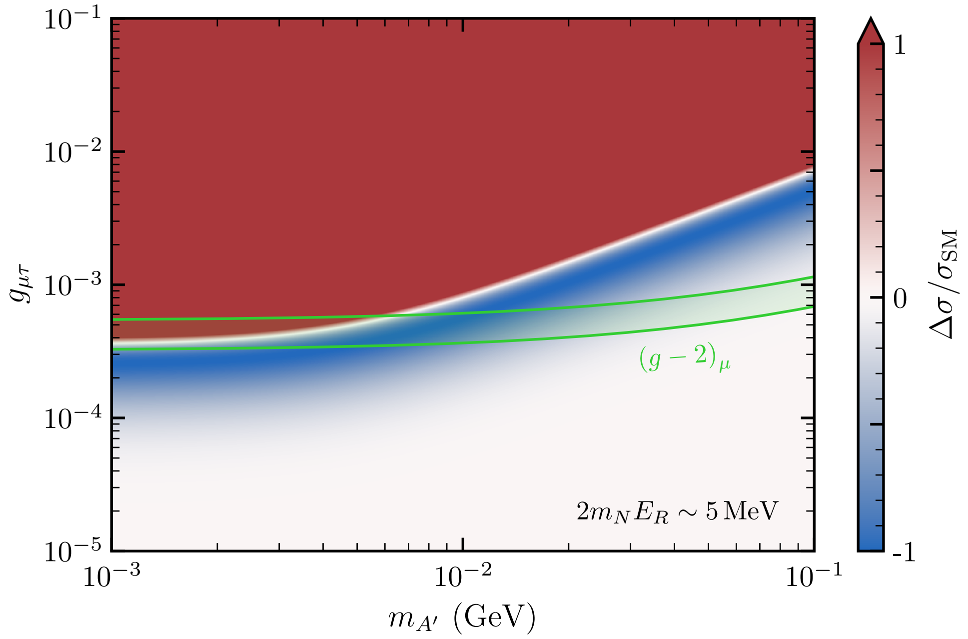

Figure 4.7: The fractional change in the total CEνNS differential cross section, shown in Eq. (4.2.11), across the $U(1)_{L_\mu - L_\tau}$ parameter space for the muon neutrino. A positive change, shown in red, resembles an enhancement of the cross section, while a negative change, shown in blue, indicates a suppression of the cross section. The $(g-2)_\mu$ 2σ preferred region is overlayed. The cross sections are evaluating for a three-momentum transfer of $q \approx 5\,\mathrm{MeV}$.

negative. Due to the relative sizes of each of these terms, this results in regions of the $U(1)_{L_\mu - L_\tau}$ parameter space in which this negative interference dominates over the positive BSM-only term, leading to an overall suppression of the CEνNS rate.

We can see this effect in action in Fig. 4.7, where we show the fractional change in the total CEνNS cross section, Eq. (4.2.11), for $\alpha = \mu$. For very high couplings, the BSM-only term dominates, resulting in an overall enhancement of the cross section. On the other hand, for very low couplings, the SM term dominates and we retrieve the usual SM result. However, for intermediate values of $g_{\mu\tau}$, we find an interference-dominated region in which the CEνNS cross section exhibits an overall suppression compared to the SM expectation. Therefore, in the case that $\alpha = \mu$, we can observe an overall deficit in the number of CEνNS events if the model parameters lie within this area. As we will see in Chapter 6, this suppression of the CEνNS cross section, not present for the tau neutrinos, will be an important clue in confirming the $U(1)_{L_\mu - L_\tau}$ hidden photon as a solution to the $(g-2)_\mu$ tension. We note that, due to the turning point between interference- and BSM-dominating regions, there is also a very finely tuned region of the parameter space where these two terms exactly cancel, yielding the SM value for non-zero values of $g_{\mu\tau}$. We also remark that the exact location of where this interference band occurs is highly dependent on the value of the three-momentum transfer, with higher momenta shifting it to higher couplings. The region shown has been derived in the particular case that $q \approx 5\,\mathrm{MeV}$.

The kinetic mixing between the SM photon and the hidden photon also affects the EνES cross section. The new physics contribution to it can be derived in much the same way as for CEνNS, as the A' only contributes to the NC process. For $\alpha = e$, the cross section is unchanged, as the electron is uncharged under the new gauge symmetry. For the remaining flavours, $\alpha = \mu, \tau$, we have that

$$\begin{aligned}\frac{\mathrm{d}\sigma^{\alpha}_{\nu e}}{\mathrm{d}E_R} =& \frac{2G_F^2 m_e}{\pi} \Bigg\{ \left[g_L^{e\,2} + g_R^{e\,2} \left(1 - \frac{E_R}{E_\nu}\right)^2 - g_L^e g_R^e \frac{m_e E_R}{E_\nu^2} \right] \\ &+ \frac{g_{\mu\tau} e \epsilon_{\mu\tau} Q'_\alpha}{\sqrt{2} G_F \left(2 m_e E_R + m_{A'}^2\right)} \left[(g_L^e + g_R^e) \left(1 - \frac{m_e E_R}{2E_\nu^2}\right) - g_R^e \frac{E_R}{E_\nu} \left(2 - \frac{E_R}{E_\nu}\right) \right] \\ &+ \frac{g_{\mu\tau}^2 e^2 \epsilon_{\mu\tau}^2 Q'^2_\alpha}{4 G_F^2 \left(2 m_e E_R + m_{A'}^2\right)^2} \left[1 - \frac{E_R}{E_\nu} \left(1 - \frac{E_R - m_e}{2E_\nu}\right) \right] \Bigg\} ,\end{aligned} \tag{4.2.12}$$

The EνES cross section also contains an interference term; however, as $g_L + g_R < 0$, it is the $\alpha = \tau$ flavour instead that exhibits the negative interference. This interference is significantly smaller than the CEνNS case, with fractional changes of order $\Delta\sigma/\sigma_{\mathrm{SM}} \lesssim 1\%$. The observational impact is thus minimal.

4.2.4 The Gauged $U(1)_{L_\mu}$

The $U(1)_{L_\mu - L_\tau}$ stands out as a particularly elegant solution to the $(g-2)_\mu$ puzzle, as it can explain it in an anomaly-free way. However, all we ultimately need to account for this tension is a model that couples to the second-generation leptons. In theory, it therefore suffices for us to add a simple $U(1)_{L_\mu}$ gauge symmetry to the SM, introducing a new mediator that couples to both μ and ν_μ. Though a simpler solution at first glance, it comes at a price. The sole gauging of L_μ does not produce an anomaly-free theory, requiring us to add additional fermionic content as well as the new $U(1)_{L_\mu}$ hidden photon in order to cancel the anomalies it introduces. While theoretically less appealing because of this, a generic $U(1)_{L_\mu}$ acts as an excellent model to compare with the $U(1)_{L_\mu - L_\tau}$ from a phenomenological stance, as it has the potential to produce remarkably similar observations. We compare and contrast their predictions in Chapter 6 with the aim of confirming the $U(1)_{L_\mu - L_\tau}$ as the true underlying model, and it is thus instructive for us to give a brief introduction to how such a $U(1)_{L_\mu}$ symmetry might be added to the SM.

The $U(1)_{L_\mu}$ Lagrangian is similar to that of the $U(1)_{L_\mu - L_\tau}$, shown in Eq. (4.2.1). The two key differences lie in the charged current, j^μ_α, and the kinetic mixing parameter, ϵ_μ. Both of these differences are due to the fact that additional field content must be added to cancel out the anomalies introduced. The charged current, which now excludes a coupling to the third-generation leptons, reads

$$j^\mu_\alpha = \overline{L}^2 \gamma_\alpha L^2 + \overline{\mu}_R \gamma_\alpha \mu_R + \sum_\psi Q_\psi \overline{\psi} \gamma_\alpha \psi \,. \tag{4.2.13}$$

where ψ are the new heavy fields required to UV complete the theory and Q_ψ are their charges under the $U(1)_{L_\mu}$. In this effective description, these new fields could enter the spectrum at a new physics scale, Λ_{NP}, anywhere between the electroweak scale, $v_{\text{EW}} = 246\,\text{GeV}$, and a possible GUT scale, $f_{\text{GUT}} \sim 10^{16}\,\text{GeV}$, with its ultimate value dictated by the choice of UV completion.

Moreover, this choice impacts the value of the kinetic mixing parameter. In the

$U(1)_{L_\mu - L_\tau}$ case, this was set by the mass scale of the τ lepton. However, with no explicit constraint on $\Lambda_{\rm NP}$, the value of ϵ_μ can, in general, lie within a range set by this new physics scale. Within the same approximations we made in Section 4.2.1—that the mixing occurs principally with the SM photon and that the three-momentum transfer is smaller than the mass of the muon—we can write that

$$\epsilon_\mu \approx \frac{e g_\mu}{6\pi^2} \ln\left(\frac{m_\mu}{\Lambda_{\rm NP}}\right) . \tag{4.2.14}$$

This mixing is identical to that of the $U(1)_{L_\mu - L_\tau}$, except for two key differences: the gauge coupling, g_μ, is now particular to the $U(1)_{L_\mu}$, and the new physics scale, $\Lambda_{\rm NP}$ now replaces the m_τ scale. As the most general assumption we can make on the new physics scale is that $\Lambda_{\rm NP} \in [v_{\rm EW}, f_{\rm GUT}]$, we have that $\epsilon_\mu \in [-g_\mu/10, -g_\mu/100]$. Thus, even with a broad, largely agnostic treatment of $\Lambda_{\rm NP}$, we can still make a reasonable approximation of where the value of this kinetic mixing parameter might lie for the $U(1)_{L_\mu}$ given a realistic potential choice for UV completion.

Owing to their similarities, the $U(1)_{L_\mu}$ and $U(1)_{L_\mu - L_\tau}$ have almost identical CEνNS and EνES cross sections. The key difference lies in the $U(1)_{L_\mu}$ model's lack of a coupling to the third-generation leptons. To account for this, we can set $Q'_{\nu_\tau} = 0$ in Eq. (4.2.7). The CEνNS and EνES cross sections for the case of a $U(1)_{L_\mu}$ hidden photon then follow directly from Eq. (4.2.11) and Eq. (4.2.12), respectively.

As a potential BSM explanation of $(g-2)_\mu$, the $U(1)_{L_\mu}$ model is significantly less elegant than the $U(1)_{L_\mu - L_\tau}$ model. In addition to requiring additional field contend on top of the $U(1)_{L_\mu}$ hidden photon to remove anomalous diagrams from the theory, the $U(1)_{L_\mu}$ is subject to strong constraints from flavour-changing neutral current (FCNC) processes, such as $K \to \pi X$ and $B \to K X$ [316]. These constraints arise from the enhanced production of the longitudinal mode of a potential $U(1)_{L_\mu}$ gauge boson coupled to an anomalous current [317]. In the low-energy regime of our effective $U(1)_{L_\mu}$ description, the electroweak-charge-carrying heavy fields, ψ, can be integrated out, producing Wess-Zumino (WZ) terms that couple the new gauge boson to the weak gauge bosons and, therefore, produce flavour-changing penguin diagrams. The coefficients of these WZ terms are controlled by the underlying UV completion of the $U(1)_{L_\mu}$ model and do not necessarily vanish. These FCNC constraints place harsh limits on the allowed coupling strengths of the new $U(1)_{L_\mu}$ hidden photon, pushing them well beneath the $(g-2)_\mu$ favoured region [317].

However, should experiments begin to favour a $U(1)_{L_\mu}$ explanation of the $(g-2)_\mu$ tension, it is not impossible to evade these constraints. While contrived, it is possible that there could be some finely tuned cancellation of FCNCs that render these constraints obsolete. Alternatively, there could be a scenario in which these FCNC constraints are absent to begin with. For instance, the UV-completing heavy fields, ψ, could be SM-chiral with masses that break the broader EW symmetry of the SM.

Phenomenologically, observational differences between different realisations of a $U(1)_{L_\mu}$ and a $U(1)_{L_\mu-L_\tau}$ depend on the nature of the experiment. For instance, experiments that are only sensitive to the second-generation gauge interactions of these models, such as muon beam experiments, will observe exactly the same phenomenology regardless of the underlying model. On the other hand, experiments that are sensitive to these propagators via their mixing with the SM photon would potentially measure a difference. As we discussed above, the value of this mixing for the $U(1)_{L_\mu}$ is generally different to that of the $U(1)_{L_\mu-L_\tau}$, leading to observable differences in these experiments; however, this is not necessarily the case. The range of possible values of ϵ_μ contains the concrete value of $\epsilon_{\mu\tau} \approx -g_{\mu\tau}/70$, so a $U(1)_{L_\mu}$ hidden photon could perfectly mimic the phenomenology of a $U(1)_{L_\mu-L_\tau}$ hidden photon through this higher-order process. Indeed, only experiments that can probe the biggest predicted difference between these models—a coupling to the third-generation leptons—are able to definitively discriminate between them.

Due to the level of overlap in the phenomenology of these models, even though a $U(1)_{L_\mu}$ is a theoretically less elegant BSM possibility, an effective realisation of it forms an excellent foil with which to pit against the $U(1)_{L_\mu-L_\tau}$. Indeed, the $U(1)_{L_\mu}$ landscape (with the same kinetic mixing value) looks identical to that of the $U(1)_{L_\mu-L_\tau}$ in Fig. 4.5, excepting for bounds by BaBar and Charm-II, which are scaled downwards by the factor $\sqrt{\mathrm{BR}^{\mu-\tau}_{\mathrm{A}'\to\mu\mu}/\mathrm{BR}^{\mu}_{\mathrm{A}'\to\mu\mu}} \approx 0.87\,(0.71)$ below (above) the ditau threshold.

Thus, should the $U(1)_{L_\mu - L_\tau}$ prove to be a promising avenue of new physics, we will need a strategy to be able to confirm it as the true underlying model over a more generic $U(1)_{L_\mu}$. We show how these models can be discriminated from one another in Chapter 6, where we will build exactly this strategy using muon beam, spallation source, and DD experiments. Crucially, we will see how DD experiments can provide us with the final piece of the puzzle—the coupling to the third-generation—in the event that these models are maximally degenerate.

4.2.5 Neutrino Non-Standard Interactions

Thus far, we have treated model-specific new physics extensions to the SM, requiring us to introduce a concrete mediator that communicates the new force of Nature. However, we can be much more general than this. By providing an effective, model-agnostic formalism to the possible BSM physics that neutrinos can be broadly subjected to, we can curtail the need to introduce a mediator, placing the importance instead on the effective strength of any possible new interaction. Known as neutrino non-standard interactions (NSIs), this framework is the subject of Chapter 7, where we extend a typical parametrisation of this formalism to include non-standard interactions with electrons and use this to explore the power of DD experiments in constraining NSI parameters.

We can theoretically motivate NSIs by recalling a curious fact from Section 2.4.6. If we treat the SM as being a low-energy realisation of a broader higher energy theory, then we can, in effect, Taylor expand around the dimension-4 ($d = 4$) SM operators, adding higher dimensional operators to it and introducing BSM physics as a result. The lowest order correction we can make occurs at $d = 5$, and, in fact, we can only add one operator at this dimension: the Weinberg operator we saw in Eq. (2.4.51). Suggestively, after SSB, this operator contributes a BSM mass term to the EW Lagrangian that is of the same form as that needed to invoke a Majorana mass term for the neutrino. However, we need not stop there. At $d = 6$, we can introduce Lagrangian terms of the form [318–320]

$$\mathcal{L}_{\mathrm{NSI}} = -2\sqrt{2}\, G_F \sum_{\substack{f=e,u,d \\ \alpha,\beta=e,\mu,\tau}} \varepsilon_{\alpha\beta}^{fP} \left[\overline{\nu}_\alpha \gamma_\mu P_L \nu_\beta\right] \left[\overline{f} \gamma^\mu P f\right] , \tag{4.2.15}$$

which are indicative of new, effective four-fermion contact interactions between neutrinos and fermions $f \in \{e, u, d\}$[5]. Here, $P \in \{P_L, P_R\}$ and the NSI parameters $\varepsilon_{\alpha\beta}^{fP}$ quantify the strength of each possible new interaction relative to that of the weak force, characterised by the Fermi constant, G_F.

Neutrino Propagation in the Presence of NSIs

The effective framework of NSIs was first introduced by Wolfenstein to account for the SM matter effects that impact solar neutrino propagation [23]. This is the MSW effect that we discussed in Section 2.4.4. Indeed, we can use this same formalism but with non-standard to model this propagation with BSM physics. These effects enter at the level of the matter Hamiltonian in the three-neutrino picture, which we first considered in Section 2.4.5. In the presence of NSIs, it becomes

$$\mathcal{H}_{\mathrm{matter}} = \sqrt{2} G_F N_e(x) \begin{pmatrix} 1 + \mathcal{E}_{ee}(x) & \mathcal{E}_{e\mu}(x) & \mathcal{E}_{e\tau}(x) \\ \mathcal{E}_{e\mu}^*(x) & \mathcal{E}_{\mu\mu}(x) & \mathcal{E}_{\mu\tau}(x) \\ \mathcal{E}_{e\tau}^*(x) & \mathcal{E}_{\mu\tau}^*(x) & \mathcal{E}_{\tau\tau}(x) \end{pmatrix} , \tag{4.2.16}$$

where we have defined

$$\mathcal{E}_{\alpha\beta}(x) \equiv \sum_f \frac{N_f(x)}{N_e(x)}\, \varepsilon_{\alpha\beta}^f , \tag{4.2.17}$$

with $N_f(x)$ the density of fermion f in the propagation medium (in our case the Sun). Here, we have also defined the vector-like NSI parameters, $\varepsilon_{\alpha\beta}^f$, to be the sum

---

[5] Note that here we have assumed that the final-state and initial-state fermions are the same, resembling an NC interaction. However, CC NSIs could also exist, where these two states are different. Since these are subject to harsher constraints and DD experiments do not probe CC interactions in NRs, we do not consider them here but rather direct the reader to, for example, Refs. [318, 321, 322].

of left- and right-handed couplings,

$$\varepsilon^{f}_{\alpha\beta} \equiv \varepsilon^{fL}_{\alpha\beta} + \varepsilon^{fR}_{\alpha\beta} \,. \tag{4.2.18}$$

It is convenient to define these as only vector-like NSIs contribute to matter effects. This is because any axial contributions, where left- and right-handed components enter with opposite signs, ultimately lead to non-standard matter effects cancelling out. Moreover, since quarks are always confined to be within hadrons such as the proton (p) and the neutron (n), we can usefully define the nucleon-specific NSI parameters

$$\varepsilon^{p}_{\alpha\beta} \equiv 2\varepsilon^{u}_{\alpha\beta} + \varepsilon^{d}_{\alpha\beta} \qquad \text{and} \qquad \varepsilon^{n}_{\alpha\beta} \equiv \varepsilon^{u}_{\alpha\beta} + 2\varepsilon^{d}_{\alpha\beta} \,. \tag{4.2.19}$$

If we now make the assumption that the density of each quark is distributed in the same way as their total count, such that $N_u(x) = 2N_p(x) + N_n(x)$ and $N_d(x) = N_p(x) + 2N_n(x)$, then Eq. (4.2.18) becomes

$$\mathcal{E}_{\alpha\beta}(x) \equiv \left(\varepsilon^{p}_{\alpha\beta} + \varepsilon^{e}_{\alpha\beta}\right) + Y_n(x)\varepsilon^{n}_{\alpha\beta} \,, \tag{4.2.20}$$

where we have defined the neutron-to-electron ratio $Y_n(x) \equiv N_e(x)/N_p(x)$ and made use of the fact that the Sun is approximately electrically neutral to set $N_p(x) \equiv N_e(x)$.

We will explore the impact of NSIs on neutrino oscillations in greater detail in Chapter 7. Presently, we only note that, from Eq. (4.2.20), the overall effect of NSIs is to introduce new terms to the matter Hamiltonian that include, as well as a contribution from the neutron, an overall charged contribution from both the proton and the electron. Consequently, from a phenomenological standpoint, the same non-standard behaviour could be effected through either a single proton/electron contribution or an appropriate combination of both proton and electron contributions. As NSIs with the electron also have the potential to impact the EνES scattering cross section, which affects the phenomenology at the interaction point, global analyses of NSIs assume that only NSIs with the proton exist [24,25]. Similarly, studies of NSIs in the context of CEνNS experiments make the same assumption [323]. This greatly reduces the complexity of the problem; however, it comes at the cost of providing a less general treatment. In Chapter 7, by re-introducing the electron contribution to the usual electron-absent NSI parametrisation, we explore the potential impact that a more general charged contribution can have on limits that have previously been set on NSI parameters under the assumption that only one of these charged components exists.

CEνNS and EνES in the Presence of NSIs

In the general NSI case, we must be careful when calculating the differential rate spectrum for neutrino scattering events. As was recently pointed out by Ref. [26], when new physics effects introduce potential flavour-changing NCs, we must be careful to retain the full flavour-structure of the cross section when dealing with a neutrino flux composed of an admixture of flavour eigenstates. This is in contrast with the SM case and indeed with both the $U(1)_{L_\mu - L_\tau}$ and $U(1)_{L_\mu}$ cases above, which all lead to interactions that are diagonal in the flavour basis. In the general case, it is no longer appropriate to project the neutrino state that arrives on Earth, which does so in a superposition of flavour eigenstates, onto any one particular flavour state and convolve the result with flavour-pure cross sections (as we did in Eq. (3.3.1)). Instead, we must consider the full flavour-structure of both the cross section and the density matrix describing the evolution of the initial neutrino state.

To illustrate this, we can consider the amplitude of the general elastic scattering process between a neutrino of initial flavour α and a target T, given by

$$\mathcal{A}_{\alpha\beta} = \langle \nu_\beta | \, S \, | \nu_\alpha \rangle \; . \tag{4.2.21}$$

Here, $S \equiv S^{(i)} S^{(p)}$ is the S-matrix describing the full scattering process, from the propagation of the initial state $|\nu_\alpha\rangle$ to its eventual interaction with the detector material, encoded in the matrices $S^{(p)}$ and $S^{(i)}$, respectively. The differential rate due to a neutrino initially born in the flavour α is then proportional to the sum of the square amplitudes for the neutrino to scatter into all possible flavours. That is,

$$\begin{aligned}\frac{\mathrm{d}R}{\mathrm{d}E_R} &\propto \sum_\beta |A_{\alpha\beta}|^2 \\ &= \mathrm{Tr}\left(\rho^{(\alpha)}|M|^2\right) ,\end{aligned} \tag{4.2.22}$$

where we have defined the density matrix $\rho^{(\alpha)} \equiv S^{(p)}\pi^{(\alpha)}S^{(p)\dagger}$, with $\pi^{(\alpha)}$ the projector onto the initial state $|\nu_\alpha\rangle$, and the scattering matrix $M \equiv S^{(i)}$. In the case of solar neutrinos, where all neutrinos are born in the pure flavour eigenstate ν_e, the projector is given by $\pi^{(e)}_{\gamma\delta} = \delta_{\gamma e}\delta_{\delta e}$, and we get that

$$\rho^{(e)}_{\alpha\beta} = S^{(p)}_{\alpha e}(S^{(p)})^\dagger_{e\beta} = \psi^\dagger_{e\beta}\psi_{e\alpha} , \tag{4.2.23}$$

with $\boldsymbol{\psi}_e$ satisfying Eq. (2.4.39). Note that the diagonal elements of $\rho^{(e)}$ give us the probabilities of a transition from flavour e to flavour α. The non-diagonal elements describe the *flavour* coherence of the neutrino state arriving on Earth, which is not to be confused with the *mass* eigenstate coherence we discussed in Chapter 2[6]. Decorating the interaction matrix elements with the relevant phase-space factors, which promotes it to a differential cross section, we arrive at the general relation for calculating the differential rate spectrum in the presence of flavour-changing NSIs [26],

$$\frac{\mathrm{d}R}{\mathrm{d}E_R} = n_T \int_{E_\nu^{\mathrm{min}}} \frac{\mathrm{d}\phi_\nu}{\mathrm{d}E_\nu}\,\mathrm{Tr}\left(\rho^{(e)}\frac{\mathrm{d}\sigma}{\mathrm{d}E_R}\right)\,\mathrm{d}E_\nu , \tag{4.2.24}$$

We stress that the traditional way of calculating the number of neutrino scattering events in the presence of new physics, given by

$$N_\nu \propto \sum_\alpha P_{e\alpha}\frac{\mathrm{d}\sigma^\alpha_{\nu T}}{\mathrm{d}E_R} , \tag{4.2.25}$$

where $P_{e\alpha}$ is the transition probability to a neutrino of flavour α, is only appropriate in two cases. If the flux of neutrinos incident on a target is pure—i.e. it is only composed of one flavour—then this simplified treatment is appropriate. On the

---

[6] The loss of coherence that occurs with the mass eigenstates greatly simplifies the calculation of $\boldsymbol{\psi}_e$; however, there is, in general, a coherence of the flavour eigenstates, as the neutrino flux arrives in a mixed state.

other hand, if the flux is composed of a mixture of flavour eigenstates, then it is still appropriate as long as the new physics contribution is flavour-conserving—in other words, the generalised cross section is diagonal. However, if this cross section is non-diagonal and the incident neutrino flux is in a mixed state, we must resort to the more general treatment of Eq. (4.2.24).

For CEνNS, we can follow the approach of Ref. [324] to derive the generalised cross section, which describes both flavour-conserving and flavour-changing processes. However, we must stop short of summing over all possible final states at the cross section level, as this is not appropriate for the case of a non-diagonal interaction cross section with a mixed-state neutrino beam. Instead, we give the full cross section describing the scattering process $\nu_\alpha N \to \nu_\beta N$,

$$\begin{aligned}\left(\frac{\mathrm{d}\sigma_{\nu N}}{\mathrm{d}E_R}\right)_{\alpha\beta} &= \frac{G_F^2 m_N}{\pi}\left(1-\frac{m_N E_R}{2E_\nu^2}\right) \\ &\quad\times\left(\frac{1}{4}Q_{\nu N}^2\delta_{\alpha\beta} - Q_{\nu N}G_{\alpha\beta}^{\mathrm{NSI}} + \sum_\gamma G_{\alpha\gamma}^{\mathrm{NSI}}G_{\gamma\beta}^{\mathrm{NSI}}\right)F^2(E_R)\,.\end{aligned} \tag{4.2.26}$$

where the NSI coupling to the nucleus is defined as

$$G_{\alpha\beta}^{\mathrm{NSI}} = Z\varepsilon_{\alpha\beta}^p + N\varepsilon_{\alpha\beta}^n\,. \tag{4.2.27}$$

In the case of EνES, the generalised cross section is given by [26]

$$\begin{aligned}\left(\frac{\mathrm{d}\sigma_{\nu e}}{\mathrm{d}E_R}\right)_{\alpha\beta} = \frac{2G_F^2 m_e}{\pi}\sum_\gamma\Bigg\{&G_{\alpha\gamma}^L G_{\gamma\beta}^L + G_{\alpha\gamma}^R G_{\gamma\beta}^R\left(1-\frac{E_R}{E_\nu}\right)^2 \\ &-\left(G_{\alpha\gamma}^L G_{\gamma\beta}^R + G_{\alpha\gamma}^R G_{\gamma\beta}^L\right)\frac{m_e E_R}{2E_\nu^2}\Bigg\}\,,\end{aligned} \tag{4.2.28}$$

where the generalised, parity-dependent couplings are given by

$$G_{\alpha\beta}^L = g_1^\alpha\delta_{\alpha\beta} + \frac{1}{2}\varepsilon_{\alpha\beta}^e \qquad \text{and} \qquad G_{\alpha\beta}^R = g_2^\alpha\delta_{\alpha\beta} + \frac{1}{2}\varepsilon_{\alpha\beta}^e\,, \tag{4.2.29}$$

with g_1^α and g_2^α given by Eq. (3.3.10). We note that, in general, the neutrino-electron cross section can be composed of both a vector and an axial-vector part. However, we have ignored the axial-vector contribution, as such an interaction affects neither CEνNS nor neutrino propagation.

CHAPTER 5

Probing the $U(1)_{L_\mu - L_\tau}$ with Neutrinos

Having introduced the neutrino, DD experiments, and potential BSM neutrino physics, we are now ready to turn to the thesis of this work: that DD experiments will prove to be key players in the search for new neutrino physics. We will begin exploring this idea by considering the constraining power of DD experiments in the context of the $U(1)_{L_\mu - L_\tau}$ hidden photon, which we introduced in Section 4.2.1. This model of new physics is particularly well-motivated by the increasing tension in $(g-2)_\mu$, which can be completely accounted for with the new mediator introduced by the gauged $U(1)_{L_\mu - L_\tau}$. While vast expanses of the $U(1)_{L_\mu - L_\tau}$ parameter space have now been excluded by a variety of neutrino experiments, a large region of it where the $(g-2)_\mu$ solution survives has yet to be probed. As we will see, future DD experiments are on course to explore precisely this region.

In this chapter, we will explore the sensitivities of DD experiments to the $U(1)_{L_\mu - L_\tau}$ hidden photon, comparing them to those of neutrino-dedicated experiments. We will begin by deriving constraints from the recent LAr run of the COHERENT experiment, setting up the necessary details of this type of experiment as we do so. We will then move on to solar neutrino probes of the $U(1)_{L_\mu - L_\tau}$ hidden photon, beginning with a brief discussion on the SSMs we have considered. Our analysis with solar neutrinos commences by exploring the potential constraints from neutrino oscillation experiments, leading us to consider the limits that can be derived from the most recent run of the Borexino experiment. Finally, we come to constraints from DD experiments, first computing the limits that the XENON1T collaboration has already set for the $U(1)_{L_\mu - L_\tau}$ hidden photon. We conclude with the main analysis of this chapter: projecting the constraints that next-generation and far-future DD experiments will be able to place in the $U(1)_{L_\mu - L_\tau}$ parameter space. We show the resulting limits from all of our analyses at the end of the chapter, which we separate into those stemming from past data and those projected from future experiments.

5.1 Constraints from COHERENT

We begin by considering how the recent CEνNS measurement of the COHERENT experiment with LAr can be used to constrain the properties of the $U(1)_{L_\mu - L_\tau}$ hidden photon. As we saw in Section 3.3.1, this elusive process was first observed in 2017 by the COHERENT collaboration, who first measured the CEνNS rate using a CsI target [325]. In 2020, they observed this process again using an LAr target, measuring no deviation from the SM prediction [8]. Indeed, all of their results have thus far been consistent with SM predictions, allowing them to set constraints on possible new physics scenarios that affect the CEνNS rate. These new physics bounds are particularly relevant for models containing light mediators [323,326–329], though the potential of this type of experiment to set bounds on general NSIs has also been studied extensively [25, 140, 173, 323, 326, 330–339]. While a limit on the $U(1)_{L_\mu - L_\tau}$ has already been derived using the CsI run [326], a limit using the LAr has not. We compute this limit below, first outlining the theory behind spallation source experiments such as COHERENT, as they will form a driving force behind both our present analysis and the analysis we conduct in Chapter 6.

5.1.1 CEνNS at Spallation Source Experiments

The COHERENT experiment is in a category of experiments known as spallation source (SS) experiments. SS experiments generate high-intensity beams of neutrinos that are aimed at stationary nuclear targets, where CEνNS is searched for. The neutrinos themselves are produced via two possible decay channels, beginning with the decay of the unstable pions created through high-energy proton spallations. Neutrinos are produced either from the prompt decay of these charged pions or from the delayed decay of the daughter muons,

$$\begin{aligned} &\pi^+ \to \mu^+ \nu_\mu \\ &\mu^+ \to e^+ \nu_e \overline{\nu}_\mu \end{aligned} \tag{5.1.1}$$

At SS experiments, the neutrino flux arriving at a target is thus composed of individual beams of ν_μ, $\overline{\nu}_\mu$, and ν_e. The most dominant of these is due to the prompt decay of the pions, producing a monochromatic beam of muon neutrinos whose energy is dependent on the muon and pion rest masses,

$$E_{\nu_\mu} = \frac{m_\pi^2 - m_\mu^2}{2m_\pi} \approx 30\,\mathrm{MeV}\,. \tag{5.1.2}$$

The remaining, sub-leading components are from the delayed decay of the μ^+. Unlike the prompt flux of muon neutrinos, the fluxes of these delayed neutrinos follow continuous energy distributions. The energy spectra of all of these neutrinos can be derived from two-body and three-body decay kinematics. Their normalised spectra are given by [340]

$$\begin{aligned} f_{\nu_\mu}(E_\nu) &= \delta\left(E_\nu - \frac{m_\pi^2 - m_\mu^2}{2m_\pi}\right)\,, \\ f_{\bar{\nu}_\mu}(E_\nu) &= \frac{64}{m_\mu}\left[\left(\frac{E_\nu}{m_\mu}\right)^2\left(\frac{3}{4} - \frac{E_\nu}{m_\mu}\right)\right]\,, \\ f_{\nu_e}(E_\nu) &= \frac{192}{m_\mu}\left[\left(\frac{E_\nu}{m_\mu}\right)^2\left(\frac{1}{2} - \frac{E_\nu}{m_\mu}\right)\right]\,, \end{aligned} \tag{5.1.3}$$

where, from kinematics, $E_\nu \in \left[0, m_\mu/2\right]$ for the continuous spectra. For reference, we show these spectra in Fig. 5.1. Note that, when calculating the differential

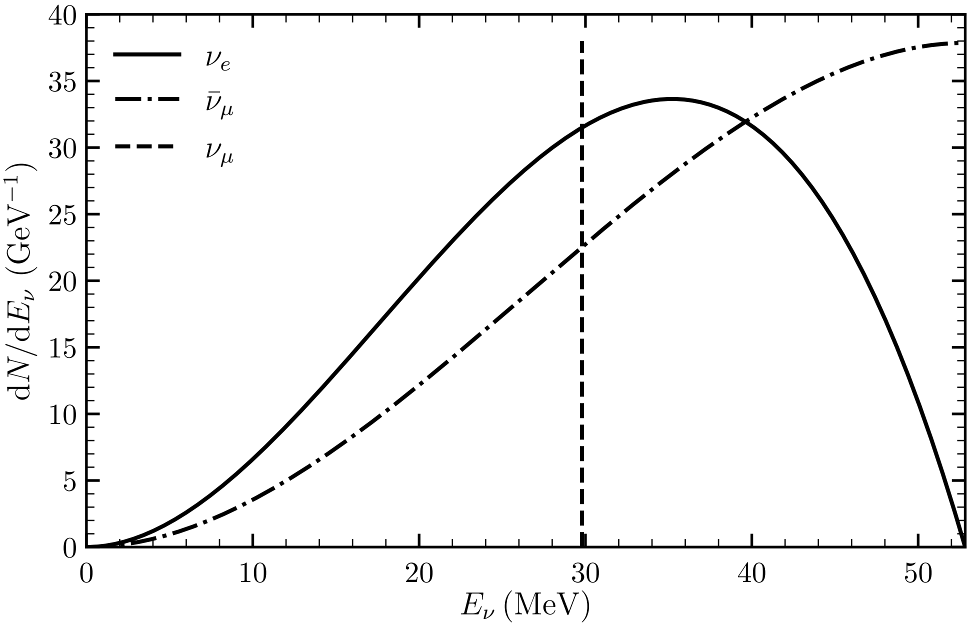

Figure 5.1: The normalised energy spectra of the neutrino fluxes arriving on target at SS experiments. These are the prompt monochromatic muon neutrino flux (solid, height arbitrary) and the two delayed continuous fluxes of electron neutrinos (dashed) and muon anti-neutrinos (dash-dotted).

rate spectrum, these energy spectra must be normalised to account for the total beam luminosity of any given experiment. This is done by scaling them by the normalisation factor $\eta \equiv r N_{\mathrm{POT}}/(4\pi L^2)$, where r is the number of neutrinos of any given flavour produced per proton collision, N_{POT} is the number of protons on target, and L is the total length of the experimental baseline. This yields the total expected neutrino flux, $\phi_\alpha(E_\nu) \equiv \eta f_\alpha(E_\nu)$, where $\alpha \in \{\nu_\mu, \nu_e, \bar{\nu}_\mu\}$.

The differential rate spectrum for each neutrino flux is given by

$$\frac{\mathrm{d}N_\alpha}{\mathrm{d}E_R} = n_T \int_{E_{\nu_{\mathrm{min}}}}^{E_{\nu_{\mathrm{max}}}} \phi_\alpha(E_\nu)\, \frac{\mathrm{d}\sigma^\alpha_{\nu N}}{\mathrm{d}E_R}\, \mathrm{d}E_\nu\,, \tag{5.1.4}$$

where $n_T \equiv M_{\mathrm{det}}/m_N$ is the total number of targets per unit mass in a given experiment, $E_{\nu_{\mathrm{min}}}$ is the minimum neutrino energy required to produce a recoil of energy E_R (given by Eq. (3.3.2)), and $E_{\nu_{\mathrm{max}}} = m_\mu/2$ is the maximum allowed neutrino energy (determined from the three-body decay kinematics). We can then find the number of expected CEνNS events by integrating Eq. (5.1.4) over the recoil energy, taking into account a generally energy-dependent efficiency function, $\epsilon(E_R)$, that captures the sensitivity of a detector to the produced signal,

$$N_{\mathrm{CE}\nu\mathrm{NS}} = \int_{E_{\mathrm{th}}} \epsilon(E_R) \frac{\mathrm{d}N_\alpha}{\mathrm{d}E_R} \, \mathrm{d}E_R \, . \tag{5.1.5}$$

Note that the integration in recoil energy runs from the threshold of the particular experiment. With an efficiency function that is energy dependent, this threshold energy is implicitly already taken into account by the fact that the efficiency quickly drops to zero below some recoil energy. As in the case of DD experiments, SS experiments typically quote their threshold energy to be that recoil energy at which the efficiency curve drops below $\sim 50\%$.

5.1.2 Constraints from the CENNS-10 LAr Experiment

As part of their mission, the COHERENT collaboration deployed the CENNS-10 LAr detector to measure CEνNS with a liquid argon target. We summarise the details for the CENNS-10 LAr experiment in Table 5.1, which we have taken from Ref. [8]. For simplicity, we assume a 100% isotopic abundance of ^{40}Ar in the experiment. For our efficiency function, we take the Analysis A curve given in Fig. 2 of Ref. [8].

Like DD experiments, CEνNS experiments such as COHERENT do not directly measure nuclear recoil energies. Instead, they measure energies stemming from strictly electronic processes. In the case of scintillation-based SS experiments, the measured signal is the number of photoelectrons produced, which itself is related to the electron-equivalent energy that was needed to release that number of photoelectrons. Thus, to relate nuclear recoil energies to the electron-equivalent energy scale, we proceed in much the same way as we did for DD experiments in Section 3.3.3: by applying an energy-dependent quenching factor. In this case, we convert the nuclear recoil energies of the expected differential CEνNS rate spectra

M_{det} (kg)	N_{POT} ($\times 10^{23}$ year^{-1})	r	L (m)	σ_{sys}
24	1.37	0.08	27.5	8.5%

Table 5.1: The relevant experimental details of the CENNS-10 LAr experiment.

to their electron-equivalent counterparts by applying the quenching factor presented in Ref. [8]

$$Q_F(E_R) = 0.246 + (7.8 \times 10^{-4}\,\text{keV}_{\text{nr}}{}^{-1})E_R\,. \tag{5.1.6}$$

This allows us to map to electron-equivalent energies using the relation $E_{ee} = Q_F E_R$. To compute our limit, we perform a χ^2-fit similar to that of Ref. [323, 341]. In particular, for each point in the $U(1)_{L_\mu - L_\tau}$ parameter space, $(m_{A'}, g_{\mu\tau})$, we minimise the function

$$\chi^2\left(m_{A'}, g_{\mu\tau}\right) = \min_{\alpha}\left[\left(\frac{N_{\text{exp}} - N_{\text{CE}\nu\text{NS}}\left(m_{A'}, g_{\mu\tau}\right)[1+\alpha]}{\sqrt{N_{\text{exp}} + N_{\text{bkg}}}}\right)^2 + \left(\frac{\alpha}{\sigma_\alpha}\right)^2\right], \tag{5.1.7}$$

where we allow the overall normalisation of the theoretical count, α, to run in the fit with a systematic uncertainty of $\sigma_\alpha = 8.5\%$, acting as a nuisance parameter in our analysis. The total number of measured events is $N_{\text{exp}} = 159$, with the total number of background events given by $N_{\text{bkg}} = 563$. We show our results, along with the limits derived from the previous CsI run in Ref. [326], in Fig. 5.4.

5.2 Solar Neutrino Probes of the $U(1)_{L_\mu - L_\tau}$

We now turn our attention to solar neutrinos and explore how experiments sensitive to them can place bounds in the $U(1)_{L_\mu - L_\tau}$ parameter space. However, before we begin, we briefly comment on the SSMs we have used. As we mentioned in Section 2.3, the size of each predicted solar neutrino flux depend on the particular choice of SSM. Therefore, the constraints we can place with these types of experiments depends on which SSM we take as the underlying solar model. As we are about to see, there is currently no unequivocal choice for this.

5.2.1 The Choice of Solar Model

Modern SSMs typically use one of two popular spectroscopic studies on which to base their assumed solar abundances during calibration: the GS98 [77] and AGSS09 [78] studies. Importantly, these studies differ in what they report for the overall photospheric metallicity. The older GS98 results, based on one-dimensional atmospheric modelling [77, 342], point towards a higher metallicity solar atmosphere than the newer AGSS09 results, based on improved hydrodynamical modelling and line formation study techniques [78, 343, 344]. Although one might prefer to take the more recent, low-metallicity results, SSMs based on these solar abundances predict values for other quantities, such as the solar sonic speed, that are in tension with helioseismological measurements, which instead favour a high-metallicity Sun [74]. This dissonance between spectroscopic and helioseismological data has given rise to the so-called solar metallicity problem—an ongoing difficulty in choosing the model to take as the underlying SSM [82–84, 345, 346].

An orthogonal line of attack to helioseismology is to consider the solar neutrino flux predictions of these SSMs. Each of these models predicts a different value for the total expected flux of each solar neutrino population. Therefore, by measuring these fluxes as precisely as possible, we can test for which SSM best fits the data. Crucially, the predicted fluxes from the CNO cycle reactions, which are highly dependent on the abundance of heavy elements in the Sun, are the most impacted by the choice of SSM, varying by as much as $\sim 30\%$ [72] between high-metallicity (HZ) and low-metallicity (LZ) solar models. The CNO neutrino fluxes in particular thus form important probes of the underlying SSM.

At the foreground of neutrino flux measurements is the Borexino experiment, which infers the various components of the solar neutrino flux by measuring the solar EνES rate with its organic liquid scintillator target. Borexino has measured events across the entire range of the solar neutrino spectrum, observing ^{8}B [347], pp, ^{7}Be, pep [348], and, most recently, CNO [72] neutrinos. This last measurement is the first direct observation of neutrinos produced in the CNO cycle, and their results showed a slight preference for the HZ case. However, their precision will need to be improved before a clear preference is shown. We discuss the Borexino experiment in greater detail in Section 5.2.3, where we use the results of its most recent run to constrain new regions in the $U(1)_{L_\mu - L_\tau}$ parameter space.

For our analyses below, we will explore the effect that the choice of SSM has on our computed limits for Borexino and DD experiments. In particular, we will take the solar neutrino fluxes of the B16-GS98 and B16-AGSS09met models of Tab. 6 of Ref. [74]. We will refer to these fluxes as being associated with either an HZ or an LZ Sun, respectively.

5.2.2 The $U(1)_{L_\mu - L_\tau}$ Model and Oscillation Experiments

As we saw in Chapter 4, new physics in the neutrino sector can impact neutrino oscillations by introducing non-standard matter effects. Experiments that are sensitive to neutrino oscillations, such as Super-Kamiokande, SNO, and Borexino can use deviations induced by these effects to place bounds on the strength of BSM neutrino physics. Through global analyses, stringent bounds can be placed on these interaction strengths [25, 138], and therefore one of the first ways we might think of constraining the potential parameter space of the $U(1)_{L_\mu - L_\tau}$ is by considering the observational impact that a $U(1)_{L_\mu - L_\tau}$ hidden photon could have on neutrino oscillations.

However, the $U(1)_{L_\mu - L_\tau}$ does not induce any non-standard effect, and the propagation is equivalent to that predicted by the SM. We can see this from the effective couplings we presented in Table 4.2: the $U(1)_{L_\mu - L_\tau}$ induces interactions that are equal and opposite in magnitude on the proton and the electron, and no non-standard effect is introduced to the neutron. Since non-standard matter effects enter through the total matter Hamiltonian in Eq. (4.2.16), and since both $\varepsilon^p_{\alpha\beta} + \varepsilon^e_{\alpha\beta} = 0$ and $\varepsilon^n_{\alpha\beta} = 0$, this Hamiltonian vanishes.Thus, despite introducing non-standard effects through the CEνNS and EνES scattering cross section, the $U(1)_{L_\mu-L_\tau}$ does not lead to non-standard oscillation effects. In this special case, then, the bounds set by oscillation experiments can be completely evaded.

Nevertheless, while the $U(1)_{L_\mu-L_\tau}$ does not directly impact the behaviour of neutrino oscillations, it has the potential to affect global fits of neutrino oscillation parameters. The parameters θ_{12} and Δm^2_{21} are inferred by solar neutrino oscillation experiments by measuring processes involving EνES, which a $U(1)_{L_\mu-L_\tau}$ gauge boson does alter [349, 350] (c.f. the cross sections of Section 4.2.3). Thus, should a $U(1)_{L_\mu-L_\tau}$ hidden photon exist, fitting to these oscillation parameters using the SM prediction will lead them to be incorrectly determined. This kind of observational degeneracy has been studied in the context of quark NSIs [24], but it has yet to be explored with electron NSIs. While we do not conduct this analysis ourselves, we provide a framework with which it could be performed in the future in Chapter 7.

Interestingly, a tension currently exists between the oscillation parameters inferred using data from KamLand [351], a reactor experiment, and those inferred from solar neutrino data [138]. This tension is especially pronounced for Δm^2_{21}. It is possible that this discrepancy could be a sign that the SM assumption for the EνES cross section is at fault, pointing towards potential new neutrino physics. To determine whether this is an appropriate explanation, we would need to perform a global fit to this data including both the mixing parameters and the NSI couplings. Such an analysis might indicate that the electron NSIs induced by the $U(1)_{L_\mu-L_\tau}$ model could rectify this tension, and, in so doing, oscillation experiments would be able to place preferred regions within the $U(1)_{L_\mu-L_\tau}$ parameter space. However, in the absence of such an analysis, we will not conjecture on the constraining power of oscillation experiments in the $U(1)_{L_\mu-L_\tau}$ case. Instead, we will take the oscillation parameters found by the global fit of Ref. [138], using them to compute solar neutrino oscillation probabilities under the SM.

5.2.3 Constraints from the Borexino Experiment

The Borexino experiment, based in the Laboratori Nazionali del Gran Sasso, aims to provide us with world-leading precision measurements of the solar neutrino flux by looking for solar EνES with its liquid scintillator target. To date, the Borexino collaboration has observed neutrinos with energies in the full range of the solar neutrino spectrum, detecting ^{8}B [347], pp, ^{7}Be, pep [348], and, most recently, CNO [72] neutrinos. Its most recent accomplishment has been the first-ever *directional* measurement of sub-MeV neutrinos [352]. Thus far, all of their results have shown excellent agreement with the SM expectation for the EνES rate, enabling them to set stringent constraints on new physics models that can impact the EνES cross section and/or neutrino oscillations.

Among the various sources of solar neutrinos, ^{7}Be neutrinos in particular are prime candidates with which to constrain the properties of a $U(1)_{L_\mu - L_\tau}$ hidden photon. This is because, firstly, Borexino has measured the ^{7}Be flux to the best precision (2.7%) [10] and, secondly, new light mediators induce the greatest change to the EνES cross section at low recoil energies, which ^{7}Be neutrinos tend to produce (c.f. Fig. 3.6). Indeed, Ref. [353] took advantage of these facts to derive precisely these constraints in the $U(1)_{L_\mu - L_\tau}$ parameter space. By remapping limits that had already been set on a $U(1)_{B-L}$ model [174], they were able to set one of the first limits on the $U(1)_{L_\mu - L_\tau}$ using solar neutrino data from the Borexino experiment.

However, their approach was subject to a number of improvable factors. Firstly, by performing a simple re-mapping, Ref. [353] did not take into account the interference term in the $U(1)_{L_\mu - L_\tau}$ cross section of Eq. (4.2.12), which can have appreciable phenomenological consequences. Secondly, the original $U(1)_{B-L}$ result neither incorporated the uncertainty in the SM rate prediction nor considered the ambiguity in the choice of SSM. Thirdly, at the time of the original analysis, Borexino had only measured the ^{7}Be rate to a precision of 5% [9]—almost twice that obtained with the Phase-II run of 2.7% [10].

In light of these potential improvements, we have re-computed the Borexino limit in the $U(1)_{L_\mu - L_\tau}$ parameter space, incorporating all of them in our analysis. We have used both the lower Phase-I and higher Phase-II precisions to calculate our $U(1)_{L_\mu - L_\tau}$ constraints, which we have done for both the LZ and HZ cases. Note that, ideally, we would set a single limit using a combination of these results; however, we would need a more complete understanding of the systematic uncertainties associated with them, including any cross-correlations between their measurements.

To derive our limits, we perform a $\Delta\chi^2$ test, setting bounds on the gauge coupling at the 90% CL for each SSM. We find that the Phase-II result, which measured a higher flux of ^{7}Be neutrinos, gives us a weaker constraint, as a lower coupling is required to achieve the same excess. Similarly, as the ^{7}Be flux predicted from an LZ Sun is $\sim 10\%$ lower than that from an HZ Sun [74], the EνES rate can be more significantly enhanced in the former while still predicting the same number of events, resulting in a weaker bound for an LZ Sun. We show our results in Fig. 5.4 for both runs of the Borexino experiment, as well as for both of our considered SSMs. Note that, in the LZ case, the results from each run lead to very similar limits, so we show only the line derived from the Phase-II data set for an LZ Sun.

We note that our analysis, while providing an improvement on previous results, could be enhanced further. A complete method for deriving constraints on the $U(1)_{L_\mu - L_\tau}$ would see all of the measurements of the various solar neutrino rates taken into account in a single analysis. Such an analysis would require a careful treatment of each of the various uncertainties associated with these measurements, ultimately making for a more expensive global flux analysis. Such a dedicated analysis is beyond the scope of this study.

5.2.4 The Constraining Power of Direct Detection Experiments

The main contention of this work is that DD experiments will play a key role in teaching us about the nature of potential BSM neutrino physics. As we argued in Chapter 3, both forthcoming and far-future DD experiments will begin to delve beneath the neutrino floor, giving them sensitivity to new physics in the neutrino sector. Through both CEνNS and EνES, these experiments will be able to probe the MeV-scale neutrinos produced in solar fusion reactions [180,182,354]. By virtue of ever-decreasing energy thresholds and ever-increasing fiducial volumes, future DD experiments will provide us with complementary probes of new physics in the neutrino sector beyond neutrino-dedicated experiments. The well-motivated $U(1)_{L_\mu - L_\tau}$ hidden photon therefore serves as an excellent case study to demonstrate the power of DD experiments in this new direction.

The XENON1T Result

Before turning to future DD experiments, however, we will briefly consider the constraining power of the XENON1T experiment. As we saw in Section 3.2, this experiment, which is the predecessor of the now-operational XENONnT detector, has already become sensitive to the ^{8}B shoulder of the neutrino floor [172]. Indeed, it has even performed a ^{8}B-neutrino dedicated search. Thus, as a sign of what to expect from the near future in the field, we take a brief interlude to discuss the impact of a recent XENON1T result on our work—a result that was published during the preparation of Ref. [1].

In 2020, the XENON1T collaboration [153] released the results of their Science Run 1 (SR1), focused on electron recoils [12]. Excitingly, their data showed a discernable excess at very low recoil energies, $E_R \approx 2$–$3\,\mathrm{keV_{ee}}$, tantamount to a 3.3σ deviation from the expected background. Ref. [12] explored several potential explanations for this excess, including both an additional tritium background component and potential new physics scenarios—scenarios such as a neutrino magnetic moment, solar axions, and bosonic dark matter. Of course, a plethora of works has since attempted to either explain or refute new physics explanations of the XENON1T excess. These have primarily focused on models including new light vector mediators, dark matter in various forms, and neutrino non-standard interactions [355–409]. It is therefore natural for us to attempt to account for this excess ourselves through a light $U(1)_{L_\mu - L_\tau}$ gauge boson, or otherwise to use it to place on constraint in this parameter space[1].

The results of the SR1 are shown in Fig. 5.2, the data for which we have taken from Ref. [12]. We also show the background-only spectrum, B_0, which is the result of a high-dimensional fit to the expected background sources in the XENON1T experiment. These sources include the irreducible background from the β-decays of ^{214}Pb, backgrounds from other material contaminants, the irreducible solar EνES background, and backgrounds from unstable xenon isotopes. Interpreting the SR1 data as a signal of a $U(1)_{L_\mu - L_\tau}$ hidden photon would require us to reject B_0 for a better fit with the total rate predicted by B_0 and the signal from this new mediator.

In computing the XENON1T exclusion line, we improve slightly on the analysis we first performed in Ref. [1]. Firstly, we now perform a multi-bin analysis across the XENON1T region of interest instead of a one-bin analysis. Secondly, we now take into account the energy-dependent efficiency function of Ref. [12]. We find that this more sophisticated analysis slightly improves on the limit we first derived in Ref. [1].

To perform our binned analysis, we calculate the sum of the χ^2 values across the 29 bins shown in Fig. 5.2. Under the assumption of the background-only hypothesis, we find that $\chi^2_{B_0} = 46.4$ (29 d.o.f.), which corresponds to a significance of $p \approx 2.1\%$. This suggests a tension with the B_0 hypothesis, pointing towards effects that are not included in the background-only model. Such an effect could arise from a $U(1)_{L_\mu - L_\tau}$ hidden photon, and, indeed, a hidden photon with $m_{A'} \approx 40\,\mathrm{keV}$ and $g_{\mu\tau} \approx 7 \times 10^{-6}$

---

[1] We note that, very recently, the XENONnT experiment has explained away this tension [11]. The previous XENON1T excess was accounted for by an excess of background tritium events.

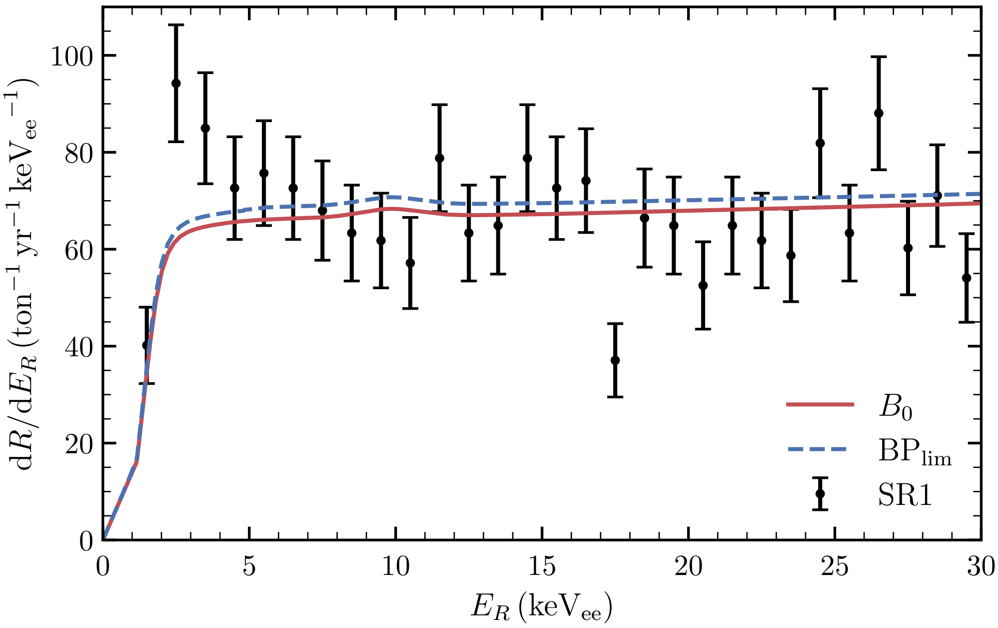

Figure 5.2: The electron-recoil excess reported by the XENON1T collaboration [12]. We show the data points of the binned spectrum attained by the SR1 (black) and the fitted background-only spectrum, B_0 (red). We also show the resulting spectrum from a $U(1)_{L_\mu - L_\tau}$ hidden photon that is just excluded by the data at the 90% CL (blue, dashed).

can slightly ameliorate this tension. Incorporating this new particle results in the lower value of $\chi^2 = 40.2$ (27 d.o.f.), decreasing the significance of the result slightly to $p \approx 4.9\%$. However, not only is this an unremarkable improvement, but such a hidden photon is deep within the excluded region of the $U(1)_{L_\mu - L_\tau}$ parameter space (mainly due to ΔN_{eff} constraints). Therefore, we do not treat this as a potential solution to the XENON1T excess.

Nevertheless, instead of performing a reconstruction of a potential $U(1)_{L_\mu - L_\tau}$ hidden photon solution, we can derive an exclusion limit on the $U(1)_{L_\mu - L_\tau}$ parameter space at which we can reject this new particle. To compute the 90% CL limit, we first find, for a fixed $m_{A'}$, that coupling that minimises the χ^2 statistic under the combined background and signal hypothesis, the value of which is almost identical to $\chi^2_{B_0}$. We then find those couplings for which $\Delta\chi^2 = 2.71$, corresponding to a 1 d.o.f. exclusion.

The ensuing limit is shown in Fig. 5.4. We also visualise the expected spectrum for the benchmark point $\mathrm{BP}_{\mathrm{lim}} = (m_{A'} = 15\,\mathrm{MeV},\ g_{\mu\tau} = 10^{-3})$ in Fig. 5.2, corresponding to a hidden photon with a mass in the H_0 solution region but with a coupling that is just beyond the 90% exclusion limit.

In deriving this limit, we have assumed that the fitted background, B_0, acts as a proxy for the true background of the experiment—a necessary assumption to compute this limit without profiling over a high-dimensional space including the many background components. While drawing such an equivalence would be appropriate in the case that the individual backgrounds had small systematic uncertainties, this is not true for the case of the XENON1T result. In particular, there is a large systematic uncertainty on the number of expected events from the β-decay of ^{214}Pb, which is reported to lie in the range $N_{\mathrm{Pb}} \in (3450, 8530)$. This is by far the dominant background in the low-energy part of the spectrum, where the number of expected solar neutrino events, $N_\nu = 220.7 \pm 6.6$, is over an order of magnitude smaller than it. Thus, the small increase necessary to set the limit we have calculated for the $U(1)_{L_\mu - L_\tau}$ model could, in principle, be completely accounted for by a slight increase in the fitted value for the lead background.

However, as such a re-fitting of the background would lead to a relaxation of the limit we have derived here, and since our (over-constrained) limit does not cut into any new regions of the $U(1)_{L_\mu - L_\tau}$ parameter space, we posit that any limit that could be derived from the XENON1T data would also not constrain any new regions of this space. Therefore, our limit acts as a most constraining possibility. A more detailed analysis would require a full profile likelihood analysis, allowing the backgrounds to vary within their expected ranges. Such a dedicated analysis is beyond the scope of this study.

5.2.5 Future Direct Detection Experiments

We now turn to exploring the power of future DD experiments, which are set to plunge beneath the neutrino floor. To determine their sensitivities to a new $U(1)_{L_\mu - L_\tau}$ hidden photon, we use a set of simplified experimental configurations that are representative of the upcoming and far-future DD experiments we introduced in Section 3.4. Combined with each of these setups, we undertake three different types of analyses, differing in the type of recoil event they focus on.

The reason for these separate studies is that, generally, we expect far more background events from ERs than from NRs. As we discussed in Section 3.3.3, a common way of reducing these backgrounds in searches for NRs is by combining multiple detection channels, with NRs and ERs having different signal profiles. However, this typically limits the energy threshold of the analysis, as higher thresholds are usually needed to ensure the survival of both signals. We therefore consider three types of analyses, each with their own unique energy ranges: an NR, ER, and NR + ER analysis. In the first two of these, we choose our energy ranges to allow for good discrimination between NR and ER events, enabling us to study the signals of each kind of recoil event separately. In the final analysis, we sacrifice the low-background NR analysis for a lower threshold, giving us access to lower energy NRs. For this last analysis, we first convert all recoil energies to the same energy scale using the relevant quenching factor before combining the signals; arbitrarily, we choose this scale to be in nuclear-recoil equivalent energies. The NR spectra are integrated up to the maximum kinematically allowed energies for the NR analysis, which follow from a collision with the highest energy solar neutrinos (here, the tail of the hep neutrinos).

In our first study of DD experiments in this vein, we do not include more sophisticated experimental details, such as the energy resolution effects and the energy-dependent efficiency functions (though we do include flat efficiencies, as we detail below) that we introduced in Section 3.3.3. As we are only interested in an initial

Exp.	Insp.	NR (keV_{nr})	ER (keV_{ee})	NR + ER (keV_{nr})
G2-Xe	LZ [14] XENONnT [15]	$[3, 5.8]$	$[2, 30]$	$[0.7, 100]$
G3-Xe	DARWIN [16]	$[3, 5.8]$	$[2, 30]$	$[0.6, 100]$
G2-Ge	SuperCDMS iZIP [13]	$[0.272, 10.4]$	$[0.120, 50]$	—
	SuperCDMS HV [13]	—	—	$[0.040, 2]$
G3-Ar	DarkSide-20k [17]	—	$[0.7, 50]$	$[0.6, 15]$

Table 5.2: The DD setups we have used in this study. We label each of them according to their generation (G2 or G3) and their target, and we note the real-life experiment that has inspired each configuration (c.f. Section 3.4 for more details). A configuration is crucially defined by the energy window we consider when calculating the new physics signal.

estimate of the sensitivities of DD experiments, we will reserve these considerations for the next chapter, where we fold these details into our analysis.

We summarise the details of the experimental configurations we have considered in Table 5.2, where we specify the label for each experiment, the detector that has inspired it, and the energy range used in each analysis. We will briefly discuss each of these setups below, explaining our choices of detector properties and highlighting any assumptions that we have made. For more details on each of the experiments that have inspired these configurations, please refer to Section 3.4.

G2-Ge This second-generation setup is based on the planned configuration of the SuperCDMS experiment at SNOLAB [13], focusing on its Ge crystal iZIP and HV detectors[2]. In the iZIP configuration, we compute separate bounds for ERs and NRs, as this detector allows for NR/ER discrimination. The NR + ER limits, however, are calculated using the lower threshold HV configuration. The NR threshold energies, both assumed to have been derived from a phonon

---

[2] We note that, while SuperCDMS will employ both Si and Ge crystal targets, we focus on Ge as it will be more abundant in the experiment. Its greater exposure therefore makes it more suitable to probe the subtle effects of light mediators, though the lower threshold of the Si iZIP detectors will play a complementary role in the case of very light mediators.

signal, have been converted into electron-equivalent energies as per Eq. (8) of Ref. [210] using the Lindhard model for the ionisation yield [206] (c.f. Section 3.4.2). The maxima of the energy windows approximately resemble the range of the detectors in each analysis. For each of them, we have taken the backgrounds from Ref. [210].

G2-Xe This second-generation configuration has been inspired by the upcoming multi-ton LXe experiments LZ and XENONnT. To place a slightly more conservative bound, we use the lower exposure of the former of 15 ton yr. The NR thresholds for these experiments have been designed to lie above the maximum of the solar neutrino spectrum, minimising what is typically a background in their searches for DM. However, as this constitutes a signal for us, we must justify lowering this threshold as much as possible.

To do so, we note that the LUX collaboration has been able to set energy thresholds as low as $1.1\,\mathrm{keV_{nr}}$, with a $3.3\,\mathrm{keV_{nr}}$ threshold at 50% detector efficiency in both the S1 and S2 signal channels required for NR/ER discrimination [410]. In light of this and the advent of new analysis techniques that allow for even lower thresholds [411], we have set the low end of the NR energy window to be $3\,\mathrm{keV_{nr}}$, corresponding to $\approx 2\,\mathrm{keV_{ee}}$ for the ER analysis. Above this threshold, we can perform an NR analysis with a 99.5% rejection of ER background and a 50% acceptance cut of NR signal events [183, 214]. We take our backgrounds from Ref. [214]; however, we extend our analyses beyond the energy range for which these backgrounds are specified to give us a greater signal. At these extended energies, we make the conservative assumption of a flat background spectrum, justified by the treatments of Ref. [14]

For the combined analysis, we use the S2-only threshold achieved by XENON100, lying at $0.7\,\mathrm{keV_{nr}}$ [412]. We have conservatively assumed that the threshold for this NR + ER analysis is equivalent in both $\mathrm{keV_{nr}}$ and $\mathrm{keV_{ee}}$ to avoid extrapolating the Lindhard model to energies at which it has not yet been experimentally tested[3]. The maximum recoil energy has been set at 30 $\mathrm{keV_{ee}}$ ($\approx$ 100 $\mathrm{keV_{nr}}$ using the Lindhard model), corresponding to the energy at which the double-β decay of ^{136}Xe is expected to dominate over solar neutrino events [214].

G3-Xe This far-future detector is based on the proposed DARWIN experiment [16], though this also acts as a proxy for other high-exposure LXe experiments, such as PandaX [413]. This configuration is similar to that of G2-Xe, only with an order of magnitude higher exposure, slightly lower backgrounds (taken instead from Ref. [16]), and a slightly lower energy threshold for the combined NR + ER analysis. For this far-future threshold, we have instead been inspired by the lowest energy measurement in LXe of an S2 signal to date, occurring at an energy equivalent to 0.3 $\mathrm{keV_{nr}}$ for NRs and 0.186 $\mathrm{keV_{ee}}$ for ERs [414]. Abandoning the NR/ER discrimination power, which requires the additional S1 signal, we have set the lower threshold to approximately twice this value for our combined analysis. All other considerations for this setup are equivalent to those of the G2-Xe setup.

G3-Ar The final, far-future detector has been based on the DarkSide-20k detector. The energy threshold required for signal discrimination in this setup is too high to give competitive constraints from CEνNS [415], residing well beyond the end of the CEνNS spectrum. Thus, we only perform an ER analysis at this threshold, equivalent to 7 $\mathrm{keV_{ee}}$.

Nonetheless, for our NR + ER analysis, we have taken the lower 0.6 $\mathrm{keV_{nr}}$ energy threshold achieved by the DarkSide-50 collaboration in an S2-only analysis. The maximum of the energy window has been taken from Ref. [17] for the ER analysis and placed at 15 $\mathrm{keV_{nr}}$ for the combined analysis. We have taken the backgrounds from Fig. 7 of [415]. Similar to our xenon setups, these backgrounds do not extend to the maximum of our energy windows, so we

---

[3] We have, however, explicitly checked that such an extrapolation to lower energies would yield, at most, a 30% improvement in our computed limits, occurring in the very low mass plateau, where $m_{A'} \ll 10^{-1}$ MeV. In the region of interest for our work, where $m_{A'} \gtrsim 1$ MeV, we see a negligible difference.

extend them conservatively assuming a flat background above 15 keV$_{\rm nr}$. We justify this by comparison with Fig. 3 in Ref. [415].

For each of these experimental configurations, we derive the 90% CL exclusion line assuming that no new physics signal is observed. For a given mediator mass, $m_{A'}$, we determine the value of the coupling, $g_{\mu\tau}$, for which 90% of hypothetical experiments would expect to see an excess over the SM prediction. For simplicity, we consider a one-bin analysis, finding the total number of recoil events expected with energies in the windows presented in Table 5.2.

Concretely, for a CL of significance α, where in our case $\alpha = 0.9$, we find that coupling that gives us an expected number of counts, $N_{\rm BSM}$, exceeding the number of observed events, $N_{\rm SM}$, satisfying

$$\sum_{n \leq N_{\rm SM}} p(n, N_{\rm BSM}(m_{A'}, g_{\mu\tau})) = 1 - \alpha \,, \tag{5.2.1}$$

where $p(n, \mu)$ is the Poisson probability mass function with number of observed events n and mean μ. This procedure is equivalent to finding the expectation value, μ, necessary to reject the background-only hypothesis with confidence α. We show the DD limits at $\alpha = 0.9$ for each of our analyses and experimental configurations in Fig. 5.3 in the case of an HZ Sun. We reserve the LZ limits, which are all less constraining as the main contributing fluxes are lower in the LZ case, for when we present our results in the broader context of the $U(1)_{L_\mu - L_\tau}$ landscape in Fig. 5.5. Before doing so, however, we comment on the behaviour of our DD bounds.

A common feature seen in all of our limits is that they have two characteristic mass regimes. The first, which occurs at the lightest mediator masses, sees the limits plateauing and losing their dependence on $m_{A'}$. The second sees the limits following a constant proportionality relationship in $m_{A'}$. The point at which the transition between these regimes occurs corresponds to the point where the minimum transferred momentum, occurring at a recoil energy equal to the threshold energy of the experiment, is of the same order as the mediator mass: $q \approx m_{A'}$. If the

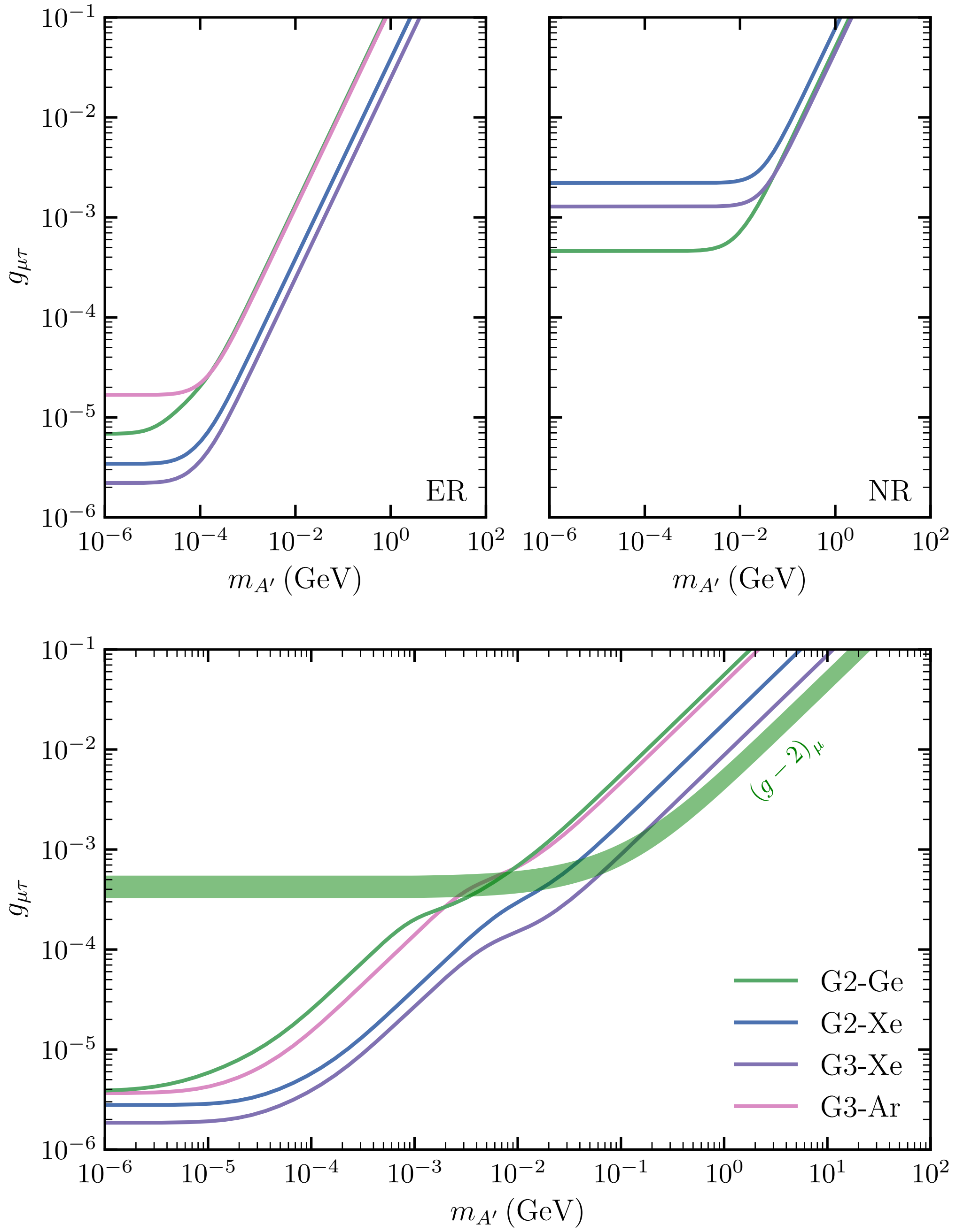

Figure 5.3: The 90% CL exclusion limits derived for the DD configurations we have considered in the case of an HZ Sun. Shown are the limits derived through the NR-only (top left), ER-only (top right), and NR + ER analyses (bottom). Also shown in the bottom panel is the $(g-2)_\mu$ 2σ preferred region (green).

transferred momentum is consistently higher than $m_{A'}$, the number of events in excess of the SM will not depend on the mass of the mediator. This explains why we observe the ER limits extending to much lower masses than the NR limits, as the threshold energy at which the momentum transfer with the much lighter electron is of the same order as $m_{A'}$ occurs at much lower values.

With the exception of the G2-Ge configuration, the limits set with the ER analysis are stronger than those set with the NR analysis. This is principally a consequence of the high thresholds, which are near where the solar CEνNS spectrum ends. This leads to few events being detected from the outset over the background—a situation that is exacerbated further by the 50% cut after NR/ER discrimination. By comparison, the relatively low-background ER analysis for the Xe setups uses thresholds that capture the EνES spectrum well, and the limits derived from them are therefore slightly better. On the other hand, the thresholds used for the G2-Xe configuration are low enough to allow for a high number of CEνNS events to be detected. This lower background analysis leads to a better limit than the ER analysis. Owing to its high threshold, the G3-Ar setup does not feature an NR limit.

Generally, the NR + ER analyses yield the best limits. Despite the higher background, the significantly lower thresholds in these analyses not only give us more events but also lower the transition points at which the limits plateau. We see that at very low mediator masses, for which $m_{A'} \lesssim 1\,\mathrm{MeV}$, the ER limit dominates. Above these masses, we transition to NR domination, signified by the kink in the limit at $m_{A'} \approx 1\,\mathrm{MeV}$. With an appreciable number of both NR and ER events, we indeed see that ERs are optimal when testing very light mediator masses, whereas NRs excel for higher masses [180]. When we come to place these limits in the broader $U(1)_{L_\mu - L_\tau}$ landscape, we will see that the masses for which ERs set the best limits have already been confidently excluded, and it will therefore be limits set with the combined NR + ER analyses that will be important in the $(g-2)_\mu$ region of interest.

We note that the limits we have derived here could be improved. Firstly, we have only considered a one-bin analysis, and the $U(1)_{L_\mu - L_\tau}$ spectrum contains spectral features (especially at lower masses) that could provide us with greater constraining power. Indeed, a binned study would allow us to exploit spectral information that we have thrown away in our study, possibly giving us considerably stronger limits for very light mediators. Secondly, we have not optimised our energy windows to minimise the signal-to-noise ratio. A more careful analysis would ensure that the recoil energies integrated over are such that the $U(1)_{L_\mu - L_\tau}$ signal is maximised over the experimental backgrounds. Taken together, these points could serve to improve our computed limits throughout the mass regime of interest.

5.3 Present Constraints on the $U(1)_{L_\mu - L_\tau}$

We begin our discussion on our computed limits by considering the constraints we can place on the $U(1)_{L_\mu - L_\tau}$ landscape today. These are shown in Fig. 5.4 for the case of an HZ and LZ Sun. The details of the solar model only non-trivially affect the Borexino result. This is because this result is derived from the ^{7}Be flux, which varies by as much as $\sim 10\%$ between the HZ and LZ cases. On the other hand, the XENON1T limit is dominated by EνES with pp neutrinos, whose flux is only reduced by $\sim 1\%$ in the LZ case.

The COHERENT LAr limit is similar to that of the older CsI run, but it is slightly less constraining. This is because the LAr run saw a result that was less consistent with the SM than the latter, such that a larger coupling is required to yield the same level of disagreement with the measured value.

The XENON1T limit is complementary to the limit placed from white dwarf cooling, but it does not cut into any new regions of the $U(1)_{L_\mu - L_\tau}$ parameter space. As we commented on in Section 5.2.4, this limit was derived with a simplistic treatment of the backgrounds inherent in the XENON1T data set. Nonetheless, since our treatment can only over-constrain the allowed couplings, our limit acts as the most optimistic case scenario. Once again, note that, as the pp neutrino flux, which dominates the XENON1T measurement, is marginally modified by the choice of

LZ or HZ abundances, there is no appreciable change in the calculated limit when choosing between these models.

The Borexino limits are based on both the older Phase-I data set [9] and the newer Phase-II data set [10] for the HZ Sun. The central value of the rate based on the latter is closer to the SM result, giving us a less constraining, and thus more conservative, limit. Despite this conservative result, our updated Borexino limit is significantly more constraining than that derived by Ref. [416]. These rule out previously untested regions of the parameter space relevant for the $U(1)_{L_\mu - L_\tau}$ explanation of both the $(g-2)_\mu$ and the H_0 tension in the case of an HZ Sun. This makes them the most stringent low-mass constraint in this region of the parameter space, already constraining part of the space in which simultaneous explanations of the $(g-2)_\mu$ and H_0 can be realised. In the LZ case, the general picture is similar, but the limit derived is weaker due to the lower ^{7}Be neutrino flux. The LZ limits, which are virtually identical for both Phase-I and Phase-II runs, do not cut into any new regions of the parameter space, though they do make for a complementary bound to that derived from white dwarf cooling. In either SSM case, however, the intriguing fact remains that a simultaneous $U(1)_{L_\mu - L_\tau}$ explanation of both the $(g-2)_\mu$ and H_0 phenomena is still allowed, making this region of the parameter space a prime target for future experimental searches.

5.4 Future Constraints on the $U(1)_{L_\mu - L_\tau}$

We show the future of the $U(1)_{L_\mu - L_\tau}$ landscape in Fig. 5.5, where we have zoomed in on the region of this space that is relevant for the $(g-2)_\mu$ and H_0 tensions. As well as including the projected limits that we have computed from future DD experiments, we show previously derived projections from kaon decays at NA62 [417], neutrino trident production at DUNE [418, 419], and a future 10 ton yr run of COHERENT with an NaI/Ar target [326] for comparison. In the case of our DD limits, we show the envelope of the most constraining limits from our NR, ER, and NR +

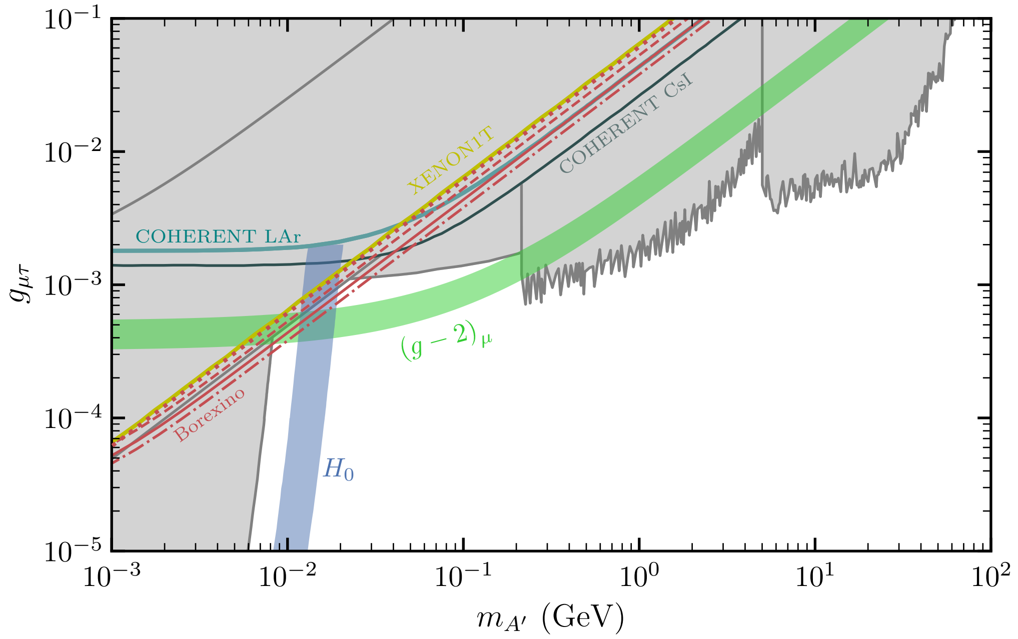

Figure 5.4: The present $U(1)_{L_\mu - L_\tau}$ landscape with our 90% CL limits from completed experiments included. These include the bounds from COHERENT LAr (blue), XENON1T (yellow), and Borexino (red). For Borexino, we show the limit calculated by Ref. [353] (dotted) and the limits we have derived from the Phase-I run (dash-dotted) and Phase-2 run with the HZ Sun (solid) and LZ Sun (dashed). We also show the H_0 (blue) and $(g-2)_\mu$ 2σ (green) preferred regions.

ER analyses. Note that this envelope is dominated by the results of the NR + ER analysis, which provides us with the best constraints in the region of interest[4]. We show our limits for both the HZ Sun and LZ Sun, with the former being slightly more constraining due to the higher fluxes predicted by a high-metallicity solar model. Also shown are our calculated limits from the Phase-I and Phase-II runs of Borexino in the case of an HZ Sun, which we show here in dark grey for comparison. Note that we do not show the LZ result as this does not cut into any new regions of the parameter space.

We see that the configuration based on SuperDMS (G2-Ge) will not be able to im-

---

[4] Below this region, the ER-only limits slightly dominate due to the reduced backgrounds. Due to the reduced threshold of the NR + ER analyses, the NR-only limits remain subdominant in the high-mass regime.

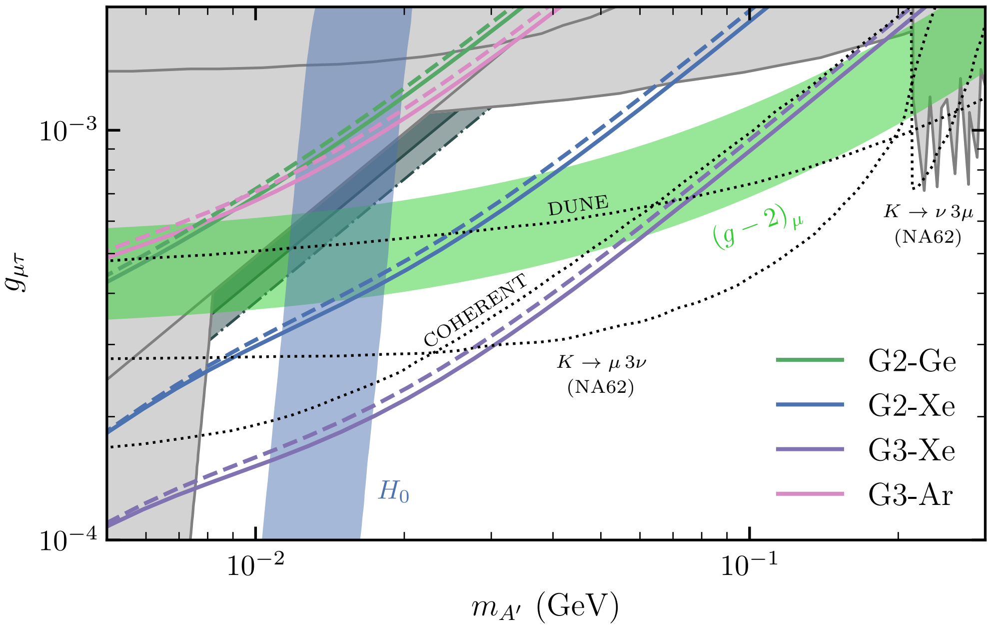

Figure 5.5: The future of the $U(1)_{L_\mu-L_\tau}$ landscape in the region of parameter space relevant for the $(g-2)_\mu$ and H_0 tensions, shown as the green and blue bands, respectively. We show the projected 90% CL limits for the next-generation and far-future experiments we have considered (coloured lines). We also include our updated Borexino limit in the case of an *HZ* Sun (grey) using both the Phase-I data (dash-dotted) and Phase-II data (solid). Our DD limits have been derived using the higher flux *HZ* Sun (solid) and lower flux *LZ* Sun (dashed). For comparison, we show the projected bounds from the COHERENT, DUNE, and NA62 experiments (black, dotted).

prove on the updated Borexino limits. Despite the low-threshold NR analysis based on the iZIP detector, it is the combined NR + ER analysis of the HV detector that yields the most constraining limit; the higher background of the HV configuration is more than compensated for by its extremely low 40 eV threshold. The major limitation of SuperCDMS is a nuclear background of ^{206}Pb decays, the reduction of which would have the most effect on this limit, potentially allowing SuperCDMS to gain sensitivity to unprobed regions of the $U(1)_{L_\mu-L_\tau}$ parameter space.

For the setup motivated by the far-future DarkSide-20k detector (G3-Ar) the derived limit is very similar in reach to the G2-Ge setup. The envelope is coincident with the NR + ER exclusion line, with the majority of the sensitivity arising from the NRs visible with the lower threshold of this analysis. Despite its larger volume, this configuration suffers from the large background that can be seen in Ref. [415]. Similar to the G2-Ge configuration, this setup would greatly benefit from lower backgrounds.

However, by far the most exciting results are those of the multi-ton LXe detectors (G2-Xe and G3-Xe), based on LZ/XENONnT and DARWIN, respectively. We see that these configurations will achieve the greatest sensitivity to solar neutrino scattering events out of all of our considered experiments, with the far-future DARWIN experiment showing the most promising results. Both of these experiments will be sensitive to the region of parameter space where the $(g-2)_\mu$ and the H_0 tensions can be simultaneously ameliorated, presenting them with the exciting opportunity to test two modern anomalies at once. This is a particularly exciting prospect for experiments such as LZ and XENONnT, as these G2 experiments have recently begun taking data [11, 159]. The far-future DARWIN experiment, however, will be able to probe the majority of the allowed $(g-2)_\mu$ explanation region and place the most stringent limits out of the neutrino-dedicated experiments considered in the allowed low-mass region of the $U(1)_{L_\mu - L_\tau}$ parameter space. For both of these experiments, the limits, which are dominated by the CEνNS signal, could be made better still with further reductions to the threshold—increased exposures would only have a minimal effect[5].

Our results show that the optimal search strategy to cover the $(g-2)_\mu$ solution with DD experiments is to look for CEνNS and push for lower backgrounds and thresholds. We have only been able to probe such large, untested regions of the $U(1)_{L_\mu - L_\tau}$ parameter space with LXe-based experiments by pushing for lower-threshold S2-only analyses, where low thresholds are achieved through the sacrifice of NR/ER discrimination. Experiments such as SuperCDMS, however, already

---

[5] This is due the very weak $g_{\mu\tau}^{\text{lim}} \propto \varepsilon^{-1/8}$ dependence on the total exposure. Reducing the threshold at this point would instead lower the turnover point at which the limits transition to being dominated by the ER signals.

boast low thresholds and are only held back by high NR backgrounds. Improving this background could enable SuperCDMS to be competitive with LXe experiments. Nonetheless, when all thresholds are equal, it is the heavy-nuclei, high-volume LXe detectors that will ultimately have the dominant sensitivities in the $U(1)_{L_\mu - L_\tau}$ parameter space.

CHAPTER 6

Confirming the $U(1)_{L_\mu - L_\tau}$ as the Solution to $(g-2)_\mu$

We have now seen that DD experiments are powerful probes of the $U(1)_{L_\mu - L_\tau}$ hidden photon, achieving sensitivities beyond even dedicated neutrino experiments. In particular, DD experiments based on LXe TPC technology will be sensitive to the $(g-2)_\mu$ solution region of the $U(1)_{L_\mu - L_\tau}$ parameter space. With this tantalising hint of new physics recently strengthened by the first results of Fermilab's E989 experiment in 2021, we must be prepared to test BSM explanations of this tension now more than ever. The $U(1)_{L_\mu - L_\tau}$, as a theoretically well-motivated model of new physics, will no doubt be among the first in line to resolve this mystery should it be confirmed. With no experimental strategy to confirm the $U(1)_{L_\mu - L_\tau}$ as the true solution in sight, we now offer not only a way to confirm it, but also a series of steps to disentangle the $U(1)_{L_\mu - L_\tau}$ solution from that of a generic, and theoretically less elegant, $U(1)_{L_\mu}$ hidden photon.

In this chapter, we will develop a strategy to confirm the $U(1)_{L_\mu - L_\tau}$ solution to the $(g-2)_\mu$ tension. We will begin by outlining the analysis strategy we employ throughout this study to determine the sensitivities of each of our chosen experiments. We will then commence building our strategy, which will consist of determining the reconstruction power of the muon beam experiment NA64μ, future LAr-based SS experiments, and, most pertinently, multi-ton LXe DD experiments. We will dissect the strengths and weaknesses of these experiments in confirming the $U(1)_{L_\mu - L_\tau}$ solution to $(g-2)_\mu$, highlighting how well-suited they will be in discriminating between a $U(1)_{L_\mu - L_\tau}$ and a $U(1)_{L_\mu}$ hidden photon.

6.1 Analysis Strategy

We will be exploring how concrete realisations of a $U(1)_{L_\mu - L_\tau}$ hidden photon can be probed at various experiments. To do this, we will first define a series of benchmark points (BPs) within the $(g-2)_\mu$ solution region of the $U(1)_{L_\mu - L_\tau}$ parameter space. We will then introduce the parameter reconstruction technique we have used throughout this work, enabling us to quantify the sensitivities of each of our considered experiments. Lastly, as we will be comparing the phenomenology of a $U(1)_{L_\mu - L_\tau}$ hidden photon to that of a generic $U(1)_{L_\mu}$, we will highlight the key ways in which their phenomenologies differ.

6.1.1 Benchmark Points

Throughout this chapter, we will be exploring the sensitivities of various experiments to potential solutions of the $(g-2)_\mu$ tension in terms of a muon-philic hidden photon, A'. To this effect, we define four BPs within the region of the $U(1)_{L_\mu - L_\tau}$ parameter space that can solve this tension. We tabulate them in Table 6.1 and situate them in the $U(1)_{L_\mu - L_\tau}$ parameter space in Fig. 6.1. BP1 is the lowest in mass and has been specifically chosen to lie within the coincidence region of both the $(g-2)_\mu$ solution and H_0 alleviation regions. The remaining BPs are then chosen to be increasingly heavier, with the heaviest, BP4, lying just inside the unconstrained region of the $(g-2)_\mu$ solution. To assess the sensitivity of our considered experiments to these

	BP1	BP2	BP3	BP4
$m_{A'}$ (MeV)	15	25	50	100
$g_{\mu\tau}$ ($\times 10^{-4}$)	5	6	6	10

Table 6.1: The benchmark points we consider within the $(g_{\mu\tau}, m_{A'})$ parameter space of the $U(1)_{L_\mu - L_\tau}$ that can explain the $(g-2)_\mu$ tension. We use these same benchmark points for a $U(1)_{L_\mu}$ when comparing model reconstructions.

BPs, we will perform a parameter reconstruction, attempting to reconstruct the properties of the hidden photon responsible for the signal observed.

6.1.2 Parameter Reconstruction

Generally, suppose that we observe the data $\boldsymbol{x} \equiv (x_1, x_2, \ldots, x_n)^\top$. We wish to quantify how statistically likely these data are to have been produced by the model of interest, which will be defined by some set of model parameters, $\boldsymbol{\theta} \equiv (\theta_1, \theta_2, \ldots, \theta_m)^\top$. The likelihood function, $\mathcal{L}(\boldsymbol{\theta})$, tells us the probability of having observed these data given the parameters $\boldsymbol{\theta}$, $p(\boldsymbol{x}|\boldsymbol{\theta})$. Thus, for any point in the parameter space of our model, the likelihood function assigns a probabilistic measure of how well-suited this model is in explaining the observed data.

We can compare the likelihood of two competing models to determine whether one can be rejected over the other. Given the model of interest, typically called the null hypothesis and defined by a set of model parameters $\boldsymbol{\theta}_0$, and a more general competing model, called the alternative hypothesis and defined by the model parameters $\boldsymbol{\theta}_1$, we can construct the likelihood ratio

$$\lambda \equiv \frac{\max_{\boldsymbol{\theta}_0} \left[\mathcal{L}\left(\boldsymbol{\theta}_0\right)\right]}{\max_{\boldsymbol{\theta}_1} \left[\mathcal{L}\left(\boldsymbol{\theta}_1\right)\right]}, \tag{6.1.1}$$

where each likelihood is maximised with respect to the free parameters of the relevant model. Note that, since the alternative hypothesis generally contains more degrees of freedom than the null hypothesis, it will always be a better description of

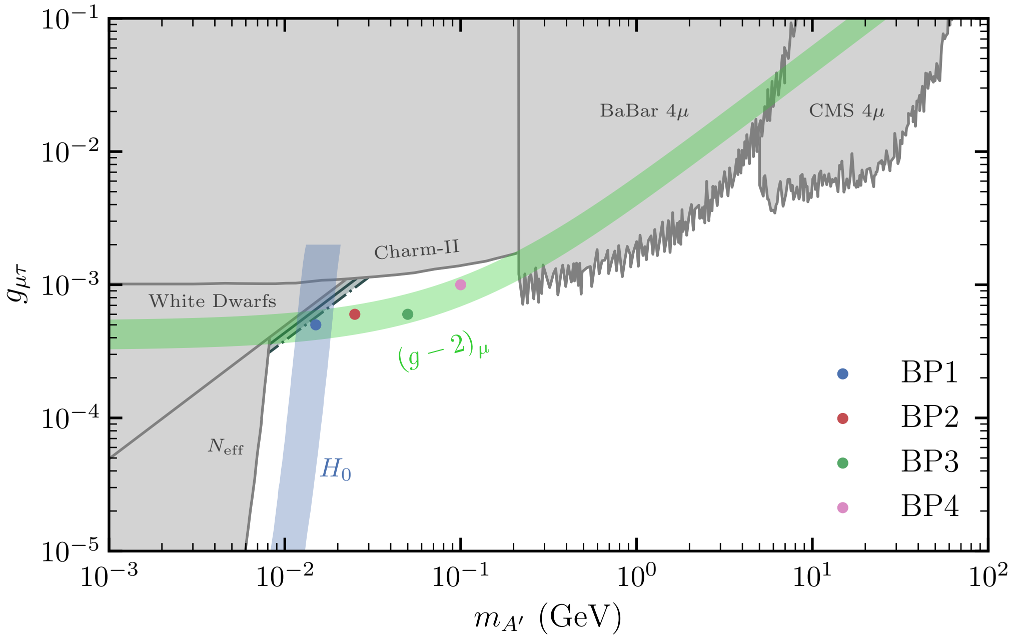

Figure 6.1: The BPs we consider here in the context of the current $U(1)_{L_\mu - L_\tau}$ landscape. The 90% exclusion limits (grey) shown are as per Fig. 4.5; however, we now include the Borexino limits we derived in Section 5.2.3 with the HZ SSM (dark grey) using the Phase-I (dash-dotted) and Phase-II (solid) data. For the case of a $U(1)_{L_\mu}$ hidden photon of the same kinetic mixing, recall that all limits are the same except for those from BaBar and Charm-II (c.f. Section 4.2.4). Also shown are the $(g-2)_\mu$ 2σ (green) and H_0 (blue) preferred regions.

the data, and the ratio in Eq. (6.1.1) will be bounded in the interval $\lambda \in (0, 1]$. A higher value for λ therefore indicates a greater level of statistical agreement between the two hypotheses. If $\boldsymbol{\theta}_1$ are the parameters that maximise the alternative hypothesis likelihood, and we are testing it against some fixed parameters, $\boldsymbol{\theta}$, of the null hypothesis, then λ can be interpreted as a function of the null hypothesis parameters,

$$\lambda(\boldsymbol{\theta}) = \frac{\mathcal{L}(\boldsymbol{\theta})}{\mathcal{L}(\boldsymbol{\theta}_1)} \,. \tag{6.1.2}$$

Typically, it is more useful to work with the logarithm of the likelihood ratio, $\ln \lambda(\boldsymbol{\theta})$. Indeed, if the null hypothesis is the true descriptor of the data, Wilks' theorem tells us that the distribution of the test statistic $q_{\boldsymbol{\theta}} \equiv -2 \ln \lambda(\boldsymbol{\theta})$ asymptotically approaches a χ^2-distribution with number of degrees of freedom, k, equal to the difference in the number of free parameters between the two models. This result holds true as long as the sample size is large enough and the true parameter value does not lie on the boundary of the assumed parameter space[1]. A log-likelihood-ratio test then consists of evaluating q given the measured data, $q_{\boldsymbol{\theta},\,\mathrm{obs}}$, and calculating the probability of finding a value of $q_{\boldsymbol{\theta}}$ at least as extreme as the one observed:

$$p_{\boldsymbol{\theta}} = \int_{q_{\boldsymbol{\theta},\,\mathrm{obs}}}^{\infty} f(q_{\boldsymbol{\theta}}|\boldsymbol{\theta})\,\mathrm{d}q_{\boldsymbol{\theta}} = 1 - F_{\chi^2}(q_{\boldsymbol{\theta},\,\mathrm{obs}}; k)\,. \tag{6.1.3}$$

To replace the integral over the distribution function of $q_{\boldsymbol{\theta}}$, $f(q_{\boldsymbol{\theta}}|\boldsymbol{\theta})$, we have used Wilks' theorem to set $f \equiv 1 - F_{\chi^2}(q_{\boldsymbol{\theta},\mathrm{obs}}; k)$, where the function F_{χ^2} is the cumulative χ^2-distribution function with k degrees of freedom. In performing a parameter reconstruction, we compare the likelihood of the fitted model to that of the model at a different point in parameter space.

We can use this $p_{\boldsymbol{\theta}}$-value to construct confidence regions within our parameter space by performing an inverted-hypothesis test. For some confidence level α, we can define a confidence region at the level α as all those points for which $p_{\boldsymbol{\theta}} \geq 1 - \alpha$. Finding the boundaries of this region then amounts to finding the contours in parameter space for which the equality holds, whereupon those parameters would be rejected against the observed data with confidence α[2].

For our particular case, since all of the experiments we will be considering are counting experiments, we will use a binned likelihood function based on Poisson distributed events,

$$\mathcal{L}(\boldsymbol{\theta}) = \prod_{i=1}^{N} \frac{\mu_i^{n_{\mathrm{obs},\,i}} e^{-\mu_i}}{n_{\mathrm{obs},\,i}!}\,. \tag{6.1.4}$$

Here, N is the total number of bins considered in an experiment, $n_{\mathrm{obs},\,i}$ is the number of observed events in bin i, and $\mu_i \equiv s_i + b_i$ is the expected number of events within each bin, which is built from the expected signal and background within that bin. To determine the reconstruction power of each of our experiments, we will use Asimov

---

[1] We have checked that Wilks' theorem holds for all reliant analyses in this work.

[2] From a frequentist perspective, these confidence regions can be interpreted as containing the true value of the model parameter α% of the time that experiments construct the α-confidence region.

data sets [420], such that the number of observed events within each bin is set to its respective expectation value under the SM, $n_{\mathrm{obs},\,i} \equiv \mu_i^{\mathrm{SM}}$, leading to the likelihood being maximised for $\mu_i = n_{\mathrm{obs},\,i}$. Then, for an expected number of events $\mu_i(\boldsymbol{\theta})$ under any particular model, we have that the test statistic is given by

$$q_{\boldsymbol{\theta}} = 2\sum_i^N \left[\mu_i(\boldsymbol{\theta}) - n_{\mathrm{obs},\,i} + n_{\mathrm{obs},\,i} \ln \frac{n_{\mathrm{obs},\,i}}{\mu_i(\boldsymbol{\theta})}\right] . \tag{6.1.5}$$

In this chapter, we will use this test statistic to construct confidence regions in the 2D $U(1)_{L_\mu - L_\tau}$ parameter space, $\boldsymbol{\theta} = (g_{\mu\tau}, m_{A'})$. We will build the 68% and 95% confidence regions, which, using Eq. (6.1.3) with $k = 2$, corresponds to finding those parameters for which $q_{\boldsymbol{\theta}} > 2.30$ and $q_{\boldsymbol{\theta}} > 6.18$, respectively.

6.1.3 Comparison to a Generic $U(1)_{L_\mu}$ Model

As we discussed in Section 4.2.4, all that we need to explain the $(g-2)_\mu$ tension is a muon-philic mediator. Thus, extending the SM with a gauged $U(1)_{L_\mu}$ would suffice. However, this model is not as theoretically elegant as the $U(1)_{L_\mu - L_\tau}$, requiring the addition of further field content to cancel the introduced anomalies, and it is also subject to stringent FCNC constraints. However, it is not impossible that such a model exists in nature, and, should it do so, we will need a way to discriminate between it and the more elegant $U(1)_{L_\mu - L_\tau}$.

The $U(1)_{L_\mu - L_\tau}$ hidden photon exhibits three characteristic phenomenological properties:

P1 A vector-like coupling to the second-generation leptons.

P2 A specific value for its kinetic mixing with the SM photon—namely, $\epsilon_{\mu\tau} \approx -g_{\mu\tau}/70$.

P3 A vector-like coupling to the third-generation leptons, which is equal and opposite to that of the second generation.

As explained above, to account for the $(g-2)_\mu$ tension, we only require that the introduced hidden photon satisfies P1, which both a $U(1)_{L_\mu - L_\tau}$ and $U(1)_{L_\mu}$ hidden photon can fulfil. Therefore, to confirm the $U(1)_{L_\mu - L_\tau}$ as the true underlying model, we must further experimentally verify P2 and P3. Since a generic $U(1)_{L_\mu}$-type mediator satisfies P1, has the freedom to satisfy P2, but does not satisfy P3, it is an excellent model to pit against the $U(1)_{L_\mu - L_\tau}$ due to its similar, but not identical, physical predictions.

To explore how well each of our considered experiments will be able to disentangle a $U(1)_{L_\mu - L_\tau}$ signal from a competing effective $U(1)_{L_\mu}$ signal, we will conduct our parameter reconstructions separately under both models. We will collectively refer to the gauge couplings and kinetic mixing parameters of both models as g_x and ϵ_x, respectively. When we need to distinguish between them, we will label them with their respective indices of μ or $\mu\tau$.

6.2 Muon Beam Experiments

Should the $(g-2)_\mu$ tension prove to be a sign of new physics, muon beam experiments will be crucial in determining its true nature. As we have discussed, a new, light muon-philic vector boson, A', can solve this tension, and it would leave a signature in such experiments as missing energy in the muon beam. Detecting this smoking gun signature will be of paramount importance in testing the $U(1)_{L_\mu - L_\tau}$ solution to $(g-2)_\mu$, as this new gauge boson necessarily couples to the second-generation leptons. Including these experiments in our search strategy is therefore a necessity, and we will see that they will be able to tightly constrain the gauge coupling of a muon-philic vector boson.

The planned NA64μ [18, 19] and M^3 [421] experiments at CERN and Fermilab, respectively, are prime candidates with which to look for such muon-philic hidden photons. In these experiments, the hidden photon is produced via Bremsstrahlung radiation in muon-nucleus collisions, decaying into undetectable neutrinos in the case where $m_{A'} < 2m_\mu \approx 200\,\text{MeV}$—the mass regime relevant for solving the $(g-2)_\mu$ tension[3]. The first pilot run of the NA64μ experiment was planned to begin at the end of 2021 [422], completing its full Phase-I run in 2023 with a total of 10^{11} muons on target (MOT) [18]. This will be the first experiment to be sensitive to the $(g-2)_\mu$ solution region, and we will therefore constrain our analysis to NA64μ. We note, however, that our results can also be re-interpreted to pertain to Fermilab's M^3 experiment[4].

Searches for the invisible decay of a muon-philic mediator in rare kaon decay experiments, such as those conducted at NA62 [417], could also be included in our reconstruction strategy. In these experiments, the A' could be produced from the final state muon in the kaon decay $K \to \mu\nu$ and then decay invisibly, producing a missing energy signature. NA62 is also capable of probing the $(g-2)_\mu$ preferred region; however, it will need its total planned number of 10^{13} collected kaons to do so [417]. Moreover, its experimental systematics will need to be reduced to be sensitive to this region [417]. Thus, while NA62 would be an excellent future addition to our search strategy, we presently focus on NA64μ.

6.2.1 Confirming $U(1)_{L_\mu - L_\tau}$ with NA64μ

In the NA64μ experiment, a beam of muons with initial energy $E_0 \approx 160\,\text{GeV}$ is dumped onto a lead target with thickness $L_T \approx 20\,\text{cm}$. The energy and momentum of the scattered muons are measured within the fiducial volume of the detector. This consists of an active target that is surrounded by a high-efficiency electromagnetic calorimeter to remove charged backgrounds, a series of magnetic spectrometers and tracker system to measure the momenta of the incident and scattered muons,

---

[3] If, on the other hand, the new gauge boson is such that $m_{A'} > 2m_\mu$, we could directly search for it in visible decays into muon pairs.

[4] A full sensitivity study to a $U(1)_{L_\mu - L_\tau}$ hidden photon using a sophisticated, realistic beam simulation for NA64μ was recently performed in Ref. [423]. They found that, should the NA64μ results be in line with simulation expectations, it will be able to rule out the entirety of the $(g-2)_\mu$ preferred region after its Phase-I run. This differs from our analysis, which focuses on parameter reconstruction over exclusion.

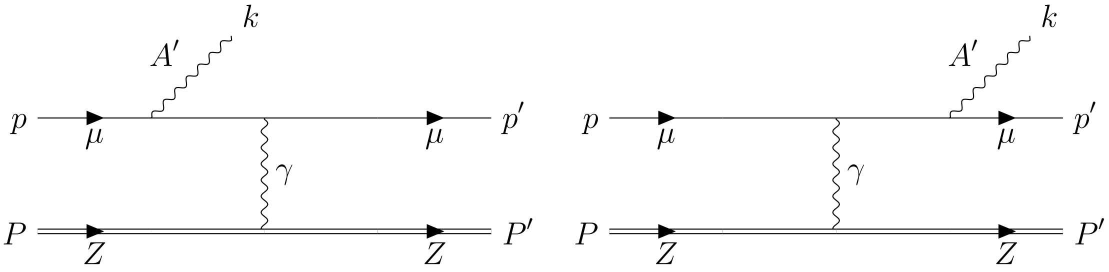

Figure 6.2: Producing a muon-philic vector boson in muon-nucleus scattering through Bremsstrahlung radiation. This can occur either with the initial- (left) or final-state (right) muon.

and hermetic hadronic calorimeters to detect both charged and neutral secondaries produced in the muon-target collisions [18].

Within the muon beam, a light muon-philic vector boson can be produced via the Bremsstrahlung process

$$\mu + Z \to \mu + Z + A' \,, \tag{6.2.1}$$

which we illustrate in Fig. 6.2. The hidden photon produced, A', will carry away some fraction of the initial muon energy, $x \equiv E_{A'}/E_0$. If this hidden photon is lighter than the dimuon threshold, which within the $(g-2)_\mu$ solution region is always true, it will only decay invisibly into a pair of neutrinos. Energy fractions carried away within a particular range, $x^i \in [x^i_{\mathrm{min}}, x^i_{\mathrm{max}}]$, can be translated into a number of hidden photons having been produced within the detector, $N^i_{A'}$. This is given by [424, 425]

$$N^i_{A'} = (\mathrm{MOT}) N_T L_T \int_{x^i_{\mathrm{min}}}^{x^i_{\mathrm{max}}} \frac{\mathrm{d}\sigma_{2\to 3}}{\mathrm{d}x}\,\mathrm{d}x \,, \tag{6.2.2}$$

where N_T is the number of target atoms in the detector, and the differential cross section $\mathrm{d}\sigma_{2\to3}/\mathrm{d}x$ is the $2 \to 3$ production cross section of the process illustrated in Eq. (6.2.1). In the Weizsäcker-Williams approximation, this is given by [424, 425]

$$\frac{\mathrm{d}\sigma}{\mathrm{d}x} \simeq \frac{\alpha^2}{2\pi^2}\frac{g_x^2 \chi \beta_{A'}}{1-x}\left[\frac{C_2}{V} + \frac{C_3}{2V^2} + \frac{C_4}{3V^3}\right] . \tag{6.2.3}$$

The terms in the square parentheses are defined through the relations

$$C_2 \equiv (1-x) + (1-x)^3 \,, \tag{6.2.4}$$

$$C_3 \equiv -2x(1-x)^2 m_{A'}^2 - 4m_\mu^2 x(1-x)^2\,, \tag{6.2.5}$$

$$C_4 \equiv 2m_\mu^4 x(1-x)^3 + (1-x)^2\left\{4m_\mu^4 + 2m_\mu^2 m_{A'}^2\left[x^2+(1-x)^2\right]\right\}\,, \tag{6.2.6}$$

with the virtuality of the hidden photon, V, given by

$$V \equiv \left(\frac{1-x}{x}\right) m_{A'}^2 + m_\mu^2 x\,. \tag{6.2.7}$$

The effective photon flux, χ, sourced by the nucleus is given by [424, 425]

$$\chi \equiv \int_{t_{\min}(m_{A'})}^{t_{\max}(m_{A'})} \frac{t - t_{\min}(m_{A'})}{t^2} G_2(t)\,\mathrm{d}t\,, \tag{6.2.8}$$

with $t_{\min}(m_{A'}) \equiv (m_{A'}^2/(2E_0))^2 \approx 0$, $t_{\max} \approx m_{A'}^2$, and $G_2(t)$ is the electric form factor of the nucleus, explored in detail in, for example, Ref. [426]. Finally, $\beta_{A'} \approx 1$ is the boost factor of the hidden photon, and α is the fine-structure constant.

In the NA64μ experiment, a missing energy signature is identified according to measurements of the total energy by the calorimeters and the energy of a single outgoing muon. Specifically, if the total energy satisfies $E_{\text{tot,cal}} \lesssim 12\,\text{GeV}$ and the outgoing muon has an energy of $E'_\mu \lesssim E_0/2$, energy is deemed to be missing. Detailed studies of the expected backgrounds, such as low-energy muons from the low-energy tail of the produced muons, have demonstrated that imposing a cut of $E'_\mu \lesssim 100\,\text{GeV}$ to the maximum muon energy makes this search essentially background free [18, 427]. Furthermore, while the momentum resolution of the incoming muon beam is predicted to be $\sigma_p \sim 1\,\text{GeV}$ [18], we use a more conservative bin width of $10\,\text{GeV}$ to ensure that we have approximately $N_{A'} \gtrsim 3$ events per bin for each of our benchmark points. Following Ref. [427], we also assume a signal window of 10–100 GeV to minimise backgrounds.

We show our predicted muon spectra for each of our benchmark points in Fig. 6.3. We have assumed an average signal reconstruction efficiency of $\epsilon = 0.3$ across the entire energy range, which is an approximation of realistic efficiencies, lying in the range 0.1–0.5 for masses $m_{A'} \sim 10^{-3}$–$1\,\text{GeV}$ [18]. Using these signal templates, we perform parameter reconstructions for each of our BPs under both a $U(1)_{L_\mu-L_\tau}$ and

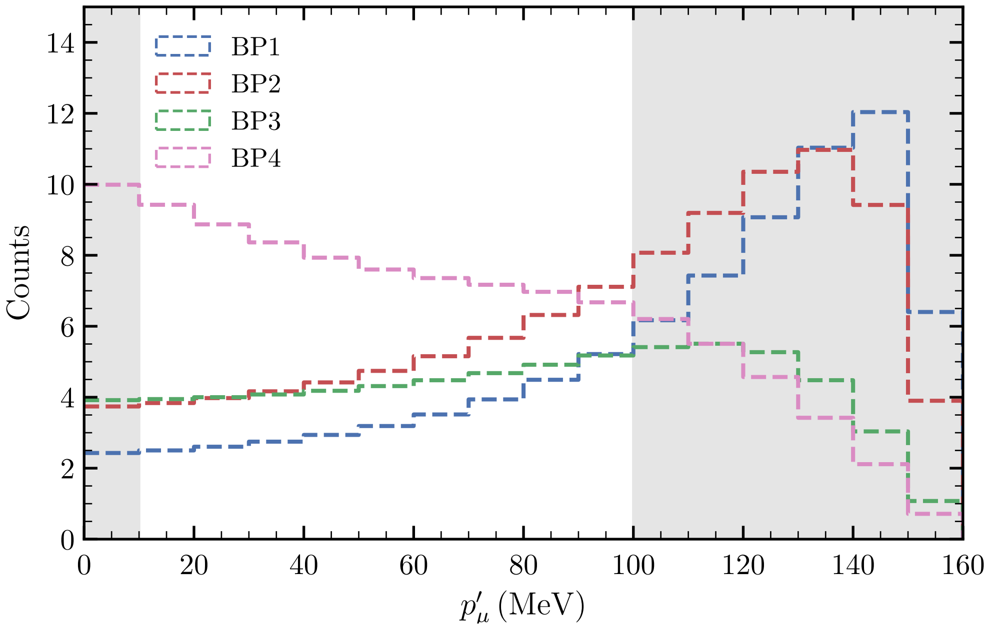

Figure 6.3: The computed muon spectra at NA64μ due to an invisibly decaying muon-philic A' for each of our BPs. The grey shaded areas show the experimental energy cut we have applied to remove any backgrounds.

$U(1)_{L_\mu}$ model.

Reconstructing the $U(1)_{L_\mu - L_\tau}$ Solution to $(g-2)_\mu$

We show the results of our parameter reconstructions in Fig. 6.4. We first note that NA64μ has excellent sensitivity to hidden photon masses of the order of the muon mass, $m_{A'} \sim m_\mu \approx 100\,\mathrm{MeV}$. This corresponds to the case of BP4, where both the 1σ and 2σ contours bound a small region around the true parameter point. However, for the lower mass benchmark points BP1-BP3, NA64μ can only place an upper bound on the mass, though it can still provide tight reconstructions of the coupling.

We can understand this by looking at the low-mass limit of the $2 \to 3$ cross section in Eq. (6.2.3). For $m_{A'} \ll m_\mu$, we have that

$$\frac{\mathrm{d}\sigma}{\mathrm{d}x} \sim \frac{g_x^2 \chi(m_{A'})}{m_\mu^2}\,, \tag{6.2.9}$$

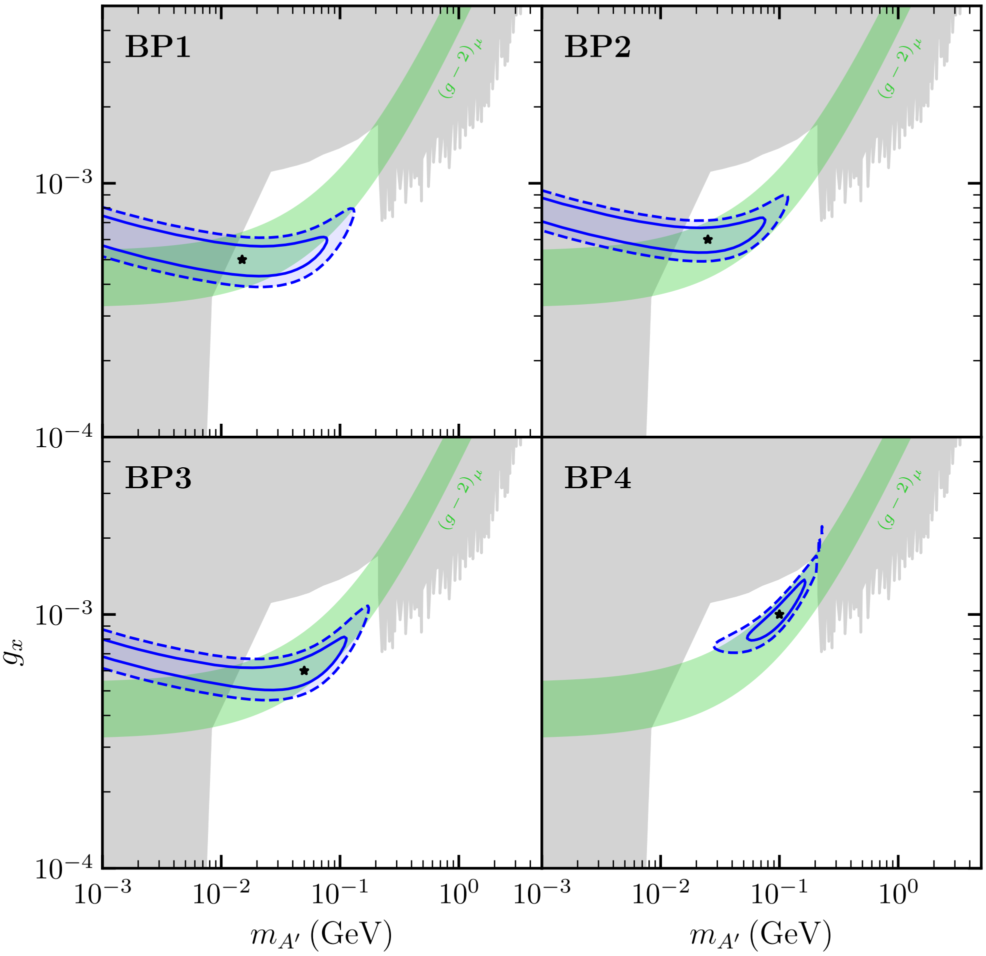

Figure 6.4: Parameter reconstructions for each of our BPs using the NA64μ experiment. The solid (dashed) contours represent the boundaries of the 1σ (2σ) confidence regions. The contours of both the $U(1)_{L_\mu - L_\tau}$ and $U(1)_{L_\mu}$ parameter reconstructions coincide for all of our BPs. The black stars represent the BPs. The $(g-2)_\mu$ 2σ preferred region is shown in green.

such that the number of hidden photons produced is proportional to the product of $g_x^2\chi$. The mass dependence is thus entirely confined in the effective photon flux, which acts as a normalisation factor. A decrease in the mass serves to lower this flux, which can be compensated for by an increase in the coupling strength; this is the behaviour we see in the low mass regime of Fig. 6.4 for the first three BPs. The spectral shape of the signal, which is dictated by the mass, is lost within this regime.

We can also see this from the template spectra in Fig. 6.3. For the lower mass BP1-BP3, we see that the spectra are very similar in shape, differing only in their overall scaling. This issue is exacerbated by the cut in the energy window, where the residual shape signatures of the BPs at higher energies is masked. BP3 in particular suffers from this masking, as its characteristic spectral peak is produced outside of the region of interest. This BP, with a mass of $m_{A'} = 50\,\mathrm{MeV}$, which is of the same order of magnitude as m_μ, is at the turning point of this asymptotic low-mass behaviour, and it could generally still be well reconstructed, masking notwithstanding.

The reconstructions are performed equally well under both a $U(1)_{L_\mu - L_\tau}$ and a $U(1)_{L_\mu}$ model; indeed, the contours shown in Fig. 6.4 coincide in both cases. This is because there is no difference in the predicted signals for BPs with masses $m_{A'} < 2m_\mu$. For masses above this threshold, the contours would deviate due to their different invisible branching ratios.

Crucially, as the kinetic mixing parameter, ϵ_x, has no impact on the predicted signals of either of these models, NA64μ is completely blind to it. As we have discussed, this is a critical difference between potential realisations of a $U(1)_{L_\mu}$ and $U(1)_{L_\mu - L_\tau}$. Thus, while NA64μ can reconstruct the coupling well, it is incapable of differentiating between these models. To do this, we need a complementary probe that can access this parameter, giving us this kind of discriminating power. CEνNS experiments, which can access this dark sector through the kinetic mixing portal, are able to provide us with precisely this discrimination.

6.3 Spallation Source Experiments

As we saw in Chapter 5, SS experiments, which measure the coherent scattering of neutrinos on nuclei, can place competitive bounds on the $U(1)_{L_\mu - L_\tau}$ parameter space. Previously, we computed the limit that the LAr run of the CENNS-10 experiment [8]

Exp.	M (ton)	E_{th} (keV$_{\text{nr}}$)	N_{POT} ($\times 10^{23}$ year^{-1})	r	L (m)	σ_{sys}
CENNS-610	0.61	20	1.5	0.08	28.4	8.5%
ESS-10	0.01	0.1	2.8	0.3	20	5%
ESS	1	20	2.8	0.3	20	5%
CCM	7	10	0.177	0.0425	20	5%

Table 6.2: The experimental configurations of the SS experiments we consider here. For more details on what each quantity represents, see Section 5.1.

places in this parameter space, finding it to be competitive with the CsI run of COHERENT [185]. Spallation source experiments thus form powerful probes of the $U(1)_{L_\mu - L_\tau}$ hidden photon, and their sensitivity to the kinetic mixing parameter gives them the discriminating power that we need to distinguish between the $U(1)_{L_\mu - L_\tau}$ and $U(1)_{L_\mu}$ models. To explore the potential of these experiments in helping us to confirm the $U(1)_{L_\mu - L_\tau}$ solution to $(g-2)_\mu$, we will consider a selection of future LAr detectors that have been proposed to measure CEνNS ever more precisely. Note that, as we outlined how spallation source experiments operate in Section 5.1, we will skip most of the details here, making reference to any material from that section where appropriate.

6.3.1 Confirming $U(1)_{L_\mu - L_\tau}$ with SS Experiments

Inspired by the analysis of Ref. [338], we consider the four detector configurations shown in Table 6.2. We will briefly discuss the relevant details of each experiment below.

CENNS-610 CENNS-610 will be the next iteration of the CENNS-10 LAr detector, featuring an increased fiducial mass of 610 kg [20]. We discussed the CENNS-10 detector in detail in Section 5.1, and we base our realisation of the upgraded detector on it. We keep the quenching factor used to convert between nuclear and electron-equivalent energies, given by Eq. (5.1.6), the same. The efficiency is also expected to be similar, reaching 50% at an energy of $\sim 4\,\mathrm{keV_{ee}}$ (approximately equivalent to $20\,\mathrm{keV_{nr}}$); we model it via

$$\epsilon(E_R) = \frac{1}{2}\left[1 + \tanh(E_R - 4\,\mathrm{keV_{ee}})\right] . \tag{6.3.1}$$

Finally, we use the same fixed systematic uncertainty on the overall predicted rate of $\sigma_{\mathrm{sys}} = 8.5\%$

CCM The Coherent Captain-Mills (CCM) experiment, while a future experiment at the time of writing Ref. [2], recently released the results from its first new physics search [21]. Located at Los Alamos National Laboratory, CCM was projected to have a 7 ton mass of LAr. It is planned to run for a total of 2.5 years in both a near and far configuration; however, since the expected number of CEνNS events will be larger in the near configuration, we only consider this former setup, which features a baseline of $L = 20\,\mathrm{m}$. For simplicity, we use a flat efficiency of 100% with a sharp cutoff at $E_{\mathrm{th}} = 20\,\mathrm{keV_{nr}}$, where the CENNS-10 LAr efficiency drops to 50%. We assume a more optimistic systematic uncertainty of $\sigma_{\mathrm{sys}} = 5\%$, as per Ref. [338].

ESS(-10) The European Spallation Source (ESS) [22], based in Sweden, is currently finishing construction. A multidisciplinary project, ESS is endeavouring to provide us with the most powerful pulsed neutron source in the world. Simultaneously, it plans to give us an order of magnitude increase in the neutrino flux compared to that produced at SNS [22]. This experiment will undergo two iterations: a low mass (10 kg) but very low threshold ($E_{\mathrm{th}} = 1\,\mathrm{keV_{ee}}$) iteration (which we shall call ESS-10), and a higher mass (1 ton) iteration with the same threshold energy as CCM and CENNS (which we shall refer to as ESS). For both of these configurations, we use a baseline of $L = 20\,\mathrm{m}$ and assume a 1 yr operation period. We use an efficiency of 100% with a sharp cutoff at the relevant threshold. We employ the same systematic uncertainty of $\sigma_{\mathrm{sys}} = 5\%$ for both setups.

To generate our signal templates, we use a four-bin analysis across the energy window of 20–100 $\mathrm{keV_{ee}}$. This allows for some reconstruction of the mediator mass in the event of an observation while reducing the effect of systematic errors. Within all of our bins, we assume that the number of background events will be 10% of the number of SM events observed, matching the number of beam-related neutrons that CENNS-10 observed [20].

We show our simulated events in Fig. 6.5. As we mentioned in Section 4.2.1, all BPs exhibit a deficit of events with respect to the SM prediction due to the negative interference effects with the muon flavour. We see that the greatest new physics effects are exhibited by the lowest energy bins—an excellent motivator for lowering energy thresholds as much as possible. Note that, due to the sharp energy cutoff we have employed in CCM and ESS to emulate the effects of the energy threshold, the effects in the first bin are completely hidden from these experiments.

Reconstructing the $U(1)_{L_\mu - L_\tau}$ Solution to $(g-2)_\mu$

To perform our parameter reconstruction, we use a binned version of the same χ^2 function we implemented in Section 5.1 for CENNS-10 LAr, given in Eq. (5.1.7). In the limit of high statistics, $\chi^2(\boldsymbol{\theta}) \to 2\ln\mathcal{L}(\boldsymbol{\theta})$, allowing us to use $\Delta\chi^2$ as an equivalent test statistic to $q_{\boldsymbol{\theta}}$. We show the results of our parameter reconstruction in Fig. 6.6 in the particular case that the value of the kinetic mixing parameter coincides with that of the $U(1)_{L_\mu - L_\tau}$ (i.e. $\epsilon_x = -g_x/70$).

For the ESS configurations, we obtain full reconstructions at both the 1σ and 2σ levels for BP1 and BP2. This is because the masses of these hidden photons are below the minimum energy transfer that can take place within these experiments. This occurs when $m_{A'}^2 \lesssim 2m_N E_{\mathrm{th}}$, which, for our highest threshold detectors (CCM and ESS), happens at $m_{A'} \approx 40\,\mathrm{MeV}$. Above this mass, $m_{A'}$ dominates in the propagator of the new physics contribution, and the scattering cross section falls as $1/m_{A'}^2$ in the interference-dominated regime. Thus, these experiments may only

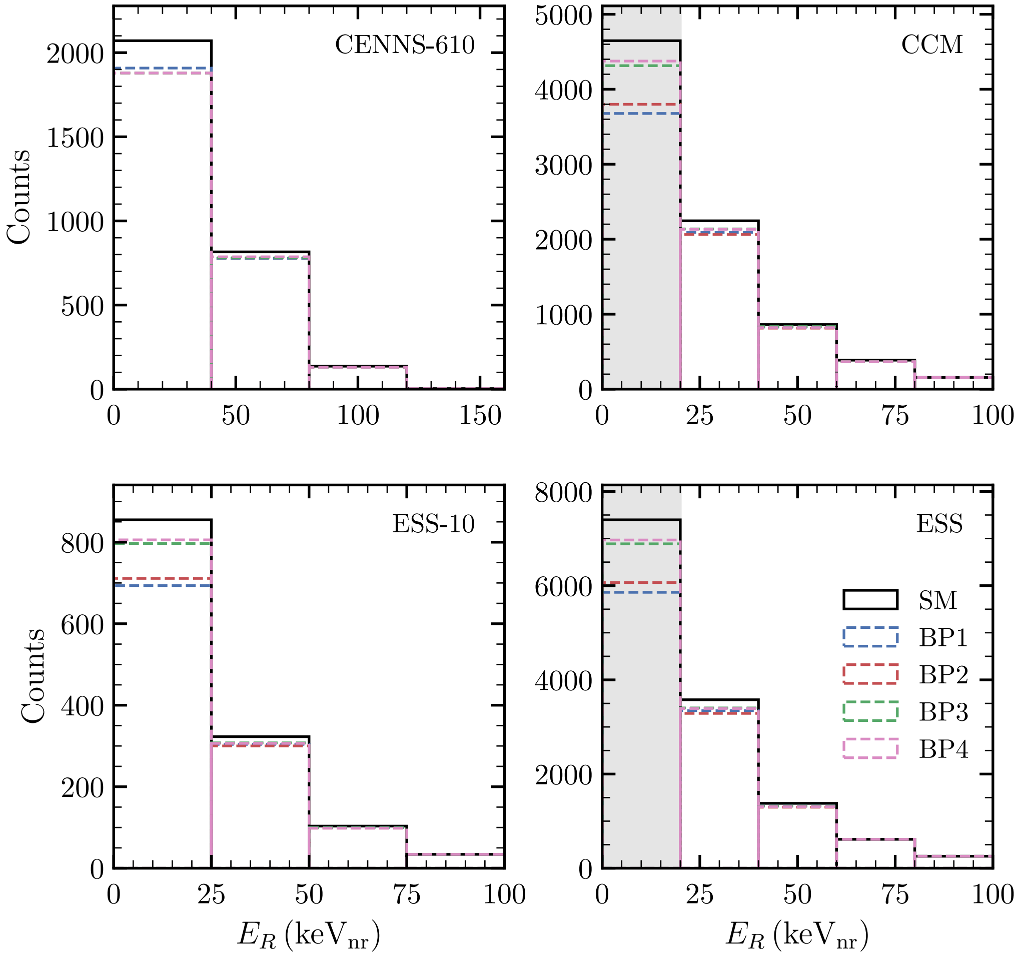

Figure 6.5: The binned CEνNS counts for the future LAr SS experiments considered for each of our $U(1)_{L_\mu - L_\tau}$ BPs. Shown are the counts expected from the SM (black) and our BPs (coloured). The grey regions for CCM and ESS highlight the fact that very low-energy bins are hidden from them due to their higher energy thresholds.

probe the low-mass window of the $(g-2)_\mu$ preferred region. For the higher mass BPs, we can only obtain upper bounds on the coupling.

The ESS-10 configuration exemplifies the advantage of having a low energy threshold. Despite having the lowest fiducial mass of our considered experiments, its low threshold gives it high sensitivity to a light mediator, since their effects are strongest at low recoil energies. This allows it to observe the low-mass BP1 and BP2 hidden

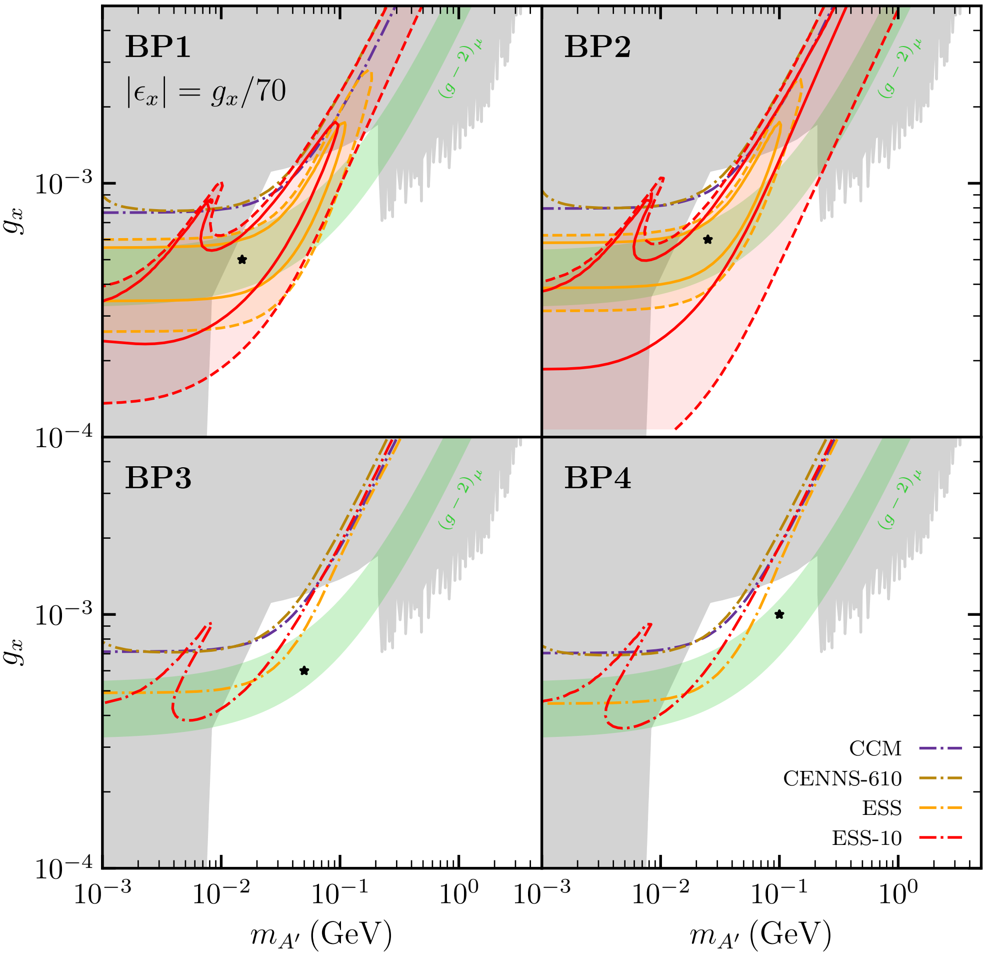

Figure 6.6: Parameter reconstructions for each of our BPs using the SS experiments considered here. The reconstructions correspond to either a $U(1)_{L_\mu - L_\tau}$ or a $U(1)_{L_\mu}$ with $|\epsilon_x| = g_x/70$. The solid (dashed) contours represent the boundaries of the 1σ (2σ) confidence regions. The black stars represent the BPs. The $(g-2)_\mu$ 2σ preferred region is shown in green.

photons, as signified by the fact that the contours close. For all BPs, the bump at $m_{A'} \approx 7\,\text{GeV}$ is due to the crossover of the interference and pure BSM terms, rendering the observed deficit consistent within two regions of the parameter space. This particular crossover is only observable at low transferred momenta, which are themselves only achievable with low threshold detectors[5].

---

[5] For a more detailed discussion on the interference-dominated regions, see Section 4.2.1.

The CENNS-610 and CCM experiments will have less sensitivity to the $U(1)_{L_\mu - L_\tau}$ hidden photon and will be unable to disentangle it from the SM expectation. As a result, these experiments can only place upper bounds in the $U(1)_{L_\mu - L_\tau}$ parameter space, reaching couplings of approximately $g_x \approx 7 \times 10^{-4}$ (for CCM, this is in agreement with the results of Ref. [339]). With increased exposures or, perhaps more realistically, lower energy thresholds, these experiments could become competitive with ESS.

While SS experiments give us sensitivity to the kinetic mixing parameter of a particular model, this sensitivity is inextricably entangled with that to the gauge coupling. The new physics contribution to CEνNS in both the $U(1)_{L_\mu - L_\tau}$ and the $U(1)_{L_\mu}$ cases is given by Eq. (4.2.11), where only the second-generation contribution is relevant for SS experiments. We see that this effect always enters through the product of the gauge coupling and mixing parameter, $g_x \epsilon_x$. Moreover, while the kinetic mixing of the $U(1)_{L_\mu - L_\tau}$ model is fixed at $|\epsilon_{\mu\tau}| \approx g_{\mu\tau}/70$, that of our effective $U(1)_{L_\mu}$ model can, in principle, take on any value in the range $|\epsilon_\mu| \in (g_\mu/100, g_\mu/10)$[6]. Thus, a $U(1)_{L_\mu}$ could mimic the signal from a $U(1)_{L_\mu - L_\tau}$ for a wide range of gauge couplings g_μ, as long as the strength of its kinetic mixing is adjusted to compensate for this. This means that SS experiments will not be able to pin down the true nature of the underlying $U(1)$ by themselves; they will need a complementary independent probe of the gauge coupling for this.

Combining Spallation and Muon Beam Experiments

As we saw in Section 6.2, NA64μ will give us a direct measurement of the gauge coupling, and it can therefore act as our independent probe of g_x. By combining the results from the NA64μ and SS experiments, we can thus get a better handle on the value of ϵ_x. To illustrate this, we will consider the combined reconstructions of both these experiments with two values of the kinetic mixing parameter: one

---

[6] This is due to our agnosticism to the particular UV completion of the $U(1)_{L_\mu}$ model. For a discussion on this, see Section 4.2.4.

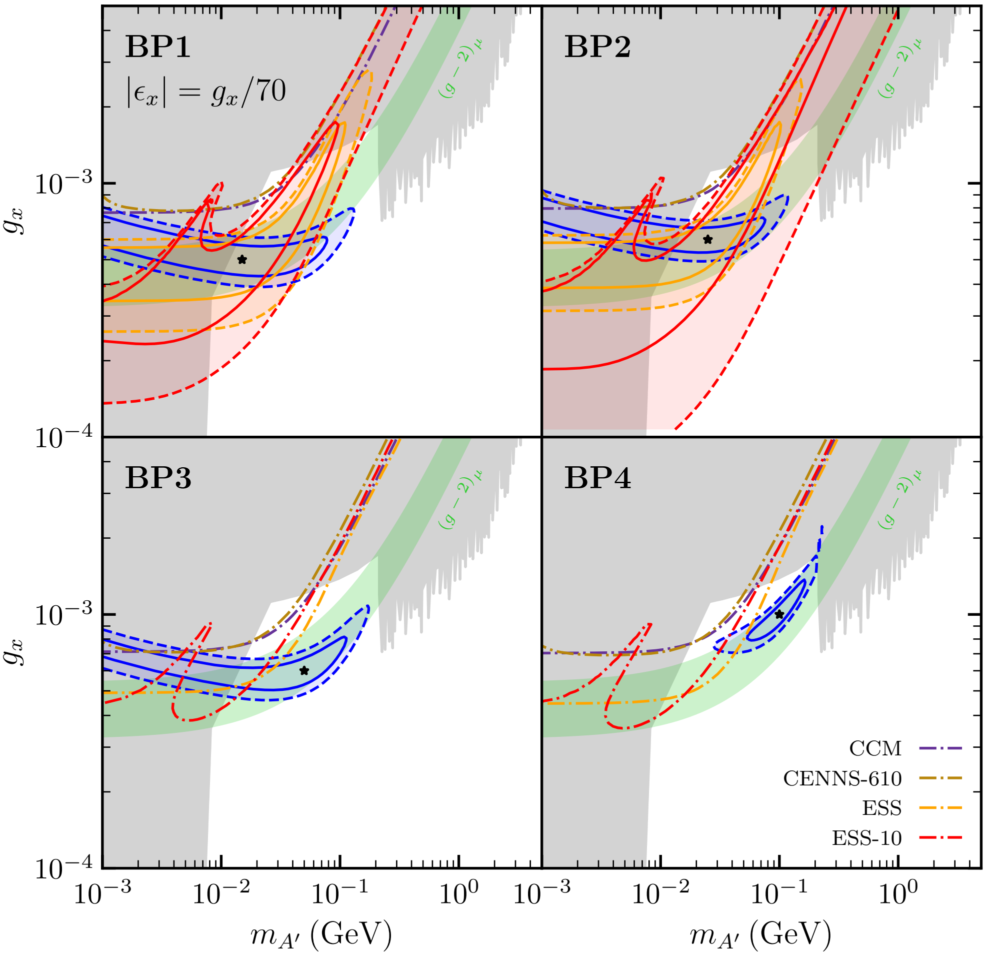

Figure 6.7: Combining the reconstructions of SS experiments and NA64μ (blue) in the case that $|\epsilon_x| = g_x/70$—the value of the kinetic mixing for the $U(1)_{L_\mu - L_\tau}$ model. The green band shows the $(g-2)_\mu$ 2σ preferred region.

consistent with both the $U(1)_{L_\mu - L_\tau}$ and $U(1)_{L_\mu}$ models and one inconsistent with the $U(1)_{L_\mu - L_\tau}$ but consistent with an effective $U(1)_{L_\mu}$ model.

We will firstly explore the situation wherein the kinetic mixing is consistent with both of these models—that is, $\epsilon_x = -g_x/70$. We show the reconstructions this case in Fig. 6.7. We see that the reconstructions achieved by NA64μ and SS experiments are consistent, with the evidence for BP1 and BP2 in particular strengthening as both of these BPs can be probed at these experiments. However, even in the case

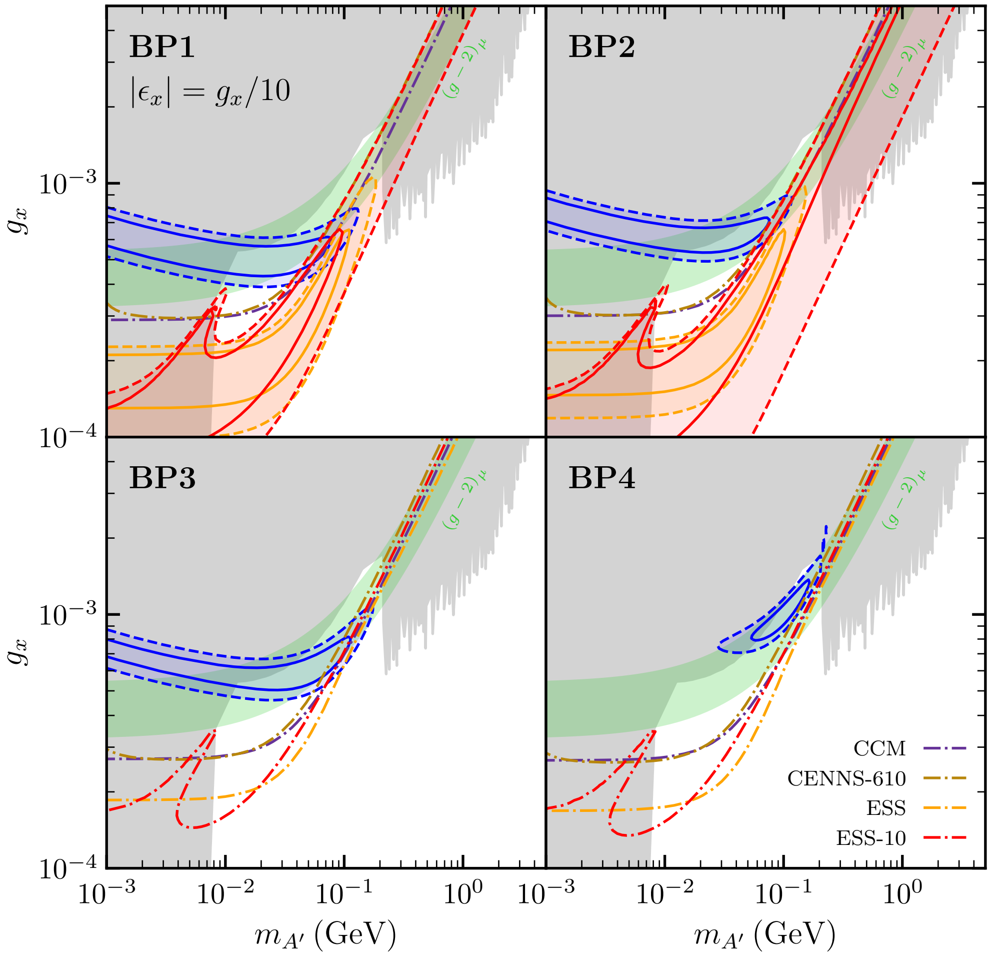

Figure 6.8: The same as in Fig. 6.7 but for $|\epsilon_x| = g_x/10$.

of BP3 and BP4, for which SS experiments cannot claim an observation, the result can nonetheless be used to narrow the region compatible with NA64μ, providing us with a better measurement of the mediator mass.

In contrast, should the new physics effect arise due to an effective $U(1)_{L_\mu}$ with a kinetic mixing of $\epsilon_x = -g_x/10$, which is inconsistent with the $U(1)_{L_\mu - L_\tau}$, we find ourselves in the situation depicted in Fig. 6.8, wherein the reconstructions are in tension. While there is some overlap in the reconstruction regions for BP1 and BP2, the NA64μ preferred regions are almost entirely excluded by SS experiments for BP3 and BP4. In this latter case, SS experiments exclude this particular realisation of a $U(1)_{L_\mu}$ gauge boson as an explanation for the observed NA64μ signal.

By combining the results from the NA64μ and SS experiments, we can therefore achieve reconstructions of both the gauge coupling and the kinetic mixing parameter, simultaneously giving us discriminating power between the $U(1)_{L_\mu - L_\tau}$ and $U(1)_{L_\mu}$ models. However, measuring ϵ_x alone is not enough to tell these two models apart. While finding an inconsistent value of ϵ_x with $U(1)_{L_\mu - L_\tau}$ would be enough to rule it out as a solution to the $(g-2)_\mu$ tension, finding a value that is consistent with it would not, since $U(1)_{L_\mu}$ realisations with the same kinetic mixing value are possible. The only way to tell these two constructions apart would then be to explore the coupling to the third-generation leptons—a feature only exhibited by the $U(1)_{L_\mu - L_\tau}$. This property, labelled P3 in Section 6.1.3, is completely hidden to both NA64μ and SS experiments, as they do not have an appreciable flux of tau neutrinos.

On the other hand, DD experiments have access to a considerable flux of tau neutrinos due to the oscillation effects that take place as neutrinos propagate from the Sun to the Earth. This gives DD experiments the ultimate discriminatory power between the $U(1)_{L_\mu - L_\tau}$ and $U(1)_{L_\mu}$ models. This, combined with the large number of CEνNS and EνES events they are poised to observe, makes them an invaluable addition to our search strategy.

6.4 Future Direct Detection Experiments

As we saw in Chapter 5, next-generation and far-future DD experiments, especially those based on Xe TPC technology, will be sensitive to the $(g-2)_\mu$ preferred region of the $U(1)_{L_\mu - L_\tau}$ parameter space. This makes them excellent additions to our reconstruction strategy beyond the neutrino-dedicated experiments we have considered so far. As we will see, not only will a DD experiment like DARWIN be able to make an observation of low-mass hidden photon solutions to $(g-2)_\mu$, but it will also give us the critical piece of the puzzle that will enable us to finally distinguish a $U(1)_{L_\mu - L_\tau}$ hidden photon from that of a $U(1)_{L_\mu}$ model. Before introducing our DD analysis, we will briefly expand on this latter point.

6.4.1 The Tau Sector: The Ultimate Discriminator

Direct detection experiments will be able to probe the most important distinguishing property of a $U(1)_{L_\mu - L_\tau}$ from an effective $U(1)_{L_\mu}$—a coupling to the third-generation leptons. This is purely a consequence of neutrino oscillations, which result in the electron neutrinos produced in solar fusion reactions transitioning into an admixture of e, μ, and τ neutrinos. This effect is missing from the previous two experiments, whose baselines do not allow for appreciable oscillations[7].

Ultimately, it is the relationship between the predicted fluxes of muon and tau neutrinos arriving at Earth and their corresponding CEνNS cross sections that allows us to discriminate between the $U(1)_{L_\mu - L_\tau}$ and $U(1)_{L_\mu}$ models. As we saw in Section 4.2.1, the new physics effect of a $U(1)_{L_\mu - L_\tau}$ hidden photon is such that an interference term is added to the CEνNS cross section. This interference is positive for tau neutrinos and negative for muon neutrinos, and the nature of the predicted event rate with respect to the SM depends on the relative size of their populations on target. Due to the value of the mixing angle θ_{23}, which largely controls these neutrino populations from the Sun (c.f. Eq. (2.4.44)), the ν_τ flux is almost always higher than that of ν_μ. Thus the $U(1)_{L_\mu - L_\tau}$ hidden photon will generally give us an excess of events in the regions of parameter space that are interference dominated.

On the other hand, the $U(1)_{L_\mu}$ hidden photon can only couple to the incoming ν_μ flux, and it therefore only features a negative interference effect. As the region of parameter space relevant for $(g-2)_\mu$ coincides with the interference-dominated region, we therefore expect a net deficit in the number of CEνNS events in the case of a $U(1)_{L_\mu}$ hidden photon and a net excess in the case of a $U(1)_{L_\mu - L_\tau}$ hidden

---

[7] We note that DUNE would make for an extremely interesting addition to our experimental strategy. In its far-detector configuration, DUNE will be able to measure an appreciable flux of ν_τ as a result of neutrino oscillations, forming a complementary probe to DD experiments in this regard.

photon. Thus, the new physics effects of these models to the predicted CEνNS rate at DD experiments are opposite in nature—this is the signature that allows us to discriminate between them.

Nonetheless, we note that $U(1)_{L_\mu}$ realisations that predict an excess similar to that predicted by our $U(1)_{L_\mu-L_\tau}$ BPs do exist. However, these occur at very high, fine-tuned values of the gauge coupling g_μ, where the positive BSM-only term dominates over the negative interference term. Such realisations would not only produce couplings that are already strongly excluded by present bounds, but they would also yield a signal that would be inconsistent with the deficit-only $U(1)_{L_\mu-L_\tau}$ data from all of our BPs for the SS experiments discussed in Section 6.3.

6.4.2 Confirming $U(1)_{L_\mu-L_\tau}$ with LXe DD Experiments

Since our best hope of observing a $U(1)_{L_\mu-L_\tau}$ hidden photon with DD experiments is through multi-ton LXe experiments, we will focus on experimental configurations based on the upcoming LZ [14] and XENONnT [15] detectors and on the far-future DARWIN observatory [16]. These configurations will be similar to the G2-Xe (in the case of LZ and XENONnT) and G3-Xe (in the case of DARWIN) setups we considered in Chapter 5. However, as we will be placing a greater emphasis on LXe experiments and performing a discovery study using these detectors, we will conduct a more sophisticated analysis.

In particular, for each of our setups, we include energy-dependent efficiency functions and perform an energy-dependent Gaussian smearing to model their finite resolutions. We detail the specifics of these considerations, as well as our background assumptions, below. For more details on the particulars of each experiment, see Section 3.4.

LZ We take the efficiency functions for both NRs and ERs from Ref. [157], which reach their 50% threshold values at $3.8\,\mathrm{keV_{nr}}$ and $1.5\,\mathrm{keV_{ee}}$, respectively. We use the resolution fit given by LUX in Ref. [158]. The ER backgrounds are taken from Fig. 1 of Ref. [171].

XENONnT We take the NR efficiency function from Ref. [428] and our ER efficiency function from the recent ER-excess measurement of Ref. [428], from which we also take the resolution function. The efficiency functions reach their 50% threshold values of $3.8\,\mathrm{keV_{nr}}$ and $1.5\,\mathrm{keV_{ee}}$ for NRs and ERs, respectively. We use the projected ER backgrounds of Ref. [15].

DARWIN We conservatively use the same efficiency and resolution functions as for XENONnT. However, we take the lower ER background predictions given by the DARWIN collaboration in Ref. [183], assuming a flat background rate for all components except for the double-β decay of ^{136}Xe, the spectrum for which we take from the same study.

In the spirit of our previous DD study, we consider an NR-only, ER-only, and combined NR + ER analysis. As before, we assume a 50% acceptance cut on the number of NR events above the energy threshold, rejecting ERs and treating this as a background-free analysis[8]. For the ER-only analysis, we once again assume 99.5% NR/ER discrimination, including the experimentally relevant ER backgrounds in this study. Finally, for the NR + ER analysis, we combine both types of events, interpreting all of them in electron-equivalent energies. We include the full background in this analysis, but we perform no cuts. In each of our analyses, we fold in the appropriate efficiency functions, with energy resolutions taken at electron-equivalent energies.

We show the expected NR and ER differential rate spectra for a generic xenon detector (before incorporating any experimental effects) in Fig. 6.9 for both a $U(1)_{L_\mu - L_\tau}$ and $U(1)_{L_\mu}$ hidden photon with the properties of BP1. We see that the spectrum,

---

[8] A small number of NR background events, along with the 0.05% of ERs that are not rejected during the discrimination, are expected to persist alongside the signal. However, CEνNS is dominant over these background contributions, so we can safely neglect them here.

which is predominantly from ^{8}B neutrinos, terminates at $E_R \sim 1\,\mathrm{keV}$, making observing them very difficult using the nominal thresholds of our detectors. Indeed, we saw this effect in Section 5.2.4, where the NR limits of our Xe configurations suffered as a result of high-energy thresholds. We can ultimately only observe a handful of CEνNS events using the nominal threshold values, with the majority of them coming from the smearing effect with the resolution near the energy threshold. Therefore, to truly exploit the CEνNS rate as a signal instead of as a background, we must push for lower experimental thresholds.

To this effect, we take the liberty of lowering these thresholds from their nominal values. The importance of this is made even clearer when we compare the expected spectra of a $U(1)_{L_\mu - L_\tau}$ to that of a $U(1)_{L_\mu}$ model. We see the effect we discussed in Section 6.4.1 that a $U(1)_{L_\mu - L_\tau}$ gauge boson predicts an excess over the SM, while a $U(1)_{L_\mu}$ predicts a deficit. However, we also see that the size of this effect increases at lower energies. Given the importance of NRs in discriminating between these models, since the ER rate is predicted to be in excess of the SM for both models, achieving a threshold that can probe these larger low-energy effects is crucial for these experiments.

In the case of ERs, we also show the expected background projected for DARWIN, whereby it is dominated by the double-β decay of ^{136}Xe at high energies. Note that, as we focus more intently on LXe experiments in this study, we employ a more careful treatment of the step-approximation in modelling the electronic binding energies. We do this by employing an LXe-centred RRPA, which leads to a further suppression in the 0.25–30 keV$_{\mathrm{ee}}$ window, according to Fig. 2 of Ref. [194]. We have implemented this by applying an energy-dependent scaling to match the predictions of the RRPA[9]. Note that, below the RRPA energy window, we have reverted to the step-function approximation, which acts as an upper bound on the expected rate in the absence of numerical solutions to the RRPA at low energies [194]. Nonetheless,

---

[9] In principle, we should take into account how the RRPA result might change in the presence of a new light mediator; however, this is beyond the scope of our present analysis.

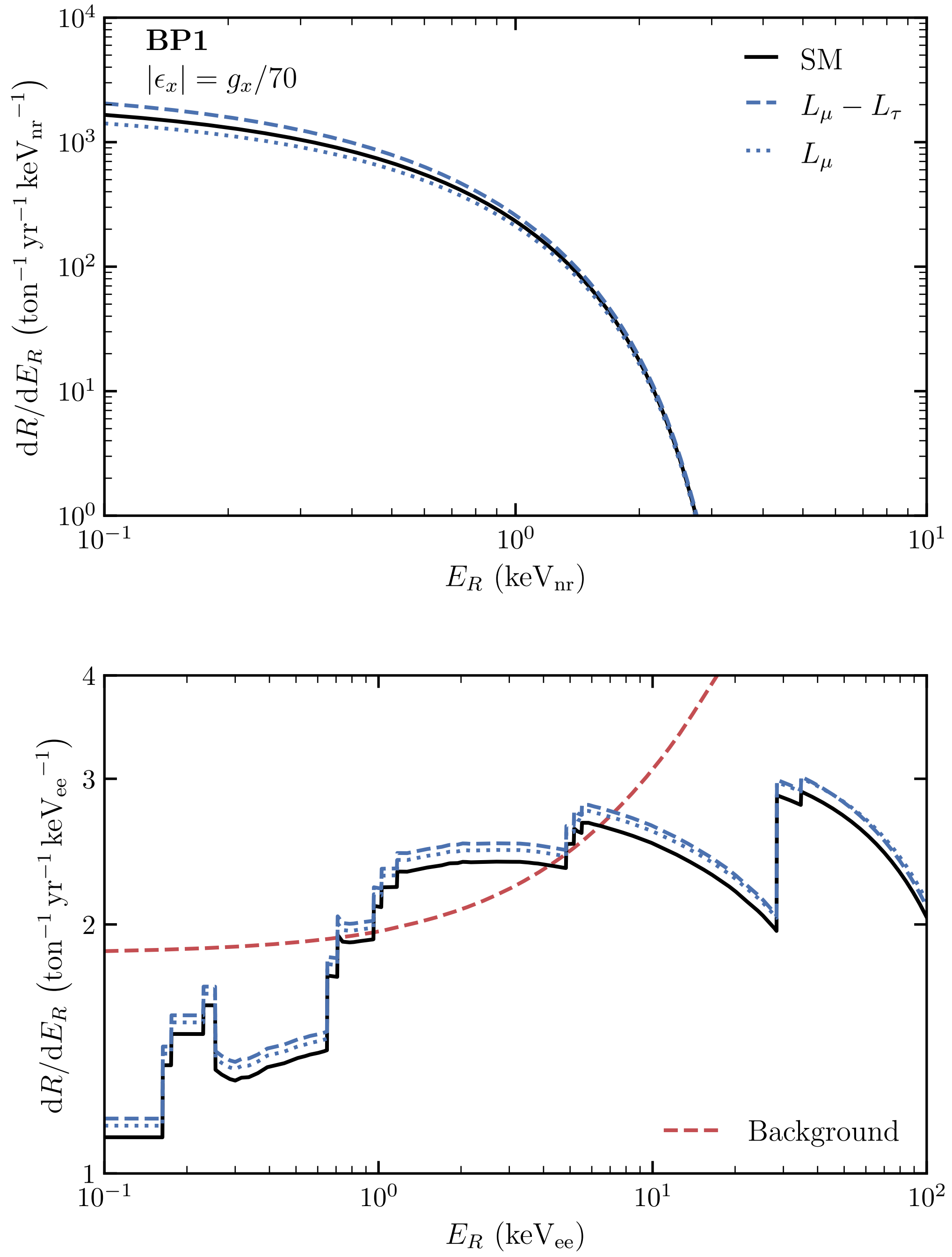

Figure 6.9: The differential rate spectra for CEνNS (top) and EνES (bottom). Rates are shown under the SM (solid black) and BP1 realisations of a $U(1)_{L_\mu - L_\tau}$ (dashed blue) and a $U(1)_{L_\mu}$ (dotted blue) model. For the latter, the maximally degenerate scenario of a kinetic mixing value equal to that of the $U(1)_{L_\mu - L_\tau}$ model has been taken, $|\epsilon_x| = g_x/70$. In the ER case, the expected background from DARWIN is also shown (red), exhibiting an upward curve where the double-β decay of ^{136}Xe begins to dominate.

as our ER thresholds always lie above this energy, this ultimately has no impact on the calculated number of events.

Discovering a $U(1)_{L_\mu - L_\tau}$ Hidden Photon

Ultimately, the most exciting prospect for DD experiments is the possibility of making an outright discovery of a $U(1)_{L_\mu - L_\tau}$ hidden photon. This constitutes satisfying two criteria: making a 5σ observation of the $U(1)_{L_\mu - L_\tau}$ signal and disentangling this from a competing $U(1)_{L_\mu}$ explanation. As we have discussed, the latter of these is satisfied by considering the NR signal, which will be affected in opposite ways by these two models. Thus, all that is left is to explore how we can satisfy the former condition.

For full generality, we study the requirements to make a 5σ discovery for all three of our analyses, considering the NR-only, ER-only, and combined NR + ER signals. As both the exposures and energy thresholds of these experiments are key quantities in determining how well the new physics effect of a new light vector mediator might be observed, we treat them as free variables, studying the minimal conditions under which a 5σ observation of the $U(1)_{L_\mu - L_\tau}$ signal could be claimed for each BP.

To compute this significance, we construct the (one-tail) p-value

$$p_\mu \equiv \sum_{N \geq N_{\mathrm{obs}}} \frac{(\mu + b)^N e^{-(\mu+b)}}{N!}\,, \tag{6.4.1}$$

where μ is the number of expected signal events, b is the number of expected background events, and N_{obs} is the number of observed counts. We then perform our discovery test by treating as the null hypothesis the SM-only expectation, such that $\mu = 0$. The background-only expectation then consists of the SM CEνNS count plus any counts from additional background components. For a discovery-level significance, the total observed count, N_{obs}, must yield a p_0-value of 2.87×10^{-7}.

In our analysis, we solve for the required threshold-exposure pairs needed to produce such a discovery-level measurement of a $U(1)_{L_\mu - L_\tau}$ for each of our BPs. The number of observed counts is then taken to be the total number of counts expected under a BP, $N(g_x, m_{A'})$, plus any additional background counts. We repeat this analysis for each type of search: NR, ER, and NR + ER. In all cases, we take the maximum of the energy window to be $30\,\mathrm{keV_{ee}}$ ($\approx 13\,\mathrm{keV_{nr}}$), where the double-$\beta$ decay of ^{136}Xe is expected to dominate over the solar neutrino signal [214], as can be seen from Fig. 6.9.

When lowering the energy threshold of an experiment, we model what a potential efficiency function might look like should the experiment be able to reach this lower threshold. To do this, we assume that the nominal efficiency function would evolve via a stretch in log-space, with the new, lower threshold placed where this extended function reaches 50%. When doing this, we are careful not to allow the experimental resolutions to increase to arbitrarily large values at low energies, making a reconstruction of a low-energy threshold unrealistic. To this end, we have capped each resolution function at its value at the original 50% threshold, shifting it linearly. Moreover, to ensure valid energy convolutions of the spectra, which are done in electron-equivalent space, we have taken $0.7\,\mathrm{keV_{nr}}$ as a minimum threshold, corresponding to the lowest energy at which the Lindhard model has been experimentally verified for LXe detectors [207].

We show the results of our analysis in Fig. 6.10 for the case of DARWIN, which will have the greatest chance of making this discovery. Within the red regions, the experimental configurations are insufficient to make an observation with discovery-level significance. However, above the line of any given analysis, the enhanced setup enables it to make a discovery of the BP signal using that particular analysis. We see that the nominal configuration of DARWIN, indicated by stars in the figure, is insufficient for it to claim a discovery for any of the BPs. Instead, DARWIN would have to either increase its exposure, lower its thresholds, or perform a combination of the two. The optimal strategy for observing the NR signal is to decrease the threshold, whereas to detect the ER signal we would ‘only’ need either a longer runtime or a larger fiducial mass.

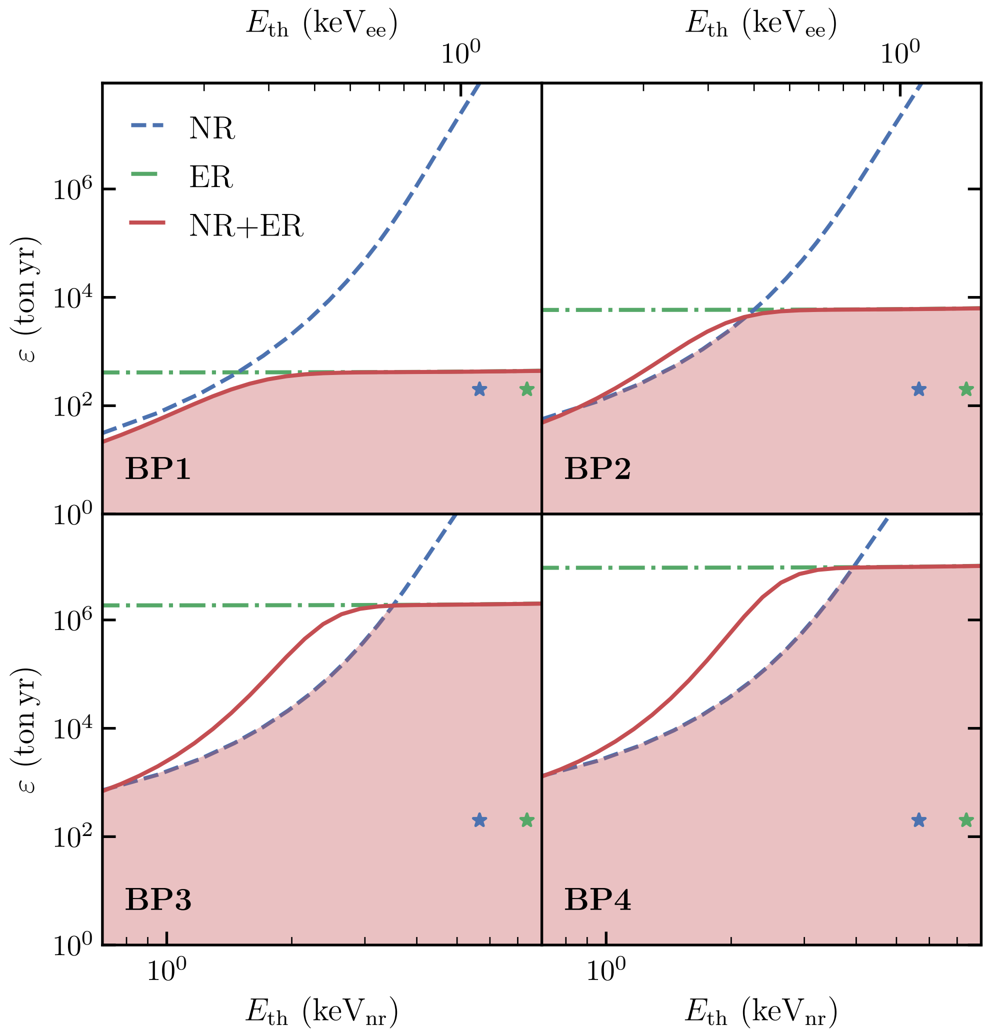

Figure 6.10: The configurations required by DARWIN to make a 5σ discovery of a $U(1)_{L_\mu - L_\tau}$ hidden photon. Above any line, which reflects each of our NR (blue), ER (green), or NR + ER (red) analyses, a 5σ discovery can be made. The stars represent the nominal NR (blue) and ER (green) configurations.

The most efficient strategy, however, would be to focus on making a discovery with NRs, as this will simultaneously give us the discriminatory power we need to distinguish a $U(1)_{L_\mu - L_\tau}$ from a $U(1)_{L_\mu}$ gauge boson. While the scenarios with BP3 and BP4 are difficult to motivate, for BP1 and BP2 we would need to lower the threshold to $\sim 1\,\mathrm{keV_{nr}}$ while retaining NR/ER discrimination. This threshold has previously been reached by LUX, who demonstrated NR calibration for energies down to $1\,\mathrm{keV_{nr}}$; however, this was by sacrificing the majority of the signal (the efficiency function dropped to 0.3% by this energy). Nonetheless, given that DARWIN is a far-future experiment, we make the optimistic assumption that such a threshold could be reached at 50% efficiency, either through the advent of more sensitive instruments or new analysis techniques. We hope that the DARWIN collaboration considers this strategy as part of its mission to explore new physics in the neutrino sector [16], motivating it to push for this lower energy threshold.

We note that, while we conducted this NR-only analysis in Ref. [2], we could have more realistically achieved the same goal by considering the combined NR + ER analysis. Since from Fig. 6.10 a discovery with this analysis can be made at a similar threshold energy of $E_R \approx 1\,\mathrm{keV_{nr}}$, and as S2-only analyses (foregoing the NR/ER discrimination) have been conducted at thresholds as low as $0.7\,\mathrm{keV_{nr}}$ [412], this combined approach is more feasible. In the parameter reconstructions that follow, we can equally well interpret the reconstruction regions as arising from an NR + ER analysis, accompanied by a slight increase in their sizes due to the additional ER background. Furthermore, since the NR signal dominates this combined analysis at this lower threshold, the same excess versus deficit discriminating feature in the $U(1)_{L_\mu - L_\tau}$ and $U(1)_{L_\mu}$ models would be seen when employing this approach.

We show the discovery lines for LZ and XENONnT in Figs. 6.11 and 6.12, respectively. Their case appears bleaker. For all analyses, a discovery seems to be unachievable given their present experimental configurations; one would have to both increase exposures by orders of magnitude and decrease energy thresholds. We show them merely for the sake of completeness and instead focus on the potential

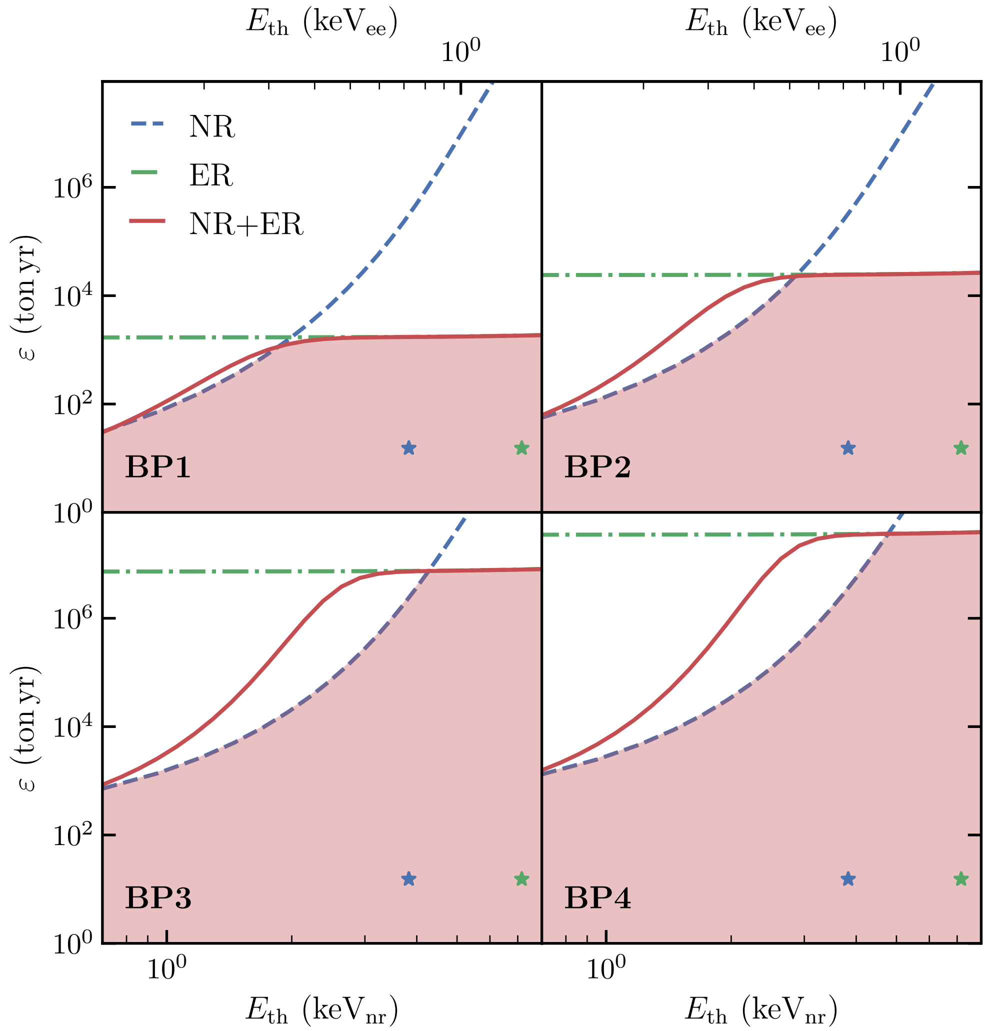

Figure 6.11: The same as in Fig. 6.10 but for LZ.

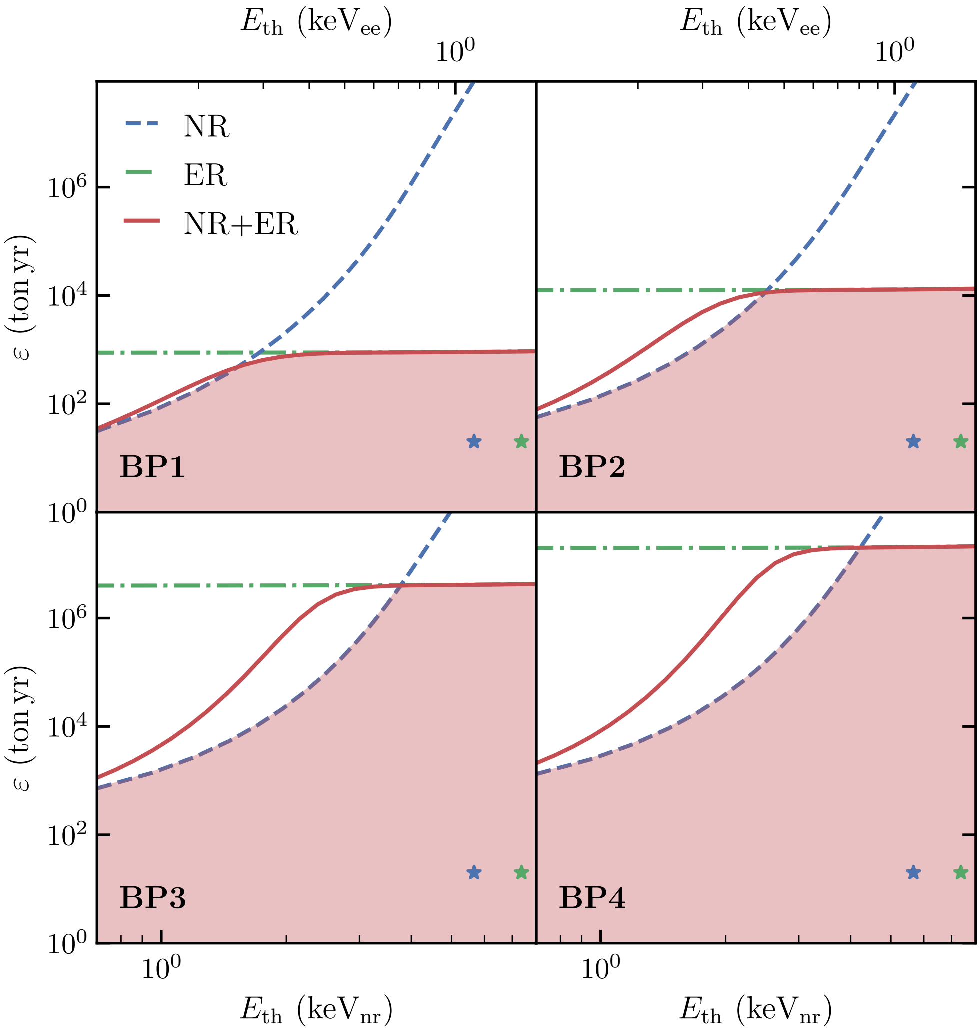

Figure 6.12: The same as in Fig. 6.10 but for XENONnT.

of DARWIN to observe the $U(1)_{L_\mu-L_\tau}$ signal.

Reconstructing the $U(1)_{L_\mu-L_\tau}$ Solution to $(g-2)_\mu$

Following our above conclusions, we complete our DD analysis by considering a hypothetical DARWIN-like experiment with an optimised $1\,\mathrm{keV_{nr}}$ threshold to perform a final set of parameter reconstructions. We show the results of the DD-only reconstruction in Fig. 6.13, where we see that BP1 and BP2 are confidently observed with this configuration. On the other hand, BP3 and BP4 are not observed, and only upper bounds can be drawn for these higher-mass realisations of a $U(1)_{L_\mu-L_\tau}$. As we noted in Section 6.1.3, reconstructions with a $U(1)_{L_\mu}$ are possible; however, they occur at very high, strongly excluded values of g_μ, where the positive BSM-only term dominates. Thus, only the reconstruction with the $U(1)_{L_\mu-L_\tau}$ yields regions that are not in tension with already existing bounds, giving us the ultimate discriminator between the $U(1)_{L_\mu-L_\tau}$ and $U(1)_{L_\mu}$ models.

6.5 The Complete Strategy

The full power of our experimental strategy becomes readily apparent when we combine the reconstructions from all of our analyses. We show the confidence regions attained with NA64μ, SS experiments, and our optimised DARWIN-like experiment in Fig. 6.14 when interpreted in terms of a $U(1)_{L_\mu-L_\tau}$ model. We see that a 5σ discovery by DARWIN gives regions that, when combined with data from both NA64μ and SS experiment, considerably narrow down the area compatible with $(g-2)_\mu$, reducing the uncertainty in both the gauge coupling and the mediator mass.

For BP3 and BP4, neither DD nor SS experiments will have enough sensitivity to claim a detection. Nonetheless, the ensuing limits can further constrain the parameter space. Like the bounds placed by SS experiments, those placed by DARWIN will be able to reduce the allowed mediator masses reconstructed by NA64μ.

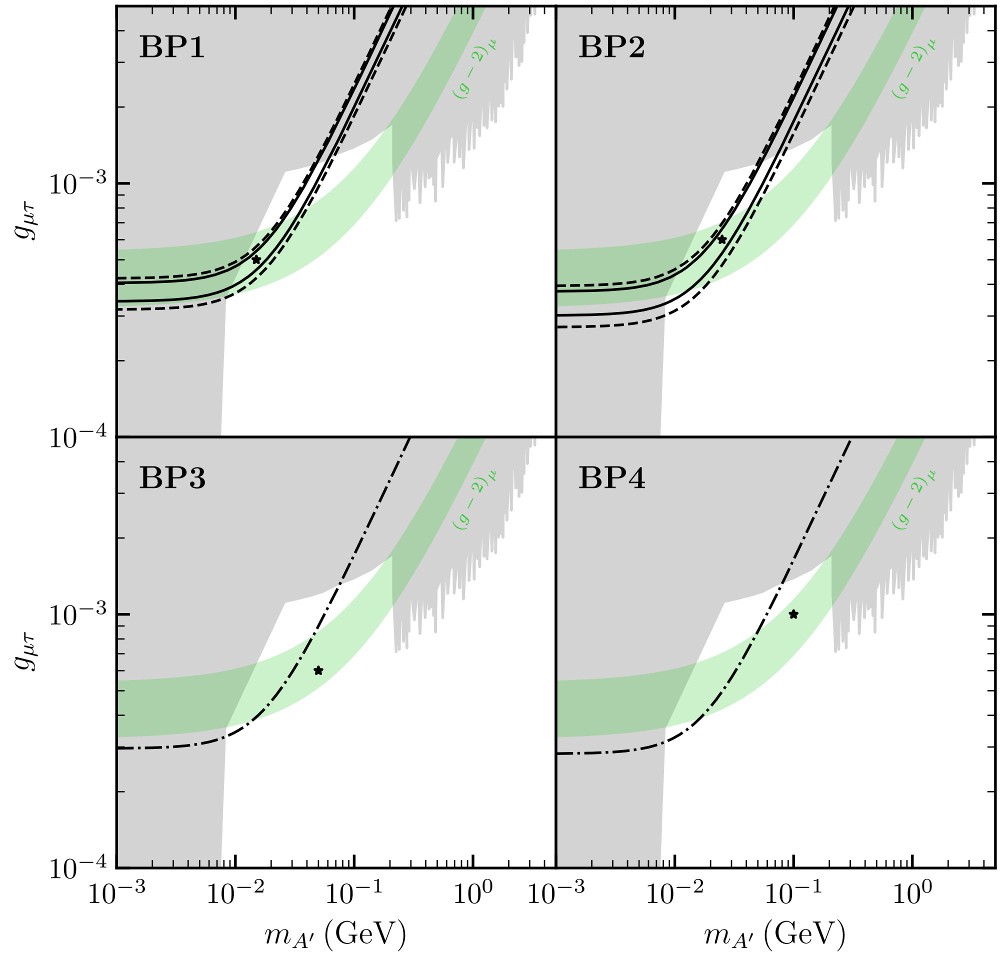

Figure 6.13: Parameter reconstructions for each of our $U(1)_{L_\mu - L_\tau}$ BPs using an enhanced, 1 keV$_{\mathrm{nr}}$ threshold-energy version of DARWIN. The solid (dashed) contours represent the boundaries of the 1σ (2σ) confidence regions. The black stars represent the BPs. The $(g-2)_\mu$ 2σ preferred region is shown in green.

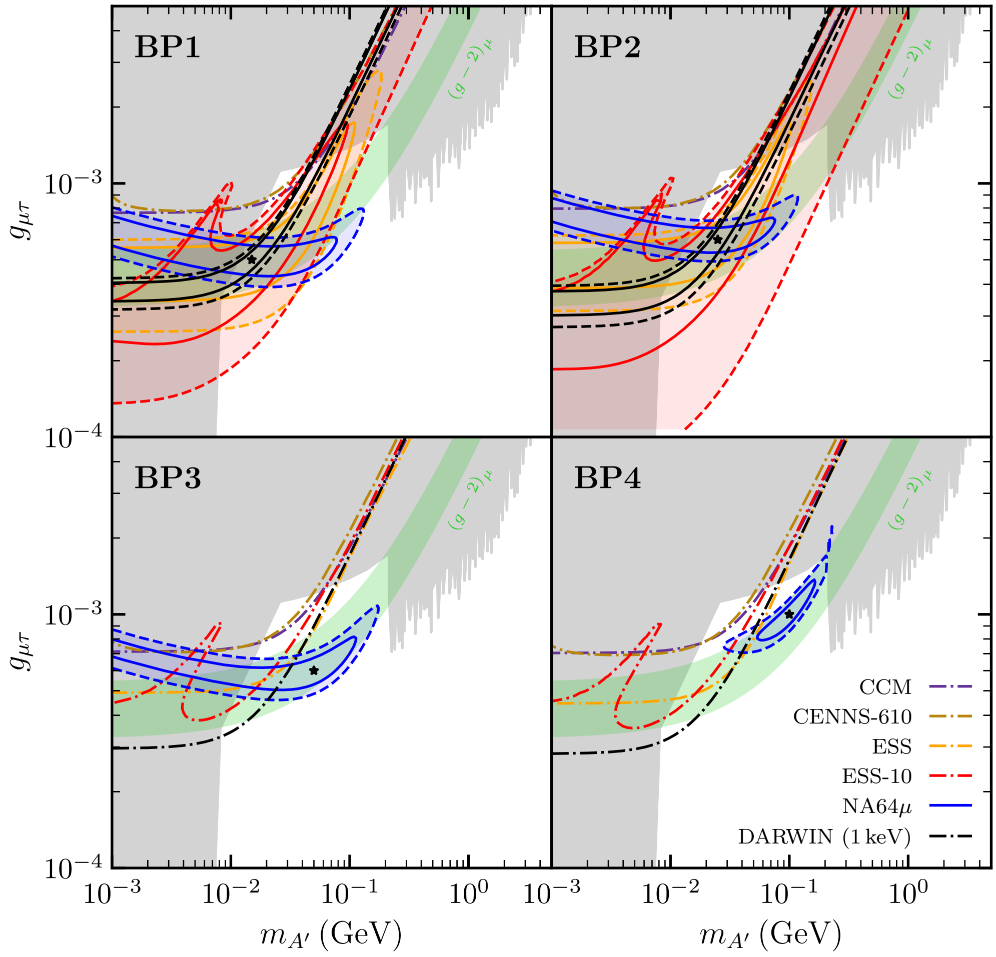

Figure 6.14: Parameter reconstructions for each of our $U(1)_{L_\mu - L_\tau}$ BPs using all of our considered experiments. The solid (dashed) contours represent the boundaries of the 1σ (2σ) confidence regions. The black stars represent the BPs. The $(g-2)_\mu$ 2σ preferred region is shown in green.

CHAPTER 7

Neutrino NSIs at Direct Detection Experiments

In the previous two chapters, we learned that near- and far-future DD experiments will be powerful probes of light new physics in the neutrino sector. We saw this in the context of the $U(1)_{L_\mu - L_\tau}$ model—a particularly well-motivated extension to the SM both theoretically and, presently, experimentally. However, this is but one potential avenue for new neutrino physics. If we are to argue that DD experiments will be more generally useful in the search for such new physics, then we must showcase their power in a model-independent way. The framework of neutrino non-standard interactions (NSIs) supplies us with precisely such a means, providing us with an effective description of BSM neutrino interactions. By situating DD and dedicated neutrino experiments alongside one another within this broader BSM landscape, we will make our final case for why future DD experiments are set to play key roles in the search for new neutrino physics.

In this chapter, we will present work based on Ref. [3], where we introduce an extended parametrisation for neutrino NSIs and use it to explore the bounds that DD experiments can place in this more general landscape of new physics. We will first discuss the typical NSI framework used in global NSI analyses to parametrise these interactions, which ignores any potential non-standard behaviour with the electron. We will then introduce our novel framework, reinstating this particular component. Using this new parametrisation and data from the CENNS-10 LAr experiment, we will explore how limits placed on neutrino NSIs are sensitive to the assumption one makes on the strength of the new interaction with the electron direction. Finally, we will explore the limits that future multi-ton LXe DD experiments can place in this extended parameter space, situating their results in the context of those achieved by dedicated neutrino experiments.

7.1 The Proton-Neutron NSI Formalism

We introduced the basics of the NSI formalism in Section 4.2.5, where we laid out the framework in terms of the NSI parameters $\varepsilon_{\alpha\beta}^{fP}$; we refer the reader to this section for further details. However, if we assume that the flavour-structure of these parameters can be factorised from the fermion-specific nature of the interaction, then we can write these parameters as [24]

$$\varepsilon_{\alpha\beta}^{fP} \equiv \varepsilon_{\alpha\beta}^{\eta} \xi^{fP} \, . \tag{7.1.1}$$

Here, $\varepsilon_{\alpha\beta}^{\eta}$ describes the neutrino-specific part of the interaction, and ξ^{fP} is a projection onto the interacting fermion. Since only vector-like interactions contribute to neutrino propagation effects, we will only focus on this type of interaction. In this case, we can further define

$$\varepsilon_{\alpha\beta}^{f} \equiv \varepsilon_{\alpha\beta}^{\eta} \xi^{f} \, , \tag{7.1.2}$$

where $\xi^f \equiv \xi^{fL} + \xi^{fR}$. This separates the relation we initially had in Eq. (4.2.18) into neutrino-only and fermion-only parts, allowing us to explore the phenomenology of these two components separately.

As we did in Section 4.2.5, we can restrict our NSIs to take place only with the first-generation fermions. This enables us to define the angle η, which controls how much of the new interaction takes place with the proton and the neutron. Defining the up- and down-quark projectors as [138]

$$\xi^u = \frac{\sqrt{5}}{3}\left(2\cos\eta - \sin\eta\right) \qquad \text{and} \qquad \xi^d = \frac{\sqrt{5}}{3}\left(2\sin\eta - \cos\eta\right) , \tag{7.1.3}$$

we can use Eq. (4.2.19) to write

$$\xi^p = \sqrt{5}\cos\eta \qquad \text{and} \qquad \xi^n = \sqrt{5}\sin\eta\,. \tag{7.1.4}$$

Note the normalisation of these parameters, which makes for an up-quark NSI of 1 when the down-quark NSI is chosen to be 0 (and vice versa). In this framework, a value of $\eta = 0$ corresponds to a pure QED-like interaction that only couples to the electric charge. Restricting this angle to lie in the range $\eta \in [-\pi/2, \pi/2]$, we must allow for positive and negative values of $\varepsilon^{\eta}_{\alpha\beta}$ to ensure we can have positive and negative values of the proton NSI.

In this parametrisation, pioneered by Ref. [24], we see that NSIs with the electron are ignored. This is because their work focused on setting NSI bounds with oscillation experiments. As we saw in Eq. (4.2.20), non-standard matter effects enter the matter Hamiltonian via a contribution from the neutron and an overall charged contribution from both the proton and the electron. This means that, phenomenologically, the same non-standard behaviour can be elicited from either a proton or an electron contribution, as well as some appropriate combination of the two. Since NSIs with the electron can also impact the EνES cross section, it reduces the complexity of the problem to consider this charged contribution to only arise in the proton. This allows one to explore the bounds that oscillation experiments can set without considering non-standard changes to the expected EνES rate.

However, this makes for a non-general treatment. Since we have no reason to believe that ‘charged’ neutrino NSIs should only take place with the proton, we should allow for the possibility that this contribution is instead divided between both the proton and the electron. While such a decomposition can be designed to not impact neutrino oscillations, allowing for electron NSIs can instead lead to changes in the EνES cross section. This, in turn, can impact the bounds set by oscillation experiments, which could instead be dominated by NSI effects at the detection point [138]. Indeed, we presented precisely such an argument in Section 5.2.2 in the context of the $U(1)_{L_\mu - L_\tau}$, which affects the EνES rate without introducing non-standard oscillation effects.

Furthermore, if one wishes to add bounds from CEνNS experiments, as was done in Refs. [24, 25], then one must be careful to stipulate that the predicted effects can be maximal within this framework. This is because, for a given η, one always assumes that the NSI is in the proton-neutron plane. If the charged NSI contribution had instead been assumed to be only along the electron direction, then the corresponding non-standard CEνNS effect would only arise from the neutron, generally weakening the expected effect[1]. Thus, a framework that includes the electron is imperative to set general bounds on neutrino NSIs. Such a framework is also crucial for DD experiments since they can probe both CEνNS and EνES interactions at once.

7.2 A New Framework: Reinstating the Electron

We extend the parametrisation of Ref. [24] by re-introducing neutrino NSIs with the electron. We do this by including a second angle, φ, dictating how much of the total charged NSI takes place with either the proton or the electron. Concretely, we define the three fermion directions

$$\begin{aligned}
\xi^p &= \sqrt{5}\cos\eta\cos\varphi\,, \\
\xi^e &= \sqrt{5}\cos\eta\sin\varphi\,, \qquad (7.2.1)\\
\xi^n &= \sqrt{5}\sin\eta\,,
\end{aligned}$$

and we re-define the flavour-structure coefficient to be $\varepsilon^{\eta}_{\alpha\beta} \to \varepsilon^{\eta,\varphi}_{\alpha\beta}$, where $\varepsilon^{\eta}_{\alpha\beta} \equiv \varepsilon^{\eta,0}_{\alpha\beta}$.

We visualise our parametrisation in Fig. 7.1, where we show a generic NSI vector,

---

[1] Of course, it is possible that the electron NSI can be strong enough to cause appreciable EνES in CEνNS experiments, allowing them to place bounds on the electron NSI [429].

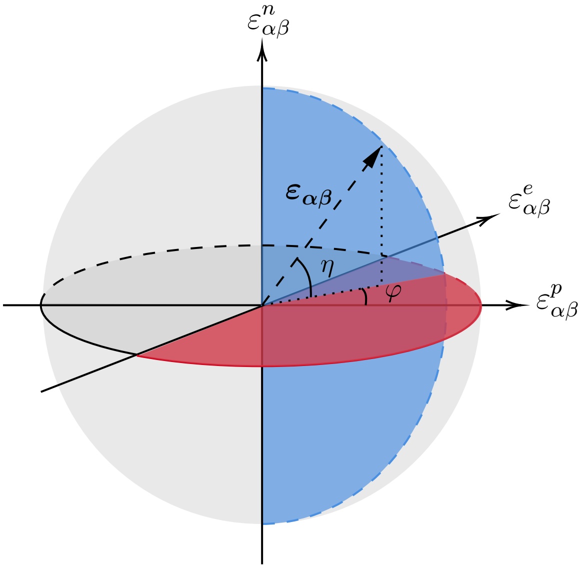

Figure 7.1: The novel NSI parametrisation we propose. A given NSI is defined by a radial component, $\sqrt{5}\varepsilon^{\eta,\varphi}_{\alpha\beta}$ (which can be either positive or negative), an angle between the charged $(\varepsilon^p_{\alpha\beta}, \varepsilon^e_{\alpha\beta})$-plane and the neutron direction, η, and the new angle φ, which defines the NSI direction along either the proton or the electron direction. The domains of these angles are η, $\varphi \in [-\pi/2, \pi/2]$, as visualised by the blue and red half-discs, respectively.

$\boldsymbol{\varepsilon_{\alpha\beta}}$, embedded in our three-dimensional space with coordinates $(\varepsilon^p_{\alpha\beta}, \varepsilon^e_{\alpha\beta}, \varepsilon^n_{\alpha\beta})$. The angle η now controls the direction of the NSI vector with respect to the $(\varepsilon^p_{\alpha\beta}, \varepsilon^e_{\alpha\beta})$-plane and the neutron direction. The novel angle φ dictates the nature of the charged contribution, with $\varphi = 0$ corresponding to a (positive) proton-only contribution (recovering the above formalism) and $\varphi = \pi/2$ to a (positive) electron-only contribution. To match our notation with that of Ref. [24], we allow for both positive and negative values of $\varepsilon^{\eta,\varphi}_{\alpha\beta}$, requiring us to restrict our angles to the ranges $\eta, \varphi \in [-\pi/2, \pi/2]$.

We can re-write the elements of the NSI matter Hamiltonian, given in Eq. (4.2.20), in terms of our novel parametrisation as

$$\mathcal{E}_{\alpha\beta}(x) = \varepsilon^{\eta,\varphi}_{\alpha\beta}\left[(\xi^p + \xi^e) + Y_n(x)\xi^n\right] . \tag{7.2.2}$$

This allows us to retain the electron contribution to the non-standard propagation effects, which can also affect the EνES cross section. The full NSI matter

Hamiltonian of Eq. (4.2.16), once rotated to the solar neutrino basis we introduced in Section 2.4.5, then reads [24]

$$\tilde{\mathcal{H}}^{\text{eff}}_{\text{matter}} \equiv \sqrt{2} G_F N_e(x) \left[\begin{pmatrix} c_{13}^2 & 0 \\ 0 & 0 \end{pmatrix} + \left[(\xi^p + \xi^n) + Y_n(x) \xi^n \right] \begin{pmatrix} -\varepsilon_D^{\eta,\varphi} & \varepsilon_N^{\eta,\varphi} \\ \varepsilon_N^{\eta,\varphi *} & \varepsilon_D^{\eta,\varphi} \end{pmatrix} \right] , \tag{7.2.3}$$

where the coefficients $\varepsilon_N^{\eta,\varphi}$ and $\varepsilon_D^{\eta,\varphi}$ are related to our parametrisation via

$$\begin{aligned} \varepsilon_D^{\eta,\varphi} \equiv & \, c_{13} s_{13} \operatorname{Re}\left(s_{23} \varepsilon_{e\mu}^{\eta,\varphi} + c_{23} \varepsilon_{e\tau}^{\eta,\varphi} \right) - \left(1 + s_{13}^2 \right) c_{23} s_{23} \operatorname{Re}\left(\varepsilon_{\mu\tau}^{\eta,\varphi} \right) \\ & - \frac{c_{13}^2}{2} \left(\varepsilon_{ee}^{\eta,\varphi} - \varepsilon_{\mu\mu}^{\eta,\varphi} \right) + \frac{s_{23}^2 - s_{13}^2 c_{23}^2}{2} \left(\varepsilon_{\tau\tau}^{\eta,\varphi} - \varepsilon_{\mu\mu}^{\eta,\varphi} \right) \end{aligned} \tag{7.2.4}$$

and

$$\varepsilon_N^{\eta,\varphi} \equiv c_{13} \left(c_{23} \varepsilon_{e\mu}^{\eta,\varphi} - s_{23} \varepsilon_{e\tau}^{\eta,\varphi} \right) + s_{13} \left[s_{23}^2 \varepsilon_{\mu\tau}^{\eta,\varphi} - c_{23}^2 \varepsilon_{\mu\tau}^{\eta,\varphi *} + c_{23} s_{23} \left(\varepsilon_{\tau\tau}^{\eta,\varphi} - \varepsilon_{\mu\mu}^{\eta,\varphi} \right) \right] . \tag{7.2.5}$$

To perform this rotation, we note that we require both that $\Delta m_{31}^2 \gg \Delta m_{21}^2 \sim A_{\text{cc}}$, as in Section 2.4.5, and that $\Delta m_{31}^2 \gg G_F E_\nu \sum_f N_f(x) \varepsilon_{\alpha\beta}^f$. This ensures that the more complicated three-neutrino problem can be reduced to the simpler two-neutrino picture, whereby the third mass eigenstate propagates freely without mixing with the remaining two. For the NSI parameters we consider in this work, we have checked that these conditions hold. Throughout this chapter, we will take $\delta_{\text{CP}} = 0$, as in Ref. [24, 25] so that we only need to consider real-valued NSI parameters in Eqs. (7.2.4) and (7.2.5).

Diagonalising the effective Hamiltonian of Eq. (7.2.3), we arrive at almost identical relations to those we found in Section 2.4.4. The only changes we must make are to p and q parameters we introduced in Eq. (2.4.29). Allowing for non-standard interactions, they become

$$\begin{aligned} p &= \sin 2\theta_{12} + 2\, \xi(x)\, \varepsilon_N^{\eta,\varphi} \frac{A_{\text{CC}}(x)}{\Delta m_{21}^2} , \\ q &= \cos 2\theta_{12} + \left[2\, \xi(x)\, \varepsilon_D^{\eta,\varphi} - c_{13}^2 \right] \frac{A_{\text{CC}}(x)}{\Delta m_{21}^2} , \end{aligned} \tag{7.2.6}$$

where we have defined $\xi(x) \equiv \xi^p + \xi^e + Y_n(x) \xi^n$. We therefore see that the effect of NSIs on neutrino propagation is to shift these two parameters, effectively changing where the MSW resonance occurs in the Sun. We emphasize that the novelty in our parametrisation arises from retaining the electron projector, ξ^e, with all results thus far being equivalent to those of Ref. [24] when setting $\xi^e \equiv 0$.

As the quantities p and q also impact the adiabaticity parameter, Eq. (2.4.36), we must be careful to quantify how non-standard interactions propagate to its calculation. Using Eqs. (2.4.30) and (2.4.31), we can write this parameter as

$$\gamma = \left(\frac{|p^2 + q^2|^{3/2}}{|\dot{p}q - p\dot{q}|} \right) \frac{\Delta m_{21}^2}{2E_\nu} \, . \tag{7.2.7}$$

Then, for any given value of the NSI parameters, we can evaluate γ at the point of maximum violation of adiabaticity to test the adiabaticity condition that $\gamma \gg 1$. Since this point is, in general, different from the resonance point [430, 431], we evaluate Eq. (7.2.7) over the entire solar radius for the maximum energy neutrinos, checking that this condition holds for the maximum calculated γ value. When we come to explore the limits that DD experiments can set in the NSI landscape in Section 7.4, we check whether the adiabatic approximation is valid using this approach.

To illustrate how neutrino NSIs can impact neutrino oscillations, we show the oscillation probabilities for ^{8}B neutrinos in two non-standard cases in Fig. 7.2. Both of these cases have been calculated assuming $\varepsilon_{\alpha\beta}^{\eta,\varphi} = 0.1$ and equal contributions from the proton, neutron, and electron—that is, $\eta = \varphi = \pi/4$. They have been computed assuming either a flavour-conserving electron NSI or a flavour-conserving muon NSI ($\varepsilon_{\alpha\beta}^{\eta,\varphi} = 0.1\delta_{ee}$ and $\varepsilon_{\alpha\beta}^{\eta,\varphi} = 0.1\delta_{\mu\mu}$, respectively). Compared to the SM probabilities, first depicted in Fig. 2.9, we see that the former case results in stronger matter effects, while the latter leads to weaker effects.

We note that the CEνNS and EνES cross sections within the NSI framework, respectively given by Eqs. (4.2.26) and (4.2.28), can be re-written within this new framework. This can be done via suitable substitutions for $\varepsilon_{\alpha\beta}^p$, $\varepsilon_{\alpha\beta}^n$, and $\varepsilon_{\alpha\beta}^e$. In what follows, we will refer to these cross sections in terms of our framework. We note that the results of our implementation are in good agreement with those of

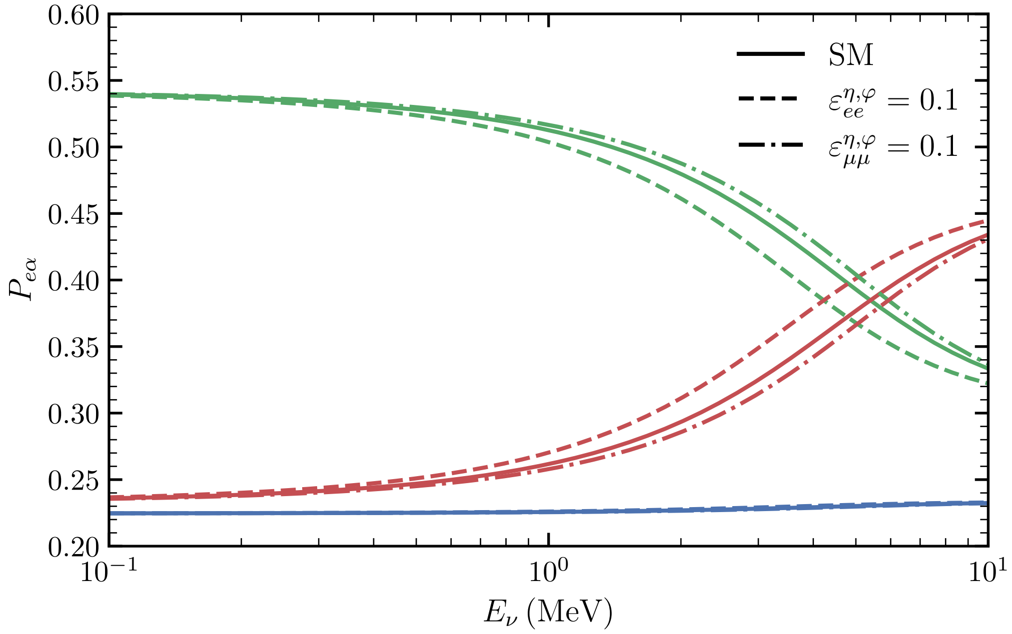

Figure 7.2: The effect of neutrino NSIs on the ^{8}B electron neutrino survival (green) and transition (blue for $\alpha = \mu$ and red for $\alpha = \tau$) probabilities. Shown are the SM probabilities (solid) and two example sets of non-standard probabilities, both of which assume equal non-standard contributions from the proton, neutron, and electron ($\eta = \varphi = \pi/4$). These are new flavour-conserving interactions, which take place with either the electron with $\varepsilon_{ee}^{\eta,\varphi} = 0.1$ (dashed) or the muon with $\varepsilon_{\mu\mu}^{\eta,\varphi} = 0.1$ (dash-dotted).

other works [178, 432].

7.3 CEνNS Constraints

To illustrate how different assumptions for the NSI contribution from the electron can lead to a non-trivial effect on the derived NSI bounds, we consider the results from the CENNS-10 LAr experiment [8]. Indeed, we considered this experiment in Section 5.1.2, and we treat it identically here. The experimental details are contained therein for reference.

As in Section 5.1.2, we consider deviations from the total number of measured events at the CENNS-10 LAr experiment. We use the same χ^2 statistic as in

Eq. (5.1.7), only the expected number of CEνNS events is now parametrised as $N_{\mathrm{CE}\nu\mathrm{NS}} \equiv N_{\mathrm{CE}\nu\mathrm{NS}}(\varepsilon^{\eta,\varphi}_{\alpha\beta},\, \eta,\, \varphi)$, reflecting our novel NSI parametrisation. The theoretical count rate is given by Eq. (5.1.4), with the CEνNS cross section under the NSI framework given by Eq. (4.2.26).

Since the neutrino beam at SS experiments does not undergo significant decoherence over the experimental baseline, it can be treated as being composed of independent ν_e, ν_μ, and $\overline{nu}_\mu$ parts. As we argued at the end of Section 4.2.5, this means that we can simply take the overlap of the appropriately flavoured flux and cross section. The result is that the cross section that we must consider in Eq. (5.1.4) is simply

$$\frac{\mathrm{d}\sigma^{\alpha}_{\nu N}}{\mathrm{d}E_R} = \left(\frac{\mathrm{d}\sigma_{\nu N}}{\mathrm{d}E_R}\right)_{\alpha\alpha}, \tag{7.3.1}$$

with $(\mathrm{d}\sigma_{\nu N}/\mathrm{d}E_R)_{\alpha\alpha}$ given by Eq. (4.2.26) and where $\alpha \in \{e, \mu, \overline{\mu}\}$.

Following the analysis of Ref. [323], we perform our statistical analysis by varying one NSI parameter at a time. However, unlike their study, we compute the bounds on these parameters under different assumptions for the electron contribution, varying φ over its full range. We fix $\eta = \tan^{-1}(1/2)$, corresponding to a pure up-quark NSI when $\varphi = 0$.

To demonstrate how φ can affect the NSI parameter bounds, we show the χ^2 function as a function of φ in Fig. 7.3 for the usual assumption of $\varphi = 0$ and an extreme case of $\varphi = \pi/2$. The black, dashed line highlights the point at which $\Delta\chi^2 = 2.71$: the 1 d.o.f. 90% CL value. Since we keep η fixed and treat φ as a fixed assumption, the only d.o.f. in the fit is the NSI parameter. We see that, for every $\varepsilon^{\eta,\varphi}_{\alpha\beta}$, there is a weakening of the constraints. This is because a non-zero φ leads to a weaker contribution to the non-standard CEνNS signal from the proton, with that of the neutron remaining the same (since η is fixed). For the same reason, the locations of the minima shift to higher values of $|\varepsilon^{\eta,\varphi}_{\alpha\beta}|$. As a muon beam SS experiment, CENNS-10 has no sensitivity to $\varepsilon^{\eta,\varphi}_{\tau\tau}$ since there is not an appreciable component of tau neutrinos.

Note that there are two χ^2 minima for all flavours. This is due to the fact that the CENNS-10 LAr experiment measured a slight excess in the number of total counts, resulting in preferable fits to models that can reproduce this. In the case of neutrino NSIs, this can be achieved in different ways depending on whether we have diagonal or non-diagonal NSI parameters and can be seen by examining the form of the CEνNS cross section in Eq. (4.2.26). For non-diagonal NSIs, any positive or negative shift from $\varepsilon_{\alpha\beta}^{\eta,\varphi} = 0$ produces an excess, as these parameters enter the flavour-conserving cross section of Eq. (7.3.1) quadratically. However, since the SM result is not in tension with the observation, we cannot place bounds on the two minima individually. For the flavour-diagonal parameters, the additional interference term leads to greater changes to the CEνNS cross section for non-zero values of $\varepsilon_{\alpha\alpha}^{\eta,\varphi}$. Thus, we can place bounds on them these minima since parameter values intermediate to them lead to more appreciably different counts.

We repeat this analysis for the full range of values of φ, drawing the 90% CL bound in φ-space in Fig. 7.4. The bound that would usually be quoted corresponds to the intersection of each of the red regions with the $\varphi = 0$ line. However, we see that this bound evolves in a non-trivial way for non-zero φ, generally worsening for increasing $|\varphi|$ up to $|\varphi| = \pi/2$. While this trend is partially led by our parametrisation—whereby the strength of the $\varepsilon_{\alpha\beta}^{\eta,\varphi}$ should scale as $(1/\cos\varphi)$ for a constant contribution in any one of the proton, neutron, and electron directions—we see that the bounds do not all evolve via the same scaling. This is particularly true for the bounds drawn for the second minima in the cases of $\varepsilon_{ee}^{\eta,\varphi}$ and $\varepsilon_{\mu\mu}^{\eta,\varphi}$, both of which scale more dramatically than the first minima bounds. Moreover, the neutron bounds, which are independent of φ, would see a definite increase (for fixed η), reflecting the need for a stronger NSI with the neutron to account for the same effect.

Since we make an assumption on the value of φ and are considering the more general flavour structure of neutrino NSIs, parametrised by $\varepsilon_{\alpha\beta}^{\eta,\varphi}$, we can draw constraints in the electron direction despite not having direct sensitivity to ERs. In effect, the weakened bounds in the proton direction are translated into bounds in the electron direction. Knowledge of φ thus allows us to place limits on electron NSIs with

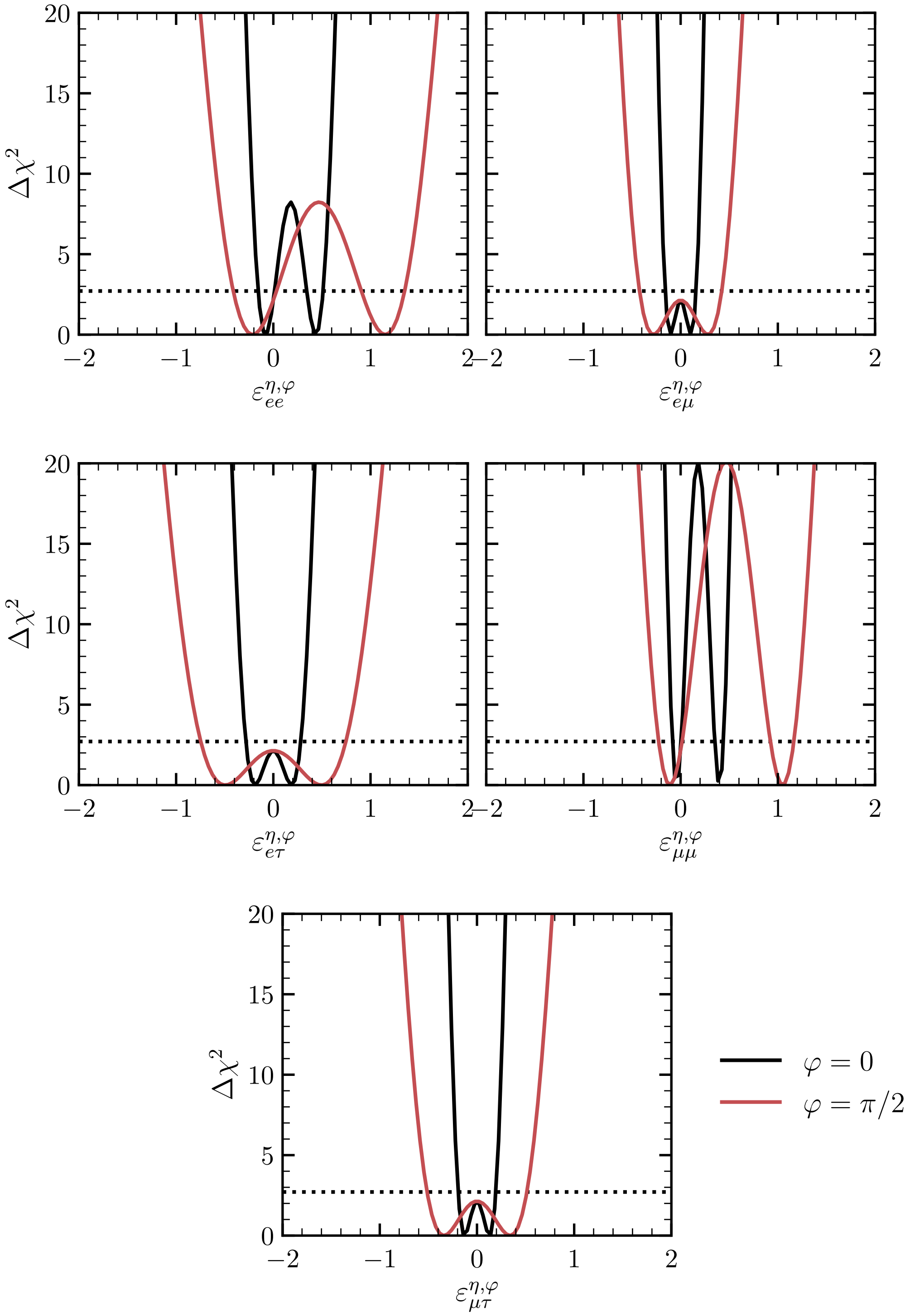

Figure 7.3: The variation in the $\Delta\chi^2$ statistic when altering each NSI parameter in turn under two assumptions for φ. Shown are the resulting statistics under the usual assumption that $\varphi = 0$ (black) and the extreme case that $\varphi = \pi/2$ (red). We have fixed $\eta = \tan^{-1}(1/2)$, corresponding to a pure up-quark NSI in the case that $\varphi = 0$. The dashed line highlights the value of $\Delta\chi^2 = 2.71$: the deviation in a 1 d.o.f. problem required for a 90% CL limit.

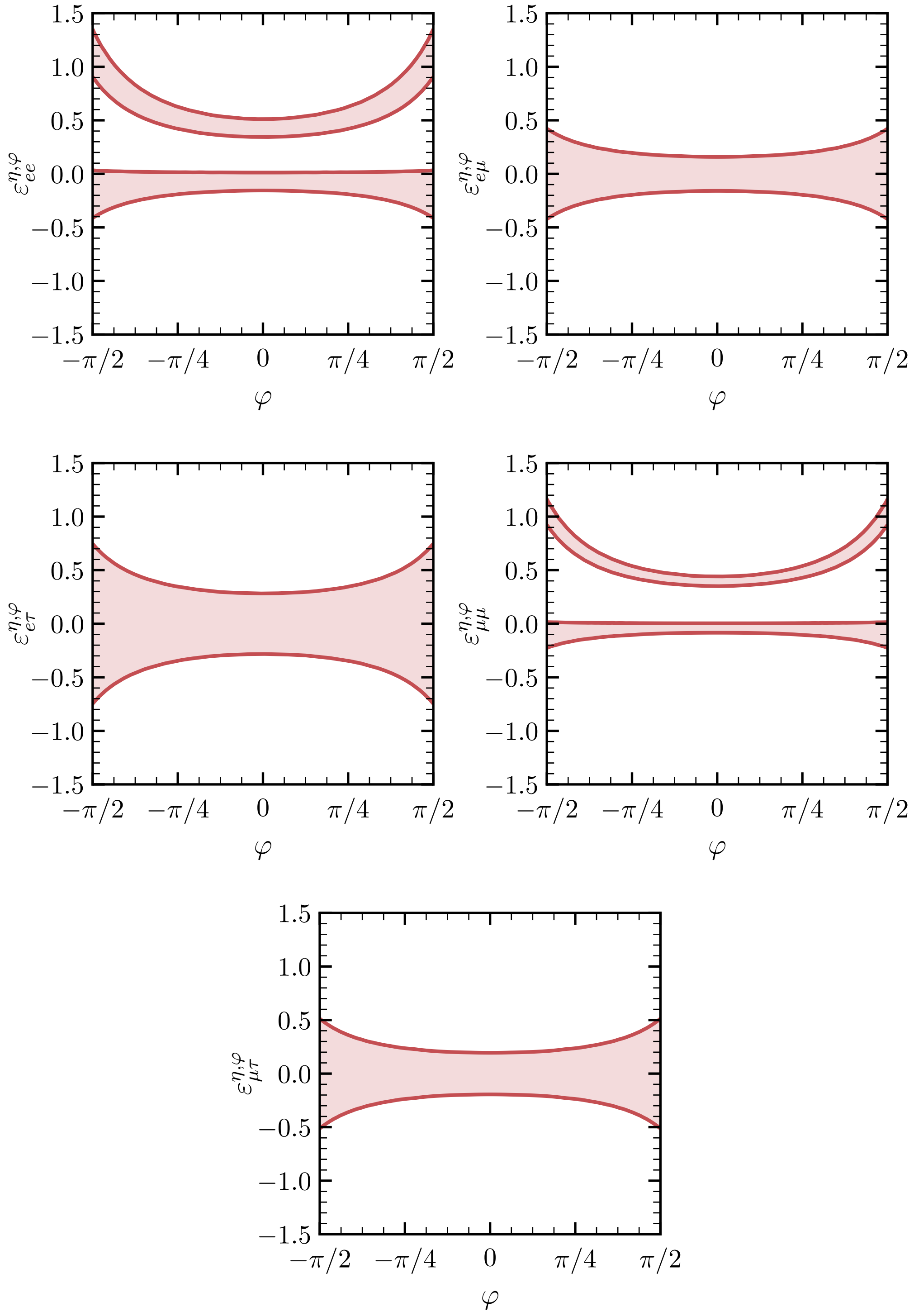

Figure 7.4: The 90% CL allowed regions for each NSI parameter under different assumptions for φ using the CENNS-10 LAr experiment. The bounds usually quoted correspond to the NSI parameter values at $\varphi = 0$.We have fixed $\eta = \tan^{-1}(1/2)$, corresponding to a pure up-quark NSI in the case that $\varphi = 0$.

CEνNS experiments.

Nonetheless, we note that we have only considered the bounds that can be set due to deviations in the CEνNS rate as ERs are typically subdominant to NRs. However, a strong NSI contribution from the electron can lead to ERs that pass NR selection cuts, leading to an additional signal component that can be used to further constrain NSI parameters [429]. A future study could include this ER contribution, causing a more complex evolution of the bounds.

7.4 Probing Neutrino NSIs at DD Experiments

We now turn to exploring the power of DD experiments in constraining the neutrino NSI landscape. As we focused on multi-ton LXe experiments in Section 6.4.2, we will similarly restrict our attention to them here given their success with the $U(1)_{L_\mu - L_\tau}$ model. Indeed, considering the effective NSI space instead of a specific model will situate these experiments in the broader landscape of BSM neutrino physics, providing a more general picture of their potential in this field. Though still ongoing, this final study will highlight the essential point of this thesis.

We note, however, that we are not the first to highlight the utility of DD experiments in probing neutrino NSIs [178, 432]. However, Ref. [432] approached this problem from the angle of the neutrino floor, arguing that non-standard enhancements to the neutrino rate could further exacerbate the search for DM. On the other hand, Ref. [178] did focus on the use of DD experiments in probing neutrino NSIs. However, we improve on their work in several ways. Firstly, we place the sensitivities of DD experiments to NSIs in the broader context of neutrino experiments using the global studies of Refs. [24, 25]. Secondly, we perform a more sophisticated experimental analysis, including efficiency and resolution effects, the impact of the RRPA in xenon [194], and, as we discuss further in Section 7.4.1, the effect of including the systematic uncertainty in the ^{8}B neutrino flux. Thirdly, not only do we allow for our NSIs to lie in directions other than the up- and down-quark directions in the case of our NR results, but, through our novel framework, we also allow for the total charged contribution to be split into electron and proton parts in our ER results. Lastly, we consider the blind spots that DD experiments are subject to in the NSI landscape, highlighting the limits of their constraining power in this parameter space.

To derive our limits, we perform a similar analysis to those of Chapters 5 and 6, constraining NSIs by considering the deviation in the total number of solar neutrino events. As we are only interested in providing motivation to use DD experiments in future global studies, we simplify our computation by varying only one NSI parameter at a time, as has been done in various similar studies of NSIs [26,323,433]. We use the same experimental configurations as those in Chapter 6 for the resolutions, efficiencies, and backgrounds. However, for our NR energy thresholds, we do not take the nominal values controlled by the 50%-efficiency points. Instead, we extend them down to $3\,\mathrm{keV}_{\mathrm{nr}}$, enabling these experiments to observe a greater number of ^{8}B neutrinos and thus more fairly pitting them against dedicated neutrino experiments. This threshold is guided by the NR analysis we performed in Chapter 5 for our G2-Xe experiment (the value of which was motivated by results from the LUX collaboration [410]) as well as a recent ^{8}B-dedicated search conducted by the XENON1T experiment [172]. For our ER analysis, our configuration is identical to that of Section 6.4.2, as the nominal thresholds already give DD experiments an appreciable number of EνES events.

For reasons that we will discuss in Section 7.4.2, we add an additional layer of sophistication to this particular analysis by considering the xenon target as being composed of different xenon isotopes. We take the isotopic abundance of the xenon in the liquid TPC to be equal to that of naturally occurring xenon [434, 435]. We take the weighted sum of their predicted rates to be our best estimate of the total, isotope-averaged differential rate spectrum.

7.4.1 Accounting For Neutrino Flux Uncertainties

Thus far, we have ignored any potential systematic uncertainties in calculating our DD limits. In our present statistical treatment, we additionally consider the uncertainty in the total ^{8}B flux in our NR analysis[2]. Fluctuations in this quantity act as effective scalings in the total theoretical rate, which can be modelled by introducing a randomly distributed scale factor as a nuisance parameter. Indeed, we modelled the uncertainty in the normalisation of the total predicted CEνNS rate at SS experiments in an identical way in Section 5.1.2.

Presently, we introduce the scale factor $\alpha \sim \mathcal{N}(0, \sigma_\alpha)$, where $\mathcal{N}(\mu, \sigma)$ is a normal distribution with mean μ and standard deviation σ. In this case, $\sigma_\alpha = 12\%$, reflecting the fractional uncertainty in the ^{8}B flux in the B16-GS98 SSM [74]. The resulting test statistic is given by

$$q_\mu = \min_\alpha \left\{ 2\left[(1+\alpha)\mu(\boldsymbol{\theta}) - n_{\text{obs}} + n_{\text{obs}} \ln \frac{n_{\text{obs}}}{(1+\alpha)\mu(\boldsymbol{\theta})} \right] + \left(\frac{\alpha}{\sigma_\alpha} \right)^2 \right\}, \tag{7.4.1}$$

which has the same form as Eq. (6.1.5) except for the scaling by $(1+\alpha)$, the additional quadratic penalty term, and the absence of the sum since we are only considering a single bin. The number of observed events is calculated from the SM prediction, with the total ^{8}B flux set to its expectation value to reflect our use of Asimov data sets. The nuisance parameter α is profiled over such that any excess or deficit predicted by the new physics contribution has the potential to be explained by a non-zero fluctuation in α. As in Eq. (5.1.7), any shift in α from $\alpha = 0$ might be able to account for any such deviations; however, the larger this shift, the larger the penalty incurred.

This systematic uncertainty can have a large effect on our computed limits. We illustrate this in Fig. 7.5, where we show the q_μ test statistic when both ignoring and accounting for fluctuations in the ^{8}B flux for the case of $\varepsilon_{ee}^{\eta,\varphi}$ with $\eta = \varphi = 0$. The dashed line, like that in Fig. 7.3, highlights the value of $q_\mu = 2.71$, corresponding

---

[2] Recall that ^{8}B neutrinos dominate the CEνNS signal, with hep neutrinos being subdominant. We have explicitly checked that accounting for both flux uncertainties has a negligible effect.

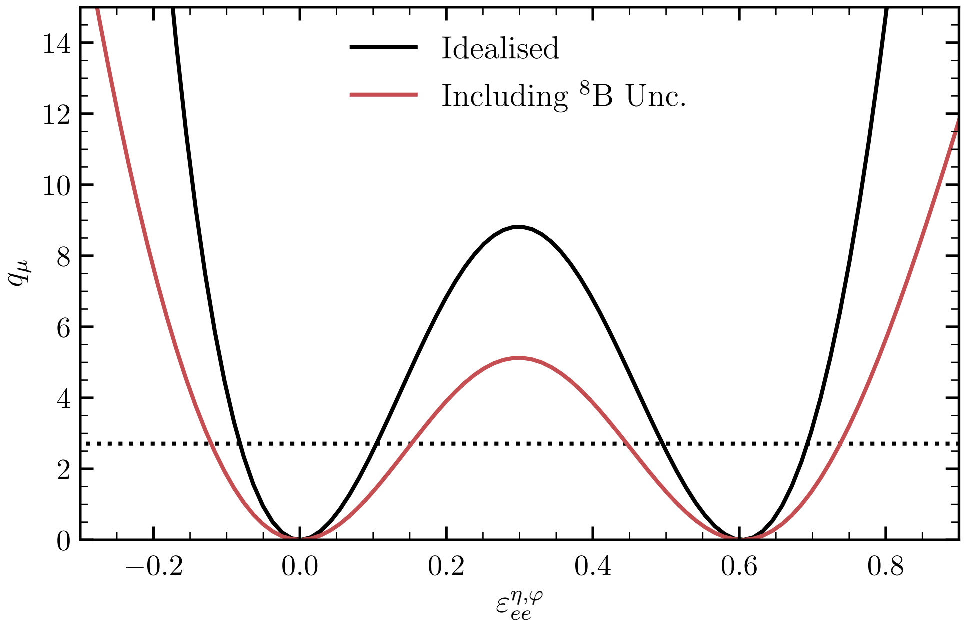

Figure 7.5: The effect of the ^{8}B uncertainty on the derived limit for $\varepsilon_{ee}^{\eta,\varphi}$. The idealised result (black), without including this uncertainty, is contrasted with the more realistic result (red) including the $\sim 12\%$ uncertainty in the total ^{8}B neutrino flux.

to the test statistic required to place a 1 d.o.f. 90% CL limit.

As ^{8}B neutrinos are the dominant component of the CEνNS signal, one might expect that our previous NR-based DD results in Chapters 5 and 6 might be similarly impacted by this consideration. However, for the gauged $U(1)$ models we discussed, the coupling strength always entered at least as g^2 due to the kinetic mixing portal (c.f. Eq. (4.2.11)). Consequently, in contrast to the NSI parametrisation where new physics effects enter linearly, in the case of our $U(1)$ models they enter quadratically. Thus, to produce a deviation in the total number of counts that admits the same level of statistical significance, a smaller change in the gauge coupling is required compared to the NSI parameter $\varepsilon_{\alpha\beta}^{\eta,\varphi}$. Nonetheless, our previous results should be interpreted as ultimate goals for DD experiments in the case that such an uncertainty, which stems from the modelling techniques used in making predictions from the SSM, can be reduced below any inherent statistical uncertainties.

For ERs, the neutrino flux uncertainties have a much smaller effect. Since we are only considering the total number of counts, and, as we saw in Fig. 3.6, pp neutrinos are the dominant contributors to the EνES count, it suffices to consider the pp flux uncertainty. This currently rests at $\sigma_{\mathrm{pp}} \approx 0.5\%$ in the B16-GS98 model [74], allowing us to neglect this effect, with the statistical uncertainty dominating.

We note that the uncertainty in the ^{8}B flux can be reduced to a value as low as $\sigma_{^8\mathrm{B}} \approx 2\%$ if experimental data from solar neutrino, reactor, and atmospheric neutrinos are included [436]. However, we cannot use this more constraining result as it relies on interpreting the data in terms of standard neutrino oscillations and interactions. We must therefore rely solely on the theoretical predictions from SSMs, which concern themselves with neutrino production at the source. Indeed, since these production processes are based on CC interactions, they are not impacted by NC NSIs. Thus, we use the higher uncertainty value predicted by the B16-GS98 model [74, 77], giving us both consistency with our previous studies and, ultimately, more conservative results.

Lastly, we have also checked that our limits are not greatly impacted by uncertainties in the neutrino oscillation parameters when these uncertainties are computed using standard neutrino oscillations and interactions. While including NSIs can significantly impact the best-fit values of and uncertainties in these parameters, especially those derived from solar neutrino experiments [24], we note that the future medium-baseline reactor experiment JUNO [437] will be largely insensitive to the effects of NSIs. In particular, the fits to the solar neutrino parameters, θ_{12} and Δm_{12}^2, and the reactor neutrino angle, θ_{13}, will be robust in the presence of NSIs [438]. Moreover, the atmospheric angle (θ_{23}), which impacts the muon and tau neutrino fractions, is not greatly changed by the inclusion of NSIs [24]. Thus, we take the liberty of ignoring these systematics in this first study, taking the best-fit values for these parameters from Ref. [128], as in our previous work.

7.4.2 CEνNS Limits in the NSI Landscape

Our NR limits are presented in Fig. 7.6. To compare with the results of dedicated neutrino experiments, we consider the results of the global fit performed by Ref. [25]. This study incorporated the energy and timing information released by the COHERENT collaboration [439] to the earlier global NSI fit performed by Ref. [24]. This latter fit included oscillation data from the solar neutrino experiments Homestake [85,86], GALLEX [103–106], SAGE [97–102], Super-Kamiokande [124,125], and Borexino [9, 347]; the reactor neutrino experiments KamLAND [351], Chooz [136], and Daya-Bay [137]; the atmospheric neutrino data of Super-Kamiokande IV [440] and IceCube [441, 442]; and the accelerator experiments MINOS [130], T2K [131], and NOvA [132].

We extract the 90% CL bounds from Table 3 of Ref. [25], which are visualised as red bars in Fig. 7.6. These bars are placed at those values of η corresponding to NSIs with the proton ($\eta = 0°$), the up quark ($\eta \approx 27°$), and the down quark ($\eta \approx 63°$) to directly compare with the results of Ref. [25]. The grey regions highlight those points in each parameter space where the adiabaticity parameter, given by Eq. (7.2.7), admits the values $\gamma < 100$, where we consider the adiabatic approximation to begin to falter [67]. Since our limits generally lie outside of these regions, including for those regions of parameter space relevant for comparing to global fit bounds, we will not comment on them further. For the first time, our study places the potential power of DD experiments in the neutrino NSI landscape within the context of dedicated neutrino experiments.

Promisingly, we see that not only can the far-future DARWIN experiment cut into unbounded values of multiple NSI parameters, but so too can the next-generation experiments LZ and XENONnT. In particular, all of them probe regions thus far unconstrained by global studies in the cases of $\varepsilon_{ee}^{\eta,\varphi}$, $\varepsilon_{e\tau}^{\eta,\varphi}$, and $\varepsilon_{\tau\tau}^{\eta,\varphi}$. DARWIN, with its $\sim$10-fold increase in exposure, can additionally probe $\varepsilon_{e\mu}^{\eta,\varphi}$, as well as more stringently constrain the previous three parameters. XENONnT and LZ are equally matched in

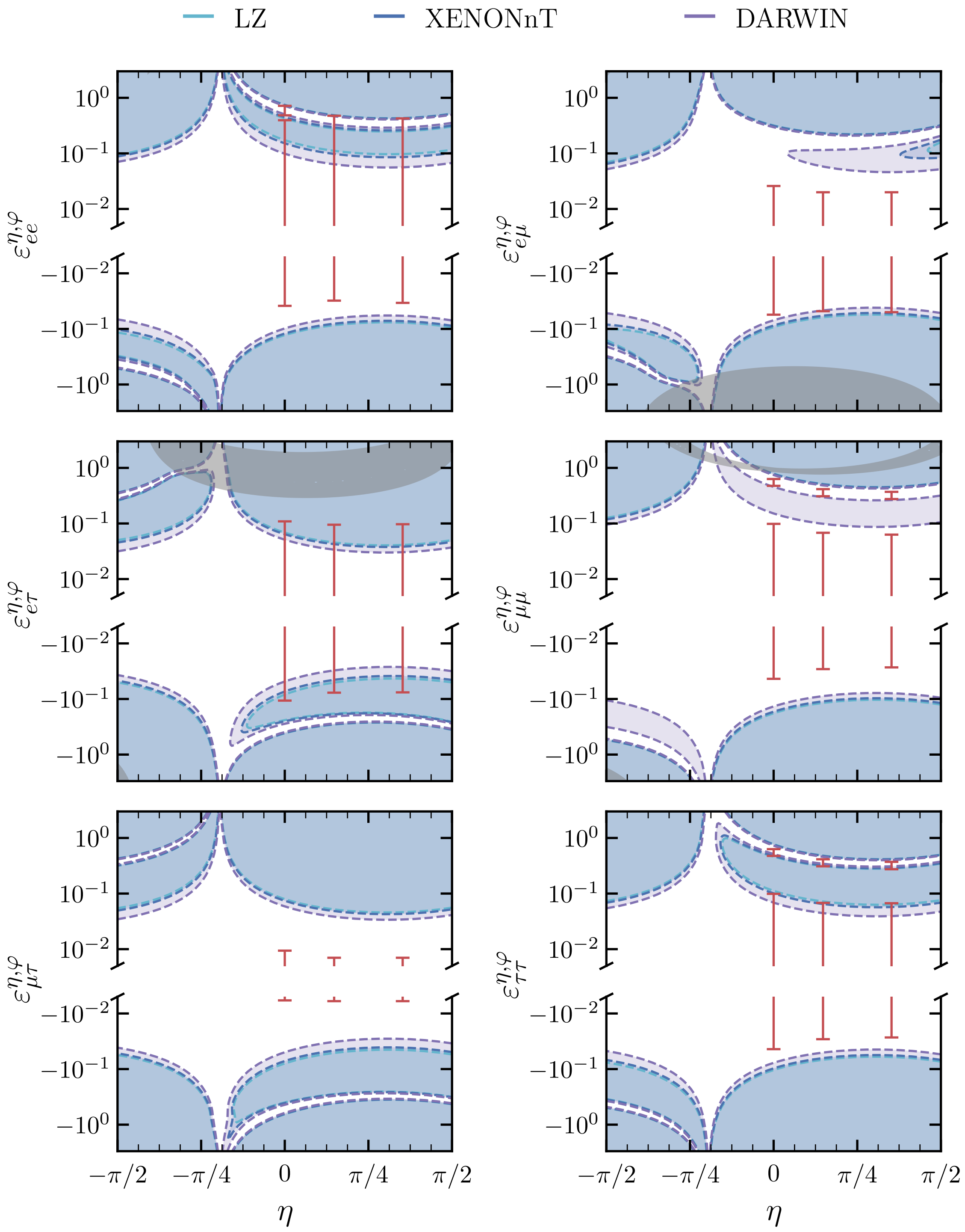

Figure 7.6: The 90% CL limits set by multi-ton LXe DD experiments in the NSI parameter space using NRs. Each panel shows the resulting limits when turning on each given NSI parameter. Shown are the limits from LZ (cyan), XENONnT (blue), and DARWIN (purple) in the typically assumed case that the NSI contribution is entirely in the proton-neutron plane ($\varphi = 0$). The bounds from the global analysis of Ref. [25] are shown for comparison (red bars). The grey regions indicate where the adiabaticity parameter is such that $\gamma < 100$, where we consider the adiabatic approximation to begin to falter [67].

this parameter space, with XENONnT performing slightly better due to its slightly higher exposure (20 ton yr over LZ's ~15 ton yr exposure).

Of particular note is the richness of the features exhibited by our limits. Specifically, we see that there are regions in each parameter space where every one of our DD experiments loses sensitivity. The two most remarkable of these are, firstly, the asymptote in η occurring at $\eta \approx -35^\circ$ and, secondly, the band of insensitivity in $\varepsilon_{\alpha\beta}^{\eta,\varphi}$ across the full range of η values. To explain them, we must examine the form of the NSI cross section in Eq. (4.2.26) in conjunction with the fact that the differential rate now contains a trace operation due to the potential of having flavour-changing interactions. These blind spots present a challenge to DD experiments if they are to maximise their constraining power in the NSI landscape, and it is therefore instructive to consider ways in which they could, at least in part, be guarded against.

We first consider the asymptote in η, which occurs at the same point regardless of the nature of the NSI. From Eq. (4.2.26), we see that the non-standard contribution to the CEνNS cross section disappears when $\xi^p Z + \xi^n N$ vanishes, retrieving the SM cross section regardless of the value of $\varepsilon_{\alpha\beta}^{\eta,\varphi}$. For a generic nuclear target, this occurs when

$$\eta = \tan^{-1}\left(-\frac{Z}{N}\cos\varphi\right) . \tag{7.4.2}$$

The location of this asymptote is therefore dependent on the chosen target material. This is why we have considered the full isotopic average in our calculation, as its location shifts depending on the nuclear composition of the isotopes. By performing an isotopic average, we find that the asymptote indeed occurs when $\eta \approx -35^\circ$ for $\varphi = 0$. Since this loss of sensitivity is inextricably tied to the choice of target, to gain sensitivity to this region of the parameter space we must choose a target with an appreciably different proton-to-neutron fraction. However, since stable nuclei tend to have similar such ratios, the location of this asymptote does not shift significantly for different target choices. Indeed, out of all of the targets we have considered in this work, argon gives us the largest difference from xenon, with $\eta \approx -39^\circ$—only a 4° difference.

Our second blind spot occurs at intermediate values of $\varepsilon^{\eta,\varphi}_{\alpha\beta}$, which stretches across the full range of η. The position of these bands depends on whether we have flavour-conserving or flavour-violating NSIs. We consider both of them in turn, beginning with the former.

In the case of flavour-conserving NSIs, we have a similar effect to that of Section 7.3 for the CENNS-10 LAr experiment, whereby two values of $\varepsilon^{\eta,\varphi}_{\alpha\alpha}$ can account for the same number of observed counts. As we have assumed that our DD experiments observe a number of counts equal to the SM expectation, we can use the cross section of Eq. (4.2.26) to derive an analytical formula for the locations of the second minimum. This relation, which defines the centres of each of these bands, is given by

$$\varepsilon^{\eta,\varphi}_{\alpha\alpha} = \frac{Q_{\nu N}}{\xi^p Z + \xi^n N} \, . \tag{7.4.3}$$

The dependence on η, encoded in ξ^p and ξ^n, gives us the band over different values of $\varepsilon^{\eta,\varphi}_{\alpha\alpha}$. We see that as the denominator of Eq. (7.4.3) tends to zero, realising the asymptote condition of Eq. (7.4.2), the value of $\varepsilon^{\eta,\varphi}_{\alpha\alpha}$ diverges, as expected. Note that the location of this minimum, as with the location of the asymptote, is dependent on the choice of target material. For $\eta = 0$, for instance, Eq. (7.4.3) gives $\varepsilon^{\eta,\varphi}_{\alpha\alpha} \approx 0.60$ for xenon, whereas it yields the lower $\varepsilon^{\eta,\varphi}_{\alpha\alpha} \approx 0.51$ for argon. This gives us one possible avenue to mitigate this particular sensitivity loss.

Interestingly, the bound in $\varepsilon^{\eta,\varphi}_{\tau\tau}$ from the global fit study, depicted by the red bars, also has a second minimum. Such a minimum is purely a consequence of the above effect, and it therefore stems from the inclusion of data from COHERENT. One might be curious as to why information from COHERENT has an impact on this parameter since it does not see an appreciable number of tau neutrinos. However, the key difference is that the global analysis of Ref. [25] included oscillation experiments, which are sensitive to the combinations $\varepsilon^{\eta,\varphi}_{ee} - \varepsilon^{\eta,\varphi}_{\mu\mu}$ and $\varepsilon^{\eta,\varphi}_{\tau\tau} - \varepsilon^{\eta,\varphi}_{\mu\mu}$. Combining this information with that given by COHERENT on $\varepsilon_{\mu\mu}^{\eta,\varphi}$ gives them sensitivity to $\varepsilon_{\tau\tau}^{\eta,\varphi}$ [25]. The bounds in the insensitivity region of $\varepsilon_{\tau\tau}^{\eta,\varphi}$ are then due to COHERENT losing sensitivity to $\varepsilon_{\mu\mu}^{\eta,\varphi}$, inhibiting them from providing oscillation experiments with this information.

In the case of flavour-changing NSIs, the cancellation relation becomes more complicated. Due to the flavour-coherence effects, we still expect regions where the interference term cancels the BSM-only term. This condition, however, now depends on the density matrix elements. To simplify matters, we consider where the differential rate spectrum returns to its SM value for a given recoil energy, removing the need to integrate over E_R. From Eqs. (4.2.24) and (4.2.26), we find that, for $\alpha \neq \beta$, the condition that must be satisfied is

$$\begin{aligned}\int_{E_\nu^{\text{min}}} \frac{\mathrm{d}\phi_{\nu_e}}{\mathrm{d}E_\nu}\left(1-\frac{m_N E_R}{2E_\nu^2}\right)\Big[(\xi^p Z+\xi^n N)(\rho_{\alpha\alpha}+\rho_{\beta\beta})\varepsilon_{\alpha\beta}^{\eta,\varphi}& \\ -\,2Q_{\nu N}\rho_{\alpha\beta}\Big]\,\mathrm{d}E_\nu = 0\,.&\end{aligned} \tag{7.4.4}$$

The difference between this relation and that of Eq. (7.4.3) is why the locations of these bands are generally different for $\alpha \neq \beta$. For instance, the sign flip that occurs for the cases of $\varepsilon_{e\tau}^{\eta,\varphi}$ and $\varepsilon_{\mu\tau}^{\eta,\varphi}$ is because the density matrix elements $\rho_{e\tau}$ and $\rho_{\mu\tau}$ are negative. For $\alpha = \beta$, there is no flavour-specific dependence, so all bands occur at the same points.

We note that, while we have computed our limits under the assumption of a pure-proton charged contribution ($\varphi = 0$), the power of our framework lies in giving one the ability to make a different assumption. We emphasize that the reasoning for taking $\varphi = 0$ was to be able to directly compare to the results from global-fit studies. In the future, it would be interesting to explore how our NR limits are impacted by taking different values for φ, similarly to our analysis in Section 7.3.

7.4.3 EνES Limits on the NSI Space

To conclude this chapter, we explore the limits that DD experiments could set using a search for deviations in the EνES rate. As far as we are aware, no global studies exist for $\varepsilon^{e}_{\alpha\beta}$. Nonetheless, to make contact with dedicated neutrino experiments, we consider the recent results of Ref. [26], which used the spectral data from Phase-II of the Borexino experiment [10] to constrain these parameters. As they do not mention the potential impact of either proton or neutron NSIs on neutrino oscillations, we assume that they have only considered NSIs with the electron, with no contribution from the other fermions. As a result, we assume $\eta = 0$, and we place their bounds at $\varphi = \pi/2$, corresponding to electron-only NSIs. We note that, while other studies have also constrained electron NSIs, most of them place individual bounds on the left- and right-handed components of the interaction [319, 443–446]. This makes it difficult to compare with our results on the electron's vector interactions since the bounds from those studies would translate in a non-trivial way to this type of interaction.

We show our results in Fig. 7.7. Interestingly, we see that DD experiments form powerful probes of electron NSIs, with all of our limits cutting into portions of the bounds placed from the Borexino experiment. Indeed, except for the parameters $\varepsilon^{\eta,\varphi}_{\mu\mu}$ and $\varepsilon^{\eta,\varphi}_{\mu\tau}$, even next-generation experiments can provide us with new information on NSIs[3]. DARWIN can give us considerably more sensitivity on all NSI parameters, showcasing its considerable potential in searching for new physics in the neutrino sector.

Of course, this potential warrants further investigation. We emphasise that we have undertaken an idealised statistical treatment for the ER case, ignoring all potential systematics in our results. For instance, we have not incorporated the systematic uncertainties inherent in the background components that our experiments are susceptible to. Furthermore, though we do not believe them to be important, we have

---

[3] This loss of sensitivity to the muon sector is likely due to the lower flux of solar muon neutrinos predicted compared to the other flavours (c.f.Fig. 2.9).

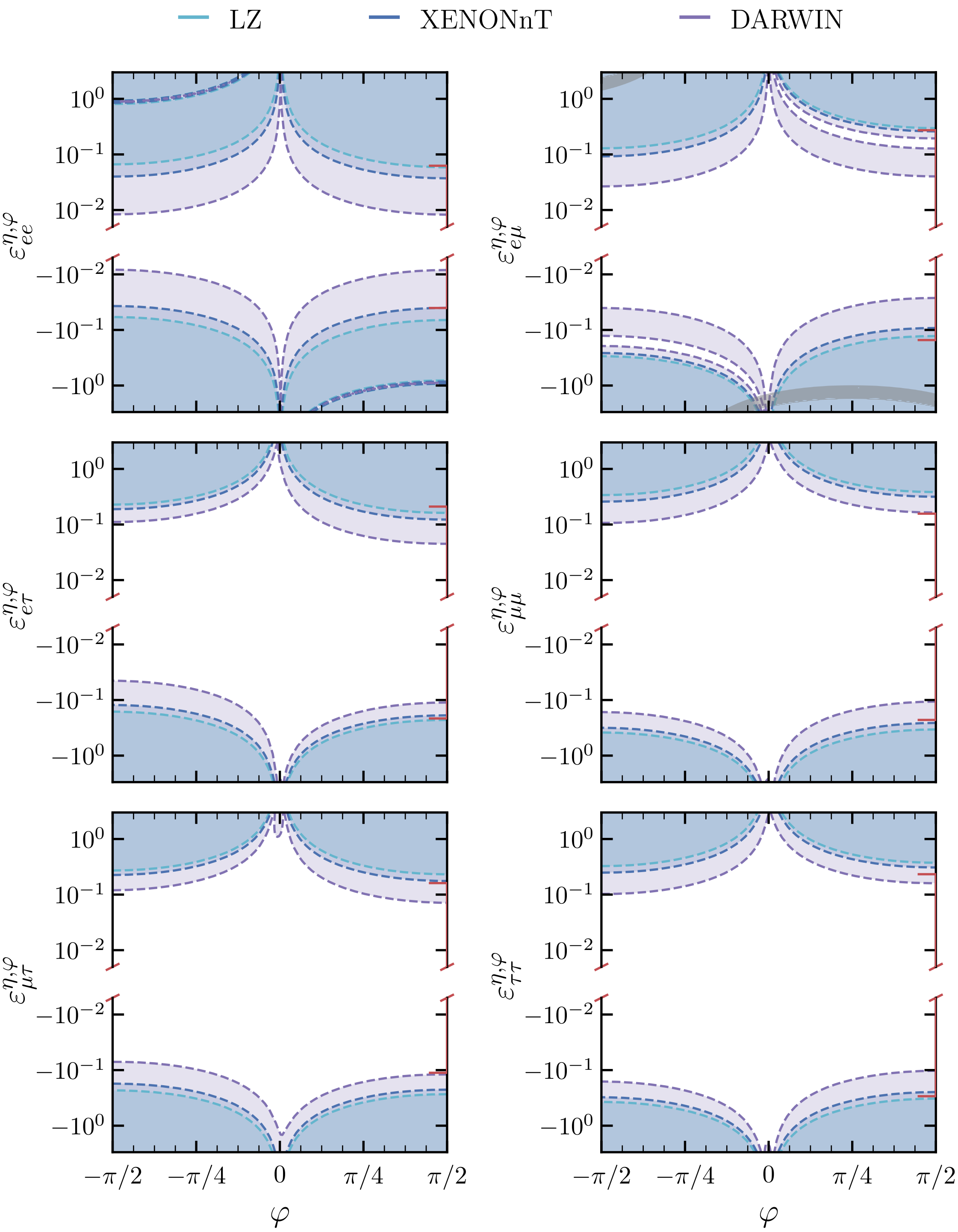

Figure 7.7: Same as in Fig. 7.6 but for electron recoils. The interactions are assumed to take place entirely in the proton-electron plane ($\eta = 0$). The bounds from the Borexino analysis of Ref. [26] are shown for comparison (red bars at the edge of the figure).

not considered the neutrino flux uncertainties in the pp and ^{7}Be neutrinos, which principally contribute to the neutrino rate in our energy range of interest. Ref. [26] took these factors into account when performing their Borexino analysis. While these potential systematics would make for a more sophisticated comparison, we stress that our results should be taken only as motivators to include DD experiments in future global studies of NSIs.

As in the CEνNS case, the limits for the EνES case exhibit clear phenomenological blind spots. We once again observe a divergence of the limits at some value of the angle and a series of bands where DD experiments appear to lose sensitivity. However, there are two notable differences between this case and the CEνNS case, arising from both the different CEνNS and EνES cross sections and the way in which non-standard matter effects enter. We discuss these differences below.

Firstly, we have no asymptote for the ER limits. While one might expect a complete loss of sensitivity when $\varphi = 0$, where the EνES cross section is unchanged by the presence of NSIs, neutrino oscillations are still impacted by the *proton* contribution to the matter Hamiltonian. Thus, for high enough values of $\varepsilon^{\eta,\varphi}_{\alpha\beta}$, the effect of NSIs on the neutrino flavour fractions is large enough to give us an observable deviation from the SM expectation. Consequently, while we do lose sensitivity as φ approaches zero, our limits ultimately reach a finite value. Note that this is only possible as the cross section for electron neutrinos contains the extra CC contribution, making it different from that of the muon and tau neutrinos. Changes in the electron neutrino fraction then lead to measurable changes in the total number of CC interactions in the detector; the NC interactions from all flavours, on the other hand, remain equal.

Secondly, we have fewer bands of insensitivity over φ than we did for the NR case over η. The location of these bands can be calculated through identical arguments to the CEνNS case, whereby those values of the NSI parameters where the NSI-augmented rate is equal to the expected SM rate must be found. However, as the EνES cross section, given in Eq. (4.2.29), is more complicated than the CEνNS cross section, the condition that must be satisfied is more complex, and we therefore do not give its form explicitly here. Nevertheless, we expect bands similar to those in the CEνNS case, but generally at much lower values of the NSI parameters. This is due to the terms involving the left- and right-handed parts of the NSI cross section being of similar order, generally requiring small values of $\varepsilon_{\alpha\beta}^{\eta,\varphi}$ to cancel them completely, retrieving the SM cross section. While there are some parameters for which DD experiments witness this region of insensitivity—namely $\varepsilon_{ee}^{\eta,\varphi}$ and $\varepsilon_{e\mu}^{\eta,\varphi}$—the majority of them occur at values that are too small for these experiments to see.

We re-iterate that the limits presented in Figs. 7.6 and 7.7 have been calculated by switching on only one NSI parameter at a time. Due to potential interference effects between different NSI parameters, a global analysis that allows all NSI parameters to vary, before marginalising to compute the limits on any one parameter, would generally lead to weaker limits [429]. However, the point of our study is only to illustrate the potential of DD experiments in this direction. We believe our study makes the case for them to be included in future global analyses including this marginalisation.

Combined with our CEνNS results, our EνES limits indicate that DD experiments will form powerful probes of neutrino NSIs. Though we have neglected certain complicating considerations in our study, such as additional potential systematic uncertainties, we believe that the conclusion is clear: multi-ton, LXe-based DD experiments are poised to make a considerable impact in the neutrino NSI landscape. We therefore recommend that they should be included in future global NSI studies, incorporating a more complete treatment of the systematics.

CHAPTER 8

Conclusions

Direct detection experiments are on a collision course with the solar part of the neutrino floor. This will inevitably complicate the search for dark matter; however, a new era of neutrino research will dawn on these experiments. Since BSM neutrino physics can lead to deviations in the expected solar CEνNS and EνES rates, these processes can be used in indirect searches for new physics in the neutrino sector. The power of DD experiments in probing this kind of BSM physics has been the subject of this thesis.

We began in Chapter 5 by exploring the competitiveness of these experiments in searching for a new hidden photon stemming from a gauged $U(1)_{L_\mu - L_\tau}$. This model is a theoretically well-motivated extension to the SM that can solve the increasing tension in the measured value of the muon's anomalous magnetic moment, $(g-2)_\mu$, as well as help to alleviate the tension in the present-day value of the Hubble parameter, H_0. We derived limits in the $U(1)_{L_\mu - L_\tau}$ parameter space using a selection of DD experiments and the dedicated neutrino experiments Borexino and COHERENT. For Borexino, we updated previously computed limits by making several improvements to the previous calculation, finding that the limits based on the fluxes of a high-metallicity Sun cut into previously unexplored regions of the $U(1)_{L_\mu - L_\tau}$ parameter space. On the other hand, for COHERENT, we calculated new limits based on its recent LAr run, finding them to be competitive with its first CsI run. We explored the sensitivity of DD experiments inspired by next-generation and far-future detectors, such as SuperCDMS, LZ, XENONnT, DARWIN, and DarkSide-20k. Excitingly, we discovered that the multi-ton LXe experiments can probe new regions of the $U(1)_{L_\mu - L_\tau}$ space that can both explain $(g-2)_\mu$ and alleviate the H_0 tension. In particular, we found that DARWIN could completely exclude the $(g-2)_\mu$ preferred region.

Motivated by the increased tension in $(g-2)_\mu$ measured by Fermilab in 2021, we sought to provide an experimental strategy with which to confirm the $U(1)_{L_\mu - L_\tau}$ hidden photon as the solution to this modern hint of new leptonic physics in Chapter 6. Our strategy featured the muon beam experiment NA64μ, a selection of future LAr SS experiments, and, critically, multi-ton LXe DD experiments. To judge their sensitivities, we performed a series of parameter reconstructions based on a set of benchmark points along the $(g-2)_\mu$ solution region of the $U(1)_{L_\mu - L_\tau}$ parameter space. We found that the NA64μ experiment will be able to provide excellent reconstructions of both the gauge couplings and mediator mass for $m_{A'} \approx 100\,\mathrm{MeV}$, providing only an upper bound on the coupling for lighter mediators. SS experiments searching for CEνNS will be able to set constraints for hidden photons of masses $m_{A'} \lesssim 50\,\mathrm{MeV}$, with larger volumes and lower thresholds allowing for an observation of the lower mass mediators. Finally, the far-future DARWIN experiment will not only be able to discover hidden photons in the mass range $m_{A'} \lesssim 50\,\mathrm{MeV}$, but it will also allow us to tightly constrain their gauge couplings.

Throughout the above study, we compared the $U(1)_{L_\mu - L_\tau}$ model to an effective $U(1)_{L_\mu}$ due to its remarkably similar phenomenology. We did this by performing the parameter reconstructions with each of our experiments under the assumption of a $U(1)_{L_\mu - L_\tau}$ and a $U(1)_{L_\mu}$ in turn. In the case of the NA64μ experiment, we found that its results can be equally well interpreted as arising from either model due to its sensitivity to only muon interactions. Conversely, SS experiments, probing the new physics effect of these new vector mediators via their kinetic mixing with the SM photon, will have sensitivity to the value of the kinetic mixing parameter. Combined with the NA64μ experiment, SS experiments will be able to tell us if the value of this kinetic mixing is consistent with only one of these models or, in the maximally degenerate scenario, consistent with both. In this latter case, the only way to disentangle the $U(1)_{L_\mu - L_\tau}$ hidden photon from that of the $U(1)_{L_\mu}$ is to probe its interaction with the third-generation leptons—a feat achievable with DD experiments looking for CEνNS with solar neutrinos. We found that a hypothetical realisation of a DARWIN-like experiment with a lower $1\,\mathrm{keV_{nr}}$ threshold will be able to provide us with this important, final piece of the puzzle in the case that these two models are maximally entangled.

Finally, in Chapter 7, we moved beyond gauged $U(1)$ models, exploring instead the sensitivities of multi-ton LXe DD experiments to more general neutrino physics through the neutrino NC-NSI framework. We did this by first introducing a new NSI parametrisation that allowed us to include NSIs with the electron—an important consideration for DD experiments since they can probe both CEνNS and EνES. To illustrate the broader importance of including the electron component, we studied how limits set by the LAr CENNS-10 experiment were impacted by varying this contribution, finding their evolution to be non-trivial. We then explored how sensitive future realisations of LZ, XENONnT, and DARWIN would be to NSI parameters using the CEνNS and EνES rates, including the effect of the ^{8}B flux uncertainty in the case of CEνNS. We placed these sensitivities in the context of the results from dedicated neutrino experiments, consisting of a global fit of oscillation, reactor, and spallation source experiments in the case of CEνNS, and a recent analysis of the Borexino Phase-II data in the case of EνES. By varying one NSI parameter at a time, we found that realistic realisations of xenon-based DD experiments can, in most cases, provide additional constraining power in the NSI parameter space. Our preliminary results indicate that next-generation and far-future multi-ton LXe DD experiments should be included in future global NSI analyses.

In this thesis, we have shown that DD experiments are on course to become key players in the field of neutrino physics. By reinterpreting the irreducible background of solar neutrinos as an invaluable signal of new physics in the neutrino sector, we have shown that DD experiments will be able to provide either leading or complementary results to those of dedicated neutrino experiments searching for BSM neutrino physics. In doing so, we have reinforced the importance of DD experiments in this novel direction, adding value to a powerful research mission beyond their search for dark matter.

Bibliography

[1] D. W. P. d. Amaral, D. G. Cerdeno, P. Foldenauer and E. Reid, *Solar neutrino probes of the muon anomalous magnetic moment in the gauged* $\mathrm{U}(1)_{L_\mu - L_\tau}$, *JHEP* **12** (2020) 155, [`2006.11225`].

[2] D. W. P. Amaral, D. G. Cerdeno, A. Cheek and P. Foldenauer, *Confirming* $U(1)_{L_\mu - L_\tau}$ *as a solution for* $(g-2)_\mu$ *with neutrinos*, *Eur. Phys. J. C* **81** (2021) 861, [`2104.03297`].

[3] D. W. P. Amaral, D. Cerdeno, A. Cheek and P. Foldenauer, *A direct detection view of the neutrino NSI landscape*, `2302.12846`.

[4] Muon g-2 collaboration, G. W. Bennett et al., *Measurement of the negative muon anomalous magnetic moment to 0.7 ppm*, *Phys. Rev. Lett.* **92** (2004) 161802, [`hep-ex/0401008`].

[5] Muon g-2 collaboration, B. Abi et al., *Measurement of the Positive Muon Anomalous Magnetic Moment to 0.46 ppm*, *Phys. Rev. Lett.* **126** (2021) 141801, [`2104.03281`].

[6] Planck collaboration, N. Aghanim et al., *Planck 2018 results. VI. Cosmological parameters*, `1807.06209`.

[7] A. G. Riess et al., *A Comprehensive Measurement of the Local Value of the Hubble Constant with 1 km/s/Mpc Uncertainty from the Hubble Space Telescope and the SH0ES Team*, `2112.04510`.

[8] COHERENT collaboration, D. Akimov et al., *First Measurement of Coherent Elastic Neutrino-Nucleus Scattering on Argon*, *Phys. Rev. Lett.* **126** (2021) 012002, [`2003.10630`].

[9] G. Bellini et al., *Precision measurement of the 7Be solar neutrino interaction rate in Borexino*, *Phys. Rev. Lett.* **107** (2011) 141302, [`1104.1816`].

[10] BOREXINO collaboration, M. Agostini et al., *First Simultaneous Precision Spectroscopy of pp, ^{7}Be, and pep Solar Neutrinos with Borexino Phase-II*, *Phys. Rev.* **D100** (2019) 082004, [`1707.09279`].

[11] XENON collaboration, E. Aprile et al., *Search for New Physics in Electronic Recoil Data from XENONnT*, `2207.11330`.

[12] XENON collaboration, E. Aprile et al., *Observation of Excess Electronic Recoil Events in XENON1T*, `2006.09721`.

[13] SUPERCDMS collaboration, R. Agnese et al., *Projected Sensitivity of the SuperCDMS SNOLAB experiment*, *Phys. Rev.* **D95** (2017) 082002, [`1610.00006`].

[14] LZ collaboration, D. S. Akerib et al., *LUX-ZEPLIN (LZ) Conceptual Design Report*, `1509.02910`.

[15] XENON collaboration, E. Aprile et al., *Projected WIMP sensitivity of the XENONnT dark matter experiment*, *JCAP* **11** (2020) 031, [`2007.08796`].

[16] DARWIN collaboration, J. Aalbers et al., *DARWIN: towards the ultimate dark matter detector*, *JCAP* **1611** (2016) 017, [`1606.07001`].

[17] C. E. Aalseth et al., *DarkSide-20k: A 20 tonne two-phase LAr TPC for direct dark matter detection at LNGS*, *Eur. Phys. J. Plus* **133** (2018) 131, [`1707.08145`].

[18] NA64 Collaboration collaboration, S. Gninenko, *Proposal for an experiment to search for dark sector particles weakly coupled to muon at the SPS*, Tech. Rep. CERN-SPSC-2019-002. SPSC-P-359, CERN, Geneva, Jan, 2019.

[19] NA64 Collaboration collaboration, S. Gninenko, *Addendum to the Proposal P348: Search for dark sector particles weakly coupled to muon with NA64μ*, Tech. Rep. CERN-SPSC-2018-024. SPSC-P-348-ADD-3, CERN, Geneva, Sep, 2018.

[20] COHERENT collaboration, D. Akimov et al., *Sensitivity of the COHERENT Experiment to Accelerator-Produced Dark Matter*, *Phys. Rev. D* **102** (2020) 052007, [`1911.06422`].

[21] CCM collaboration, A. A. Aguilar-Arevalo et al., *First Dark Matter Search Results From Coherent CAPTAIN-Mills*, `2105.14020`.

[22] D. Baxter et al., *Coherent Elastic Neutrino-Nucleus Scattering at the European Spallation Source*, *JHEP* **02** (2020) 123, [`1911.00762`].

[23] L. Wolfenstein, *Neutrino Oscillations in Matter*, *Phys. Rev. D* **17** (1978) 2369–2374.

[24] I. Esteban, M. C. Gonzalez-Garcia, M. Maltoni, I. Martinez-Soler and J. Salvado, *Updated Constraints on Non-Standard Interactions from Global Analysis of Oscillation Data*, *JHEP* **08** (2018) 180, [`1805.04530`].

[25] P. Coloma, I. Esteban, M. C. Gonzalez-Garcia and M. Maltoni, *Improved global fit to Non-Standard neutrino Interactions using COHERENT energy and timing data*, *JHEP* **02** (2020) 023, [`1911.09109`].

[26] P. Coloma, M. C. Gonzalez-Garcia, M. Maltoni, J. a. P. Pinheiro and S. Urrea, *Constraining New Physics with Borexino Phase-II spectral data*, 2204.03011.

[27] H. Becquerel, *Sur les radiations émises par phosphorescence*, *Comptes Rendus* **122** (1896) .

[28] H. Becquerel, *Sur les propriétés différentes des radiations invisibles émises par les sels d'uranium, et du rayonnement de la paroi anticathodique d'un tube de crookes*, *Comptes Rendus* **122** (1896) 762 – 767.

[29] H. Becquerel, *Sur les radiations invisibles émises par les sels d'uranium*, *Comptes Rendus* **122** (1896) 689 – 694.

[30] H. Becquerel, *Sur quelques propriétés nouvelles des radiations invisibles émises par divers corps phosphorescents*, *C. R. Acad. Sci.* **122** (1896) 559 – 564.

[31] H. Becquerel, *Sur les radiations invisibles émises par les corps phosphorescents*, *Comptes Rendus* **122** (1896) 501 – 503.

[32] M. Curie, *Rayons émis par les composés de l'uranium et du thorium*, *Comptes Rendus* **126** (1898) 1101 – 1103.

[33] P. Curie, M. Curie and G. Bémont, *Sur une nouvelle substance fortement radio-active, contenue dans la pechblende*, *Comptes Rendus* **127** (1898) 1215 – 1217.

[34] P. Curie and M. Curie, *Sur une substance nouvelle radio-active, contenue dans la pechblende*, *Comptes Rendus* **127** (1898) 175 – 178.

[35] E. Rutherford, *Uranium radiation and the electrical conduction produced by it*, *Philos. Mag.* **47** (1899) 109.

[36] P. Villard, *Sur la réflexion et la réfraction des rayons cathodiques et des rayons déviables du radium*, *Comptes Rendus* **130** (1900) 1010 – 1012.

[37] H. Geiger and E. Marsden, *On a diffuse reflection of the α-particles*, *Proceedings of the Royal Society of London. Series A, Containing Papers of a Mathematical and Physical Character* **82** (1909) 495–500.

[38] E. Rutherford, *The scattering of alpha and beta particles by matter and the structure of the atom*, *Phil. Mag. Ser. 6* **21** (1911) 669–688.

[39] J. J. Thomson, *Cathode rays*, *Phil. Mag. Ser. 5* **44** (1897) 293–316.

[40] A. Bécquerel, *Sur la transparence de l'aluminium pour la rayonnement du radium*, *CR Acad. Sci. Paris* **130** (1900) 1154.

[41] J. Chadwick, *Intensitätsverteilung im magnetischen spectrum der β-strahlen von radium b+ c*, *Verhandl. Dtsc. Phys. Ges.* **16** (1914) 383.

[42] C. Jensen, F. Aaserud, H. Kragh, E. Rüdinger and R. H. Stuewer, *From anomaly to explanation: The continuous beta spectrum, 1929–1934*, in *Controversy and Consensus: Nuclear Beta Decay 1911–1934*, pp. 145–184. Springer, 2000.

[43] W. Pauli, *Dear radioactive ladies and gentlemen*, *Phys. Today* **31N9** (1978) 27.

[44] S. M. Bilenky, *Neutrino. History of a unique particle*, *Eur. Phys. J. H* **38** (2013) 345–404, [`1210.3065`].

[45] E. Fermi, *An attempt of a theory of beta radiation. 1.*, *Z. Phys.* **88** (1934) 161–177.

[46] H. Bethe and R. Peierls, *The 'neutrino'*, *Nature* **133** (1934) 532.

[47] F. Reines and C. L. Cowan, *The neutrino*, *Nature* **178** (1956) 446–449.

[48] L. Bonolis, *Bruno pontecorvo: From slow neutrons to oscillating neutrinos*, *American journal of physics* **73** (2005) 487–499.

[49] C. L. Cowan, F. Reines, F. B. Harrison, H. W. Kruse and A. D. McGuire, *Detection of the free neutrino: A Confirmation*, *Science* **124** (1956) 103–104.

[50] C. S. Wu, E. Ambler, R. W. Hayward, D. D. Hoppes and R. P. Hudson, *Experimental Test of Parity Conservation in β Decay*, *Phys. Rev.* **105** (1957) 1413–1414.

[51] T. D. Lee and C.-N. Yang, *Parity Nonconservation and a Two Component Theory of the Neutrino*, *Phys. Rev.* **105** (1957) 1671–1675.

[52] R. H. Dalitz, *On the analysis of tau-meson data and the nature of the tau-meson*, *Phil. Mag. Ser. 7* **44** (1953) 1068–1080.

[53] G. Danby, J. M. Gaillard, K. A. Goulianos, L. M. Lederman, N. B. Mistry, M. Schwartz et al., *Observation of High-Energy Neutrino Reactions and the Existence of Two Kinds of Neutrinos*, *Phys. Rev. Lett.* **9** (1962) 36–44.

[54] M. Schwartz, *Feasibility of using high-energy neutrinos to study the weak interactions*, *Phys. Rev. Lett.* **4** (1960) 306–307.

[55] B. Pontecorvo, *Electron and Muon Neutrinos*, *Zh. Eksp. Teor. Fiz.* **37** (1959) 1751–1757.

[56] M. Goldhaber, L. Grodzins and A. W. Sunyar, *Helicity of Neutrinos*, *Phys. Rev.* **109** (1958) 1015–1017.

[57] A. Salam, *On parity conservation and neutrino mass*, *Nuovo Cim.* **5** (1957) 299–301.

[58] L. D. Landau, *On the conservation laws for weak interactions*, *Nucl. Phys.* **3** (1957) 127–131.

[59] J. J. Sakurai, *Mass reversal and weak interactions*, *Il Nuovo Cimento (1955-1965)* **7** (1958) 649–660.

[60] E. C. G. Sudarshan and R. e. Marshak, *Chirality invariance and the universal Fermi interaction*, *Phys. Rev.* **109** (1958) 1860–1860.

[61] R. P. Feynman and M. Gell-Mann, *Theory of Fermi interaction*, *Phys. Rev.* **109** (1958) 193–198.

[62] S. L. Glashow, *Partial Symmetries of Weak Interactions*, *Nucl. Phys.* **22** (1961) 579–588.

[63] S. Weinberg, *A Model of Leptons*, *Phys. Rev. Lett.* **19** (1967) 1264–1266.

[64] A. Salam, *Weak and Electromagnetic Interactions*, *Conf. Proc. C* **680519** (1968) 367–377.

[65] M. E. Peskin and D. V. Schroeder, *An Introduction to quantum field theory*. Addison-Wesley, Reading, USA, 1995.

[66] M. D. Schwartz, *Quantum Field Theory and the Standard Model*. Cambridge University Press, 3, 2014.

[67] C. Giunti and C. W. Kim, *Fundamentals of neutrino physics and astrophysics*. Oxford university press, 2007.

[68] M. Gell-Mann, *The interpretation of the new particles as displaced charge multiplets*, *Nuovo Cim.* **4** (1956) 848–866.

[69] K. Nishijima, *Charge Independence Theory of V Particles*, *Prog. Theor. Phys.* **13** (1955) 285–304.

[70] PARTICLE DATA GROUP collaboration, R. L. Workman and Others, *Review of Particle Physics*, *PTEP* **2022** (2022) 083C01.

[71] E. G. Adelberger et al., *Solar fusion cross sections II: the pp chain and CNO cycles*, *Rev. Mod. Phys.* **83** (2011) 195, [`1004.2318`].

[72] BOREXINO collaboration, M. Agostini et al., *Experimental evidence of neutrinos produced in the CNO fusion cycle in the Sun*, *Nature* **587** (2020) 577–582, [2006.15115].

[73] E. Vitagliano, J. Redondo and G. Raffelt, *Solar neutrino flux at keV energies*, *JCAP* **12** (2017) 010, [1708.02248].

[74] N. Vinyoles, A. M. Serenelli, F. L. Villante, S. Basu, J. Bergström, M. C. Gonzalez-Garcia et al., *A new Generation of Standard Solar Models*, *Astrophys. J.* **835** (2017) 202, [1611.09867].

[75] V. Castellani, S. Degl'Innocenti, G. Fiorentini, M. Lissia and B. Ricci, *Solar neutrinos: Beyond standard solar models*, *Phys. Rept.* **281** (1997) 309–398, [astro-ph/9606180].

[76] J. N. Bahcall, M. H. Pinsonneault and S. Basu, *Solar models: Current epoch and time dependences, neutrinos, and helioseismological properties*, *Astrophys. J.* **555** (2001) 990–1012, [astro-ph/0010346].

[77] N. Grevesse and A. J. Sauval, *Standard Solar Composition*, *Space Science Reviews* **85** (May, 1998) 161–174.

[78] M. Asplund, N. Grevesse, A. J. Sauval and P. Scott, *The chemical composition of the Sun*, *Ann. Rev. Astron. Astrophys.* **47** (2009) 481–522, [0909.0948].

[79] J. N. Bahcall, A. M. Serenelli and S. Basu, *New solar opacities, abundances, helioseismology, and neutrino fluxes*, *Astrophys. J. Lett.* **621** (2005) L85–L88, [astro-ph/0412440].

[80] F. Delahaye and M. Pinsonneault, *The solar heavy element abundances. 1. constraints from stellar interiors*, *Astrophys. J.* **649** (2006) 529–540, [astro-ph/0511779].

[81] S. Basu and H. M. Antia, *Constraining solar abundances using helioseismology*, *Astrophys. J. Lett.* **606** (2004) L85, [`astro-ph/0403485`].

[82] S. Basu and H. M. Antia, *Helioseismology and Solar Abundances*, *Phys. Rept.* **457** (2008) 217–283, [`0711.4590`].

[83] J. N. Bahcall, S. Basu, M. Pinsonneault and A. M. Serenelli, *Helioseismological implications of recent solar abundance determinations*, *Astrophys. J.* **618** (2005) 1049–1056, [`astro-ph/0407060`].

[84] A. Serenelli, S. Basu, J. W. Ferguson and M. Asplund, *New Solar Composition: The Problem With Solar Models Revisited*, *Astrophys. J. Lett.* **705** (2009) L123–L127, [`0909.2668`].

[85] J. N. Bahcall, *Solar neutrinos. I: Theoretical*, *Phys. Rev. Lett.* **12** (1964) 300–302.

[86] R. Davis, *Solar neutrinos. II: Experimental*, *Phys. Rev. Lett.* **12** (1964) 303–305.

[87] B. Pontecorvo, *Inverse beta process*, *Camb. Monogr. Part. Phys. Nucl. Phys. Cosmol.* **1** (1991) 25–31.

[88] R. Davis, Jr., D. S. Harmer and K. C. Hoffman, *Search for neutrinos from the sun*, *Phys. Rev. Lett.* **20** (1968) 1205–1209.

[89] J. N. Bahcall, N. A. Bahcall and G. Shaviv, *Present status of the theoretical predictions for the Cl-36 solar neutrino experiment*, *Phys. Rev. Lett.* **20** (1968) 1209–1212.

[90] KAMIOKANDE-II collaboration, K. S. Hirata et al., *Search for B-8 solar neutrinos at KAMIOKANDE-II*, in *2nd Workshop on Elementary Particle Picture of the Universe*, pp. 150–162, 1988.

[91] KAMIOKANDE-II collaboration, K. S. Hirata et al., *Observation of B-8 Solar Neutrinos in the Kamiokande-II Detector*, *Phys. Rev. Lett.* **63** (1989) 16.

[92] Kamiokande-II collaboration, K. S. Hirata et al., *Search for day / night and semiannual variations in the solar neutrino flux observed in the Kamiokande-II detector*, *Phys. Rev. Lett.* **66** (1991) 9–12.

[93] Kamiokande-II collaboration, K. S. Hirata et al., *Constraints on neutrino oscillation parameters from the Kamiokande-II solar neutrino data*, *Phys. Rev. Lett.* **65** (1990) 1301–1304.

[94] Kamiokande-II collaboration, K. S. Hirata et al., *Results from one thousand days of real time directional solar neutrino data*, *Phys. Rev. Lett.* **65** (1990) 1297–1300.

[95] Kamiokande-II collaboration, K. S. Hirata et al., *Real time, directional measurement of B-8 solar neutrinos in the Kamiokande-II detector*, *Phys. Rev. D* **44** (1991) 2241.

[96] Kamiokande-II collaboration, K. S. Hirata et al., *Observation of a small atmospheric muon-neutrino / electron-neutrino ratio in Kamiokande*, *Phys. Lett. B* **280** (1992) 146–152.

[97] SAGE collaboration, A. I. Abazov et al., *Search for neutrinos from the sun with the reaction Ga-71(nu/e,e-)Ge-71 by the Soviet-American Gallium Experiment (SAGE)*, in *International Workshop on Neutrino Telescopes, 3rd*, 1991.

[98] SAGE collaboration, J. N. Abdurashitov et al., *Results from SAGE*, *Phys. Lett. B* **328** (1994) 234–248.

[99] SAGE collaboration, J. N. Abdurashitov et al., *Measurement of the response of the Russian-American gallium experiment to neutrinos from a Cr-51 source*, *Phys. Rev. C* **59** (1999) 2246–2263, [`hep-ph/9803418`].

[100] SAGE collaboration, J. N. Abdurashitov et al., *Measurement of the solar neutrino capture rate with gallium metal*, *Phys. Rev. C* **60** (1999) 055801, [`astro-ph/9907113`].

[101] SAGE collaboration, J. N. Abdurashitov et al., *Solar neutrino flux measurements by the Soviet-American Gallium Experiment (SAGE) for half the 22 year solar cycle*, *J. Exp. Theor. Phys.* **95** (2002) 181–193, [`astro-ph/0204245`].

[102] SAGE collaboration, J. N. Abdurashitov et al., *Measurement of the solar neutrino capture rate with gallium metal. III: Results for the 2002–2007 data-taking period*, *Phys. Rev. C* **80** (2009) 015807, [`0901.2200`].

[103] GALLEX collaboration, P. Anselmann et al., *GALLEX solar neutrino observations: The Results from GALLEX-I and early results from GALLEX-II*, *Phys. Lett. B* **314** (1993) 445–458.

[104] GALLEX collaboration, P. Anselmann et al., *GALLEX solar neutrino observations: Complete results for GALLEX II*, *Phys. Lett. B* **357** (1995) 237–247.

[105] GALLEX collaboration, W. Hampel et al., *GALLEX solar neutrino observations: Results for GALLEX III.*, *Phys. Lett. B* **388** (1996) 384–396.

[106] GALLEX collaboration, W. Hampel et al., *GALLEX solar neutrino observations: Results for GALLEX IV*, *Phys. Lett. B* **447** (1999) 127–133.

[107] J. N. Bahcall and R. K. Ulrich, *Solar Models, Neutrino Experiments and Helioseismology*, *Rev. Mod. Phys.* **60** (1988) 297–372.

[108] J. N. Bahcall and H. A. Bethe, *Do solar neutrino experiments imply new physics?*, *Phys. Rev. D* **47** (1993) 1298–1301, [`hep-ph/9212204`].

[109] B. Pontecorvo, *Neutrino Experiments and the Problem of Conservation of Leptonic Charge*, *Zh. Eksp. Teor. Fiz.* **53** (1967) 1717–1725.

[110] V. N. Gribov and B. Pontecorvo, *Neutrino astronomy and lepton charge*, *Phys. Lett. B* **28** (1969) 493.

[111] S. P. Mikheyev and A. Y. Smirnov, *Resonance Amplification of Oscillations in Matter and Spectroscopy of Solar Neutrinos*, *Sov. J. Nucl. Phys.* **42** (1985) 913–917.

[112] S. P. Mikheev and A. Y. Smirnov, *Resonant amplification of neutrino oscillations in matter and solar neutrino spectroscopy*, *Nuovo Cim. C* **9** (1986) 17–26.

[113] L. Wolfenstein, *Neutrino Oscillations and Stellar Collapse*, *Phys. Rev. D* **20** (1979) 2634–2635.

[114] E. Roulet, *MSW effect with flavor changing neutrino interactions*, *Phys. Rev. D* **44** (1991) R935–R938.

[115] M. M. Guzzo, A. Masiero and S. T. Petcov, *On the MSW effect with massless neutrinos and no mixing in the vacuum*, *Phys. Lett. B* **260** (1991) 154–160.

[116] J. N. Bahcall, N. Cabibbo and A. Yahil, *Are neutrinos stable particles?*, *Phys. Rev. Lett.* **28** (1972) 316–318.

[117] C.-S. Lim and W. J. Marciano, *Resonant Spin - Flavor Precession of Solar and Supernova Neutrinos*, *Phys. Rev. D* **37** (1988) 1368–1373.

[118] E. K. Akhmedov, *Resonant Amplification of Neutrino Spin Rotation in Matter and the Solar Neutrino Problem*, *Phys. Lett. B* **213** (1988) 64–68.

[119] A. Cisneros, *Effect of neutrino magnetic moment on solar neutrino observations*, *Astrophys. Space Sci.* **10** (1971) 87–92.

[120] SNO collaboration, J. Boger et al., *The Sudbury neutrino observatory*, *Nucl. Instrum. Meth. A* **449** (2000) 172–207, [`nucl-ex/9910016`].

[121] SNO collaboration, Q. R. Ahmad et al., *Measurement of the rate of* $\nu_e + d \to p + p + e^-$ *interactions produced by* ^8B *solar neutrinos at the Sudbury Neutrino Observatory*, *Phys. Rev. Lett.* **87** (2001) 071301, [`nucl-ex/0106015`].

[122] SNO collaboration, Q. R. Ahmad et al., *Measurement of day and night neutrino energy spectra at SNO and constraints on neutrino mixing parameters*, *Phys. Rev. Lett.* **89** (2002) 011302, [`nucl-ex/0204009`].

[123] SNO collaboration, Q. R. Ahmad et al., *Direct evidence for neutrino flavor transformation from neutral current interactions in the Sudbury Neutrino Observatory*, *Phys. Rev. Lett.* **89** (2002) 011301, [`nucl-ex/0204008`].

[124] SUPER-KAMIOKANDE collaboration, Y. Fukuda et al., *Measurements of the solar neutrino flux from Super-Kamiokande's first 300 days*, *Phys. Rev. Lett.* **81** (1998) 1158–1162, [`hep-ex/9805021`].

[125] SUPER-KAMIOKANDE collaboration, Y. Fukuda et al., *Measurement of the solar neutrino energy spectrum using neutrino electron scattering*, *Phys. Rev. Lett.* **82** (1999) 2430–2434, [`hep-ex/9812011`].

[126] SUPER-KAMIOKANDE collaboration, Y. Fukuda et al., *Evidence for oscillation of atmospheric neutrinos*, *Phys. Rev. Lett.* **81** (1998) 1562–1567, [`hep-ex/9807003`].

[127] C. Giganti, S. Lavignac and M. Zito, *Neutrino oscillations: The rise of the PMNS paradigm*, *Prog. Part. Nucl. Phys.* **98** (2018) 1–54, [`1710.00715`].

[128] I. Esteban, M. C. Gonzalez-Garcia, M. Maltoni, T. Schwetz and A. Zhou, *The fate of hints: updated global analysis of three-flavor neutrino oscillations*, *JHEP* **09** (2020) 178, [`2007.14792`].

[129] J. N. Bahcall, A. M. Serenelli and S. Basu, *10,000 standard solar models: a Monte Carlo simulation*, *Astrophys. J. Suppl.* **165** (2006) 400–431, [astro-ph/0511337].

[130] MINOS collaboration, P. Adamson et al., *Electron neutrino and antineutrino appearance in the full MINOS data sample*, *Phys. Rev. Lett.* **110** (2013) 171801, [1301.4581].

[131] T2K collaboration, K. Abe et al., *The T2K Experiment*, *Nucl. Instrum. Meth. A* **659** (2011) 106–135, [1106.1238].

[132] NOvA collaboration, D. S. Ayres et al., *NOvA: Proposal to Build a 30 Kiloton Off-Axis Detector to Study $\nu_\mu \to \nu_e$ Oscillations in the NuMI Beamline*, hep-ex/0503053.

[133] Super-Kamiokande collaboration, Y. Fukuda et al., *The Super-Kamiokande detector*, *Nucl. Instrum. Meth. A* **501** (2003) 418–462.

[134] IceCube collaboration, R. Abbasi et al., *The Design and Performance of IceCube DeepCore*, *Astropart. Phys.* **35** (2012) 615–624, [1109.6096].

[135] KamLAND collaboration, K. Eguchi et al., *First results from KamLAND: Evidence for reactor anti-neutrino disappearance*, *Phys. Rev. Lett.* **90** (2003) 021802, [hep-ex/0212021].

[136] Double Chooz collaboration, F. Ardellier et al., *Double Chooz: A Search for the neutrino mixing angle theta(13)*, hep-ex/0606025.

[137] Daya Bay collaboration, F. P. An et al., *Measurement of electron antineutrino oscillation based on 1230 days of operation of the Daya Bay experiment*, *Phys. Rev. D* **95** (2017) 072006, [1610.04802].

[138] I. Esteban, M. C. Gonzalez-Garcia, A. Hernandez-Cabezudo, M. Maltoni and T. Schwetz, *Global analysis of three-flavour neutrino oscillations: synergies*

and tensions in the determination of θ_{23}, δ_{CP}, and the mass ordering, *JHEP* **01** (2019) 106, [`1811.05487`].

[139] I. M. Shoemaker and J. Wyenberg, *Direct Detection Experiments at the Neutrino Dipole Portal Frontier*, *Phys. Rev. D* **99** (2019) 075010, [`1811.12435`].

[140] I. M. Shoemaker and E. Welch, *Sailing the CEνNS Seas of Non-Standard Neutrino Interactions with the Coherent CAPTAIN Mills Experiment*, `2103.08401`.

[141] M. J. Dolinski, A. W. P. Poon and W. Rodejohann, *Neutrinoless Double-Beta Decay: Status and Prospects*, *Ann. Rev. Nucl. Part. Sci.* **69** (2019) 219–251, [`1902.04097`].

[142] S. M. Bilenky and C. Giunti, *Neutrinoless Double-Beta Decay: a Probe of Physics Beyond the Standard Model*, *Int. J. Mod. Phys. A* **30** (2015) 1530001, [`1411.4791`].

[143] W. Rodejohann, *Neutrino-less Double Beta Decay and Particle Physics*, *Int. J. Mod. Phys. E* **20** (2011) 1833–1930, [`1106.1334`].

[144] S. F. King, *Neutrino mass models*, *Rept. Prog. Phys.* **67** (2004) 107–158, [`hep-ph/0310204`].

[145] R. N. Mohapatra and A. Y. Smirnov, *Neutrino Mass and New Physics*, *Ann. Rev. Nucl. Part. Sci.* **56** (2006) 569–628, [`hep-ph/0603118`].

[146] A. Vicente and C. E. Yaguna, *Probing the scotogenic model with lepton flavor violating processes*, *JHEP* **02** (2015) 144, [`1412.2545`].

[147] T. Toma and A. Vicente, *Lepton Flavor Violation in the Scotogenic Model*, *JHEP* **01** (2014) 160, [`1312.2840`].

[148] A. Drukier and L. Stodolsky, *Principles and Applications of a Neutral Current Detector for Neutrino Physics and Astronomy*, *Phys. Rev. D* **30** (1984) 2295.

[149] M. W. Goodman and E. Witten, *Detectability of Certain Dark Matter Candidates*, *Phys. Rev. D* **31** (1985) 3059.

[150] G. Jungman, M. Kamionkowski and K. Griest, *Supersymmetric dark matter*, *Phys. Rept.* **267** (1996) 195–373, [`hep-ph/9506380`].

[151] M. Schumann, *Direct Detection of WIMP Dark Matter: Concepts and Status*, *J. Phys. G* **46** (2019) 103003, [`1903.03026`].

[152] T. Marrodán Undagoitia and L. Rauch, *Dark matter direct-detection experiments*, *J. Phys. G* **43** (2016) 013001, [`1509.08767`].

[153] XENON collaboration, E. Aprile et al., *The XENON1T Dark Matter Experiment*, *Eur. Phys. J.* **C77** (2017) 881, [`1708.07051`].

[154] G. Battistoni, A. Ferrari, T. Montaruli and P. R. Sala, *The FLUKA atmospheric neutrino flux calculation*, *Astropart. Phys.* **19** (2003) 269–290, [`hep-ph/0207035`].

[155] J. F. Beacom, *The Diffuse Supernova Neutrino Background*, *Ann. Rev. Nucl. Part. Sci.* **60** (2010) 439–462, [`1004.3311`].

[156] G. Fiorentini, M. Lissia and F. Mantovani, *Geo-neutrinos and Earth's interior*, *Phys. Rept.* **453** (2007) 117–172, [`0707.3203`].

[157] LUX-ZEPLIN collaboration, D. S. Akerib et al., *Projected WIMP sensitivity of the LUX-ZEPLIN dark matter experiment*, *Phys. Rev. D* **101** (2020) 052002, [`1802.06039`].

[158] XENON collaboration, E. Aprile et al., *Dark Matter Search Results from a One Ton-Year Exposure of XENON1T*, *Phys. Rev. Lett.* **121** (2018) 111302, [`1805.12562`].

[159] LZ collaboration, J. Aalbers et al., *First Dark Matter Search Results from the LUX-ZEPLIN (LZ) Experiment*, `2207.03764`.

[160] J. Billard et al., *Direct detection of dark matter—APPEC committee report**, *Rept. Prog. Phys.* **85** (2022) 056201, [`2104.07634`].

[161] J. Billard, L. Strigari and E. Figueroa-Feliciano, *Implication of neutrino backgrounds on the reach of next generation dark matter direct detection experiments*, *Phys. Rev. D* **89** (2014) 023524, [`1307.5458`].

[162] F. Ruppin, J. Billard, E. Figueroa-Feliciano and L. Strigari, *Complementarity of dark matter detectors in light of the neutrino background*, *Phys. Rev. D* **90** (2014) 083510, [`1408.3581`].

[163] S. Sassi, A. Dinmohammadi, M. Heikinheimo, N. Mirabolfathi, K. Nordlund, H. Safari et al., *Solar neutrinos and dark matter detection with diurnal modulation*, *Phys. Rev. D* **104** (2021) 063037, [`2103.08511`].

[164] J. H. Davis, *Dark Matter vs. Neutrinos: The effect of astrophysical uncertainties and timing information on the neutrino floor*, *JCAP* **03** (2015) 012, [`1412.1475`].

[165] P. Grothaus, M. Fairbairn and J. Monroe, *Directional Dark Matter Detection Beyond the Neutrino Bound*, *Phys. Rev. D* **90** (2014) 055018, [`1406.5047`].

[166] C. A. J. O'Hare, A. M. Green, J. Billard, E. Figueroa-Feliciano and L. E. Strigari, *Readout strategies for directional dark matter detection beyond the neutrino background*, *Phys. Rev. D* **92** (2015) 063518, [`1505.08061`].

[167] C. A. J. O'Hare, *Dark matter astrophysical uncertainties and the neutrino floor*, *Phys. Rev. D* **94** (2016) 063527, [`1604.03858`].

[168] G. B. Gelmini, V. Takhistov and S. J. Witte, *Casting a Wide Signal Net with Future Direct Dark Matter Detection Experiments*, *JCAP* **07** (2018) 009, [`1804.01638`].

[169] C. A. J. O'Hare, *New Definition of the Neutrino Floor for Direct Dark Matter Searches*, *Phys. Rev. Lett.* **127** (2021) 251802, [2109.03116].

[170] A. Gaspert, P. Giampa and D. E. Morrissey, *Neutrino backgrounds in future liquid noble element dark matter direct detection experiments*, *Phys. Rev. D* **105** (2022) 035020, [2108.03248].

[171] LZ collaboration, D. S. Akerib et al., *Projected sensitivities of the LUX-ZEPLIN (LZ) experiment to new physics via low-energy electron recoils*, 2102.11740.

[172] XENON collaboration, E. Aprile et al., *Search for Coherent Elastic Scattering of Solar* ^8B *Neutrinos in the XENON1T Dark Matter Experiment*, *Phys. Rev. Lett.* **126** (2021) 091301, [2012.02846].

[173] D. Aristizabal Sierra, B. Dutta, S. Liao and L. E. Strigari, *Coherent elastic neutrino-nucleus scattering in multi-ton scale dark matter experiments: Classification of vector and scalar interactions new physics signals*, *JHEP* **12** (2019) 124, [1910.12437].

[174] R. Harnik, J. Kopp and P. A. N. Machado, *Exploring nu Signals in Dark Matter Detectors*, *JCAP* **1207** (2012) 026, [1202.6073].

[175] Y. Cui, M. Pospelov and J. Pradler, *Signatures of Dark Radiation in Neutrino and Dark Matter Detectors*, *Phys. Rev. D* **97** (2018) 103004, [1711.04531].

[176] J. Billard, L. E. Strigari and E. Figueroa-Feliciano, *Solar neutrino physics with low-threshold dark matter detectors*, *Phys. Rev. D* **91** (2015) 095023, [1409.0050].

[177] B. Dutta and L. E. Strigari, *Neutrino physics with dark matter detectors*, *Ann. Rev. Nucl. Part. Sci.* **69** (2019) 137–161, [1901.08876].

[178] B. Dutta, S. Liao, L. E. Strigari and J. W. Walker, *Non-standard interactions of solar neutrinos in dark matter experiments*, *Phys. Lett. B* **773** (2017) 242–246, [1705.00661].

[179] J. L. Newstead, L. E. Strigari and R. F. Lang, *Detecting CNO solar neutrinos in next-generation xenon dark matter experiments*, *Phys. Rev. D* **99** (2019) 043006, [1807.07169].

[180] D. G. Cerdeño, M. Fairbairn, T. Jubb, P. A. N. Machado, A. C. Vincent and C. Bœhm, *Physics from solar neutrinos in dark matter direct detection experiments*, *JHEP* **05** (2016) 118, [1604.01025].

[181] A. de Gouvêa, E. McGinness, I. Martinez-Soler and Y. F. Perez-Gonzalez, *pp Solar Neutrinos at DARWIN*, 2111.02421.

[182] R. Essig, M. Sholapurkar and T.-T. Yu, *Solar Neutrinos as a Signal and Background in Direct-Detection Experiments Searching for Sub-GeV Dark Matter With Electron Recoils*, *Phys. Rev.* **D97** (2018) 095029, [1801.10159].

[183] L. Baudis, A. Ferella, A. Kish, A. Manalaysay, T. Marrodan Undagoitia and M. Schumann, *Neutrino physics with multi-ton scale liquid xenon detectors*, *JCAP* **1401** (2014) 044, [1309.7024].

[184] D. Z. Freedman, *Coherent Neutrino Nucleus Scattering as a Probe of the Weak Neutral Current*, *Phys. Rev. D* **9** (1974) 1389–1392.

[185] COHERENT collaboration, D. Akimov et al., *Observation of Coherent Elastic Neutrino-Nucleus Scattering*, *Science* **357** (2017) 1123–1126, [1708.01294].

[186] D. Akimov et al., *Measurement of the Coherent Elastic Neutrino-Nucleus Scattering Cross Section on CsI by COHERENT*, 2110.07730.

[187] D. Z. Freedman, D. N. Schramm and D. L. Tubbs, *The Weak Neutral Current and Its Effects in Stellar Collapse*, *Ann. Rev. Nucl. Part. Sci.* **27** (1977) 167–207.

[188] J. D. Lewin and P. F. Smith, *Review of mathematics, numerical factors, and corrections for dark matter experiments based on elastic nuclear recoil*, *Astropart. Phys.* **6** (1996) 87–112.

[189] R. H. Helm, *Inelastic and Elastic Scattering of 187-Mev Electrons from Selected Even-Even Nuclei*, *Phys. Rev.* **104** (1956) 1466–1475.

[190] G. Fricke, C. Bernhardt, K. Heilig, L. A. Schaller, L. Schellenberg, E. B. Shera et al., *Nuclear Ground State Charge Radii from Electromagnetic Interactions*, *Atom. Data Nucl. Data Tabl.* **60** (1995) 177–285.

[191] D. Aristizabal Sierra, J. Liao and D. Marfatia, *Impact of form factor uncertainties on interpretations of coherent elastic neutrino-nucleus scattering data*, *JHEP* **06** (2019) 141, [`1902.07398`].

[192] D. Aristizabal Sierra, V. De Romeri, L. J. Flores and D. K. Papoulias, *Impact of COHERENT measurements, cross section uncertainties and new interactions on the neutrino floor*, *JCAP* **01** (2022) 055, [`2109.03247`].

[193] W. J. Marciano and Z. Parsa, *Neutrino electron scattering theory*, *J. Phys.* **G29** (2003) 2629–2645, [`hep-ph/0403168`].

[194] J.-W. Chen, H.-C. Chi, C. P. Liu and C.-P. Wu, *Low-energy electronic recoil in xenon detectors by solar neutrinos*, *Phys. Lett. B* **774** (2017) 656–661, [`1610.04177`].

[195] V. I. Kopeikin, L. A. Mikaelyan, V. V. Sinev and S. A. Fayans, *Scattering of reactor antineutrinos by electrons*, *Physics of Atomic Nuclei* **60** (Nov., 1997) 1859–1864.

[196] K. A. Kouzakov, A. I. Studenikin and M. B. Voloshin, *Neutrino-impact ionization of atoms in searches for neutrino magnetic moment*, *Phys. Rev. D* **83** (2011) 113001, [`1101.4878`].

[197] K. A. Kouzakov and A. I. Studenikin, *Electromagnetic Neutrino-Atom Collisions: The Role of Electron Binding*, *Nucl. Phys. B Proc. Suppl.* **217** (2011) 353–356, [`1108.2872`].

[198] M. B. Voloshin, *Neutrino scattering on atomic electrons in searches for neutrino magnetic moment*, *Phys. Rev. Lett.* **105** (2010) 201801, [`1008.2171`].

[199] J.-W. Chen, H.-C. Chi, K.-N. Huang, C. P. Liu, H.-T. Shiao, L. Singh et al., *Atomic ionization of germanium by neutrinos from an ab initio approach*, *Phys. Lett. B* **731** (2014) 159–162, [`1311.5294`].

[200] K.-N. Huang, W. Johnson and K. Cheng, *Theoretical photoionization parameters for the noble gases argon, krypton, and xenon*, *Atomic Data and Nuclear Data Tables* **26** (1981) 33–45.

[201] K. N. Huang, W. R. Johnson and K. T. Cheng, *Theoretical study of spin polarization of photoelectrons from noble gases*, *Phys. Rev. Lett.* **43** (Nov, 1979) 1658–1661.

[202] W. R. Johnson and K. T. Cheng, *Photoionization of the outer shells of neon, argon, krypton, and xenon using the relativistic random-phase approximation*, *Phys. Rev. A* **20** (Sep, 1979) 978–988.

[203] W. R. Johnson and C. D. Lin, *Multichannel relativistic random-phase approximation for the photoionization of atoms*, *Phys. Rev. A* **20** (Sep, 1979) 964–977.

[204] J.-W. Chen, H.-C. Chi, K.-N. Huang, H.-B. Li, C. P. Liu, L. Singh et al., *Constraining neutrino electromagnetic properties by germanium detectors*, *Phys. Rev. D* **91** (2015) 013005, [1411.0574].

[205] C.-C. Hsieh, L. Singh, C.-P. Wu, J.-W. Chen, H.-C. Chi, C. P. Liu et al., *Discovery potential of multiton xenon detectors in neutrino electromagnetic properties*, *Phys. Rev. D* **100** (2019) 073001, [1903.06085].

[206] J. Lindhard, V. Nielsen, M. Scharff and P. V. Thomsen, *Integral equations governing radiation effects. (notes on atomic collisions, iii)*, .

[207] LUX collaboration, D. S. Akerib et al., *Low-energy (0.7-74 keV) nuclear recoil calibration of the LUX dark matter experiment using D-D neutron scattering kinematics*, 1608.05381.

[208] B. J. Scholz, A. E. Chavarria, J. I. Collar, P. Privitera and A. E. Robinson, *Measurement of the low-energy quenching factor in germanium using an ^{88}Y/Be photoneutron source*, *Phys. Rev. D* **94** (2016) 122003, [1608.03588].

[209] P. Agnes et al., *Measurement of the liquid argon energy response to nuclear and electronic recoils*, *Phys. Rev. D* **97** (2018) 112005, [1801.06653].

[210] SuperCDMS collaboration, R. Agnese et al., *Low-mass dark matter search with CDMSlite*, *Phys. Rev.* **D97** (2018) 022002, [1707.01632].

[211] A. Bonhomme et al., *Direct measurement of the ionization quenching factor of nuclear recoils in germanium in the keV energy range*, 2202.03754.

[212] A. N. Khan, $\sin^2\theta_W$ *and neutrino electromagnetic interactions in CE$\bar{\nu}_e$NS with different quenching factors*, 2203.08892.

[213] Y. Sarkis, A. Aguilar-Arevalo and J. C. D'Olivo, *Study of the ionization efficiency for nuclear recoils in pure crystals*, 2001.06503.

[214] B. J. Mount et al., *LUX-ZEPLIN (LZ) Technical Design Report*, 1703.09144.

[215] XENON collaboration, E. Aprile et al., *Physics reach of the XENON1T dark matter experiment*, *JCAP* **1604** (2016) 027, [`1512.07501`].

[216] XENON10 collaboration, J. Angle et al., *A search for light dark matter in XENON10 data*, *Phys. Rev. Lett.* **107** (2011) 051301, [`1104.3088`].

[217] XENON collaboration, E. Aprile et al., *Low-mass dark matter search using ionization signals in XENON100*, *Phys. Rev. D* **94** (2016) 092001, [`1605.06262`].

[218] XENON collaboration, E. Aprile et al., *Light Dark Matter Search with Ionization Signals in XENON1T*, *Phys. Rev. Lett.* **123** (2019) 251801, [`1907.11485`].

[219] P. Sorensen and C. E. Dahl, *Nuclear recoil energy scale in liquid xenon with application to the direct detection of dark matter*, *Phys. Rev. D* **83** (2011) 063501, [`1101.6080`].

[220] P. Sorensen et al., *Lowering the low-energy threshold of xenon detectors*, *PoS* **IDM2010** (2011) 017, [`1011.6439`].

[221] PandaX-II collaboration, B. Yan et al., *Determination of responses of liquid xenon to low energy electron and nuclear recoils using a PandaX-II detector*, *Chin. Phys. C* **45** (2021) 075001, [`2102.09158`].

[222] H. Araújo, *Revised performance parameters of the ZEPLIN-III dark matter experiment*, `2007.01683`.

[223] M. Horn et al., *Nuclear recoil scintillation and ionisation yields in liquid xenon from ZEPLIN-III data*, *Phys. Lett. B* **705** (2011) 471–476, [`1106.0694`].

[224] XENON100 collaboration, E. Aprile et al., *Response of the XENON100 Dark Matter Detector to Nuclear Recoils*, *Phys. Rev. D* **88** (2013) 012006, [`1304.1427`].

[225] XENON10 collaboration, P. Sorensen et al., *The scintillation and ionization yield of liquid xenon for nuclear recoils*, *Nucl. Instrum. Meth. A* **601** (2009) 339–346, [`0807.0459`].

[226] XENON collaboration, E. Aprile et al., *XENON1T Dark Matter Data Analysis: Signal Reconstruction, Calibration and Event Selection*, *Phys. Rev. D* **100** (2019) 052014, [`1906.04717`].

[227] XENON collaboration, E. Aprile et al., *XENON1T dark matter data analysis: Signal and background models and statistical inference*, *Phys. Rev. D* **99** (2019) 112009, [`1902.11297`].

[228] M. Szydagis et al., *A Review of Basic Energy Reconstruction Techniques in Liquid Xenon and Argon Detectors for Dark Matter and Neutrino Physics Using NEST*, *Instruments* **5** (2021) 13, [`2102.10209`].

[229] SuperCDMS collaboration, R. W. Schnee et al., *The SuperCDMS Experiment*, in *5th International Heidelberg Conference on Dark Matter in Astro and Particle Physics*, 2, 2005, `astro-ph/0502435`.

[230] P. N. Luke, *Voltageassisted calorimetric ionization detector*, *Journal of Applied Physics* **64** (1988) 6858–6860, [`https://doi.org/10.1063/1.341976`].

[231] B. S. Neganov and V. N. Trofimov, *Colorimetric method measuring ionizing radiation*, *Otkryt. Izobret.* **146** (1985) 215.

[232] SuperCDMS collaboration, M. F. Albakry et al., *Ionization yield measurement in a germanium CDMSlite detector using photo-neutron sources*, *Phys. Rev. D* **105** (2022) 122002, [`2202.07043`].

[233] K. W. Jones and H. W. Kraner, *Stopping of 1- to 1.8-kev* ^{73}Ge *atoms in germanium*, *Phys. Rev. C* **4** (Jul, 1971) 125–129.

[234] K. W. Jones and H. W. Kraner, *Energy lost to ionization by 254-ev* ^{73}Ge *atoms stopping in ge*, *Phys. Rev. A* **11** (Apr, 1975) 1347–1353.

[235] CoGeNT collaboration, C. E. Aalseth et al., *CoGeNT: A Search for Low-Mass Dark Matter using p-type Point Contact Germanium Detectors*, *Phys. Rev. D* **88** (2013) 012002, [`1208.5737`].

[236] CDMS-II collaboration, Z. Ahmed et al., *Results from a Low-Energy Analysis of the CDMS II Germanium Data*, *Phys. Rev. Lett.* **106** (2011) 131302, [`1011.2482`].

[237] Y. Messous, *Calibration of a Ge crystal with nuclear recoils for the development of a dark matter detector*, *Astropart. Phys.* **3** (1995) 361–366.

[238] T. Shutt, B. Ellman, P. D. Barnes, A. Cummings, A. Da Silva, J. Emes et al., *Measurement of ionization and phonon production by nuclear recoils in a 60 g crystal of germanium at 25 mk*, *Phys. Rev. Lett.* **69** (Dec, 1992) 3425–3427.

[239] C. Chasman, K. W. Jones, H. W. Kraner and W. Brandt, *Band-gap effects in the stopping of* ge^{72*} *atoms in germanium*, *Phys. Rev. Lett.* **21** (Nov, 1968) 1430–1433.

[240] EDELWEISS collaboration, A. Benoit et al., *Measurement of the response of heat-and-ionization germanium detectors to nuclear recoils*, *Nucl. Instrum. Meth. A* **577** (2007) 558–568, [`astro-ph/0607502`].

[241] A. R. Sattler, F. L. Vook and J. M. Palms, *Ionization produced by energetic germanium atoms within a germanium lattice*, *Phys. Rev.* **143** (Mar, 1966) 588–594.

[242] J. I. Collar, A. R. L. Kavner and C. M. Lewis, *Germanium response to sub-keV nuclear recoils: a multipronged experimental characterization*, *Phys. Rev. D* **103** (2021) 122003, [`2102.10089`].

[243] L. Baudis, J. Hellmig, H. V. Klapdor-Kleingrothaus, Y. A. Ramachers, J. W. Hammer and A. Mayer, *High purity germanium detector ionization pulse shapes of nuclear recoils, gamma interactions and microphonism*, *Nucl. Instrum. Meth. A* **418** (1998) 348–354, [`hep-ex/9901028`].

[244] M. Schumann, *Dark Matter Search with liquid Noble Gases*, `1206.2169`.

[245] M. G. Boulay and A. Hime, *Technique for direct detection of weakly interacting massive particles using scintillation time discrimination in liquid argon*, *Astropart. Phys.* **25** (2006) 179–182.

[246] D. M. Mei, Z. B. Yin, L. C. Stonehill and A. Hime, *A Model of Nuclear Recoil Scintillation Efficiency in Noble Liquids*, *Astropart. Phys.* **30** (2008) 12–17, [`0712.2470`].

[247] J. B. Birks, *Scintillations from Organic Crystals: Specific Fluorescence and Relative Response to Different Radiations*, *Proc. Phys. Soc. A* **64** (1951) 874–877.

[248] DarkSide collaboration, P. Agnes et al., *Simulation of argon response and light detection in the DarkSide-50 dual phase TPC*, *JINST* **12** (2017) P10015, [`1707.05630`].

[249] W. Creus, Y. Allkofer, C. Amsler, A. D. Ferella, J. Rochet, L. Scotto-Lavina et al., *Scintillation efficiency of liquid argon in low energy neutron-argon scattering*, *JINST* **10** (2015) P08002, [`1504.07878`].

[250] M. Kimura, M. Tanaka, T. Washimi and K. Yorita, *Measurement of the scintillation efficiency for nuclear recoils in liquid argon under electric fields up to 3 kV/cm*, *Phys. Rev. D* **100** (2019) 032002, [`1902.01501`].

[251] SCENE collaboration, H. Cao et al., *Measurement of Scintillation and Ionization Yield and Scintillation Pulse Shape from Nuclear Recoils in Liquid Argon*, *Phys. Rev. D* **91** (2015) 092007, [`1406.4825`].

[252] P. A. M. Dirac, *The quantum theory of the electron. part ii*, *Proceedings of the Royal Society of London. Series A, Containing Papers of a Mathematical and Physical Character* **118** (1928) 351–361.

[253] D. E. Nagle, R. S. Julian and J. R. Zacharias, *The Hyperfine Structure of Atomic Hydrogen and Deuterium*, *Phys. Rev.* **72** (1947) 971–971.

[254] J. E. Nafe, E. B. Nelson and I. I. Rabi, *The Hyperfine Structure of Atomic Hydrogen and Deuterium*, *Phys. Rev.* **71** (1947) 914–915.

[255] J. Schwinger, *Schwinger 1948b*, *Phys. Rev* **73** (1948) 416.

[256] G. Colangelo, M. Hoferichter, A. Nyffeler, M. Passera and P. Stoffer, *Remarks on higher-order hadronic corrections to the muon g−2*, *Phys. Lett. B* **735** (2014) 90–91, [`1403.7512`].

[257] T. Blum, N. Christ, M. Hayakawa, T. Izubuchi, L. Jin, C. Jung et al., *Hadronic Light-by-Light Scattering Contribution to the Muon Anomalous Magnetic Moment from Lattice QCD*, *Phys. Rev. Lett.* **124** (2020) 132002, [`1911.08123`].

[258] G. Colangelo, F. Hagelstein, M. Hoferichter, L. Laub and P. Stoffer, *Longitudinal short-distance constraints for the hadronic light-by-light contribution to $(g-2)_\mu$ with large-N_c Regge models*, *JHEP* **03** (2020) 101, [`1910.13432`].

[259] J. Bijnens, N. Hermansson-Truedsson and A. Rodríguez-Sánchez, *Short-distance constraints for the HLbL contribution to the muon anomalous magnetic moment*, *Phys. Lett. B* **798** (2019) 134994, [`1908.03331`].

[260] A. Gérardin, H. B. Meyer and A. Nyffeler, *Lattice calculation of the pion transition form factor with $N_f = 2+1$ Wilson quarks*, *Phys. Rev. D* **100** (2019) 034520, [`1903.09471`].

[261] G. Colangelo, M. Hoferichter, M. Procura and P. Stoffer, *Dispersion relation for hadronic light-by-light scattering: two-pion contributions*, *JHEP* **04** (2017) 161, [1702.07347].

[262] M. Hoferichter, B.-L. Hoid, B. Kubis, S. Leupold and S. P. Schneider, *Dispersion relation for hadronic light-by-light scattering: pion pole*, *JHEP* **10** (2018) 141, [1808.04823].

[263] P. Masjuan and P. Sanchez-Puertas, *Pseudoscalar-pole contribution to the* $(g_\mu - 2)$*: a rational approach*, *Phys. Rev. D* **95** (2017) 054026, [1701.05829].

[264] K. Melnikov and A. Vainshtein, *Hadronic light-by-light scattering contribution to the muon anomalous magnetic moment revisited*, *Phys. Rev. D* **70** (2004) 113006, [hep-ph/0312226].

[265] A. Kurz, T. Liu, P. Marquard and M. Steinhauser, *Hadronic contribution to the muon anomalous magnetic moment to next-to-next-to-leading order*, *Phys. Lett.* **B734** (2014) 144–147, [1403.6400].

[266] T. Aoyama et al., *The anomalous magnetic moment of the muon in the Standard Model*, *Phys. Rept.* **887** (2020) 1–166, [2006.04822].

[267] T. Aoyama, M. Hayakawa, T. Kinoshita and M. Nio, *Complete Tenth-Order QED Contribution to the Muon g-2*, *Phys. Rev. Lett.* **109** (2012) 111808, [1205.5370].

[268] T. Aoyama, T. Kinoshita and M. Nio, *Theory of the Anomalous Magnetic Moment of the Electron*, *Atoms* **7** (2019) 28.

[269] A. Czarnecki, W. J. Marciano and A. Vainshtein, *Refinements in electroweak contributions to the muon anomalous magnetic moment*, *Phys. Rev. D* **67** (2003) 073006, [hep-ph/0212229].

[270] A. Keshavarzi, D. Nomura and T. Teubner, *$g-2$ of charged leptons, $\alpha(M_Z^2)$, and the hyperfine splitting of muonium*, *Phys. Rev. D* **101** (2020) 014029, [1911.00367].

[271] M. Davier, A. Hoecker, B. Malaescu and Z. Zhang, *A new evaluation of the hadronic vacuum polarisation contributions to the muon anomalous magnetic moment and to $\boldsymbol{\alpha}(\mathbf{m_Z^2})$*, *Eur. Phys. J. C* **80** (2020) 241, [1908.00921].

[272] M. Hoferichter, B.-L. Hoid and B. Kubis, *Three-pion contribution to hadronic vacuum polarization*, *JHEP* **08** (2019) 137, [1907.01556].

[273] A. Keshavarzi, D. Nomura and T. Teubner, *Muon $g-2$ and $\alpha(M_Z^2)$: a new data-based analysis*, *Phys. Rev.* **D97** (2018) 114025, [1802.02995].

[274] M. Davier, A. Hoecker, B. Malaescu and Z. Zhang, *Reevaluation of the hadronic vacuum polarisation contributions to the Standard Model predictions of the muon $g-2$ and $\alpha(m_Z^2)$ using newest hadronic cross-section data*, *Eur. Phys. J. C* **77** (2017) 827, [1706.09436].

[275] C. Gnendiger, D. Stöckinger and H. Stöckinger-Kim, *The electroweak contributions to $(g-2)_\mu$ after the Higgs boson mass measurement*, *Phys. Rev. D* **88** (2013) 053005, [1306.5546].

[276] J. Bailey, K. Borer, F. Combley, H. Drumm, C. Eck, F. Farley et al., *Final report on the cern muon storage ring including the anomalous magnetic moment and the electric dipole moment of the muon, and a direct test of relativistic time dilation*, *Nuclear Physics B* **150** (1979) 1–75.

[277] G. Charpak, P. Farley, E. Garwin, T. Muller, J. C. Sens and A. Zichichi, *The anomalous magnetic moment of the muon*, *Il Nuovo Cimento (1955-1965)* **37** (1965) 1241–1363.

[278] J. Bailey, W. Bartl, G. von Bochmann, R. Brown, F. Farley and M. Giesch, *Hj ostlein, s. van der meer, e. picasso and rw williams*, *Nuovo Cim. A* **9** (1972) 369.

[279] F. Combley, F. Farley and E. Picasso, *The cern muon (g-2) experiments*, *Physics Reports* **68** (1981) 93–119.

[280] D. T. Wilkinson and H. R. Crane, *Precision measurement of the g factor of the free electron*, *Phys. Rev.* **130** (May, 1963) 852–863.

[281] R. M. Carey et al., *New measurement of the anomalous magnetic moment of the positive muon*, *Phys. Rev. Lett.* **82** (1999) 1632–1635.

[282] MUON (G-2) collaboration, H. N. Brown et al., *Improved measurement of the positive muon anomalous magnetic moment*, *Phys. Rev. D* **62** (2000) 091101, [`hep-ex/0009029`].

[283] MUON G-2 collaboration, H. N. Brown et al., *Precise measurement of the positive muon anomalous magnetic moment*, *Phys. Rev. Lett.* **86** (2001) 2227–2231, [`hep-ex/0102017`].

[284] MUON G-2 collaboration, G. W. Bennett et al., *Measurement of the positive muon anomalous magnetic moment to 0.7 ppm*, *Phys. Rev. Lett.* **89** (2002) 101804, [`hep-ex/0208001`].

[285] MUON G-2 collaboration, G. W. Bennett et al., *Final Report of the Muon E821 Anomalous Magnetic Moment Measurement at BNL*, *Phys. Rev. D* **73** (2006) 072003, [`hep-ex/0602035`].

[286] MUON G-2 collaboration, J. Grange et al., *Muon (g-2) Technical Design Report*, `1501.06858`.

[287] S. Borsanyi et al., *Leading-order hadronic vacuum polarization contribution to the muon magnetic momentfrom lattice QCD*, `2002.12347`.

[288] A. Crivellin, M. Hoferichter, C. A. Manzari and M. Montull, *Hadronic vacuum polarization: $(g-2)_\mu$ versus global electroweak fits*, 2003.04886.

[289] E. Hubble, *A relation between distance and radial velocity among extra-galactic nebulae*, *Proceedings of the national academy of sciences* **15** (1929) 168–173.

[290] E. Abdalla et al., *Cosmology intertwined: A review of the particle physics, astrophysics, and cosmology associated with the cosmological tensions and anomalies*, *JHEAp* **34** (2022) 49–211, [2203.06142].

[291] J. L. Bernal, L. Verde and A. G. Riess, *The trouble with H_0*, *JCAP* **1610** (2016) 019, [1607.05617].

[292] W. L. Freedman et al., *The Carnegie-Chicago Hubble Program. VIII. An Independent Determination of the Hubble Constant Based on the Tip of the Red Giant Branch*, 1907.05922.

[293] E. Aubourg et al., *Cosmological implications of baryon acoustic oscillation measurements*, *Phys. Rev. D* **92** (2015) 123516, [1411.1074].

[294] E. M. L. Humphreys, M. J. Reid, J. M. Moran, L. J. Greenhill and A. L. Argon, *Toward a New Geometric Distance to the Active Galaxy NGC 4258. III. Final Results and the Hubble Constant*, *Astrophys. J.* **775** (2013) 13, [1307.6031].

[295] C. Dvorkin, M. Wyman, D. H. Rudd and W. Hu, *Neutrinos help reconcile Planck measurements with both the early and local Universe*, *Phys. Rev. D* **90** (2014) 083503, [1403.8049].

[296] B. Leistedt, H. V. Peiris and L. Verde, *No new cosmological concordance with massive sterile neutrinos*, *Phys. Rev. Lett.* **113** (2014) 041301, [1404.5950].

[297] Planck collaboration, P. A. R. Ade et al., *Planck 2015 results. XIV. Dark energy and modified gravity*, *Astron. Astrophys.* **594** (2016) A14, [`1502.01590`].

[298] E. Di Valentino, A. Melchiorri and J. Silk, *Reconciling Planck with the local value of H_0 in extended parameter space*, *Phys. Lett. B* **761** (2016) 242–246, [`1606.00634`].

[299] M. Escudero, D. Hooper, G. Krnjaic and M. Pierre, *Cosmology with A Very Light $L_\mu - L_\tau$ Gauge Boson*, *JHEP* **03** (2019) 071, [`1901.02010`].

[300] S. Baek, N. G. Deshpande, X. G. He and P. Ko, *Muon anomalous g-2 and gauged L(muon) - L(tau) models*, *Phys. Rev.* **D64** (2001) 055006, [`hep-ph/0104141`].

[301] E. Ma, D. P. Roy and S. Roy, *Gauged L(mu) - L(tau) with large muon anomalous magnetic moment and the bimaximal mixing of neutrinos*, *Phys. Lett. B* **525** (2002) 101–106, [`hep-ph/0110146`].

[302] M. Bauer, P. Foldenauer and J. Jaeckel, *Hunting All the Hidden Photons*, *JHEP* **07** (2018) 094, [`1803.05466`].

[303] K. Asai, K. Hamaguchi, N. Nagata, S.-Y. Tseng and K. Tsumura, *Minimal Gauged $U(1)_{L_\alpha - L_\beta}$ Models Driven into a Corner*, *Phys. Rev.* **D99** (2019) 055029, [`1811.07571`].

[304] E. J. Chun, A. Das, J. Kim and J. Kim, *Searching for flavored gauge bosons*, *JHEP* **02** (2019) 093, [`1811.04320`].

[305] K. R. Lynch, *A Note on one loop electroweak contributions to g-2: A Companion to BUHEP-01-16*, `hep-ph/0108081`.

[306] M. Pospelov, *Secluded U(1) below the weak scale*, *Phys. Rev. D* **80** (2009) 095002, [`0811.1030`].

[307] W. Altmannshofer, S. Gori, M. Pospelov and I. Yavin, *Neutrino Trident Production: A Powerful Probe of New Physics with Neutrino Beams*, *Phys. Rev. Lett.* **113** (2014) 091801, [`1406.2332`].

[308] CHARM-II collaboration, D. Geiregat et al., *First observation of neutrino trident production*, *Phys. Lett. B* **245** (1990) 271–275.

[309] BaBar collaboration, J. P. Lees et al., *Search for a muonic dark force at BABAR*, *Phys. Rev. D* **94** (2016) 011102, [`1606.03501`].

[310] CMS collaboration, A. M. Sirunyan et al., *Search for an* $L_\mu - L_\tau$ *gauge boson using* $Z \to 4\mu$ *events in proton-proton collisions at* $\sqrt{s} = 13$ *TeV*, *Phys. Lett. B* **792** (2019) 345–368, [`1808.03684`].

[311] D. A. Dicus, E. W. Kolb, A. M. Gleeson, E. C. G. Sudarshan, V. L. Teplitz and M. S. Turner, *Primordial Nucleosynthesis Including Radiative, Coulomb, and Finite Temperature Corrections to Weak Rates*, *Phys. Rev. D* **26** (1982) 2694.

[312] A. D. Dolgov, S. H. Hansen and D. V. Semikoz, *Nonequilibrium corrections to the spectra of massless neutrinos in the early universe*, *Nucl. Phys. B* **503** (1997) 426–444, [`hep-ph/9703315`].

[313] P. F. de Salas and S. Pastor, *Relic neutrino decoupling with flavour oscillations revisited*, *JCAP* **07** (2016) 051, [`1606.06986`].

[314] G. Mangano, G. Miele, S. Pastor, T. Pinto, O. Pisanti and P. D. Serpico, *Relic neutrino decoupling including flavor oscillations*, *Nucl. Phys. B* **729** (2005) 221–234, [`hep-ph/0506164`].

[315] M. Escudero Abenza, *Precision early universe thermodynamics made simple:* $N_{\rm eff}$ *and neutrino decoupling in the Standard Model and beyond*, *JCAP* **05** (2020) 048, [`2001.04466`].

[316] M. Carena, M. Quirós and Y. Zhang, *Dark CP violation and gauged lepton or baryon number for electroweak baryogenesis*, *Phys. Rev. D* **101** (2020) 055014, [1908.04818].

[317] J. A. Dror, R. Lasenby and M. Pospelov, *Dark forces coupled to nonconserved currents*, *Phys. Rev. D* **96** (2017) 075036, [1707.01503].

[318] O. G. Miranda and H. Nunokawa, *Non standard neutrino interactions: current status and future prospects*, *New J. Phys.* **17** (2015) 095002, [1505.06254].

[319] S. Davidson, C. Pena-Garay, N. Rius and A. Santamaria, *Present and future bounds on nonstandard neutrino interactions*, *JHEP* **03** (2003) 011, [hep-ph/0302093].

[320] M. C. Gonzalez-Garcia and M. Maltoni, *Atmospheric neutrino oscillations and new physics*, *Phys. Rev. D* **70** (2004) 033010, [hep-ph/0404085].

[321] T. Ohlsson, *Status of non-standard neutrino interactions*, *Rept. Prog. Phys.* **76** (2013) 044201, [1209.2710].

[322] Y. Farzan and M. Tortola, *Neutrino oscillations and Non-Standard Interactions*, *Front.in Phys.* **6** (2018) 10, [1710.09360].

[323] O. G. Miranda, D. K. Papoulias, G. Sanchez Garcia, O. Sanders, M. Tórtola and J. W. F. Valle, *Implications of the first detection of coherent elastic neutrino-nucleus scattering (CEvNS) with Liquid Argon*, *JHEP* **05** (2020) 130, [2003.12050].

[324] D. K. Papoulias and T. S. Kosmas, *Standard and Nonstandard Neutrino-Nucleus Reactions Cross Sections and Event Rates to Neutrino Detection Experiments*, *Adv. High Energy Phys.* **2015** (2015) 763648, [1502.02928].

[325] COHERENT collaboration, D. Akimov et al., *Observation of Coherent Elastic Neutrino-Nucleus Scattering*, *Science* **357** (2017) 1123–1126, [`1708.01294`].

[326] M. Abdullah, J. B. Dent, B. Dutta, G. L. Kane, S. Liao and L. E. Strigari, *Coherent elastic neutrino nucleus scattering as a probe of a Z' through kinetic and mass mixing effects*, *Phys. Rev.* **D98** (2018) 015005, [`1803.01224`].

[327] H. Banerjee, P. Byakti and S. Roy, *Supersymmetric gauged* $U(1)_{L_\mu - L_\tau}$ *model for neutrinos and the muon* $(g-2)$ *anomaly*, *Phys. Rev.* **D98** (2018) 075022, [`1805.04415`].

[328] D. K. Papoulias, *COHERENT constraints after the Chicago-3 quenching factor measurement*, `1907.11644`.

[329] A. N. Khan and W. Rodejohann, *New physics from COHERENT data with an improved quenching factor*, *Phys. Rev. D* **100** (2019) 113003, [`1907.12444`].

[330] J. Billard, J. Johnston and B. J. Kavanagh, *Prospects for exploring New Physics in Coherent Elastic Neutrino-Nucleus Scattering*, *JCAP* **11** (2018) 016, [`1805.01798`].

[331] D. Aristizabal Sierra, V. De Romeri and N. Rojas, *CP violating effects in coherent elastic neutrino-nucleus scattering processes*, *JHEP* **09** (2019) 069, [`1906.01156`].

[332] V. Brdar, W. Rodejohann and X.-J. Xu, *Producing a new Fermion in Coherent Elastic Neutrino-Nucleus Scattering: from Neutrino Mass to Dark Matter*, *JHEP* **12** (2018) 024, [`1810.03626`].

[333] Y. Farzan, M. Lindner, W. Rodejohann and X.-J. Xu, *Probing neutrino coupling to a light scalar with coherent neutrino scattering*, *JHEP* **05** (2018) 066, [`1802.05171`].

[334] L. J. Flores, N. Nath and E. Peinado, *Non-standard neutrino interactions in U(1)' model after COHERENT data*, *JHEP* **06** (2020) 045, [2002.12342].

[335] P. Coloma, M. C. Gonzalez-Garcia, M. Maltoni and T. Schwetz, *COHERENT Enlightenment of the Neutrino Dark Side*, *Phys. Rev. D* **96** (2017) 115007, [1708.02899].

[336] B. Dutta, S. Liao, S. Sinha and L. E. Strigari, *Searching for Beyond the Standard Model Physics with COHERENT Energy and Timing Data*, *Phys. Rev. Lett.* **123** (2019) 061801, [1903.10666].

[337] P. B. Denton, Y. Farzan and I. M. Shoemaker, *Testing large non-standard neutrino interactions with arbitrary mediator mass after COHERENT data*, *JHEP* **07** (2018) 037, [1804.03660].

[338] O. G. Miranda, D. K. Papoulias, O. Sanders, M. Tórtola and J. W. F. Valle, *Future CEvNS experiments as probes of lepton unitarity and light-sterile neutrinos*, *Phys. Rev. D* **102** (2020) 113014, [2008.02759].

[339] H. Banerjee, B. Dutta and S. Roy, *Probing $L\mu$-$L\tau$ models with CEνNS: A new look at the combined COHERENT CsI and Ar data*, *Phys. Rev. D* **104** (2021) 015015, [2103.10196].

[340] P. Coloma, P. B. Denton, M. C. Gonzalez-Garcia, M. Maltoni and T. Schwetz, *Curtailing the Dark Side in Non-Standard Neutrino Interactions*, *JHEP* **04** (2017) 116, [1701.04828].

[341] D. K. Papoulias, T. S. Kosmas, R. Sahu, V. K. B. Kota and M. Hota, *Constraining nuclear physics parameters with current and future COHERENT data*, *Phys. Lett.* **B800** (2020) 135133, [1903.03722].

[342] N. Grevesse and A. J. Sauval, *Standard Solar Composition*, *Space Sci. Rev.* **85** (1998) 161–174.

[343] P. Scott, M. Asplund, N. Grevesse, M. Bergemann and A. J. Sauval, *The elemental composition of the Sun II. The iron group elements Sc to Ni*, *Astron. Astrophys.* **573** (2015) A26, [1405.0287].

[344] P. Scott, N. Grevesse, M. Asplund, A. J. Sauval, K. Lind, Y. Takeda et al., *The elemental composition of the Sun I. The intermediate mass elements Na to Ca*, *Astron. Astrophys.* **573** (2015) A25, [1405.0279].

[345] S. Vagnozzi, K. Freese and T. H. Zurbuchen, *Solar models in light of new high metallicity measurements from solar wind data*, *Astrophys. J.* **839** (2017) 55, [1603.05960].

[346] D. G. Cerdeno, J. H. Davis, M. Fairbairn and A. C. Vincent, *CNO Neutrino Grand Prix: The race to solve the solar metallicity problem*, *JCAP* **1804** (2018) 037, [1712.06522].

[347] Borexino collaboration, M. Agostini et al., *Improved measurement of ^8B solar neutrinos with* 1.5ktůy *of Borexino exposure*, *Phys. Rev. D* **101** (2020) 062001, [1709.00756].

[348] Borexino collaboration, M. Agostini et al., *First Simultaneous Precision Spectroscopy of pp, ^{7}Be, and pep Solar Neutrinos with Borexino Phase-II*, *Phys. Rev. D* **100** (2019) 082004, [1707.09279].

[349] Super-Kamiokande collaboration, K. Abe et al., *Solar Neutrino Measurements in Super-Kamiokande-IV*, *Phys. Rev.* **D94** (2016) 052010, [1606.07538].

[350] SNO collaboration, B. Aharmim et al., *Combined Analysis of all Three Phases of Solar Neutrino Data from the Sudbury Neutrino Observatory*, *Phys. Rev.* **C88** (2013) 025501, [1109.0763].

[351] KamLAND collaboration, A. Gando et al., *Reactor On-Off Antineutrino Measurement with KamLAND*, *Phys. Rev.* **D88** (2013) 033001, [1303.4667].

[352] BOREXINO collaboration, M. Agostini et al., *First Directional Measurement of Sub-MeV Solar Neutrinos with Borexino*, *Phys. Rev. Lett.* **128** (2022) 091803, [2112.11816].

[353] Y. Kaneta and T. Shimomura, *On the possibility of a search for the $L_\mu - L_\tau$ gauge boson at Belle-II and neutrino beam experiments*, *PTEP* **2017** (2017) 053B04, [1701.00156].

[354] M. C. Gonzalez-Garcia, M. Maltoni, Y. F. Perez-Gonzalez and R. Zukanovich Funchal, *Neutrino Discovery Limit of Dark Matter Direct Detection Experiments in the Presence of Non-Standard Interactions*, *JHEP* **07** (2018) 019, [1803.03650].

[355] F. Takahashi, M. Yamada and W. Yin, *XENON1T Excess from Anomaly-Free Axionlike Dark Matter and Its Implications for Stellar Cooling Anomaly*, *Phys. Rev. Lett.* **125** (2020) 161801, [2006.10035].

[356] K. Kannike, M. Raidal, H. Veermäe, A. Strumia and D. Teresi, *Dark Matter and the XENON1T electron recoil excess*, *Phys. Rev. D* **102** (2020) 095002, [2006.10735].

[357] C. Boehm, D. G. Cerdeno, M. Fairbairn, P. A. N. Machado and A. C. Vincent, *Light new physics in XENON1T*, *Phys. Rev. D* **102** (2020) 115013, [2006.11250].

[358] G. Alonso-Álvarez, F. Ertas, J. Jaeckel, F. Kahlhoefer and L. J. Thormaehlen, *Hidden Photon Dark Matter in the Light of XENON1T and Stellar Cooling*, *JCAP* **11** (2020) 029, [2006.11243].

[359] B. Fornal, P. Sandick, J. Shu, M. Su and Y. Zhao, *Boosted Dark Matter Interpretation of the XENON1T Excess*, *Phys. Rev. Lett.* **125** (2020) 161804, [2006.11264].

[360] M. Du, J. Liang, Z. Liu, V. Q. Tran and Y. Xue, *On-shell mediator dark matter models and the Xenon1T excess*, *Chin. Phys. C* **45** (2021) 013114, [2006.11949].

[361] L. Su, W. Wang, L. Wu, J. M. Yang and B. Zhu, *Atmospheric Dark Matter and Xenon1T Excess*, *Phys. Rev. D* **102** (2020) 115028, [2006.11837].

[362] A. Bally, S. Jana and A. Trautner, *Neutrino self-interactions and XENON1T electron recoil excess*, *Phys. Rev. Lett.* **125** (2020) 161802, [2006.11919].

[363] K. Harigaya, Y. Nakai and M. Suzuki, *Inelastic Dark Matter Electron Scattering and the XENON1T Excess*, *Phys. Lett. B* **809** (2020) 135729, [2006.11938].

[364] U. K. Dey, T. N. Maity and T. S. Ray, *Prospects of Migdal Effect in the Explanation of XENON1T Electron Recoil Excess*, *Phys. Lett. B* **811** (2020) 135900, [2006.12529].

[365] G. Paz, A. A. Petrov, M. Tammaro and J. Zupan, *Shining dark matter in Xenon1T*, *Phys. Rev. D* **103** (2021) L051703, [2006.12462].

[366] Y. Chen, M.-Y. Cui, J. Shu, X. Xue, G.-W. Yuan and Q. Yuan, *Sun heated MeV-scale dark matter and the XENON1T electron recoil excess*, *JHEP* **04** (2021) 282, [2006.12447].

[367] N. F. Bell, J. B. Dent, B. Dutta, S. Ghosh, J. Kumar and J. L. Newstead, *Explaining the XENON1T excess with Luminous Dark Matter*, *Phys. Rev. Lett.* **125** (2020) 161803, [2006.12461].

[368] D. Aristizabal Sierra, V. De Romeri, L. J. Flores and D. K. Papoulias, *Light vector mediators facing XENON1T data*, *Phys. Lett. B* **809** (2020) 135681, [2006.12457].

[369] S.-M. Choi, H. M. Lee and B. Zhu, *Exothermic dark mesons in light of electron recoil excess at XENON1T*, *JHEP* **04** (2021) 251, [2012.03713].

[370] H. M. Lee, *Exothermic dark matter for XENON1T excess*, *JHEP* **01** (2021) 019, [2006.13183].

[371] A. N. Khan, *Can Nonstandard Neutrino Interactions explain the XENON1T spectral excess?*, *Phys. Lett. B* **809** (2020) 135782, [2006.12887].

[372] J. Bramante and N. Song, *Electric But Not Eclectic: Thermal Relic Dark Matter for the XENON1T Excess*, *Phys. Rev. Lett.* **125** (2020) 161805, [2006.14089].

[373] C. Gao, J. Liu, L.-T. Wang, X.-P. Wang, W. Xue and Y.-M. Zhong, *Reexamining the Solar Axion Explanation for the XENON1T Excess*, *Phys. Rev. Lett.* **125** (2020) 131806, [2006.14598].

[374] L. Zu, G.-W. Yuan, L. Feng and Y.-Z. Fan, *Mirror Dark Matter and Electronic Recoil Events in XENON1T*, *Nucl. Phys. B* **965** (2021) 115369, [2006.14577].

[375] M. Lindner, Y. Mambrini, T. B. de Melo and F. S. Queiroz, *XENON1T anomaly: A light Z' from a Two Higgs Doublet Model*, *Phys. Lett. B* **811** (2020) 135972, [2006.14590].

[376] A. E. Robinson, *XENON1T observes tritium*, 2006.13278.

[377] H. Alhazmi, D. Kim, K. Kong, G. Mohlabeng, J.-C. Park and S. Shin, *Implications of the XENON1T Excess on the Dark Matter Interpretation*, *JHEP* **05** (2021) 055, [2006.16252].

[378] W. Chao, Y. Gao and M. j. Jin, *Pseudo-Dirac Dark Matter in XENON1T*, 2006.16145.

[379] P. Ko and Y. Tang, *Semi-annihilating Z_3 dark matter for XENON1T excess*, *Phys. Lett. B* **815** (2021) 136181, [2006.15822].

[380] B. Bhattacherjee and R. Sengupta, *XENON1T Excess: Some Possible Backgrounds*, *Phys. Lett. B* **817** (2021) 136305, [2006.16172].

[381] T. Li, *The KSVZ Axion and Pseudo-Nambu-Goldstone Boson Models for the XENON1T Excess*, `2007.00874`.

[382] O. G. Miranda, D. K. Papoulias, M. Tórtola and J. W. F. Valle, *XENON1T signal from transition neutrino magnetic moments*, *Phys. Lett. B* **808** (2020) 135685, [`2007.01765`].

[383] N. Okada, S. Okada, D. Raut and Q. Shafi, *Dark matter Z' and XENON1T excess from $U(1)_X$ extended standard model*, *Phys. Lett. B* **810** (2020) 135785, [`2007.02898`].

[384] G. Choi, T. T. Yanagida and N. Yokozaki, *Feebly interacting $U(1)_{BL}$ gauge boson warm dark matter and XENON1T anomaly*, *Phys. Lett. B* **810** (2020) 135836, [`2007.04278`].

[385] S. Baek, J. Kim and P. Ko, *XENON1T excess in local Z_2 DM models with light dark sector*, *Phys. Lett. B* **810** (2020) 135848, [`2006.16876`].

[386] P. Athron et al., *Global fits of axion-like particles to XENON1T and astrophysical data*, *JHEP* **05** (2021) 159, [`2007.05517`].

[387] I. M. Shoemaker, Y.-D. Tsai and J. Wyenberg, *Active-to-sterile neutrino dipole portal and the XENON1T excess*, *Phys. Rev. D* **104** (2021) 115026, [`2007.05513`].

[388] C.-W. Chiang and B.-Q. Lu, *Evidence of a simple dark sector from XENON1T excess*, *Phys. Rev. D* **102** (2020) 123006, [`2007.06401`].

[389] G. Arcadi, A. Bally, F. Goertz, K. Tame-Narvaez, V. Tenorth and S. Vogl, *EFT interpretation of XENON1T electron recoil excess: Neutrinos and dark matter*, *Phys. Rev. D* **103** (2021) 023024, [`2007.08500`].

[390] J. Cao, X. Du, Z. Li, F. Wang and Y. Zhang, *Explaining The XENON1T Excess With Light Goldstini Dark Matter*, `2007.09981`.

[391] J. Kim, T. Nomura and H. Okada, *A radiative seesaw model linking to XENON1T anomaly*, *Phys. Lett. B* **811** (2020) 135862, [2007.09894].

[392] S. Karmakar and S. Pandey, *XENON1T constraints on neutrino non-standard interactions*, 2007.11892.

[393] S. Khan, *Explaining Xenon-1T signal with FIMP dark matter and neutrino mass in a $U(1)_X$ extension*, *Eur. Phys. J. C* **81** (2021) 598, [2007.13008].

[394] D. Borah, S. Mahapatra, D. Nanda and N. Sahu, *Inelastic fermion dark matter origin of XENON1T excess with muon $(g-2)$ and light neutrino mass*, *Phys. Lett. B* **811** (2020) 135933, [2007.10754].

[395] Y. Farzan and M. Rajaee, *Pico-charged particles explaining 511 keV line and XENON1T signal*, *Phys. Rev. D* **102** (2020) 103532, [2007.14421].

[396] L. Zu, R. Foot, Y.-Z. Fan and L. Feng, *Plasma dark matter and electronic recoil events in XENON1T*, *JCAP* **01** (2021) 070, [2007.15191].

[397] V. V. Khruschov, *Interpretation of the XENON1T excess in the model with decaying sterile neutrinos*, 2008.03150.

[398] S. Shakeri, F. Hajkarim and S.-S. Xue, *Shedding New Light on Sterile Neutrinos from XENON1T Experiment*, *JHEP* **12** (2020) 194, [2008.05029].

[399] S. Chakraborty, T. H. Jung, V. Loladze, T. Okui and K. Tobioka, *Solar origin of the XENON1T excess without stellar cooling problems*, *Phys. Rev. D* **102** (2020) 095029, [2008.10610].

[400] A. Aboubrahim, M. Klasen and P. Nath, *Xenon-1T excess as a possible signal of a sub-GeV hidden sector dark matter*, *JHEP* **02** (2021) 229, [2011.08053].

[401] D. Buttazzo, P. Panci, D. Teresi and R. Ziegler, *Xenon1T excess from electron recoils of non-relativistic Dark Matter*, *Phys. Lett. B* **817** (2021) 136310, [2011.08919].

[402] L.-B. Jia and T. Li, *Interpretation of XENON1T excess with MeV boosted dark matter*, 2012.07209.

[403] S. Xu and S. Zheng, *Resolving XENON Excess With Decaying Cold Dark Matter*, *Eur. Phys. J. C* **81** (2021) 446, [2012.10827].

[404] M. Dutta, S. Mahapatra, D. Borah and N. Sahu, *Self-interacting Inelastic Dark Matter in the light of XENON1T excess*, *Phys. Rev. D* **103** (2021) 095018, [2101.06472].

[405] K. Dutta, A. Ghosh, A. Kar and B. Mukhopadhyaya, *Decaying fermionic warm dark matter and XENON1T electronic recoil excess*, *Phys. Dark Univ.* **33** (2021) 100855, [2103.14664].

[406] D. Borah, M. Dutta, S. Mahapatra and N. Sahu, *Muon (g−2) and XENON1T excess with boosted dark matter in* $L\mu - L\tau$ *model*, *Phys. Lett. B* **820** (2021) 136577, [2104.05656].

[407] S. Baek, *Inelastic dark matter, small scale problems, and the XENON1T excess*, *JHEP* **10** (2021) 135, [2105.00877].

[408] D. Borah, M. Dutta, S. Mahapatra and N. Sahu, *Boosted self-interacting dark matter and XENON1T excess*, *Nucl. Phys. B* **979** (2022) 115787, [2107.13176].

[409] Y. Farzan, *A dark matter solution for the XENON1T electron excess and the galactic center 511 keV line*, in *16th Marcel Grossmann Meeting on Recent Developments in Theoretical and Experimental General Relativity, Astrophysics and Relativistic Field Theories*, 10, 2021, 2110.07219.

[410] LUX collaboration, D. S. Akerib et al., *Improved Limits on Scattering of Weakly Interacting Massive Particles from Reanalysis of 2013 LUX Data*, *Phys. Rev. Lett.* **116** (2016) 161301, [1512.03506].

[411] LUX collaboration, D. S. Akerib et al., *Extending light WIMP searches to single scintillation photons in LUX*, *Phys. Rev.* **D101** (2020) 042001, [1907.06272].

[412] XENON collaboration, E. Aprile et al., *Low-mass dark matter search using ionization signals in XENON100*, *Phys. Rev.* **D94** (2016) 092001, [1605.06262].

[413] PandaX collaboration, X. Cao et al., *PandaX: A Liquid Xenon Dark Matter Experiment at CJPL*, *Sci. China Phys. Mech. Astron.* **57** (2014) 1476–1494, [1405.2882].

[414] B. Lenardo et al., *Measurement of the ionization yield from nuclear recoils in liquid xenon between 0.3 - 6 keV with single-ionization-electron sensitivity*, 1908.00518.

[415] DarkSide collaboration, P. Agnes et al., *Low-Mass Dark Matter Search with the DarkSide-50 Experiment*, *Phys. Rev. Lett.* **121** (2018) 081307, [1802.06994].

[416] S. Bilmis, I. Turan, T. M. Aliev, M. Deniz, L. Singh and H. T. Wong, *Constraints on Dark Photon from Neutrino-Electron Scattering Experiments*, *Phys. Rev.* **D92** (2015) 033009, [1502.07763].

[417] G. Krnjaic, G. Marques-Tavares, D. Redigolo and K. Tobioka, *Probing Muonphilic Force Carriers and Dark Matter at Kaon Factories*, *Phys. Rev. Lett.* **124** (2020) 041802, [1902.07715].

[418] P. Ballett, M. Hostert, S. Pascoli, Y. F. Perez-Gonzalez, Z. Tabrizi and R. Zukanovich Funchal, *Z's in neutrino scattering at DUNE*, *Phys. Rev. D* **100** (2019) 055012, [1902.08579].

[419] W. Altmannshofer, S. Gori, J. Martín-Albo, A. Sousa and M. Wallbank, *Neutrino Tridents at DUNE*, *Phys. Rev. D* **100** (2019) 115029, [1902.06765].

[420] G. t. s. i. c. o. b. p. Cowan, ionisation electrons., K. Cranmer, E. Gross and O. Vitells, *Asymptotic formulae for likelihood-based tests of new physics*, *Eur. Phys. J. C* **71** (2011) 1554, [1007.1727].

[421] Y. Kahn, G. Krnjaic, N. Tran and A. Whitbeck, *M^3: a new muon missing momentum experiment to probe $(g-2)_\mu$ and dark matter at Fermilab*, *JHEP* **09** (2018) 153, [1804.03144].

[422] S. N. Gninenko, N. V. Krasnikov and V. A. Matveev, *Search for dark sector physics with NA64*, *Phys. Part. Nucl.* **51** (2020) 829–858, [2003.07257].

[423] H. Sieber, D. Banerjee, P. Crivelli, E. Depero, S. N. Gninenko, D. V. Kirpichnikov et al., *Prospects in the search for a new light Z' boson with the NA64μ experiment at the CERN SPS*, *Phys. Rev. D* **105** (2022) 052006, [2110.15111].

[424] Y.-S. Tsai, *AXION BREMSSTRAHLUNG BY AN ELECTRON BEAM*, *Phys. Rev. D* **34** (1986) 1326.

[425] K. J. Kim and Y.-S. Tsai, *IMPROVED WEIZSACKER-WILLIAMS METHOD AND ITS APPLICATION TO LEPTON AND W BOSON PAIR PRODUCTION*, *Phys. Rev. D* **8** (1973) 3109.

[426] J. D. Bjorken, R. Essig, P. Schuster and N. Toro, *New Fixed-Target Experiments to Search for Dark Gauge Forces*, *Phys. Rev. D* **80** (2009) 075018, [0906.0580].

[427] S. N. Gninenko, N. V. Krasnikov and V. A. Matveev, *Muon g-2 and searches for a new leptophobic sub-GeV dark boson in a missing-energy experiment at CERN*, *Phys. Rev. D* **91** (2015) 095015, [1412.1400].

[428] XENON collaboration, E. Aprile et al., *Dark Matter Search Results from a One Ton-Year Exposure of XENON1T*, *Phys. Rev. Lett.* **121** (2018) 111302, [1805.12562].

[429] P. Coloma, I. Esteban, M. C. Gonzalez-Garcia, L. Larizgoitia, F. Monrabal and S. Palomares-Ruiz, *Bounds on new physics with data of the Dresden-II reactor experiment and COHERENT*, *JHEP* **05** (2022) 037, [2202.10829].

[430] E. Lisi, A. Marrone, D. Montanino, A. Palazzo and S. T. Petcov, *Analytical description of quasivacuum oscillations of solar neutrinos*, *Phys. Rev. D* **63** (2001) 093002, [hep-ph/0011306].

[431] A. Friedland, *On the evolution of the neutrino state inside the sun*, *Phys. Rev. D* **64** (2001) 013008, [hep-ph/0010231].

[432] D. Aristizabal Sierra, N. Rojas and M. H. G. Tytgat, *Neutrino non-standard interactions and dark matter searches with multi-ton scale detectors*, *JHEP* **03** (2018) 197, [1712.09667].

[433] A. N. Khan, W. Rodejohann and X.-J. Xu, *Borexino and general neutrino interactions*, *Phys. Rev. D* **101** (2020) 055047, [1906.12102].

[434] S. Haselschwardt, B. Lenardo, P. Pirinen and J. Suhonen, *Solar neutrino detection in liquid xenon detectors via charged-current scattering to excited states*, *Phys. Rev. D* **102** (2020) 072009, [2009.00535].

[435] J. Meija, T. B. Coplen, M. Berglund, W. A. Brand, P. De Bièvre, M. Gröning et al., *Isotopic compositions of the elements 2013 (iupac technical report)*, *Pure and Applied Chemistry* **88** (2016) 293–306.

[436] J. Bergstrom, M. C. Gonzalez-Garcia, M. Maltoni, C. Pena-Garay, A. M. Serenelli and N. Song, *Updated determination of the solar neutrino fluxes from solar neutrino data*, *JHEP* **03** (2016) 132, [1601.00972].

[437] JUNO collaboration, Z. Djurcic et al., *JUNO Conceptual Design Report*, 1508.07166.

[438] P. Martínez-Miravé, S. M. Sedgwick and M. Tórtola, *Nonstandard interactions from the future neutrino solar sector*, *Phys. Rev. D* **105** (2022) 035004, [`2111.03031`].

[439] COHERENT collaboration, D. Akimov et al., *COHERENT Collaboration data release from the first observation of coherent elastic neutrino-nucleus scattering*, `1804.09459`.

[440] Super-Kamiokande collaboration, R. Wendell, *Atmospheric Results from Super-Kamiokande*, *AIP Conf. Proc.* **1666** (2015) 100001, [`1412.5234`].

[441] IceCube collaboration, M. G. Aartsen et al., *Determining neutrino oscillation parameters from atmospheric muon neutrino disappearance with three years of IceCube DeepCore data*, *Phys. Rev. D* **91** (2015) 072004, [`1410.7227`].

[442] IceCube collaboration, M. G. Aartsen et al., *Searches for Sterile Neutrinos with the IceCube Detector*, *Phys. Rev. Lett.* **117** (2016) 071801, [`1605.01990`].

[443] A. Bolanos, O. G. Miranda, A. Palazzo, M. A. Tortola and J. W. F. Valle, *Probing non-standard neutrino-electron interactions with solar and reactor neutrinos*, *Phys. Rev.* **D79** (2009) 113012, [`0812.4417`].

[444] S. K. Agarwalla, F. Lombardi and T. Takeuchi, *Constraining Non-Standard Interactions of the Neutrino with Borexino*, *JHEP* **12** (2012) 079, [`1207.3492`].

[445] M. C. Gonzalez-Garcia, M. Maltoni and J. Salvado, *Testing matter effects in propagation of atmospheric and long-baseline neutrinos*, *JHEP* **05** (2011) 075, [`1103.4365`].

[446] TEXONO collaboration, M. Deniz et al., *Constraints on Non-Standard Neutrino Interactions and Unparticle Physics with Neutrino-Electron*

Scattering at the Kuo-Sheng Nuclear Power Reactor, *Phys. Rev. D* **82** (2010) 033004, [`1006.1947`].